Doctoral Dissertations (All Dissertations, All Years)   Electronic Theses and Dissertations

2007-04-20

Development and Validation of a Method of Moments approach for modeling planar antenna structures

Shashank D. Kulkarni
Worcester Polytechnic Institute

DEVELOPMENT AND VALIDATION OF A METHOD OF MOMENTS APPROACH FOR MODELING PLANAR ANTENNA STRUCTURES

by

Shashank Kulkarni

A Dissertation

Submitted to the Faculty

of the

WORCESTER POLYTECHNIC INSTITUTE

in partial fulfillment of the requirements for the

Degree of Doctor of Philosophy

in

Electrical and Computer Engineering

13th April 2007

Abstract

In this dissertation, a Method of Moments (MoM) Volume Integral Equation (VIE)-based modeling approach suitable for a patch or slot antenna on a thin finite dielectric substrate is developed and validated. Two new key features of this method are the use of proper dielectric basis functions and proper VIE conditioning, close to the metal surface, where the surface boundary condition of the zero tangential-component must be extended into adjacent tetrahedra. The extended boundary condition is the exact result for the piecewise-constant dielectric basis functions. The latter operation allows one to achieve a good accuracy with one layer of tetrahedra for a thin dielectric substrate and thereby greatly reduces computational cost. The use of low-order basis functions also implies the use of low-order integration schemes and faster filling of the impedance matrix. For some common patch/slot antennas, the VIE-based modeling approach is found to give an error of about 1% or less in the resonant frequency for one-layer tetrahedral meshes with a relatively small number of unknowns. This error is obtained by comparison with fine finite- element method (FEM) simulations, or with measurements, or with the analytical mode matching approach. Hence it is competitive with both the method of moments surface integral equation approach and with the FEM approach for the printed antennas on thin dielectric substrates.

Along with the MoM development, the dissertation also presents the models and design procedures for a number of practical antenna configurations. They in particular include:

   i.   a compact linearly polarized broadband planar inverted-F antenna (PIFA);

  ii.   a circularly polarized turnstile bowtie antenna.

Both the antennas are designed to operate in the low UHF band and used for indoor positioning/indoor geolocation.

Acknowledgement

Table of Contents

List of Figures

List of Tables

List of Symbols

V	Dielectric volume
Ω	Boundary of dielectric volume V
S	Metal surface
$\vec{f}_n^M$	Basis function corresponding to the nth RWG element
$\vec{\rho}_n^+$	Vector drawn from free vertex of triangle t_n^+ to the observation point
$\vec{\rho}_n^-$	Vector drawn from observation point to the free vertex of triangle t_n^-
l_n	Length of the nth basis function
$\vec{r}$	Position vector of observation point
$\vec{r}'$	Position vector of integration point
t_n^+	Plus triangle corresponding to the nth RWG element
t_n^-	Minus triangle corresponding to the nth RWG element
$\vec{f}_n$	Basis function corresponding to the nth Edge element
V_n	Volume of tetrahedron corresponding to the nth edge basis
$K_\pm$	Dielectric contrast
$\hat{K}_q$	Differential contrast on face q
$\vec{S}_{mp}$	Area of projection of face p onto a plane perpendicular to edge m
S_q	Area of face q
$\vec{p}$	Vector variation for the edge basis
N_M	Total number of RWG basis
N_D	Total number of edge basis
$\vec{f}_{\perp nq}$	Normal component of basis function $\vec{f}_n$ on face q
$g(\vec{r}, \vec{r}')$	Free space Green's function
D	Total electric flux
$\vec{A}$	Magnetic vector potential

Φ	Electric scalar potential
$\vec{J}$	Surface current density
$\vec{J}_V$	Volume polarization current
σ_S	Surface charge density
υ	Voltage vector
R	Dimensionless radius

List of Abbreviations

CEM	Computational Electromagnetics
IE	Integral Equation
DE	Differential Equation
TD	Time Domain
FD	Frequency Domain
TDDE	Time Domain Differential Equations
TDIE	Time Domain Integral Equation
FDIE	Frequency Domain Integral Equation
FDDE	Frequency Domain Differential Equation
MoM	Method of Moments
VIE	Volume Integral Equation
SIE	Surface Integral Equation
FEM	Finite Element Method
FDTD	Finite Difference Time Domain
IFA	Inverted-F antenna
PIFA	Planar inverted-F antenna
RWG	Rao-Wilton-Glisson basis functions
SWG	Schaubert-Wilton-Glisson basis functions
HFSS	High Frequency Structure Simulator
UHF	Ultra High Frequency
LP	Linear Polarization
CP	Circular Polarization
RHCP	Right Hand Circular Polarization
LHCP	Left Hand Circular Polarization

ISM	Industrial Scientific and Medical radio bands
TE	Transverse Electric
TM	Transverse Magnetic
TEM	Transverse Electromagnetic
DR	Dielectric Resonator
MKL	Math Kernel Library

1 Introduction

Wireless communications have progressed very rapidly in recent years, and many mobile devices are becoming smaller and smaller. To meet the miniaturization requirement, the antennas employed in mobile terminals must have their dimensions reduced accordingly. Planar antennas, such as microstrip and printed antennas have the attractive features of low profile, small size, and conformability to mounting hosts. These features make the planar antennas promising candidates for satisfying the design consideration mentioned above [1]. For this reason, compact and broadband design techniques for planar antennas have attracted much attention from antenna researchers. However, this has resulted in the antenna shapes getting more complex and analytical models for analyzing these structures are often not available. For these antennas, modeling can only be carried out by using numerical methods i.e. computational electromagnetics (CEM). In these methods the Maxwell's equations are transformed into matrix or chain equations and solved iteratively or by matrix inversion. Furthermore, accurate modeling of such antennas often demands the full-wave analysis i.e. fields and currents vary in three dimensional spaces. This chapter is organized as follows. Section 1.1 gives a short review of computational electromagnetics and a basic introduction to Method of Moments. Section 1.2 gives a review of the common planar antenna structures like the patch antenna and the planar inverted-F antenna. Section 2.3 gives the contributions of this dissertation.

1.1 Review of computational electromagnetics

Computational Electromagnetics has evolved rapidly during the past decade to a point where extremely accurate predictions can be made for very general scattering and antenna structures [2]. In general, all the available methods may be classified broadly into two categories, viz. a) differential equation (DE) solution methods and b) integral equation (IE) methods.

Although the Maxwell equations are usually first encountered in the time domain (TD), i.e. with time as an explicit variable, until relatively recently, most electromagnetic research has taken place in the frequency domain (FD) where time-harmonic behavior is assumed [3]. A principal reason for favoring the FD over the TD in the pre-computer era had been that a FD approach was generally more tractable analytically. Furthermore, the experimental hardware available for making measurements in past years was largely confined to the FD [3].

Since the beginning of computational electromagnetics in the early 1960s, there has been a steady growth in both TD and FD modeling. This section is an attempt to summarize the current status of computational electromagnetic modeling.

1.1.1 <u>Modeling choices in CEM</u>

There are four major, first-principles, models in CEM [2]

i. Time Domain Differential Equation (TDDE) models, the use of which has increased tremendously over the past several years, primarily as a result of much larger and faster computers. The Finite difference time domain (FDTD) method uses the TDDE model. Computer Simulation Technology's Microwave Studio (http://www.cst.com/) is a commercially available FDTD simulator.

ii. Time Domain Integral Equation (TDIE) models, although available for well over 30 years, have gained increased attention in the last decade. Their use was not initially widespread because they tended to be unstable and computationally expensive.

iii. Frequency Domain Integral Equation (FDIE) models which remain the most widely studied and used models, as they were the first to receive detailed development. Method of Moments (MoM) uses the FDIE model. Agilent Momentum (http://eesof.tm.agilent.com/products/momentum_main.html) and FEKO (http://www.feko.info/) are the commercially available MoM solvers.

iv. Frequency Domain Differential Equation (FDDE) models whose use has also increased considerably in recent years. The Finite Element Method (FEM) uses the FDDE model. Ansoft HFSS (http://www.ansoft.com/products/hf/hfss/) is a commercially available FEM simulator.

These four choices can actually be narrowed down to two choices, i.e. a) IE models and b) DE models, depending on the mathematical formulation. Some basic differences between DE and IE models are as follows [2, 4]

i. In general, the differential equation methods generate a sparse matrix, while the integral equation methods generate full matrices.

ii. Homogeneous/inhomogeneous/anisotropic materials can be handled in a relatively simple manner using the DE method, while the level of complexity for the integral equation methods varies enormously for each of these cases.

iii. The code implementation is straightforward for DE methods. This is usually not the case for integral equation methods.

iv. For DE methods, the solution space includes the object's surroundings; the radiation condition is not enforced in exact sense, thus leading to certain error in the solution. For the IE solution, the solution space is confined to the object and the radiation condition is automatically enforced by using the corresponding Green's function.

v. The IE solutions are generally more accurate and efficient.

vi. Spurious solutions (numerical instability) exist in DE methods whereas such solutions are absent in IE methods.

1.1.2 General aspects of CEM modeling

For any numerical solution, it is necessary to develop the required equations and solve them on a computer. The equations thus developed must include the physics of the problem as well as the geometrical features.

The following four steps are carried out in CEM problems [2]

i.   Develop integral equations using potential theory along with appropriate boundary conditions or alternatively, begin with the time-dependent Maxwell equations or their equivalent to develop methods such as FDTD or FEM.

ii.   Sample these equations in space, and also in time if it is a time-dependent equation, utilizing an appropriate geometrical space grid and suitable basis and testing functions. Note that, depending on the choice of formulation, the space grid may cover the structure and/or the surrounding space.

iii.   Develop a set of simultaneous equations relating known and unknown quantities. Generally, the known and unknown quantities are the excitation field or its derivatives and the radiated/scattered field or induced current and charge, respectively.

iv.   Generate a computer solution of this system in space and time as an initial-value problem.

1.1.3   Integral equation solution in CEM

Mathematically speaking, an equation involving the integral of an unknown function of one or more variables is known as integral equation. One of the most common integral equations encountered in electrical engineering is the convolution integral given by

$$\int X(\tau)H(t,\tau)d\tau = Y(t) \tag{1.1.1}$$

In eq. (1.1.1), we note that the response function $Y(t)$ and the system function $H(t,\tau)$ are known and we need to determine the input $X(\tau)$. Of course, if $X(\tau)$ and $H(t,\tau)$ are known and we need to determine $Y(t)$, then eq. (1.1.1) simply represents an integral relationship which can be performed in a straightforward manner. We further note that $H(t,\tau)$ is also commonly known as impulse response if eq. (1.1.1) represents the system response of a linear system. In general, in mathematics and in engineering literature,

$H(t, \tau)$ is known as Green's function or kernel function. For some other physical systems $Y(t)$ and $X(\tau)$ may represent the driving force and response functions, respectively. Eq. (1.1.1) is known as integral equation of first kind. We also have another type of integral equation given by

$$C_1 X(t) + C_2 \int X(\tau) H(t, \tau) d\tau = Y(t) \qquad (1.1.2)$$

where C_1 and C_2 are constants.

In eq. (1.1.2), we note that the unknown function X(t) appears both inside and outside the integral sign. Such equation is known as the integral equation of second kind. Further, we also see in electrical engineering yet another type of integral equation given by

$$C_1 X(t) + C_2 \int X(\tau) H(t, \tau) d\tau + C_3 \frac{dX(t)}{dt} = Y(t) \qquad (1.1.3)$$

which is known as integro-differential equation.

For the majority of practical problems, these equations can be solved using numerical methods only. Fortunately we can obtain very accurate numerical solutions owing to the availability of fast digital computers. In the following section, we discuss a general numerical technique, popularly known as Method of Moments, to solve the integral equations (1.1.1)–(1.1.3).

1.1.4 **Method of Moments**

The MoM solution procedure was first applied to electromagnetic scattering problems by Harrington [5]. Consider a linear operator equation given by

$$\hat{A} X = Y \qquad (1.1.4)$$

where $\hat{A}$ represents the integral operator, Y is the known excitation function and X is the unknown response function to be determined. Now, let X be represented by a set of

known functions, termed as basis functions or expansion functions $(p_1, p_2, p_3, \ldots)$ in the domain of $\hat{A}$ as a linear combination:

$$X = \sum_{i=1}^{N} \alpha_i p_i \tag{1.1.5}$$

where $\alpha_i's$ are scalar constants to be determined. Substituting eq. (1.1.5) into eq. (1.1.4), and using the linearity of $\hat{A}$, we have

$$\sum_{i=1}^{N} \alpha_i \hat{A} p_i = Y \tag{1.1.6}$$

where the equality is usually approximate. Let $(q_1, q_2, q_3, \ldots)$ define a set of testing functions in the range of $\hat{A}$. Now, multiplying eq. (1.1.6) with each q_i and using the linearity property of the inner product, we obtain

$$\sum_{i=1}^{N} \alpha_i \left\langle q_i, \hat{A} p_i \right\rangle = \left\langle q_j, Y \right\rangle \tag{1.1.7}$$

for $j = 1, 2, \cdots, N$. The set of linear equations represented by eq. (1.1.7) may be solved using simple matrix methods to obtain the unknown coefficients $\alpha_i's$.

The simplicity of the method lies in choosing the proper set of expansion and testing functions to solve the problem at hand. Further, the method provides a most accurate result if properly applied. While applying the method of moments to complex practical problems, the solution region, in general, is divided into triangular or rectangular sub domains. Then, one can define suitable basis and testing functions and develop a general algorithm to solve the electromagnetic problem.

As noted in the previous section, the MoM method results in full complex matrices whose storage and computational requirements become prohibitive as the size of the structure increases. Often trade-offs must be made between accuracy and computational efforts as well as memory requirements. For complex geometries such decisions become

even more critical. One of the ways to make the code faster is by using parallel processing architecture. Researchers have investigated a scheme of generating the full impedance matrix of the MoM method by partitioning out on a row-by-row or a column-by-column basis to a suite of processors [6]. Since the computational burden on each row or column is nearly identical, the load balance between processors will be excellent. Researchers have also investigated parallel LU decomposition algorithms [7] for solving dense matrices. Another way to make the code faster is to select the proper basis function to approximate the unknown quantity.

1.2 Review of basic planar antennas

The most commonly used planar antennas in communication industry are the microstrip patch antenna and the planar inverted-F antenna. These antennas are increasing in popularity for use in wireless applications due to their low-profile structure. They can be easily integrated on the circuit board of a communication device to reduce the packaging cost [8, 9]. Therefore they are extremely compatible for embedded antennas in handheld wireless devices such as cellular phones, pagers, laptops, tablet PC's, PDA's etc [10-12]. The telemetry and communication antennas on missiles need to be thin and conformal and are often planar antennas [13-15]. Radar altimeters use small arrays of planar antennas. Another area where they have been used successfully is in satellite communication [16-22] and satellite imaging systems [9]. Smart weapon systems use planar antennas because of their thin profile [9]. Novel planar antenna designs for achieving broadband circular polarization and dual polarized radiation in the WLAN band for overcoming the multipath fading problem to enhance the system performance have been recently demonstrated [8, 23]. Planar antennas are also frequently used in remote sensing, biomedical applications and in personal communications. Nowadays PIFA's are more commonly used in RFID tags [24-29]. We look at these two antennas in a little more detail in regards to basic operation, advantages and disadvantages.

1.2.1 <u>Microstrip patch antennas</u>

In its most basic form, a microstrip patch antenna consists of a radiating patch on one side of a dielectric substrate and a ground plane on the other side as shown in Fig. 1.2-1. The patch is generally made of conducting material and can take any possible shape. The radiating patch and the feed lines are usually photo etched on the dielectric substrate. Microstrip patch antennas radiate primarily because of the fringing fields between the patch edge and the ground plane. The length L of the rectangular patch for the fundamental TM_{10} mode excitation is slightly less than $\lambda/2$. For good antenna performance, a thick dielectric substrate having a low dielectric constant is desirable since this provides better efficiency, larger bandwidth and better radiation [8]. However, such a configuration leads to a larger antenna size. In order to design a compact Microstrip patch antenna, higher dielectric constants must be used which are less efficient and result in narrower bandwidth. Hence a compromise must be reached between antenna dimensions and antenna performance.
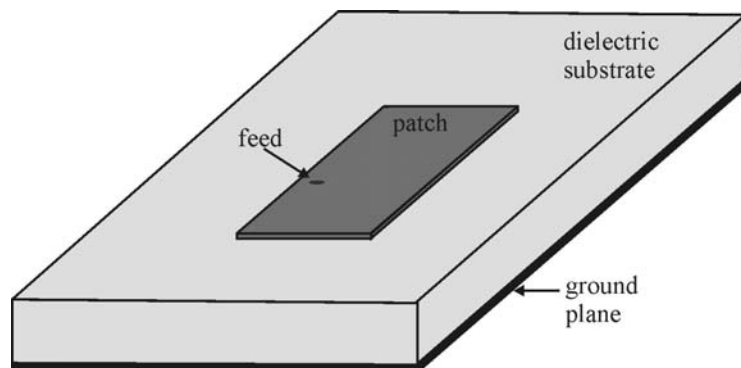
Figure 1.2-1 Structure of microstrip patch antenna

Some of the principal advantages of patch antennas are [8, 9]

  i.   Light weight, small volume and low planar configuration

  ii.   Can be easily made conformal to host surface

iii. Ease of mass production using printed-circuit technology leads to low fabrication cost

iv. Supports both linear as well as circular polarization

v. Easier to integrate with microwave integrated circuits (MIC).

vi. Capable of dual and triple frequency operations

vii. Mechanically robust when mounted on rigid surfaces

Microstrip patch antennas suffer from a number of disadvantages as compared to conventional antennas. Some of their major disadvantages are [9, 30]

i. Narrow bandwidth

ii. Low efficiency

iii. Low Gain

iv. Extraneous radiation from feeds and junctions

v. Low power handling capacity

vi. Surface wave excitation

1.2.2 Planar inverted-F antennas

The Inverted-F Antenna (IFA) typically consists of a rectangular planar element located above a ground plane, a short circuiting plate or pin, and a feeding mechanism for the planar element. The Inverted F antenna is a variant of the monopole where the top section has been folded down so as to be parallel with the ground plane. This is done to reduce the height of the antenna, while maintaining a resonant trace length. This parallel section introduces capacitance to the input impedance of the antenna, which is compensated by implementing a short-circuit stub. The stub's end is connected to the ground plane through a via. The planar inverted-F antenna (PIFA) can be considered as a kind of linear Inverted-F antenna (IFA) with the wire radiator element replaced by a plate to expand the bandwidth. Fig. 1.2-2 shows a basic PIFA structure.

9
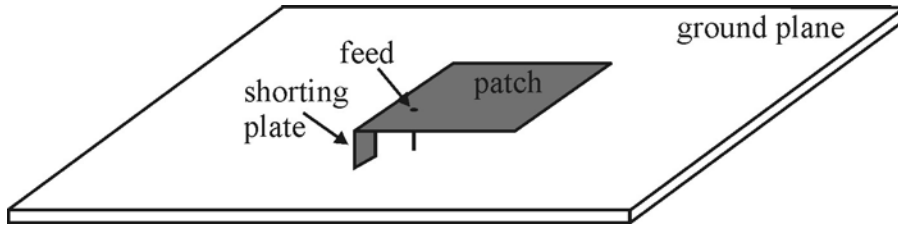
Figure 1.2-2 Basic geometry of planar inverted F antenna.

So, unlike microstrip antennas that are conventionally made of half wavelength dimensions, PIFA's are made of just quarter-wavelength. The ground plane of the antenna plays a significant role in its operation. Excitation of currents in the PIFA causes excitation of currents in the ground plane In general, the required ground plane length is roughly one quarter ($\lambda/4$) of the operating wavelength. If the ground plane is much longer than $\lambda/4$, the radiation patterns will become increasingly multi-lobed. On the other hand, if the ground plane is significantly smaller than $\lambda/4$, then tuning becomes increasingly difficult and the overall performance degrades. The optimum location of the patch element in order to achieve an omni-directional far-field pattern and 50Ω impedance matching was found to be close to the edge of the ground plane. The omni-directional behavior of the PIFA with typical gain values ensure adequate performance for indoor environments taking into account the standard values of the output power and receiver sensitivity of short range radio devices. PIFA has proved to be the most widely used internal antenna in commercial applications of cellular communication. In most of the research publications/ patents on multi-band PIFA technology, the major success has been the design of a single feed PIFA with dual resonant frequencies resulting in essentially a Dual Band PIFA. Depending upon the achievable bandwidth around the resonant frequencies, the dual resonant PIFA can potentially cover more than 2 bands. Some of their principal advantages of PIFA's are discussed below [1, 31]

    i.   PIFA's are just quarter wavelength in length and hence are much shorter than conventional patch antennas

ii. PIFA can be easily hid into the housing of the mobile phones as compared to whip/rod/helix antennas.

iii. PIFA has reduced backward radiation toward the user's head, minimizing the electromagnetic wave power absorption (SAR) and enhances antenna performance.

iv. PIFA exhibits moderate to high gain in both vertical and horizontal states of polarization. This feature is very useful in certain wireless communications where the antenna orientation is not fixed and the reflections are present from the different corners of the environment. In those cases, the important parameter to be considered is the total field that is the vector sum of horizontal and vertical states of polarization.

Narrow bandwidth characteristic of PIFA is one of the limitations for its commercial application for wireless mobile. However there are methods to increase the bandwidth of PIFA. These are discussed in detail in section 4, where a reduced size PIFA with 18% impedance bandwidth is designed.

1.3 Contribution of this dissertation

In the MoM approach for simulating the planar antennas, use of a surface integral equation (SIE) [32, 33] currently dominates for pure dielectric [34-36] and metal antenna structures [37–42]. The method of a volume integral equation (VIE), started in [43] and continued in [44–47], has a number of advantages, including applicability to various inhomogeneous materials. At the same time, it has two major drawbacks that prevent its wider use. First, the number of unknowns associated with the pulse basis functions [48] or with the most common Schaubert–Wilton–Glisson (SWG) basis functions [43] is large, considerably larger than for a SIE. The SWG basis functions require fewer unknowns than pulse bases, but they possess artificial volume charges whose effect becomes apparent close to the metal-dielectric boundary. Second, the convergence of the

method for a patch antenna configuration with significant fringing fields is very slow. Typically, a significant positive offset in the resonant frequency is observed. This error is likely related to the nature of the SWG or other low-order dielectric basis functions, which are unable to exactly satisfy the boundary condition of the vanishing tangential E-field component on the metal-dielectric surface. This condition is approximately satisfied in an integral sense, within a dielectric volume close to the metal boundary, but not on the boundary itself. As a result, the patch antenna appears to be electrically smaller than it is in fact. On the other hand, when the tangential-field is small everywhere due to geometrical reasons, the VIE approach may produce accurate results. A simple example is a thin parallel-plate metal resonator where the dielectric substrate is fully covered by the metal plates. Within the resonator volume excited in the fundamental TM mode, the tangential-field component becomes insignificant. In this case, an exceptional VIE convergence is observed [49].

This dissertation addresses the two issues stated above. A major application of this theory is the analysis of the patch or slot antenna, printed on a thin finite dielectric substrate, with moderate (two to ten) or larger relative dielectric constant. In order to reduce the number of unknowns, we employ the piecewise-constant edge basis functions [49–51]. These basis functions form a full vector basis on tetrahedral meshes in for the fields with a continuous normal component. Simultaneously, they form a subset of the SWG basis functions that do not possess the artificial volume charges. The number of these edge basis functions required is typically 40–50% fewer than the number of SWG basis functions. To improve the convergence rate of the VIE, enforcement of the boundary condition into the VIE model should be explicit. The proposed enforcement method is exact for piecewise-constant bases. For these basis functions, the tangential electric field for all tetrahedra in contact with metal faces must be zero, to ensure continuity. This tangential field will be eliminated from the VIE, using a projection operation performed on the original equation. However, the normal field for tetrahedra in contact with metal

12

faces is retained as required by the boundary condition. Such an operation is a simple yet effective method to improve the convergence rate. Various modifications on this approach are discussed in the text.

To summarize, the contributions of this dissertation are development, implementation and validation of the MoM- based method for full-wave modeling of resonant metal-dielectric structures with significant fringing fields. The new key features of the method are

   i.   *The use of the proper low order basis functions*

   ii.   *Use of low order integration scheme for calculating the integrals in the formulation*

   iii.   *Special VIE conditioning on the metal-dielectric interface*

Along with the MoM development, the dissertation also presents the models and design procedures for a number of practical antenna configurations. Two in particular include a compact linearly polarized broadband planar inverted-F antenna (PIFA) which provides an 18% impedance bandwidth and a circularly polarized turnstile bowtie antenna which provides 24% circular polarization and impedance bandwidth. Both the antennas are designed to operate in the low UHF band and used for indoor positioning/indoor geolocation.

The dissertation is organized as follows. Chapter 2 explains in detail the implementation of the MoM SIE/VIE approach along with the basis functions used and the VIE boundary condition. Chapter 3 reports on the simulation results for printed antennas on thin substrates. The results obtained are validated by comparison with data obtained from literature, measured data and with the commercially available Ansoft HFSS simulator. Chapter 4 and 5 explains the design and modeling of linear and circularly polarized antennas respectively used for indoor positioning systems. Chapter 6 presents the conclusion.

2 Implementation of the Method of Moments approach

In this chapter the MoM theory is derived for modeling the metal-dielectric structures. This chapter is organized as follows. Section 2.1 describes the MoM equations for modeling the pure metal structure using the RWG basis functions. Section 2.2 describes the MoM equations for the pure dielectric structure using the edge basis functions. Section 2.3 gives the combined metal-dielectric equations. The effect of numerical cubature on the MoM solution is discussed in section 2.4 with a few examples. Section 2.5 explains the effect of the boundary condition and the required procedure to explicitly satisfy it at the metal-dielectric interface for the MoM solution. The derivations in this section form the core of the MoM solver.

2.1 MoM Approach to a Metal Antenna

In this section, the MoM equation for a pure metal structure (an antenna or a scatterer) is derived for the electric field integral equation (EFIE) [52], utilizing the Rao-Wilton-Glisson (RWG) basis functions [53].

2.1.1 Basis functions for a metal structure
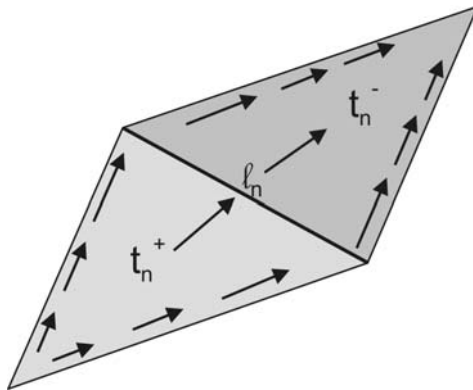
Figure 2.1-1 RWG basis with two adjacent triangles [53]

The RWG basis functions [53] on triangles are used in the present study. The basis function in Fig. 2.1.1 includes a pair of adjacent (not necessarily co-planar) triangles and resembles a small spatial dipole with linear current distribution where each triangle is associated with either positive or negative charge.

Below, we recall some properties of the most common basis functions. For any two triangular patches, t_n^+ and t_n^-, having areas A_n^+ and A_n^-, and sharing a common edge l_n, the basis function becomes

$$\vec{f}_n^M(\vec{r}) = \begin{cases} \dfrac{l_n}{2A_n^+}\vec{\rho}_n^+ & \vec{r} \text{ in } t_n^+ \\[2ex] \dfrac{l_n}{2A_n^-}\vec{\rho}_n^- & \vec{r} \text{ in } t_n^- \end{cases} \tag{2.1.1}$$

and

$$\nabla \cdot \vec{f}_n^M(\vec{r}) = \begin{cases} \dfrac{l_n}{A_n^+} & \vec{r} \text{ in } t_n^+ \\[2ex] -\dfrac{l_n}{A_n^-} & \vec{r} \text{ in } t_n^- \end{cases} \tag{2.1.2}$$

where $\vec{\rho}_n^+ = \vec{r} - \vec{r}_n^+$ is the vector drawn from the free vertex of triangle t_n^+ to the observation point $\vec{r}$; $\vec{\rho}_n^- = \vec{r}_n^- - \vec{r}$ is the vector drawn from the observation point to the free vertex of triangle t_n^-. The basis function is zero outside the two adjacent triangles t_n^+ and t_n^-. The RWG vector basis function is linear and has no flux (that is, has no normal component) through its boundary.

2.1.2 MoM equations for a metal structure

a. Scattering problem

Scattering or radiation problems are essentially identical – the only difference is that the "incident" field for the driven antenna is the applied electric field in the feed. Therefore, only the scattering problem is considered here. The total electric field is a combination of

the incident field (labeled by superscript i) and the scattered field (labeled by superscript s), i.e.

$$\vec{E} = \vec{E}^i + \vec{E}^s \tag{2.1.3}$$

The incident electric field is either the incoming signal (scattering problem) or the excitation electric field in the antenna feed (radiation problem). The scattered electric field $\vec{E}^s$ is due to surface currents and free charges on the metal surface S (the so-called mixed-potential formulation) [52]

$$\vec{E}^s = -j\omega\vec{A}_M(\vec{r}) - \nabla\Phi_M(\vec{r}) \quad \vec{r} \text{ on } S \tag{2.1.4}$$

Herein the index M denotes the metal-surface related quantities. The magnetic vector potential $\vec{A}_M(\vec{r})$ describes surface current radiation whereas the electric potential $\Phi_M(\vec{r})$ describes radiation of surface free charges. In the far field, both the Φ-contribution and the $\vec{A}$-contribution are equally important. On the metal surface S, the tangential component of the total electric field vanishes, $\vec{E}_{tan} = 0$, thus giving the electric field integral equations

$$E^i_{tan} = \left(j\omega\vec{A}_M + \nabla\Phi_M\right)_{tan} \quad \vec{r} \text{ on } S \tag{2.1.5}$$

b. Test functions

Assume that the test functions, $\vec{f}^M_m(\vec{r})$ m = 1... N_M, cover the entire surface S and do not have a component normal to the surface. Multiplication of Eq. (2.1.5) by $\vec{f}^M_m$ and integration over S gives N_M equations

$$\int_S \vec{f}^M_m \cdot \vec{E}^i \, ds = j\omega \int_S \vec{f}^M_m \cdot \vec{A}_M \, ds - \int_S \left(\nabla \cdot \vec{f}^M_m\right)\Phi_M \, ds \tag{2.1.6}$$

since, according to the Divergence theorem and using standard vector identities,

$$\int_S \nabla\Phi_M \cdot \vec{f}^M_m \, ds = -\int_S \Phi_M \left(\nabla \cdot \vec{f}^M_m\right) ds \tag{2.1.7}$$

16

if $\vec{f}_m^M$ does not have a component perpendicular to the surface boundary or edge (if any).

c. Source functions

The surface current density, $\vec{J}_M$ is expanded into the basis functions (which usually coincide with the test functions) in the form

$$\vec{J}_M(\vec{r}) = \sum_{n=1}^{N_M} I_n \vec{f}_n^M(\vec{r}) \tag{2.1.8}$$

The magnetic vector potential has the form [52]

$$\vec{A}_M(\vec{r}) = \frac{\mu_0}{4\pi} \int_S \vec{J}_M(\vec{r}) g(\vec{r}, \vec{r}') ds' \tag{2.1.9}$$

where μ_0 is the permeability in vacuum and $g(\vec{r}, \vec{r}') = \exp(-jkR)/R$, $R = |\vec{r} - \vec{r}'|$ is the free-space Green's function (time dependency $\exp(j\omega t)$ is assumed everywhere). In the expression for the Green's function $\vec{r}$ is the observation (test) point and $\vec{r}'$ is the integration (source) point; both of them belong to the metal surface. After substitution of the expansion Eq. (2.1.8), the above equation becomes

$$\vec{A}_M(\vec{r}) = \sum_{n=1}^{N_M} \left\{ \frac{\mu_0}{4\pi} \int_S \vec{f}_n^M(\vec{r}') g(\vec{r}, \vec{r}') ds' \right\} I_n \tag{2.1.10}$$

Similarly, the electric potential has the form [52]

$$\Phi_M(\vec{r}) = \frac{1}{4\pi\varepsilon_0} \int_S \sigma_M(\vec{r}) g(\vec{r}, \vec{r}') ds', \quad j\omega\sigma_M = -\nabla_S \cdot \vec{J}_M \tag{2.1.11}$$

It follows from equation (2.1.11) that σ_M can be expressed in terms of the current density, through the surface divergence using the continuity equation. Hence the electric scalar potential reduces to

$$\Phi_M(\vec{r}) = \sum_{n=1}^{N_M} \left\{ \frac{1}{4\pi\varepsilon_0} \frac{j}{\omega} \int_S \left(\nabla \cdot \vec{f}_n^M(\vec{r}') \right) g(\vec{r}, \vec{r}') ds' \right\} I_n \tag{2.1.12}$$

d. Moment equations

The moment equations are obtained if we substitute expansions (2.1.10) and (2.1.12) into the integral equation (2.1.6). In terms of symbolic notations,

$$\sum_{n=1}^{N_M} \hat{Z}_{mn}^{MM} I_n = \upsilon_m^M, \quad m = 1,...,N_M \tag{2.1.13}$$

$$\upsilon_m^M = \int_S \vec{f}_m^M \cdot \vec{E}^i ds \tag{2.1.14}$$

are the "voltage" or excitation components for every test/basis function that have units V·m. The integral expressions are the components of the impedance matrix $\hat{Z}^{MM}$ of size (N_M x N_M),

$$Z_{mn}^{MM} = \left(\frac{j\omega\mu_0}{4\pi}\right)\int_S\int_S \vec{f}_m^M(\vec{r}) \cdot \vec{f}_n^M(\vec{r}')g(\vec{r},\vec{r}')ds'ds$$
$$-\left(\frac{j}{4\pi\omega\varepsilon_0}\right)\int_S\int_S (\nabla \cdot \vec{f}_m^M)(\nabla \cdot \vec{f}_n^M)g(\vec{r},\vec{r}')ds'ds \tag{2.1.15}$$

Note that the impedance matrix is symmetric for any set of basis functions (test functions should be the same) when the corresponding surface integrals are calculated precisely. The components of the impedance matrix are the double surface integrals of the Green's function and they mostly reflect the geometrical interaction between the "dipole" RWG basis functions of the problem. In matrix form, Eq. (2.1.15) becomes

$$\hat{Z}^{MM}\vec{I} = \vec{\upsilon} \tag{2.1.16}$$

Substitution of Eqs. (2.1.1), (2.1.2) into Eq. (2.1.15) gives the components of the impedance matrix in terms of RWG basis functions in the form

$$\iint_{S\,S} \vec{f}_m^M \cdot \vec{f}_n^M \, g(\vec{r},\vec{r}')ds'ds =$$

$$+\frac{l_m l_n}{4 A_m^+ A_n^+}\iint_{t_m^+ t_n^+}\left(\vec{\rho}_m^+ \cdot \vec{\rho}_n'^+\right)g(\vec{r},\vec{r}')ds'ds +\frac{l_m l_n}{4 A_m^+ A_n^-}\iint_{t_m^+ t_n^-}\left(\vec{\rho}_m^+ \cdot \vec{\rho}_n'^-\right)g(\vec{r},\vec{r}')ds'ds \qquad (2.1.17)$$

$$+\frac{l_m l_n}{4 A_m^- A_n^+}\iint_{t_m^- t_n^+}\left(\vec{\rho}_m^- \cdot \vec{\rho}_n'^+\right)g(\vec{r},\vec{r}')ds'ds +\frac{l_m l_n}{4 A_m^- A_n^-}\iint_{t_m^- t_n^-}\left(\vec{\rho}_m^- \cdot \vec{\rho}_n'^-\right)g(\vec{r},\vec{r}')ds'ds$$

and

$$\iint_{S\,S}\left(\nabla \cdot \vec{f}_m^M\right)\left(\nabla \cdot \vec{f}_n^M\right)g(\vec{r},\vec{r}')ds'ds =$$

$$+\frac{l_m l_n}{A_m^+ A_n^+}\iint_{t_m^+ t_n^+} g(\vec{r},\vec{r}')ds'ds -\frac{l_m l_n}{A_m^+ A_n^-}\iint_{t_m^+ t_n^-} g(\vec{r},\vec{r}')ds'ds \qquad (2.1.18)$$

$$-\frac{l_m l_n}{A_m^- A_n^+}\iint_{t_m^- t_n^+} g(\vec{r},\vec{r}')ds'ds +\frac{l_m l_n}{A_m^- A_n^-}\iint_{t_m^- t_n^-} g(\vec{r},\vec{r}')ds'ds$$

2.1.3 Integral calculation

a. Base integrals

About 90% of the CPU time required for the filling of the MoM impedance matrix $\hat{Z}^{MM}$ for the RWG basis functions is spent for the calculation of the surface integrals presented in equations (2.1.17), (2.1.18). Consider a structure where all triangular patches are enumerated by $p = 1,...,P$. Then, every integral in equation (2.1.17) is built upon the term

$$\vec{A}_{M\,pq}^{ij} = \iint_{t_p\,t_q}\left(\vec{\rho}_i \cdot \vec{\rho}_j'\right)g(\vec{r},\vec{r}')ds'ds \quad p,q = 1,...,P \quad i,j = 1,2,3 \qquad (2.1.19)$$

Here, $\vec{\rho}_i = \vec{r} - \vec{r}_i$ for any vertex i of patch p whereas $\vec{\rho}'_j = \vec{r}'-\vec{r}_j$ for any vertex j of patch q. Similarly, every integral in equation (2.1.18) is built upon the term

$$\Phi_{M\,pq} = \iint_{t_p\,t_q} g(\vec{r},\vec{r}')ds'ds \quad p,q = 1,...,P \qquad (2.1.20)$$

The integrals (2.1.19) and (2.1.20) can be found in a number of ways.

b. Singularity extraction

The singularity of the free-space Green's function is integrable in 2D, but the accuracy of the Gaussian formulas is reduced if this singularity is retained. Therefore, singularity extraction may be used in Eqs. (2.1.19), (2.1.20), in the form

$$\iint_{t_p\,t_q}\left(\vec{\rho}_i\cdot\vec{\rho}_j'\right)g(\vec{r},\vec{r}')ds'ds=\iint_{t_p\,t_q}\frac{\left(\vec{\rho}_i\cdot\vec{\rho}_j'\right)}{\left|\vec{r}-\vec{r}'\right|}ds'ds+\iint_{t_p\,t_q}\frac{\left(\exp(-jk\left|\vec{r}-\vec{r}'\right|)-1\right)\left(\vec{\rho}_i\cdot\vec{\rho}_j'\right)}{\left|\vec{r}-\vec{r}'\right|}ds'ds$$

$$(2.1.21)$$

$$\iint_{t_p\,t_q}g(\vec{r},\vec{r}')ds'ds=\iint_{t_p\,t_q}\frac{1}{\left|\vec{r}-\vec{r}'\right|}ds'ds+\iint_{t_p\,t_q}\frac{\left(\exp(-jk\left|\vec{r}-\vec{r}'\right|)-1\right)}{\left|\vec{r}-\vec{r}'\right|}ds'ds \qquad (2.1.22)$$

The two first singular integrals on the right-hand side of eqs. (2.1.21), (2.1.22) (the so-called potential or static integrals) may be found with the help of the analytical results given in [54]. The double self-integrals are evaluated analytically in [55].

c. Analytical calculation of potential integrals [56]

Strictly speaking, the integration-by-parts approach of Ref. [54] allows us only to find the inner potential integral presented in Eqs. (2.1.21), (2.1.22). The outer integrals will still be found numerically, using the Gaussian cubatures [56].

Fig. 2.1.2, which is given for one triangle edge and the observation point, is useful in visualizing many variables needed to find the potential integrals using the analytic formulas. This figure and the corresponding integration formulas are adopted from Ref. [54]. Here, $\vec{\rho}$ is the projection vector of the observation point $\vec{r}$ onto the triangle plane, $\vec{\rho}'$ is the projection vector of the integration point $\vec{r}'$ onto the triangle plane, and R is the distance between the integration point and the observation point, i.e. $R=\left|\vec{r}'-\vec{r}\right|$.

Figure 2.1-2 Geometric representation of the variables in the analytical formulas

Below, we briefly review the related results of [54]. The analytic formula for the inner (potential) integral on the right-hand side of Eq. (2.1.22) has the following form:
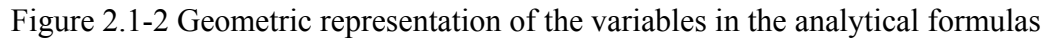
$$\int_{t_q} \frac{1}{|\vec{r}-\vec{r}'|} ds' =$$

$$-\alpha(\vec{\rho})\,|d| + \sum_{i=1}^{3} \vec{P}_i^0 \cdot \vec{u}_i \left[P_i^0 \ln \frac{R_i^+ + l_i^+}{R_i^- + l_i^-} + |\,d\,| \left(\tan^{-1} \frac{d\,|\,l_i^+}{P_i^0 R_i^+} - \tan^{-1} \frac{d\,|\,l_i^-}{P_i^0 R_i^-} \right) \right]$$

(2.1.23)

The summation is made over the three edges of the triangle. Here, $\alpha(\vec{\rho})$ is the angle factor and is either 0 or 2π depending on whether the projection of the observation point is outside the triangle or inside the triangle, respectively. The quantity d is the height of the observation point above the plane of triangle t, measured positively in the direction of the triangle normal vector $\vec{n}$. The quantity d is calculated by $d = \vec{n} \cdot (\vec{r} - \vec{r}_i^+)$, where $\vec{r}_i^+$ is a given position vector to the "upper" endpoint of edge l_i, $i = 1,2,3$. The upper endpoint is labeled with symbol "+". Triangle unit normal $\vec{n}$ is the cross product of side 1 and side 2 vectors of the triangle, where numbering the sides is arbitrary as long as it is

21

consistent for each iteration of the formula. Alternatively, $\vec{r}_i^{\,-}$, a given position vector to the "lower" endpoint of edge l_i, $i = 1,2,3$, can be used in the equation for d instead of $\vec{r}_i^{\,+}$. The perpendicular vector from the endpoint of vector $\vec{\rho}$ in Fig. 2.1.2 to the edge l_i, $i = 1,2,3$ or its extension is given by $\vec{P}_i^{\,0} = (\vec{\rho}_i^{\,\pm} - \vec{\rho}) - (l_i^{\,\pm}\vec{l}_i)/P_i^{\,0}$ where $\vec{\rho}_i^{\,\pm}$ are the vectors from point Q to the endpoints of the edge, which are equal to $\vec{r}_i^{\,\pm} - \vec{n}\,(\vec{n}\cdot\vec{r}_i^{\,\pm})$. $\vec{l}_i$ is the edge vector and is equal to $\vec{r}_i^{\,+} - \vec{r}_i^{\,-}\,\big/\,\big|\,\vec{r}_i^{\,+} - \vec{r}_i^{\,-}\,\big|$ (see Fig. 2.1-2). The endpoints of $\vec{l}_i$ are associated with distances $l_i^{\,\pm} = (\vec{\rho}_i^{\,\pm} - \vec{\rho})\cdot\vec{l}_i$ (see Fig. 2.1-2). The distance from the endpoint of vector $\vec{\rho}$ in Fig. 2.1-2 to the edge l_i, $i = 1,2,3$ or its extension is given by $P_i^{\,0} = \big|(\vec{\rho}^{\,\pm} - \vec{\rho})\cdot\vec{u}_i\big|$ (the proper sign must be taken into account). The vector $\vec{u}_i$ is the unit outer normal to the edge and is equal to $\vec{l}_i \times \vec{n}$. Distances measured from $\vec{\rho}$ to $\vec{\rho}_i^{\,\pm}$ are $P_i^{\,\pm} = \big|\vec{\rho}_i^{\,\pm} - \vec{\rho}\big| = \sqrt{\left(P_i^{\,0}\right)^2 + \left(l_i^{\,\pm}\right)^2}$. The two quantities $R_i^{\pm} = \sqrt{\left(P_i^{\pm}\right)^2 + d^2}$ are the distances measured from the observation point to the endpoints of the edge (see Fig. 2.1-2). This completes the list of variables presented in Eq. (1.5).

The inner integral in Eq. (2.1.21) is similar to that in Eq. (2.1.22) except that it is multiplied by $\vec{\rho}'_j$. This gives a vector-valued integral. The corresponding analytic formula given in [55] provides the integral

$$\int_{t_q} \frac{(\vec{r}'-\vec{r})_{\text{tan}}}{|\vec{r}-\vec{r}'|}\,ds' = \frac{1}{2}\sum_{i=1}^{3}\vec{u}_i\left[\left(R_i^0\right)^2\ln\frac{R_i^+ + l_i^+}{R_i^- + l_i^-} + l_i^+ R_i^+ - l_i^- R_i^-\right] \tag{2.1.24}$$

where subscript tan denotes the vector projection onto the triangle plane, $R_i^0 = \sqrt{\left(P_i^0\right)^2 + d^2}$ is the distance measured from the observation point to the point intersected by $\vec{P}_i^0$ and $\vec{l}$. The remaining variables are the same as in Eq. (2.1.23). The inner integral on the right-hand-side of Eq. (2.1.21) is then obtained as a combination of (2.1.23) and (2.1.24), i.e.

$$\int_t \frac{\rho'_j}{|\vec{r}-\vec{r}'|}\,ds' = \int_t \frac{(\vec{r}'-\vec{r})_{\text{tan}}}{|\vec{r}-\vec{r}'|}\,ds' + (\vec{r}-\vec{r}_j)_{\text{tan}}\int_t \frac{1}{|\vec{r}-\vec{r}'|}\,ds' \tag{2.1.25}$$

22

2.1.4 Fields

a. Scattered electric field

Once the MoM solution is known, the scattered (or radiated) electric field is given by Eq. (2.1.4)

$$\vec{E}^s = \frac{-j\omega\mu_0}{4\pi}\sum_{n=1}^{N_M}\left\{\int_S \vec{f}_n^{\,M}(\vec{r}')g(\vec{r},\vec{r}')ds'\right\}I_n$$

$$-\frac{j}{4\pi\omega\varepsilon_0}\sum_{n=1}^{N_M}\left\{\int_S \nabla\cdot\vec{f}_n^{\,M}(r')\nabla_r g(\vec{r},\vec{r}')ds'\right\}I_n \tag{2.1.26}$$

where I_n is the MoM solution for surface current density.

b. Scattered magnetic field

The scattered magnetic field created by a metal structure is given by the curl of the magnetic vector potential, i.e.

$$\vec{H}^s = \frac{1}{4\pi}\int_S\sum_{n=1}^{N_M}\left\{\left(-\vec{f}_n^{\,M}(\vec{r}')\times\nabla_r g(\vec{r},\vec{r}')\right)ds'\right\}I_n \tag{2.1.27}$$

2.1.5 Impedance matrix $\hat{\underline{Z}}^{MM}$ and the radiated/scattered fields

a. Impedance matrix

A "neighboring" sphere of dimensionless radius R is introduced for every integration facet. The radius R is a threshold value for the ratio of distance to size. The size of the facet $t_q, S(t_q)$, is measured as the distance from its center to the furthest vertex. The observation triangle t_p lies within the sphere if the following inequality is valid for the distance d between two triangle centers

$$\frac{d}{\sqrt{S(t_p)S(t_q)}} < R \tag{2.1.28}$$

23

If a pair of triangles satisfies (2.1.28), then the integrals (2.1.19) and (2.1.20) use the singularity extraction (2.1.21), (2.1.22) and the analytical formulas (2.1.23)-(2.1.25) for the inner potential integrals. The non-singular part and the outer potential integrals employ Gaussian cubatures given in [56]. Each cubature is characterized by two numbers: N, the number of integration points; and d, the degree of accuracy for the Gaussian cubature formula. If a pair of triangles does not satisfy Eq. (2.1.28), then the central-point approximation is used for all integrals, without singularity extraction.

The parameter R is initialized in the script `metal.m` in subfolder 2_basis\codes. The same is valid for N and d for the Gaussian formulas. The default values are $R = \sqrt{5}$ and $N = 3, d = 2$. The necessary potential integrals on the right-hand sides of Eqs. (2.1.21), (2.1.22) are pre-calculated in structure `geom` and are saved in the sparse matrix format.

b. Fields

The same operation as for the impedance matrix is done for the field integrals (2.1.26) and (2.1.27) but Eq. (2.1.28) is now replaced by

$$\frac{d}{S(t_q)} < R \tag{2.1.29}$$

Within the sphere, one more potential integral appears, of the form [57]

$$\int_S \nabla \frac{1}{|\vec{r} - \vec{r}'|} ds = -\vec{n} \cdot \text{sgn}(d) \cdot \beta - \sum_{i=1}^{3} \vec{u}_i \ln \frac{R_i^+ + l_i^+}{R_i^- + l_i^-} \tag{2.1.30}$$

where

$$\beta = \sum_{i=1}^{3} \left[\tan^{-1} \frac{P_i^0 l_i^+}{\left(R_i^0\right)^2 + |d| R_i^+} - \tan^{-1} \frac{P_i^0 l_i^-}{\left(R_i^0\right)^2 + |d| R_i^-} \right] \tag{2.1.31}$$

and the variables are the same as in Eqs. (2.1.23) and (2.1.24). The parameter R is initialized in the script `field.m` in subfolder 3_mom\codes. The default value is $R = 2$. The N and d for the Gaussian formula are defined as $N = 7, d = 5$ in the script

`fieldm.cpp`. Outside the sphere, the central-point approximation is used. For the far-field approximation, $R \rightarrow 0$ is an acceptable approximation.

2.1.6   List of available Gaussian integration formulas on triangles

Some Gaussian integration formulas on triangles [56] are given in the script `tri.m` in subfolder 2_basis\codes. The formulas given in Table 2.1.1 were used and tested. Each cubature is characterized by two numbers: N is the number of integration points and d is the degree of accuracy for the Gaussian cubature formula. Also, the barycentric triangle subdivision of arbitrary degree of subdivision is available in the script `tri.m`.

Table 2.1-1 List of available/ tested Gaussian formulas on triangles [56]

Formula	N	d
#1	1	1
#2	3	2
#3	4	3
#4	6	3
#5	7	5
#6	9	5
#7	13	7
#8	25	10

2.1.7   Numerical operations and associated MATLAB/C++ scripts

The summary of numerical operations related to a metal antenna/resonator/scatterer is given in Table. 2.1.2. The same summary but for a metal resonator is given in Table 2.1.3. The difference between the two cases is mostly in the antenna feed.

Table 2.1-2 Metal antenna related numerical operations.

Antenna operations			
Operation	Script	Path	Remarks
Determine the metal structure	`struct2d.m` `struct3d.m`	1_mesh	Remove all tetrahedra from the mesh while running `struct3d.m`. Do not use $\varepsilon_r = 1$.
Determine the antenna feed location	`feed.m` (obsolete; combined with struct3d)	1_mesh	The feed edges are found as the closest ones to the array POINTS. The number of feeding edges in the feed can be arbitrary.
Determine parameters of the RWG basis functions	`wrapper.m`	2_basis	Outputs structure `geom` with all the necessary data on the basis functions/pre-calculated potential integrals
Determine accuracy of impedance matrix filling – optional (see Section 2.1.5)	`metal.m`	2_basis\codes	The parameter R is initialized in the script `metal.m` in subfolder 2_basis\codes. The same is valid for N and d for the Gaussian formulas. The default values are $R = \sqrt{5}$ and $N = 3, d = 2$. The necessary potential integrals are pre-calculated in structure `geom` and are saved in the sparse matrix format.
Determine the antenna feed type	`impedance.m`	3_mom	Voltage gap is the default. Can be modified if necessary.
Determine the antenna input impedance and feed power (loop)	`impedance.m`	3_mom	Saves MoM solutions obtained at every frequency step in `out.mat`.
Determine radiation patterns (co-polar /cross-polar polarization, RHCP, LHCP)	`radpattern. m`	3_mom	`radpattern.m` uses the MoM solution obtained previously in order to compute the far fields. It finds the far field at a given frequency specified by user.
Determine charge/current distribution on the metal surface	`nearfield.m`	3_mom	`nearfield.m` uses the MoM solution obtained previously in order to compute the current/charge distributions at a given frequency specified by the user.

Table 2.1-3 Metal resonator related numerical operations

Resonator operations			
Operation	Script	Path	Remarks
Determine the metal structure	`struct2d.m` `struct3d.m`	1_mesh	Remove all tetrahedra from the mesh while running `struct3d.m`. Do not use $\varepsilon_r = 1$.
Determine parameters of RWG basis functions	`wrapper.m`	2_basis	Outputs structure `geom` with all necessary data on the basis functions/pre-calculated potential integrals
Determine accuracy of impedance matrix filling –optional (see Section 2.1.5)	`metal.m`	2_basis\ codes	The parameter R is initialized in the script `metal.m` in subfolder 2_basis\codes. The same is valid for N and d for the Gaussian formulas. The default values are $R = \sqrt{5}$ and $N = 3, d = 2$. The necessary potential integrals are pre-calculated in structure `geom` and are saved in the sparse matrix format.
Determine eigenfrequency/Q-factor	`eigenfreq.m`	3_mom	Fully interactive interface. Will not run if the antenna feed is specified.
Determine charge/current distribution on the metal surface in the resonant mode	`scatterfiel d.m`	3_mom	`scatterfield.m`. Illuminates the resonator by an incident plane wave at the resonant frequency and finds the current/charge distributions at that given frequency

The independent scattering problem may be also considered, by running `scatterfield.m` at a given frequency.

2.2 MoM VIE Approach to a Dielectric Structure

In this section, the MoM Volume Integral equations for a pure dielectric structure are derived for the EFIE, utilizing the edge basis functions [50].

2.2.1 Choice of the basis functions

The MoM solution for dielectric objects can be obtained using the method of volume integral equation [53]. This method has a number of advantages including the applicability to inhomogeneous materials [43] and a potentially better accuracy at the resonances (compared to the surface integral formulation [45]). At the same time, it suffers from a rapid growth of computational complexity with increasing grid size. Therefore, possible reduction of the number of basis functions (unknowns) will improve the performance of the method.

The simplest choice is the pulse basis functions (cf. [48]). However, they tend to be unstable when relative permittivity becomes high [52]. The face-based tetrahedral basis functions proposed by Schubert, Wilton, and Glisson [43] (SWG basis functions) are more robust and are more frequently used today [45, 48, 58]. They enforce the continuity of the normal component of the electric flux density $\overline{D}$ on the faces within the same basis function. This is in contrast to the finite element method with the edge-based basis functions, where the continuity of the tangential $\overline{E}$-field is required on the faces [59-61]. The number of unknowns for the face-based basis functions is equal to the number of the faces of the mesh. For a tetrahedral mesh, the number of faces is considerably greater than the number of the edges. This is a disadvantage compared to the edge-based FEM basis functions, where the number of independent unknowns for the system matrix is even smaller than the number of the edges [62, 63].

It is therefore inviting to employ MoM basis functions that still acquire the condition of the continuous normal $\overline{D}$-component according to [43], but include all tetrahedra sharing the edge – similar to the edge-based divergence-free FEM bases [60]. Such basis functions were first introduced by de Carvalho and de Souza Mendes [50].

2.2.2   MoM edge basis function

The edge-based basis function $\vec{f}$ introduced in [50] is shown in Fig. 2.2-1. It is similar to the first Whitney form [60]. However, the vector variation is essentially perpendicular to the base edge $\bar{l}$ (or AB). The basis function is defined by a vector of the edge $\bar{p}$ (or CD), which is opposite to the base edge $\bar{l}$. Within a tetrahedron, the basis function is a constant field given by $\vec{f} = c\vec{p}$ where c is a normalization coefficient.

The basis function may include a different number of tetrahedra that share the same base edge $\bar{l}$ .Three representative cases are depicted in Fig. 2.2.1.
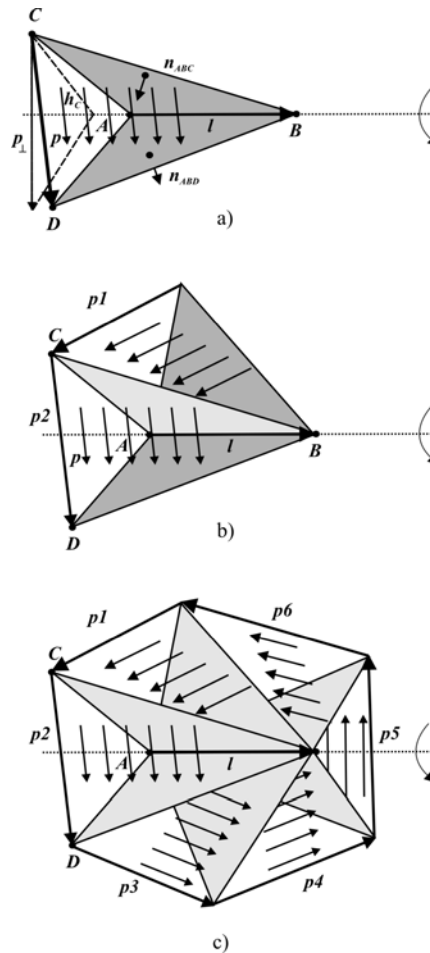
Figure 2.2-1 Three possible configurations for the edge-based function: a) – two faces on the mesh boundary and no inner face; b) – two faces on the mesh boundary and one (or more) inner face(s); c) – only inner faces and no boundary faces
(Ref. [51] of Introduction © 2004 IEEE).

29

In the first case (Fig. 2.2-1a), both grayed faces of a tetrahedron are on the mesh boundary. The basis function includes only one tetrahedron. In the second case (Fig. 2.2-1b), two faces of two adjacent tetrahedra are on the mesh boundary. The basis function includes two tetrahedra and has one inner face. In the last case (Fig. 2.2-1c), all faces of all tetrahedra sharing the base edge are the inner faces of the mesh. The basis function only has the inner faces.

The component of the basis function $\bar{f}$ normal to face ABC in Fig. 2.2-1a is given by

$$f_\perp = c\vec{p} \cdot \vec{n}_{ABC} = c\vec{p}_\perp \cdot \vec{n}_{ABC} = 2c\bar{S}/h_C = cl\bar{S}/S_{ABC} \qquad (2.2.1)$$

where $\vec{p}_\perp$ is the projection of $\vec{p}$ onto a plane perpendicular to the base edge; h_C is the height of triangle ABC perpendicular to the base edge; and $\bar{S}$ is the area of the projection of triangle ACD or triangle BCD onto a plane perpendicular to the base edge. The normalization coefficient is chosen in the form $c = 1/(l\bar{S})$. This guarantees that (i) the normal component of the basis function is continuous through the inner faces; and (ii) the total flux of the normal component through any face is equal to one.

2.2.3   Relation to SWG basis functions

It should be noted that edge basis functions can be considered as a subset of the SWG basis functions. Two examples are shown in Fig. 2.2-2. A piecewise-constant basis function in Fig.2.2-2a with four tetrahedra may be expressed as a combination of four SWG basis functions 1-4, shown in Fig. 2.2-2b. Within tetrahedron ABEF, two linear SWG fields [43] associated with edge AB are combined into a constant field parallel to edge AB by a proper choice of one weight constant. Similarly, one edge basis function with two outer faces shown in Fig. 2.2-2c is represented as a combination of three SWG basis functions 1-3 shown in Fig. 2.2.2d. Such a linear combination of two SWG basis functions in one tetrahedron eliminates the artificial volume charges [43] from consideration and creates the divergence-free edge basis functions.
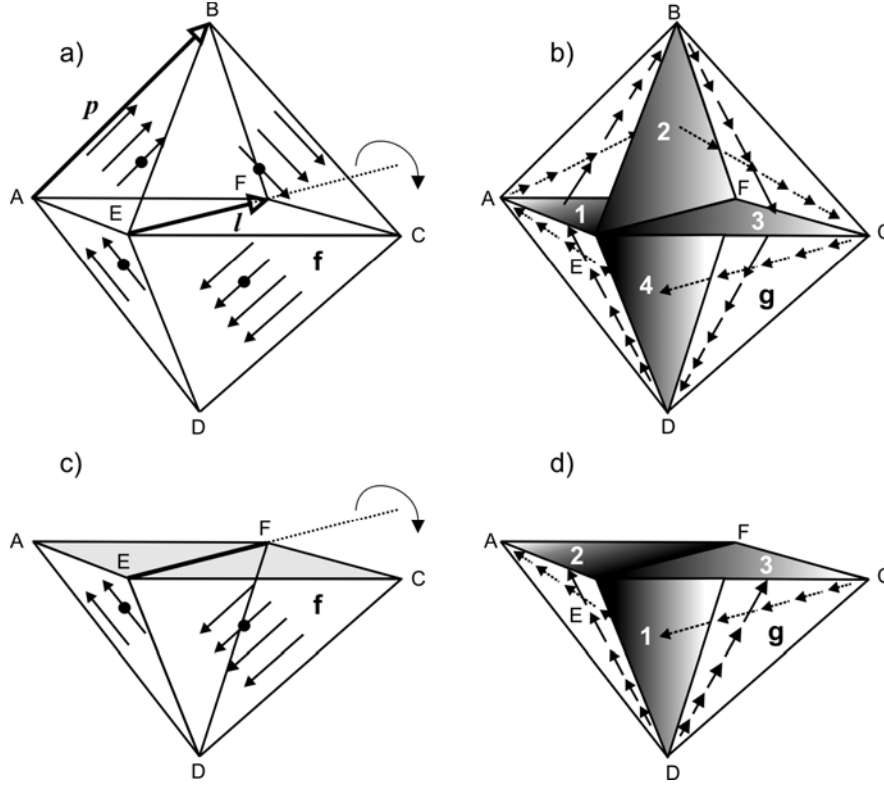
Figure 2.2-2 . a), c) – Edge basis functions with four/two tetrahedra; b), d) – associated SWG basis functions (grayed facets) for the same configuration of tetrahedra.

2.2.4   Size of the functional set

A naive guess is to assume that the number of edge basis functions is equal to the number of edges N of the tetrahedral mesh. This approach leads to the ill-conditioned Gram expansion matrix. In order to estimate the number of independent basis functions, let us first consider a mesh with one tetrahedron. Formally, there are six basis functions corresponding to six basis edges. Only three of them are linearly independent in $\Re^3$ and should therefore be retained. The number of independent basis functions is

$$N = N_F - N_T \tag{2.2.2}$$

where N_F is the number of faces (four) and N_T is the number of tetrahedra (one) in the mesh. Next, consider a mesh with two tetrahedra. The component of the electric flux perpendicular to the common face is the same in both tetrahedra, so it is supported by one

basis function. The remaining component of the flux (parallel to the face) is different in both tetrahedra and is supported by two basis functions in each tetrahedron. The number of independent basis functions (five) is again given by equation (2.2.2) with $N_F = 7, N_T = 2$.

In order to justify equation (2.2.2) in a general case the following can be mentioned. For any tetrahedral mesh, only one basis function is needed per face to support the normal flux component through the given face. This leads to the first term on the right-hand side of equation (2.2.2). On the other hand, any tetrahedron has four faces but needs only three linearly independent basis functions. Therefore, one basis function per tetrahedron must be subtracted. This leads to the second term on the right-hand side of equation (2.2.2). Equation (2.2.2) was validated directly for a number of uniform and non-uniform meshes of different size and shape. However, a formal proof has not been given.

To remove the dependent basis functions for a given tetrahedral mesh, the Gram or "covariance" matrix of a set of the basis functions on the size $N \times N$ is set in the form

$$G = \begin{bmatrix} \langle \vec{f}_1, \vec{f}_1 \rangle & \cdots & \langle \vec{f}_1, \vec{f}_N \rangle \\ \cdots & & \cdots \\ \langle \vec{f}_N, \vec{f}_1 \rangle & & \langle \vec{f}_N, \vec{f}_N \rangle \end{bmatrix}, \quad \langle \vec{f}_m, \vec{f}_n \rangle = \int_V \vec{f}_m \cdot \vec{f}_n d\vec{r}$$

The independent columns of matrix G correspond to independent basis functions. Matrix G is reduced by row operations to an echelon form, E, using Gauss-Jordan elimination with partial pivoting [64]. Then, basic columns of matrix E are in the same position as the linearly-independent columns of G [64]. Only these columns are retained. The nullspace of matrix G is eliminated from consideration, similar to the finite elements bases [62]. Since the number of edges in a large tetrahedral mesh is smaller than the number of faces by typically 30 to 40%, the matrix G is smaller than the impedance matrix for the face-based SWG basis functions. Furthermore, it is real and symmetric. Therefore, the elimination of the null space requires approximately 25% of the CPU time required by

the factorization of the complex impedance matrix for the face-based basis functions. The critical point is that the elimination of the null space should be done only once. When a frequency sweep is applied, the CPU time to eliminate the null space becomes insignificant compared to the total CPU time necessary for the solution of MoM equations for every frequency. Within the framework of the method of moments, a somewhat similar procedure was described by Rubin [65], who studied certain surface (not volume) basis functions.

2.2.5 MoM impedance matrix and MoM equations

a. Field and charge expansion

The total electric flux, $\vec{D}(\vec{r})$, has a continuous normal component and is expanded in the form

$$\vec{D}(\vec{r}) = \sum_{n=1}^{N} D_n \vec{f}_n(\vec{r}) \tag{2.2.3}$$

Once equation (2.2.3) is applied, the density of the surface bound charges is established following the continuity equation, in terms of the surface δ-functions. The equivalent result can be obtained using Gauss's theorem or the boundary condition on the dielectric-dielectric interface. Consider two arbitrary tetrahedra (plus and minus) that share a common face (which includes the base edge) but have different dielectric constants $\hat{\varepsilon}^{\pm}$. The surface charge density σ_S, from Gauss's law,

$$\sigma_S \equiv (K_+ - K_-)D_{\perp} = \hat{K}D_{\perp} \tag{2.2.4}$$

where K_+ and K_- are the dielectric contrasts of the corresponding tetrahedra and $D_{\perp}$ is the normal component of the total electric flux density on the boundary. The dielectric contrast $K_{\pm} = \hat{\varepsilon}^{\pm} - \varepsilon_o / \hat{\varepsilon}^{\pm}$ is a constant within every tetrahedron. The dielectric constant

$\hat{\varepsilon}^{\pm}$ is a complex number, $\hat{\varepsilon}^{\pm} = \varepsilon'^{\pm}(1 - j \tan \delta)$, for a lossy dielectric. The surface normal is directed from the plus (or left) tetrahedron to the minus (right) tetrahedron.

For every basis function $\vec{f}_n(\vec{r})$, and for every face that supports the normal component of this basis function, the associated surface charge is enforced to follow equation (2.2.4). The normal component of $\vec{f}_n(\vec{r})$ can be calculated from equation (2.2.1). The total surface charge density in the dielectric is obtained from a combination of the contributions of all basis functions

$$\sigma_S(\vec{r}) \equiv \hat{K}(\vec{r})D_\perp(\vec{r}) = \sum_{n=1}^{N}\left\{\sum_{q=1}^{Q}\hat{K}_q f_{\perp nq}(\vec{r})\right\}D_n \quad \vec{r} \in \Omega \tag{2.2.5}$$

where $\hat{K}_q = K_+ - K_-$ is the differential contrast on face q and $f_{\perp nq}(\vec{r})$ is the normal component of the basis function $\vec{f}_n(\vec{r})$ on face q. The inner summation in equation (2.2.5) is done over all Q faces that support the normal component of the nth basis function.

The face normal is aligned according to the right-hand rule for the base edge. Its direction follows the direction of the vector field shown in Fig. 2.2-1. The differential contrast is obtained combining the contrast data for the left and right tetrahedra. If one of them does not exist (vacuum-dielectric boundary), then either K_+ or K_- becomes zero. For a homogeneous dielectric this guarantees that (i) every basis function with only inner faces does not create any surface charges; and (ii) every basis function with two boundary faces possesses zero net surface charge.

Along with (2.2.5), the volume polarization current density in the dielectric volume, except for any of its boundaries, is given by

$$\vec{J}_V(\vec{r}) \equiv j\omega K(\vec{r})\vec{D}(\vec{r}) = j\omega \sum_{n=1}^{N}\left\{\sum_{p=1}^{P}K_p \vec{f}_{np}(\vec{r})\right\}D_n \quad \vec{r} \in V, \vec{r} \notin \Omega \tag{2.2.6}$$

The inner summation in equation (2.2.6) is done over all P tetrahedra that are contained by the nth basis function. Every tetrahedron may possess its own dielectric contrast K_p.

b. MoM equations

According to the volume equivalence principle [53], the piecewise inhomogeneous dielectric material is removed and replaced by equivalent volume polarization currents in V and by the associated surface bound charges on S. The volume EFIE is written in the mixed-potential form [43]

$$\vec{E}^i = \vec{E} + j\omega\vec{A}(\vec{r}) + \nabla\Phi(\vec{r}) \quad \vec{r} \in V, \vec{r} \in \Omega \tag{2.2.7}$$

where $\vec{E} = \vec{D}/\hat{\varepsilon}$ is the net electric field and $\vec{E}^i$ is the incident field. The magnetic vector potential $\vec{A}(\vec{r})$ describes radiation of volume polarization currents given by equation (2.2.6), whereas the electric potential $\Phi(\vec{r})$ describes radiation of the associated bound charges given by equation (2.2.5). One has

$$\vec{A}(\vec{r}) = \frac{\mu_0}{4\pi}\int_V \vec{J}_V(\vec{r}')g(\vec{r},\vec{r}')d\vec{r}', \ \Phi(\vec{r}) = \frac{1}{4\pi\varepsilon_0}\int_\Omega \sigma_S(\vec{r}')g(\vec{r},\vec{r}')ds' \tag{2.2.8}$$

where $g(\vec{r},\vec{r}') = \exp(-jkR)/R, R = |\vec{r} - \vec{r}'|$ is the free-space Green's function.

Multiplication of equation (2.2.7) by $K(\vec{r})\vec{f}_m(\vec{r})$, integration over dielectric volume V, and finally integration by parts of integrals due to $\nabla\Phi(\vec{r})$ for every individual tetrahedron contained by $\vec{f}_m(\vec{r})$ gives N moment equations. The resulting surface integrals must be combined in such a way to extract terms related to differential contrasts $\hat{K}_q$. This gives

$$\sum_{p=1}^{P} K_p \int_{V_p} \vec{f}_{mp}(\vec{r}) \cdot \vec{E}^i d\vec{r} = \sum_{p=1}^{P} \frac{K_p}{\hat{\varepsilon}_p} \int_{V_p} \vec{f}_{mp}(\vec{r}) \cdot \vec{D}(\vec{r})d\vec{r} + j\omega\sum_{p=1}^{P} K_p \int_{V_p} \vec{f}_{mp}(\vec{r}) \cdot \vec{A}(\vec{r})d\vec{r} -$$

$$\sum_{q=1}^{Q} \hat{K}_q \int_{\Omega_q} f_{\perp mq}(\vec{r})\Phi(\vec{r})d\vec{r} \quad m = 1,...,N \tag{2.2.9}$$

After substitution of (2.2.5), (2.2.6), and (2.2.8), equation (2.2.9) gives the MoM equations in the form

$$\upsilon_m = \sum_{n=1}^{N} Z_{mn} D_n, \quad \upsilon_m = \sum_{p=1}^{P} K_p \int_{V_p} \vec{f}_{mp}(\vec{r}) \cdot \vec{E}^i(\vec{r}) d\vec{r} \tag{2.2.10}$$

where the impedance matrix $\hat{Z}^{DD}$ is given by

$$\begin{aligned}
\hat{Z}_{mn}^{DD} &= \sum_{p=1}^{P} \sum_{p'=1}^{P'} \frac{K_p}{\hat{\varepsilon}_p} \int_{V_p} \vec{f}_{mp}(\vec{r}) \cdot \vec{f}_{np'}(\vec{r}) d\vec{r} \\
&\quad - \frac{\omega^2 \mu_0}{4\pi} \sum_{p=1}^{P} \sum_{p'=1}^{P'} K_p K_{p'} \int_{V_p} \int_{V_{p'}} g(\vec{r}, \vec{r}') \vec{f}_{mp}(\vec{r}) \cdot \vec{f}_{np'}(\vec{r}') d\vec{r} d\vec{r}' \\
&\quad - \frac{1}{4\pi\varepsilon_0} \sum_{q=1}^{Q} \sum_{q'=1}^{Q'} \hat{K}_q \hat{K}_{q'} \int_{\Omega_q} \int_{\Omega_{q'}} g(\vec{r}, \vec{r}') f_{\perp mq}(\vec{r}) f_{\perp nq'}(\vec{r}') ds ds' \quad m,n = 1,...,N
\end{aligned} \tag{2.2.11}$$

The symmetric impedance matrix is thus written as a combination of individual volume and surface integrals. Since both the basis/test functions and their normal components are constant for a given tetrahedron/face, equation (2.2.11) may be notably simplified. In terms of the notations of subsection 2.2.2 one has

$$\begin{aligned}
\hat{Z}_{mn}^{DD} &= \sum_{p=1}^{P} \sum_{p'=1}^{P'} \frac{K_p V_p}{\hat{\varepsilon}_p l_m l_n \bar{S}_{mp} \bar{S}_{np'}} \left(\vec{p}_{mp} \cdot \vec{p}_{np'} \right) \delta_{pp'} \\
&\quad - \frac{\omega^2 \mu_0}{4\pi} \sum_{p=1}^{P} \sum_{p'=1}^{P'} \frac{K_p K_{p'}}{l_m l_n \bar{S}_{mp} \bar{S}_{np'}} \left(\vec{p}_{mp} \cdot \vec{p}_{np'} \right) \int_{V_p} \int_{V_{p'}} g(\vec{r}, \vec{r}') d\vec{r} d\vec{r}' \\
&\quad - \frac{1}{4\pi\varepsilon_0} \sum_{q=1}^{Q} \sum_{q'=1}^{Q'} \frac{\hat{K}_q \hat{K}_{q'}}{S_q S_{q'}} \int_{\Omega_q} \int_{\Omega_{q'}} g(\vec{r}, \vec{r}') ds ds' \quad m,n = 1,...,N
\end{aligned} \tag{2.2.12}$$

Note that the first term on the right-hand side of equation (2.2.12) is only different from zero when the p-th tetrahedron of basis function m coincides with the p'-th tetrahedron of basis function n.

2.2.6 Eigenmode solution

a. Preconditioner

A simplest diagonal preconditioner preserving the matrix symmetry [66]

$$\hat{Z}^{DD} \rightarrow L^{-1}\hat{Z}^{DD}L^{-1} \qquad (2.2.13a)$$

is applied to the impedance matrix, where L^{-1} is a real diagonal matrix with the elements

$$l_{mm} = 1/\sqrt{\left|\hat{Z}^{DD}_{mn}\right|} \qquad (2.2.13b)$$

b. Solution

The eigenmode solution is then obtained by the search for the local minimum of a cost function F of two variables – the reciprocal condition number κ of the symmetric complex indefinite impedance matrix

$$F(f,f') = \frac{1}{\kappa(\hat{Z}^{DD})} = \frac{1}{\left\|\hat{Z}^{DD}\right\| \cdot \left\|\hat{Z}^{DD^{-1}}\right\|} \qquad (2.2.14)$$

Here, f is the real part of frequency on a complex search plane $f + jf'$ and $f' > 0$ is the imaginary part. If the complex angular frequency is given by $\sigma + j\omega$ [32, 67], then $f' = -\sigma/(2\pi)$.

The LAPACK condition estimator implemented in Intel® Math Kernel Library is used, based on `zsycon`, which in its turn uses Bunch-Kaufman LU factorization routine `zsytrf` for a symmetric complex matrix [68]. Additionally, it uses `zlansy` to estimate the 1-norm of the impedance matrix [68]. Typical non-resonant conditioning numbers are on the order of $10^4 - 10^7$. The search procedure implies direct evaluation of the cost function on the plane of complex frequency. The resonant frequency and the quality factor of the resonator are then obtained as (cf., for example, [69])

$$f_{res} = f_{min}, Q = \frac{f_{min}}{2f'_{min}} \tag{2.2.15}$$

The Q-factor in Eq. (2.2.15) takes into account not only the losses in the non-ideal (lossy) dielectric but also the radiation loss into free space. The latter usually dominates for an unshielded resonator. Note that in Ref. [67] the Q-factor obtained for these conditions is called the radiation Q-factor.

The direct search procedure used in the present version of the program is time-consuming but reasonably safe, especially for closely spaced resonances.

2.2.7 Modal fields

For reliable mode identification, it is necessary to compute the detailed field distribution in the resonator [37]. The modal fields are determined using the method described in Ref. [37]. The value of one D-coefficient is chosen to be a constant, corresponding to the electric field $E = 1e - 3\,V/m$ in vacuum, namely

$$D_1 = 0.001 \times \varepsilon_0 \tag{2.2.16}$$

Then, the first row and the first column of the impedance matrix are removed. The resulting truncated impedance matrix $\hat{Z}'$ is used to determine the rest of the coefficients $\vec{D}'$, which satisfy the following (presumably non-singular) system of equations

$$\hat{Z}' \cdot \vec{D}' = \vec{v}'; \quad \vec{D}' = [D_2,...,D_N]; \quad \vec{v}' = -[Z_{21}D_1,...,Z_{N1}D_1] \tag{2.2.17}$$

Eqs. (2.2.17) are solved using the LAPACK matrix solver `zsysv` with diagonal pivoting for complex symmetric matrices [68].

In some cases, assigning a fixed value to D_1 does not lead to an accurate field description, which means that the resulting Eqs. (2.2.17) are still close to singular ones. One reason may be the appearance of two (or even more) different resonant modes, at approximately the same frequency. This corresponds to double eigenvalue $\lambda = 0$ and null

space of Z of rank 2. Another reason may be numerical inaccuracy due to large variations of the modal fields.

What if the solution is not satisfactory, i.e. $|D_1|$ appears to be much larger than the magnitude of other D-coefficients obtained using Eqs. (2.2.17)? In this case one may choose another coefficient $D_{n \neq 1}$ in Eq. (2.2.16) that is the closest one to the average value of D-coefficients, and repeat the solution of Eqs. (2.2.17). Although slow, this method shows reliable results for different resonator types and modal fields, and it has been implemented in the present program (script `mode.m`).

2.2.8 <u>Electric/magnetic field and surface charges</u>

Once all D-coefficients are known, one (direct) method to find the electric field within the dielectric is to use the relation

$$\vec{E} = \vec{D} / \hat{\varepsilon} \tag{2.2.18}$$

and Eq. (2.2.3). Yet it would be difficult to find the magnetic field with this approach. The density of the surface bound charges is obtained according to Eq. (2.2.5).

The standard method for field evaluation, implemented in the program, is based on the use of the potential integrals Eqs.(2.2.8). According to Eqs. (2.2.7), (2.2.8), the scattered electric field $\vec{E}^s$ due to volume polarization currents and surface bound charges caused by the electric flux density $\vec{D}$ has the form

$$\begin{aligned}
\vec{E}^s(\vec{r}) &= \frac{\omega^2 \mu_0}{4\pi} \sum_{n=1}^{N} \left\{ \sum_{p=1}^{P} K_p \int_{V_p} g(\vec{r}, \vec{r}') \vec{f}_{np}(\vec{r}') d\vec{r}' \right\} D_n \\
&\quad - \frac{1}{4\pi\varepsilon_0} \sum_{n=1}^{N} \left\{ \sum_{q=1}^{Q} \hat{K}_q \int_{\Omega_q} \nabla_r g(\vec{r}, \vec{r}') f_{\perp nq}(\vec{r}') ds' \right\} D_n
\end{aligned} \tag{2.2.19}$$

Similarly, the scattered magnetic field $\vec{H}^s$ has the form

$$\vec{H}^s(\vec{r}') = -\frac{j\omega}{4\pi}\sum_{n=1}^{N}\left\{\sum_{p=1}^{P}K_p\int_{V_p}\left(\vec{f}_{np}(\vec{r}')\times\nabla_r g(\vec{r},\vec{r}')\right)d\vec{r}'\right\}D_n \tag{2.2.20}$$

All the notations in Eqs. (2.2.19) and (2.2.20) are identical to those used in Eqs. (2.2.11) and (2.2.12) for the impedance matrix.

Once both the electric and magnetic fields are calculated, the Poynting vector $\vec{P}$ within the dielectric material can be found in the form

$$\vec{P} = \frac{1}{2}[\vec{E}\times\vec{H}^*] \tag{2.2.21}$$

2.2.9 <u>Impedance matrix $\hat{Z}^{DD}$ and the radiated/scattered fields</u>

a. Base integrals

About 90% of the CPU time required for the filling of the MoM impedance matrix $\hat{Z}^{DD}$ for the edge basis functions is spent for the calculation of the volume/surface integrals presented in Eq. (2.2.12)

$$A_{D\,pp'} = \int_{V_p}\int_{V_{p'}} g(\vec{r},\vec{r}')d\vec{r}d\vec{r}' \tag{2.2.22}$$

$$\Phi_{D\,qq'} = \int_{\Omega_q}\int_{\Omega_{q'}} g(\vec{r},\vec{r}')d\Omega'd\Omega \tag{2.2.23}$$

In contrast to the metal surface, no vector integrals are present in the impedance matrix. Also, there are no mixed surface-to-volume integrals.

b. Singularity extraction

The singularity of the free-space Green's function is integrable in 3D or 2D but the accuracy of the Gaussian formulas is reduced if this singularity is retained. Therefore, singularity extraction may be used in Eqs. (2.2.22), (2.2.23), in the form

$$\iint\limits_{V_p V_{p'}} g(\vec{r}, \vec{r}') d\vec{r} d\vec{r}' = \iint\limits_{V_p V_q} \frac{1}{|\vec{r} - \vec{r}'|} d\vec{r} d\vec{r}' + \iint\limits_{V_p V_q} \frac{\left(\exp(-jk|\vec{r} - \vec{r}'|) - 1\right)}{|\vec{r} - \vec{r}'|} d\vec{r} d\vec{r}' \qquad (2.2.24)$$

$$\iint\limits_{\Omega_q \Omega_{q'}} g(\vec{r}, \vec{r}') d\Omega' d\Omega = \iint\limits_{\Omega_p \Omega_q} \frac{1}{|\vec{r} - \vec{r}'|} d\Omega' d\Omega + \iint\limits_{\Omega_p \Omega_q} \frac{\left(\exp(-jk|\vec{r} - \vec{r}'|) - 1\right)}{|\vec{r} - \vec{r}'|} d\Omega' d\Omega \qquad (2.2.25)$$

Two first singular integrals on the right-hand side of Eqs. (2.2.24), (2.2.25) (the potential or static integrals) may be found with the help of the analytical results given in [55].

c. Impedance matrix

A "neighboring" sphere of dimensionless radius R is introduced for every integration tetrahedron/facet. R is a threshold value for the ratio distance/size. The size of the facet $S(\Omega_q)$, is measured as the distance from its center to the furthest vertex. The size of the tetrahedron $S(V_q)$ is measured exactly in the same way. The observation face Ω_q lies within the sphere if the following inequality is valid for the distance d between two triangle centers

$$\frac{d}{\sqrt{S(\Omega_q) S(\Omega_{q'})}} < R \qquad (2.2.26)$$

If a pair of facets satisfies Eq. (2.2.26) then the integrals (2.2.23) use the singularity extraction equation (2.2.25) and the analytical formula (2.1.23) for the inner potential integrals. The non-singular part and the outer potential integrals employ Gaussian cubature given in [56]. Each cubature is characterized by two numbers: N-the number of integration points; and d-the degree of accuracy for the Gaussian cubature formula. If a pair of facets does not satisfy Eq. (2.2.26) then the central-point approximation is used for all integrals, without singularity extraction. The parameter R is initialized in the script `dielectric.m` in subfolder 2_basis\codes. The same is valid for N and d for the Gaussian formulas. The default values are $R = \sqrt{5}$ and $N = 3, d = 2$ for the surface integrals. These values are identical with the metal integration values given in section 2.1.

For tetrahedra, the same condition has to be satisfied, in the form

$$\frac{d}{\sqrt{S(V_p)S(V_{p'})}} < R \tag{2.2.27}$$

If a pair of tetrahedra satisfies Eq. (2.2.27) then the integrals (2.2.22) use the singularity extraction (2.2.24) and the following analytical formula [55]

$$\int_{V_{p'}} \frac{1}{|\vec{r} - \vec{r}'|} d\vec{r}' =$$

$$\frac{1}{2} \sum_{j=1}^{4} d_j \left\{ \sum_{i=1}^{3} \vec{P}_{ij}^0 \cdot \vec{u}_{ij} \left[\left| d_j \right| \left(\tan^{-1} \frac{P_{ij}^0 \, l_{ij}^+}{\left(R_{ij}^0\right)^2 + \left| d_j \right| \left| R_{ij}^+ \right|} - \tan^{-1} \frac{P_{ij}^0 \, l_{ij}^-}{\left(R_{ij}^0\right)^2 + \left| d_j \right| \left| R_{ij}^- \right|} \right) - P_{ij}^0 \ln \frac{R_{ij}^+ + l_{ij}^+}{R_{ij}^- + l_{ij}^-} \right] \right\} \tag{2.2.28}$$

for the inner potential integrals. The variables in Eq. (2.2.28) are similar to those used in Eqs. (2.1.23) and (2.1.24) of section 2.1. Here, the double subscript ij represents the ith edge of the jth face of a tetrahedron. The non-singular part and the outer potential integrals employ Gaussian cubature on tetrahedra given in [56]. Each cubature is also characterized by two numbers: N-the number of integration points; and d-the degree of accuracy for the Gaussian cubature formula. If a pair of tetrahedra does not satisfy Eq. (2.2.27) then the central-point approximation is used for all integrals, without singularity extraction. The parameter R is initialized in the script `dielectric.m` in subfolder 2_basis\codes. The same is valid for N and d for the Gaussian formulas. The default values are $R = 1e-3$ and $N = 1, d = 1$ for the volume integrals. They mean the lowest possible integration accuracy where only the double self-integrals use the singularity extraction Eq. (2.2.24) and the central-point approximation otherwise. The direct validation of this approximation is given in Refs. [70, 71] and is connected to the structure of the basis functions themselves. Intuitively, the higher is the integration order, the better the intrinsic "inaccuracy" of the basis functions is reproduced. This inaccuracy implies piecewise-constant field approximation and discontinuity of the tangential E-field

on the faces. Therefore, the convergence is slow for finer integration. On the other hand, the central-point approximation leaves the function behavior on faces essentially undefined. In other words, the existing MoM equations become equally valid for a better (or higher-order) set of basis functions that preserve field continuity. Hence the convergence considerably improves. The more formal discussion with regard to the numerical integration accuracy is given in section 2.2.4.

d. Test of volume/surface potential integrals

The accuracy of the numerical implementation of Eq. (2.1.23) and Eq. (2.2.28) has been extensively tested. As an example, Fig. 2.2-3 shows the integral behavior (absolute integral value) for two equal faces (Fig. 2.2-3a) and tetrahedra (Fig. 2.2-3c) separated by a varying distance s. Fig. 2.2-3b gives the potential integral from Eq. (2.2.25) for $N = 1, d = 1$ (curve 1), $N = 7, d = 5$ (curve 2), and $N = 25, d = 10$ (curve 3). N and d are related to the Gaussian cubature applied to the outer potential integral in Eq. (2.2.25). Relative error vs. the result of direct integration with 256×256 barycentric points is given by curves $1', 2', 3'$. To obtain the error percentage, the relative error should be multiplied by 100. Similarly, Fig. 2.2-3d gives the potential integral from Eq. (2.2.24) found for $N = 1, d = 1$ (curve 1), $N = 5, d = 3$ (curve 2), and $N = 15, d = 5$ (curve 3) – all these numbers are related to the outer integral. Relative error vs. the result of direct integration with 512×512 barycentric points is given by curves $1', 2', 3'$. Fig. 2.2-3e presents the magnified relative error for $N = 5, d = 3$ (curve $2'$), $N = 15, d = 5$ (curve $3'$), and $N = 33, d = 7$ (curve $4'$). These results confirm the accuracy of the potential integrals and, simultaneously, highlight the effect of the outer Gaussian integration. A similar test was made for the vector potential integrals of section 2.1.
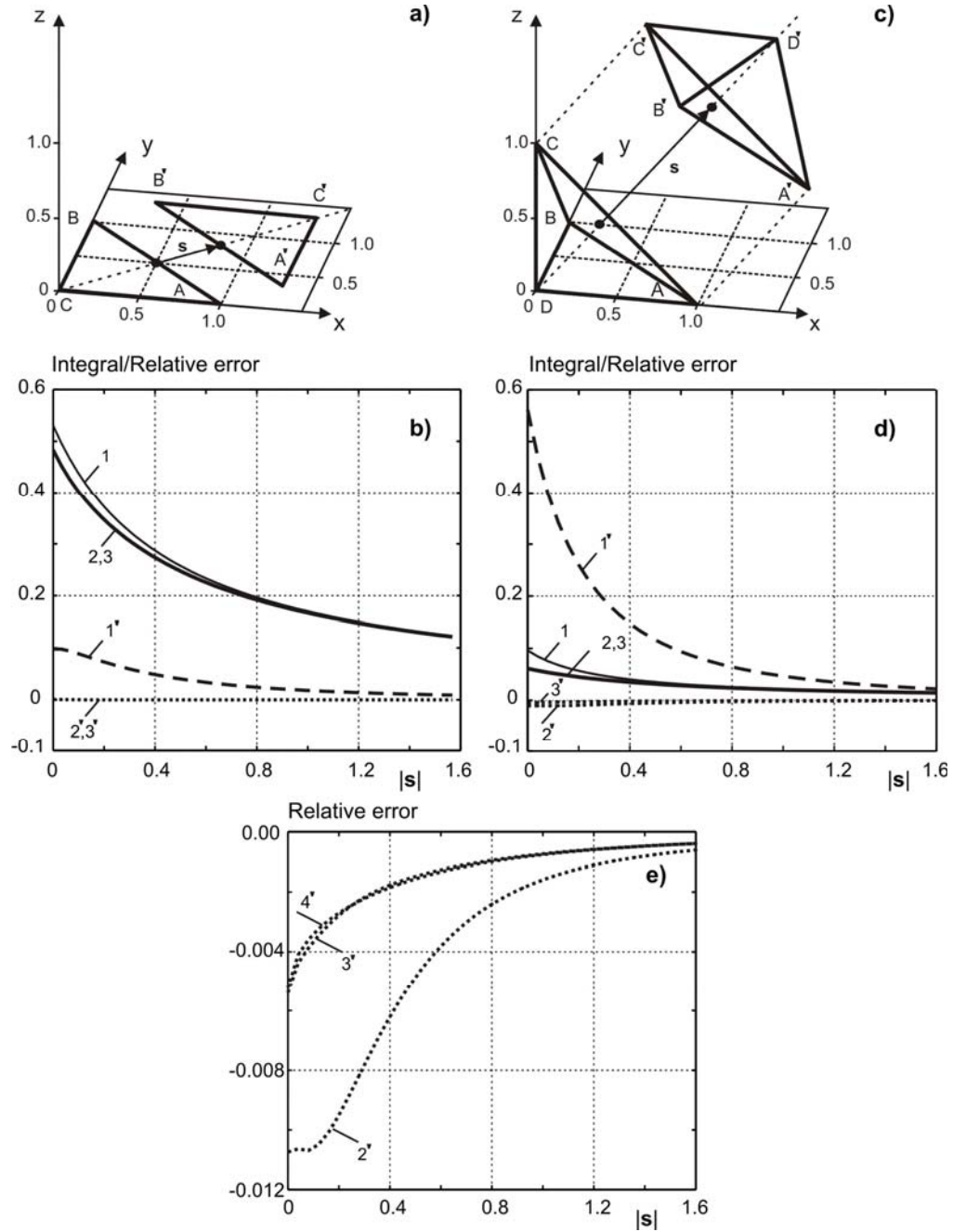
Figure 2.2-3. a) – Pair of faces used to evaluate the surface double potential integral; b) – potential integral found for $N = 1, d = 1$ (curve 1), $N = 7, d = 5$ (curve 2), and $N = 25, d = 10$ (curve 3). Relative error vs. the direct solution with 256×256 barycentric points is given by curves $1', 2', 3'$. c) – Pair of tetrahedra used to evaluate the volume double potential integral; d) –volume potential integral found for $N = 1, d = 1$ (curve 1), $N = 5, d = 3$ (curve 2), and $N = 15, d = 5$ (curve 3). Relative error vs. the direct solution with 512×512 barycentric points is given by curves $1', 2', 3'$. e) – Magnified relative error for $N = 5, d = 3$ (curve $2'$), $N = 15, d = 5$ (curve $3'$), and $N = 33, d = 7$ (curve $4'$).

e. Fields

The same operation as for the impedance matrix is done for the field integrals (2.2.19) and (2.2.20) but Eq. (2.2.26) is now replaced by

$$\frac{d}{S(\Omega_q)} < R \tag{2.2.29}$$

Eq. (2.2.27) changes accordingly. Within the sphere, all the surface potential integrals are found identical to these for the metal structure, with the use of Eqs. (2.1.23), (2.1.24), and (2.1.30). The volume potential integrals are found according to Eq. (2.2.28). Additionally, the divergence theorem is used for the potential integrals of the Green's function gradient over tetrahedra, i.e.

$$\int_{V_p} \nabla \frac{1}{|\vec{r} - \vec{r}'|} d\vec{r}' = \int_{S} \frac{1}{|\vec{r} - \vec{r}'|} \vec{n} \, ds \tag{2.2.30}$$

where $\vec{n}$ is the unit outer normal vector to the to each of the four triangular surfaces of the tetrahedron.

The parameter R is initialized in the script `field.m` in subfolder 3_mom/codes. The default value is $R = 2$. The N and d for the Gaussian formula on facets are hard coded as $N = 7, d = 5$ in the script `fieldd.cpp`. Similarly, the N and d for the Gaussian formula on tetrahedra are hard coded as $N = 5, d = 3$ in the same script. Outside the sphere, the central-point approximation is used. For the far-field approximation, $R \to 0$ is an acceptable assumption.

2.2.10 List of available Gaussian integration formulas on tetrahedra

Some Gaussian integration formulas on tetrahedra [56] are given in the script `tet.m` in subfolder 2_basis\codes. The formulas given in Table 2.2.1 were used and tested. Each cubature is characterized by two numbers: N is the number of integration points and d is the degree of accuracy for the Gaussian cubature formula.

Table 2.2-1 List of available/tested Gaussian formulas on tetrahedra [56].

Formula	N	d
#1	1	1
#2	4	2
#3	5	3
#4	11	4
#5	14	5
#6	15	5
#7	33	7
#8	53	9

Also, the barycentric tetrahedron subdivision of a low degree is available in the script `tet.m`.

2.2.11 Numerical operations and associated MATLAB/C++ scripts

The summary of numerical operations related to a dielectric resonator is given in Table. 2.2.2.

Table 2.2-2 Dielectric resonator-related numerical operations.

Operation	Script	Path	Remarks
Resonator operations			
Determine the dielectric structure	`struct2d.m` `struct3d.m`	1_mesh	Do not use $\varepsilon_r = 1$ while running `struct3d.m`. Remove all unnecessary tetrahedra from the mesh.
Determine parameters of the edge basis functions and the independent basis function set	`wrapper.m`	2_basis	Outputs structure GEOM with all the necessary data on the basis functions/pre-calculated potential integrals
Determine accuracy of impedance matrix filling –optional (see Section 2.2.9)	`dielectric.m`	2_basis\codes	The parameter R is initialized in the script `dielectric.m` in subfolder 2_basis\codes. The same is valid for N and d for the Gaussian formulas (facets, tets). The default values are $R = \sqrt{5}$ and $N = 3, d = 2$ for the facets and $R = 1e - 3$ and $N = 1, d = 1$ for tetrahedra. The necessary potential integrals are pre-calculated in

			structure `GEOM` and are saved in the sparse matrix format.
Determine eigenfrequency/Q-factor	`eigenfreq.m`	3_mom	Fully interactive interface.
Determine the eigenmode field	`mode.m`	3_mom	Follows Section 2.2.7 of this Chapter. Does not work for the metal-dielectric structure. Use `scatterfield.m` instead
Determine the electric or magnetic field distribution in the dielectric volume (or bound surface charge density) in the resonant mode	`scatterfiel d.m`	3_mom	`Scatterfield.m` illuminates the resonator by an incident plane wave at the resonant frequency and finds the current/charge distributions at that given frequency

If the modal fields obtained after running `mode.m` are not quite well developed, the search domain in `eigenfreq.m` must be refined. The independent scattering problem may be also considered for the dielectric, by running `scatterfield.m` at a given frequency.

2.3 MoM VIE Approach to a Metal-Dielectric Antenna

In this section, the MoM equations for a combined metal-dielectric structure are derived for the EFIE [52], utilizing the RWG [53] and the edge basis functions [50], following the approach as given in [48].

2.3.1 <u>MoM equations for a metal-dielectric structure</u>

a. Scattering problem

The present derivation follows the derivation given in [48] for the VIE approach to the metal-dielectric antennas. The complete moment equations essentially combine the results of section 2.1 and 2.2 together. The new feature is a (symmetric) interaction part of the total impedance matrix, which describes metal-to-dielectric (or dielectric-to-metal) interaction. Similar to Sections 2.1 and 2.2, the scattering problem is considered. The

total electric field (scattering problem) is a combination of the incident field (labeled by superscript i) and the scattered field (labeled by superscript s), i.e.

$$\vec{E} = \vec{E}^i + \vec{E}^s \qquad (2.3.1)$$

Let V (bounded by surface Ω) denote the volume of a lossy, inhomogeneous, dielectric body with (complex) dielectric constant $\hat{\varepsilon}(\vec{r}) = \varepsilon(\vec{r}) - j\sigma(\vec{r})/\omega$, where ε and σ are the medium permittivity and conductivity when $\vec{r}$ is in V. Let a metal surface S be attached to this dielectric object or be in the vicinity of it.

The incident field is the incoming signal for the scattering problem. The scattered electric field $\vec{E}^s$ in this case will have two components. One is due to volume polarization currents in the dielectric volume V and associated bound charges on the boundaries of an inhomogeneous dielectric region, and the other component is due to surface conduction currents and free charges on the metal surface S. Using the expressions for the scattered field in terms of the magnetic and electric potentials $\vec{A}$ and Φ, one has

$$\vec{E}^s = -j\omega\vec{A}(\vec{r}) - \nabla\Phi(\vec{r}) - j\omega\vec{A}_M(\vec{r}) - \nabla\Phi_M(\vec{r}) \quad \vec{r} \text{ in } V \qquad (2.3.2)$$

$$\vec{E}^s = -j\omega\vec{A}_M(\vec{r}) - \nabla\Phi_M(\vec{r}) - j\omega\vec{A}(\vec{r}) - \nabla\Phi(\vec{r}) \quad \vec{r} \text{ on } S \qquad (2.3.3)$$

where index M refers to the metal surface S. The magnetic vector potential $\vec{A}(\vec{r})$ and electric potential $\Phi(\vec{r})$ carry their usual meanings corresponding to metal and dielectric [48]. Since

$$\vec{D} = \hat{\varepsilon}\vec{E} \qquad \text{in the dielectric volume V} \qquad (2.3.4)$$

$$\vec{E}_{tan} = 0 \qquad \text{on the metal surface S} \qquad (2.3.5)$$

using the expressions for $\vec{E}$ and $\vec{E}^s$, we can write the EFIE as

$$\vec{E}^i = \frac{\vec{D}(\vec{r})}{\hat{\varepsilon}(\vec{r})} + j\omega\vec{A}(\vec{r}) + \nabla\Phi(\vec{r}) + j\omega\vec{A}_M(\vec{r}) + \nabla\Phi_M(\vec{r}) \quad \vec{r} \text{ in } V \qquad (2.3.6)$$

$$\vec{E}_{\tan}^{i} = \left[+ j\omega\vec{A}_{M}(\vec{r}) + \nabla\Phi_{M}(\vec{r}) + j\omega\vec{A}(\vec{r}) + \nabla\Phi(\vec{r})\right]_{\tan} \quad \vec{r} \text{ on } S \qquad (2.3.7)$$

b. Test functions

Assume that some test functions, $K(\vec{r})\vec{f}_{m}(\vec{r})$, $m = 1,\dots,N_{D}$, cover the entire dielectric volume V. Multiplication of equation (2.3.6) by $K(\vec{r})\vec{f}_{m}(\vec{r})$ and integration over volume V gives N_{D} equations

$$\int_{V} K(\vec{r})\vec{f}_{m}(\vec{r}) \cdot \vec{E}^{i} d\vec{r} =$$

$$\begin{bmatrix} \int_{V} K(\vec{r})\vec{f}_{m}(\vec{r}) \cdot \dfrac{\vec{D}(\vec{r})}{\hat{\varepsilon}(\vec{r})} dv + j\omega\int_{V} K(\vec{r})\vec{f}_{m}(\vec{r}) \cdot \vec{A}(\vec{r}) dv + \int_{V} K(\vec{r})\vec{f}_{m}(\vec{r}) \cdot \nabla\Phi(\vec{r}) dv \\ + j\omega\int_{V} K(\vec{r})\vec{f}_{m}(\vec{r}) \cdot \vec{A}_{M}(\vec{r}) dv + \int_{V} K(\vec{r})\vec{f}_{m}(\vec{r}) \cdot \nabla\Phi_{M}(\vec{r}) dv \end{bmatrix} \qquad (2.3.8)$$

Simplifying the last volume integral by applying Divergence theorem and standard vector identities; for every individual tetrahedron in the manner similar to the simplification of the last volume integral in Eq. (2.2.9) yields

$$\int_{V} K(\vec{r})\vec{f}_{m}(\vec{r}) \cdot \nabla\Phi_{M}(\vec{r}) dv = -\int_{V} K(\vec{r})\Phi_{M}(\vec{r})\left(\nabla \cdot \vec{f}_{m}(\vec{r})\right) dv + \int_{\Omega} K(\vec{r})\Phi_{M}(\vec{r})\left(\hat{n}(\vec{r}) \cdot \vec{f}_{m}(\vec{r})\right) ds$$

However the volume basis functions are divergenceless. Hence

$$\int_{V} K(\vec{r})\vec{f}_{m}(\vec{r}) \cdot \nabla\Phi(\vec{r}) dv = \int_{\Omega} K(\vec{r})\Phi_{S}(\vec{r})\left(\hat{n}(\vec{r}) \cdot \vec{f}_{m}(\vec{r})\right) ds = \int_{\Omega} K(\vec{r})\Phi_{S}(\vec{r}) \cdot f_{\perp mq}(\vec{r}) ds$$

$$(2.3.9)$$

where $\hat{n}$ is the unit outer normal to the surface Ω and $f_{\perp mq}(\vec{r})$ is the outer normal component of the basis function $\vec{f}_{m}(\vec{r})$ on face q. Substituting the values from equation (2.3.9) in equation (2.3.8) gives

$$\int_V K(\vec{r})\vec{f}_m(\vec{r}) \cdot \vec{E}^i dv = \begin{bmatrix} \underbrace{\int_V K(\vec{r})\vec{f}_m(\vec{r}) \cdot \dfrac{\vec{D}(\vec{r})}{\hat{\varepsilon}(\vec{r})} dv + j\omega \int_V K(\vec{r})\vec{f}_m(\vec{r}) \cdot \vec{A}(\vec{r}) dv + \int_\Omega \hat{K}_q \Phi(\vec{r}) f_{\perp mq}(\vec{r}) ds}_{Z^{DD}} \\ \underbrace{+ j\omega \int_V K(\vec{r})\vec{f}_m(\vec{r}) \cdot \vec{A}_S(\vec{r}) dv + \int_\Omega \hat{K}_q \Phi_S(\vec{r}) f_{\perp mq}(\vec{r}) ds}_{Z^{DM}} \end{bmatrix}$$

(2.3.10)

The process of converting the contrast, $K(\vec{r})$, to the differential contrast, $\hat{K}$, is exactly the same as explained in Section 2.2. The term on the right-hand side of equation (2.3.10), labeled Z^{DD}, is exactly the right-hand side of equation (2.2.9) for the pure dielectric. The term, labeled Z^{DM}, describes the contribution of radiation from the metal surface to the dielectric volume.

Now assume that the surface test functions, $\vec{f}_m^M(\vec{r})$, $m = 1, \dots, N_M$, cover the entire metal surface S and do not have a component normal to the surface. Multiplication of equation (2.3.7) by $\vec{f}_m^M(\vec{r})$ and integration over surface S gives N_M equations

$$\int_S \vec{f}_m^S(\vec{r}) \cdot \vec{E}^i ds = \begin{bmatrix} \underbrace{+ j\omega \int_S \vec{f}_m^M(\vec{r}) \cdot \vec{A}_M(\vec{r}) ds - \int_S \left(\nabla \cdot \vec{f}_m^M(\vec{r})\right) \Phi_M(\vec{r}) ds}_{Z^{MM}} \\ \underbrace{+ j\omega \int_S \vec{f}_m^M(\vec{r}) \cdot \vec{A}(\vec{r}) ds - \int_S \left(\nabla \cdot \vec{f}_m^M(\vec{r})\right) \Phi(\vec{r}) ds}_{Z^{MD}} \end{bmatrix}$$

(2.3.11)

since according to Divergence theorem and using standard vector identities,

$$\int_S \vec{f}_m^M(\vec{r}) \cdot \nabla\Phi(\vec{r}) ds = -\int_S \Phi(\vec{r})\left(\nabla \cdot \vec{f}_m^M(\vec{r})\right) ds$$

(2.3.12)

The term on the right-hand side of equation (2.3.11), labeled Z^{MM}, is exactly the right-hand side of equation (2.1.6) for the pure metal. The term, labeled Z^{MD}, describes the contribution of radiation from the dielectric volume to the metal surface.

c. Source functions and moment equations

The moment equations are obtained if we substitute expansions for potentials in terms of the corresponding source basis functions into equations (2.3.10), (2.3.11). In terms of symbolic notations,

$$\sum_{n=1}^{N_D} \hat{Z}_{mn}^{DD} D_n + \sum_{n=1}^{N_M} \hat{Z}_{mn}^{DM} I_n = \vec{\upsilon}_m^D \quad m = 1,...N_D \tag{2.3.13}$$

$$\sum_{n=1}^{N_M} \hat{Z}_{mn}^{MM} I_n + \sum_{n=1}^{N_D} \hat{Z}_{mn}^{MD} D_n = \vec{\upsilon}_m^M \quad m = 1,....N_M \tag{2.3.14}$$

where

$$\upsilon_m^D = \int_V K(\vec{r}) \vec{f}_m(\vec{r}) \cdot \vec{E}^i dv, \quad \upsilon_m^M = \int_S \vec{f}_n^M(\vec{r}) \cdot \vec{E}^i_{\tan} ds \tag{2.3.15}$$

The square impedance matrices $\hat{Z}^{MM}$ and $\hat{Z}^{DD}$ have been described in sections 2.1 and 2.2 respectively. They will not be repeated here. The new part, however, are the mutual rectangular impedance matrixes $\hat{Z}^{MD}$ and $\hat{Z}^{DM}$. One has

$$
\begin{aligned}
Z_{mn}^{MD} = \ & -\frac{\omega^2 \mu_0}{4\pi} \sum_{p=1}^{2} \sum_{p'=1}^{P} K_{p'} \int_{t_p} \int_{V_{p'}} \vec{f}_n^M(\vec{r}) \cdot \vec{f}_{mp'}(\vec{r}') g(\vec{r},\vec{r}') d\vec{r}' ds \\
& -\frac{1}{4\pi\varepsilon_0} \sum_{p=1}^{2} \sum_{q=1}^{Q} \hat{K}_q \int_{t_p} \int_{\Omega_{q'}} (\nabla_S \cdot \vec{f}_n^M(\vec{r})) f_{\perp mq}(\vec{r}') g(\vec{r},\vec{r}') d\Omega' ds \\
& m = 1,...,N_D; n = 1,...,N_M
\end{aligned}
\tag{2.3.16}
$$

$$
\begin{aligned}
Z_{mn}^{DM} = \ & \frac{j\omega\mu_0}{4\pi} \sum_{p=1}^{2} \sum_{p'=1}^{P} K_{p'} \int_{V_p} \int_{S_{p'}} \vec{f}_{np}(\vec{r}) \cdot \vec{f}_m^M(\vec{r}') g(\vec{r},\vec{r}') ds' d\vec{r} \\
& +\frac{j}{4\pi\varepsilon_0\omega} \sum_{p=1}^{2} \sum_{q=1}^{Q} \hat{K}_q \int_{\Omega_q} \int_{S_{p'}} f_{\perp nq}(\vec{r}) \cdot (\nabla_S \cdot \vec{f}_m^M(\vec{r}')) g(\vec{r},\vec{r}') ds' d\Omega \\
& n = 1,...,N_D; m = 1,...,N_M
\end{aligned}
\tag{2.3.17}
$$

From equations (2.3.16) and (2.3.17) one can see that

$$\hat{Z}^{DM} = \left(\hat{Z}^{MD}\right)^T / (j\omega) \tag{2.3.18}$$

where the superscript T denotes the transpose matrix.

2.3.2 **Total impedance matrix**

The total impedance matrix is obtained by combining the metal impedance matrix $\hat{Z}^{MM}$, the dielectric impedance matrix $\hat{Z}^{DD}$, and the mutual impedance matrices $\hat{Z}^{DM}$ and $\hat{Z}^{MD}$ in the form

$$\hat{Z} = \begin{bmatrix} \hat{Z}^{MM} & \hat{Z}^{MD} \\ \hat{Z}^{DM} & \hat{Z}^{DD} \end{bmatrix} \tag{2.3.19}$$

The impedance matrix $\hat{Z}$ can be converted to a symmetric matrix form by using trivial transformations. One way of achieving it is

$$\hat{Z} = \begin{bmatrix} j\omega\hat{Z}^{MM} & \hat{Z}^{MD} \\ j\omega\hat{Z}^{DM} & \hat{Z}^{DD} \end{bmatrix} \tag{2.3.20}$$

Once the matrix $\hat{Z}$ is obtained we solve the system of equation in the form

$$\vec{V} = \hat{Z}\vec{I} \tag{2.3.21}$$

where

$$\vec{V} = [\vec{\upsilon}^M \ \vec{\upsilon}^D] \tag{2.3.22}$$

The metal partition of the solution vector, $\vec{I}$, needs to be multiplied by $j\omega$ afterwards.

2.3.3 **Impedance matrix $\hat{\underline{Z}}$ and the radiated/scattered fields**

a. Base integrals and their calculation

Compared to the two particular cases of pure metal and dielectric considered in Sections 2.1 and 2.2 respectively, Eqs. (2.3.16) and (2.3.17) include two new integrals:

$$\vec{A}^i_{MD\,pp'} = \int\limits_{t_p} \int\limits_{V_{p'}} \vec{\rho}_i g(|\vec{r} - \vec{r}'|) d\vec{r}' ds \qquad (2.3.23)$$

$$\Phi_{MD\,qq'} = \int\limits_{t_q} \int\limits_{\Omega_{q'}} g(|\vec{r} - \vec{r}'|) d\Omega' dS \qquad (2.3.24)$$

These integrals (their potential parts) are pre-computed in the script `dielectric.m` in subfolder 2_basis\codes. The integral (2.3.24) is not really new and is identical with the integral (2.1.20) or (2.2.23). The singularity extraction and the integral calculation are done following the approach of Sections 2.2 and 2.3. A "neighboring" sphere of dimensionless radius R is introduced exactly in the same way as for the dielectric. The same default values are used: $R = \sqrt{5}$ and $N = 3, d = 2$ for the surface integrals. These parameters are initialized in the script `dielectric.m` in subfolder 2_basis\codes.

In integral (2.3.23), we calculate the inner volume integral first, using the singularity extraction and Eq. (2.2.28). The Gaussian formulas for tetrahedra are identical with those used for the pure dielectric. The Gaussian formulas for triangles (facet of the outer integral) are also identical with those from Section 2.2.

b. Solution and filling method

The full impedance matrix is symmetric, but not Hermitian [66]. Therefore, only the upper (or the lower) triangular matrices need to filled out. It is preferred to fill $\hat{Z}^{MD}$ instead of $\hat{Z}^{DM}$ (choose the upper triangular matrix). Only the upper triangular part of $\hat{Z}^{MM}$ and $\hat{Z}^{DD}$ need to be filled accordingly. Then, Eqs. (2.3.21) are solved using the LAPACK matrix solver `zsysv` with diagonal pivoting for complex symmetric matrices [68].

c. Fields

The scattered fields are calculated separately for metal and dielectric, and then are added together. This operation is done in the script `field.m` in subfolder 3_mom\codes.

2.3.4   <u>Numerical operations and associated MATLAB/C++ scripts</u>

The full code performs the antenna simulation as described in Section 2.1.7. The antenna can include dielectric in any configuration but the feed needs to be specified in the metal. The full code also performs the eigenfrequency search for a metal-dielectric resonator as described in Section 2.2. However, the `mode.m` (eigenmode field distribution) function is no longer available due to some numerical difficulties. Instead, `scatterfield.m` may be used to inspect a scattered field at the resonant frequency.

2.4 Effect of Numerical Cubature on the MoM Solution

2.4.1   <u>Introduction</u>

It has been accepted since Harrington [5] that the use of more accurate integration rules for the integrals of the impedance matrix generally improves the convergence of the MoM solution. For 2D scattering problems, comprehensive convergence studies were done in Refs. [72-75]. A significant body of work is devoted to the development of accurate integration rules for 2D or 3D potential integrals (cf. [74-77]).

At the same time, practical evidence indicates that a 3D MoM solution obtained with low-order basis functions and with a relatively small number of basis functions per wavelength (about 8-30) is rather insensitive to integration accuracy. Moreover, the use of higher-order integration rules may lead to a weaker convergence of the MoM solution when the mesh is refined. This is true in particular for the volume EFIE applied to dielectric resonators [70, 71].

The situation described above is typical for a 3D MoM problem where the number of basis functions per wavelength is relatively small and where low-order basis functions are often used (cf. Refs. [44-47] related to the volume EFIE). There seems to be no rule that predicts how accurate a particular numerical integration should be and whether or not the high-order numerical cubatures are really needed. This question is practically important

since the accurate integration including potential integrals for neighbor mesh elements is very time and memory intensive in the 3D case.

The present section investigates the effect of numerical cubature on the MoM solution for two 3D problems: an isolated dielectric resonator and a driven open-circuit microstrip metal resonator. The volume EFIE for dielectric uses the zeroth-order edge basis functions on tetrahedra [49-51]; the surface EFIE for a thin metal sheet uses the standard RWG basis functions on triangular facets [53].

The first goal of this section is to describe the effect of numerical cubature on the convergence rate quantitatively. Other potential error sources [75] including in particular the mesh quality factor are possibly eliminated from consideration. Next, an explanation of the potentially lower convergence of higher-order cubatures applied to MoM integrals for low-order (piecewise constant) basis functions is given. This explanation assumes the Galerkin method with the same source and test basis functions, and is only valid when the number of basis functions remains small. Finally, an attempt is made to contribute to a discussion with regard to optimal integration rules that would hold in a more general 3D case.

2.4.2 Dielectric resonator

a. Eigenmode solution

The direct MoM eigenmode solution is obtained by running the search for the local minimum of a cost function F of two variables as explained in section 2.2.6

$$F(f, f') = \frac{1}{\kappa(\hat{Z})} = \frac{1}{\left\|\hat{Z}\right\| \cdot \left\|\hat{Z}^{-1}\right\|} \tag{2.4.1}$$

Here, f is the real part of frequency on a complex search plane $f + jf'$ and $f' > 0$ is the imaginary part. If the complex angular frequency is given by $\sigma + j\omega$ as in Refs.[28, 63],

then $f' = -\sigma/(2\pi)$. The resonant frequency and the quality factor of the resonator are then obtained as (cf., for example, [32])

$$f_{res} = f_{min}, Q = \frac{f_{min}}{2f'_{min}}$$ (2.4.2)

A typical output of the search routine is shown in Fig. 2.4-1.
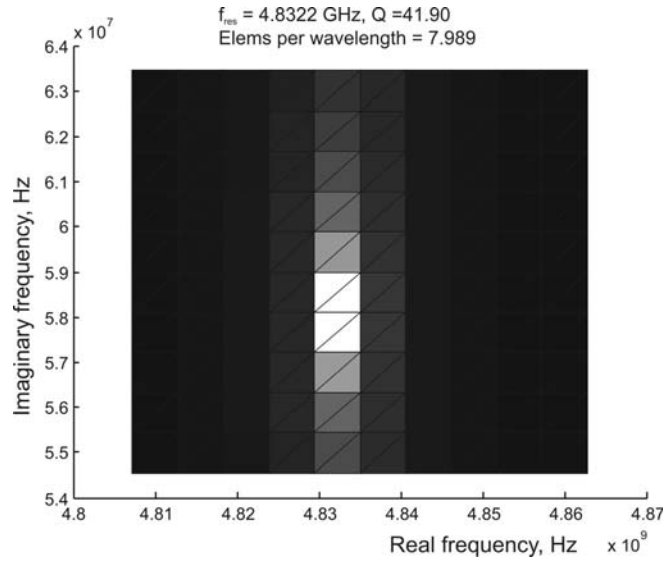
Figure 2.4-1 Typical output of the direct eigenmode search routine on the plane of complex frequency. Lighter color corresponds to the minimum of the reciprocal condition number – the resonance condition.

The direct search procedure used is very time-consuming but reasonably safe, especially for structures with closely spaced resonances. The frequency resolution is then made gradually finer in order to obtain the desired eigenmode accuracy.

b. Tetrahedral meshes

A DistMesh software for the iterative generation of high-quality unstructured tetrahedral meshes is used [76]. For the actual mesh generation, DistMesh employs the Delaunay tessellation routine and tries to optimize the node locations by a force-based smoothing procedure. The topology is regularly updated by Delaunay. The boundary points are only allowed to move tangentially to the boundary by projections using the distance function.

This iterative procedure typically results in very well-shaped meshes for the simple resonator shapes.

Using this software, a series of high-quality meshes for a given structure are generated, with gradually increasing convergence parameter

$$n_\lambda = \frac{\lambda}{\bar{\bar{S}}} \qquad (2.4.3)$$

where $\bar{S}$ is the average size of the tetrahedra in the mesh and λ is the wavelength.

c. Resonators

Two basic resonators shapes are considered: the homogeneous sphere DR and the cylindrical (rather a disk) DR shown in Fig. 2.4-2. This disk DR was first studied both numerically and experimentally in Ref. [32] where the corresponding mode charts were given.
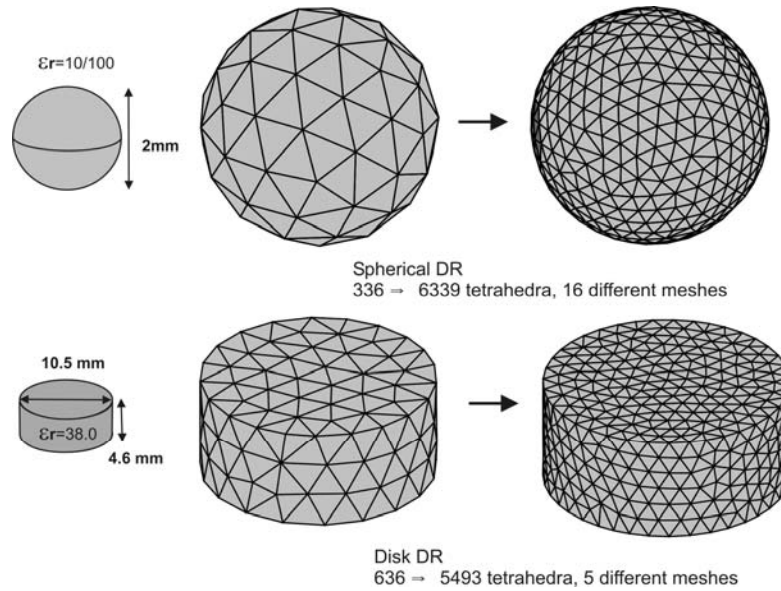
Figure 2.4-2. Tetrahedral meshes for the dielectric sphere and the dielectric disk resonators used to estimate the convergence rate. The meshes are obtained with the software [76]. Only the start and end meshes are shown.

Fig. 2.4-2 simultaneously shows the start and end tetrahedral meshes used for the convergence study. All meshes were scaled such that the net tetrahedral volume coincides with the exact sphere/cylinder volume regardless of the possible discretization error.

Table 2.4.1 below lists the resonator characteristics. For the sphere, the analytical solution based on the Mie series [77] gives the exact resonant frequency and the Q-factor. For the disk resonator we employ for comparison an FEM eigenmode solution that is obtained with Ansoft HFSS v.9.2 converging on fine meshes. Note that the FEM solution did not give the well converging results for the Q-factor of the HEM12δ mode listed in Table 2.4.1. A similar difficulty with the HEM11δ mode was observed in [32].

Table 2.4-1 DR modes used for convergence test.

Resonator	Mode	f_{res}, GHz	Q	ε_r	n_λ
Analytical					
Dielectric sphere, $r = 1\,\text{cm}$	TE$_1$	4.4840	9.150	10	6-17
Same	TM$_1$	6.4755	4.215	10	4-12
Same	TE$_1$	1.4853	174.4	100	6-17
FEM Ansoft HFSS					
Dielectric disk, $r = 5.25\,\text{cm}, h = 4.6\,\text{mm}$	TE01δ	4.86	41.0	38	8-17
Same	HEM12δ	6.65	53.7*	38	5-13
Same	TM01δ	7.54	75.0	38	5-11

d. Organization of results

The results are the convergence curves that give the absolute error in the resonant frequency, E_f and the absolute error in the Q-factor, E_Q as functions of the convergence

parameter, n_λ. These curves are approximated by an empirical "best fit" dependency of the form (cf., for example, [73])

$$E_f = An_\lambda^{-r}, \quad E_Q = Bn_\lambda^{-r} \tag{2.4.4}$$

where constants A, B are different for every mode, but the power factor r is kept the same for the given resonator type.

The convergence curves are obtained for several integration schemes of different degree of accuracy. Three common integration schemes used in the impedance matrix are

$$R_2 = 1e-3, \, N_2 = 1, \, d_2 = 1$$
$$R_3 = 1e-3, \, N_3 = 1, \, d_3 = 1 \tag{2.4.5}$$

$$R_2 = 5, \, N_2 = 7, \, d_2 = 5$$
$$R_3 = 1e-3, \, N_3 = 1, \, d_3 = 1 \tag{2.4.6}$$

$$R_2 = 5, \, N_2 = 7, \, d_2 = 5$$
$$R_3 = 5, \, N_3 = 15, \, d_3 = 5 \tag{2.4.7}$$

The scheme Eq. (2.4.5) implies that only the self integrals (surface or volume) employ the analytical formulas for the inner potential integral. All other integrals are calculated using the central-point approximation.

The scheme Eq. (2.4.6) implies that the integrals over tetrahedra are calculated exactly as in Eq. (2.4.5). However, the integrals over faces are calculated more precisely. If the distance between two face centers is smaller than 5 times their average size then the inner potential integral in Eq. (2.2.25) is calculated analytically. All other integrals are calculated using the Gaussian cubature of fifth degree of accuracy on triangles with 7 points [56]. Outside the neighboring sphere, the central-point approximation is used for all the integrals, without singularity extraction. The number of faces in the neighboring sphere of dimensionless radius 5 is typically about 30-40.

The scheme Eq. (2.4.7) implies that both integrals over faces and tetrahedra are calculated more precisely. If the distance between two simplex centers is smaller than 5 times their average size (see Eqs. (2.2.26, 2.2.27)) then the inner potential integrals in Eqs. (2.2.24, 2.2.25) are calculated analytically. All other integrals are calculated using the Gaussian cubature of fifth degree of accuracy on triangles and fifth degree of accuracy on tetrahedra [56]. Outside the neighboring sphere, the central-point approximation is used for all the integrals, without singularity extraction. The number of tetrahedra in the neighboring sphere of dimensionless radius 5 is typically about 400-500. The scheme (2.4.7) is very computationally expensive since the potential integrals need to be pre-calculated and stored in the workspace. Other (intermediate) integration schemes have also been considered [70, 71].

2.4.3 Convergence results

Figs. 2.4-3 to 2.4-10 present convergence results for the six resonator cases listed in Table 2.4.1. The left of the figure shows the eigenfrequency data, the Q-factor data is given on the right. The circled curves give the numerical convergence against the eigenmode parameters listed in Table 2.4.1. The solid curves are the approximations given by Eq. (2.4.4).

a. Sphere TE1 $\varepsilon_r = 10$

The results are given in Fig. 2.4.3. The interpolation curves have the form

$$E_f = 50n_\lambda^{-2.5}, \quad E_Q = 250n_\lambda^{-2.5} \tag{2.4.8}$$

The major observation is that low-order integration schemes (2.4.5) and (2.4.6) perform better than the most precise integration scheme (2.4.7). They give an error that is typically 2-8 times smaller. The convergence is excellent: the error in the resonant frequency is smaller than 0.1% when the number of tetrahedra per wavelength is 12 or higher. The integration accuracy for the faces has little influence on the convergence

whereas improving the integration accuracy for tetrahedra has the negative effect on the convergence rate.
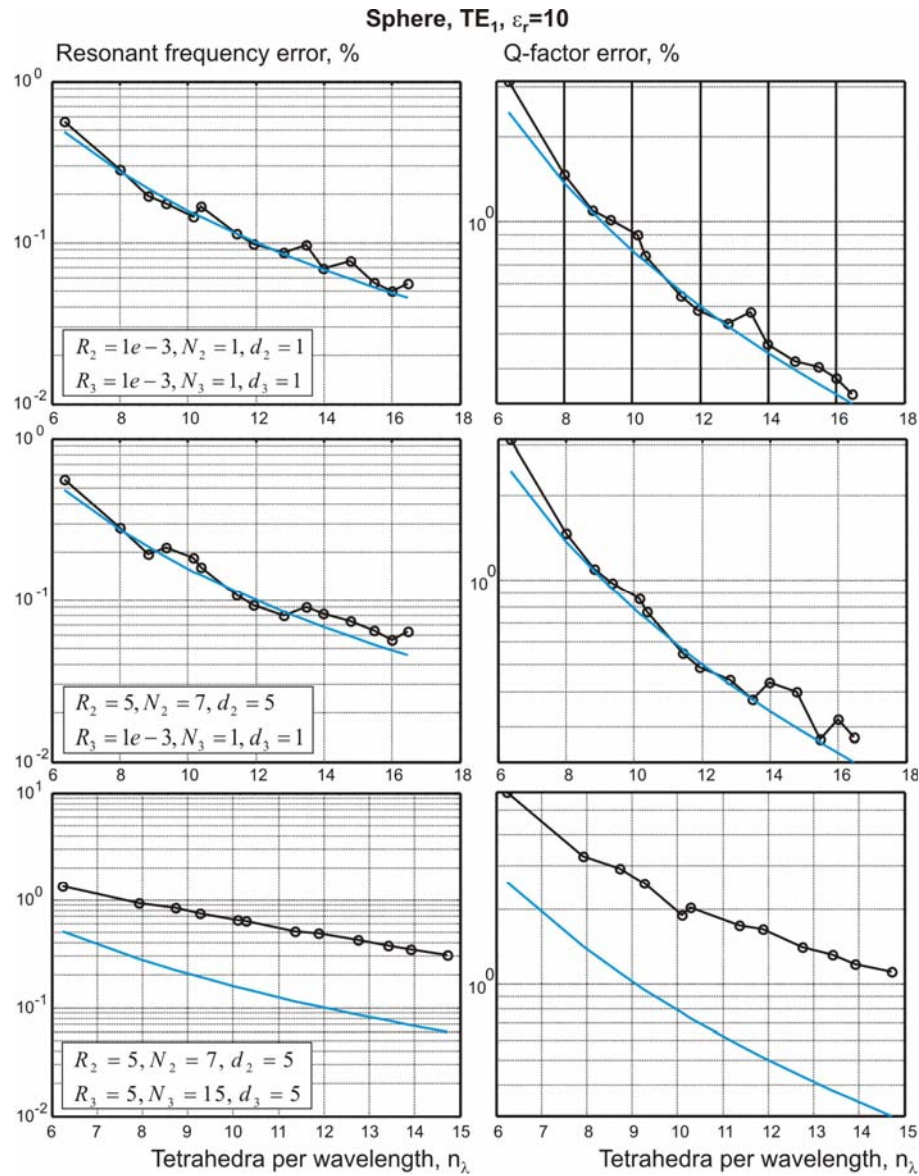
Figure 2.4-3 Convergence curves for the dielectric sphere - TE_1 mode. The corresponding analytical approximation is shown by solid curves without circles.

b. Sphere TM$_1$ $\varepsilon_r = 10$

The results are given in Fig. 2.4-4. The interpolation curves have the form

$$E_f = 200 n_\lambda^{-2.5}, \quad E_Q = 250 n_\lambda^{-2.5} \tag{2.4.9}$$

The convergence in the resonant frequency is slower than for the TE mode. The reason is perhaps connected to the nontrivial bound charge distribution on the resonator surface that needs to be supported by the basis functions, along with the volume polarization currents. Again, the low-order integration schemes (2.4.5) and (2.4.6) perform better for the resonant frequency than the most precise integration scheme (2.4.7). The results for the Q-factor are nearly unaffected by the integration accuracy.
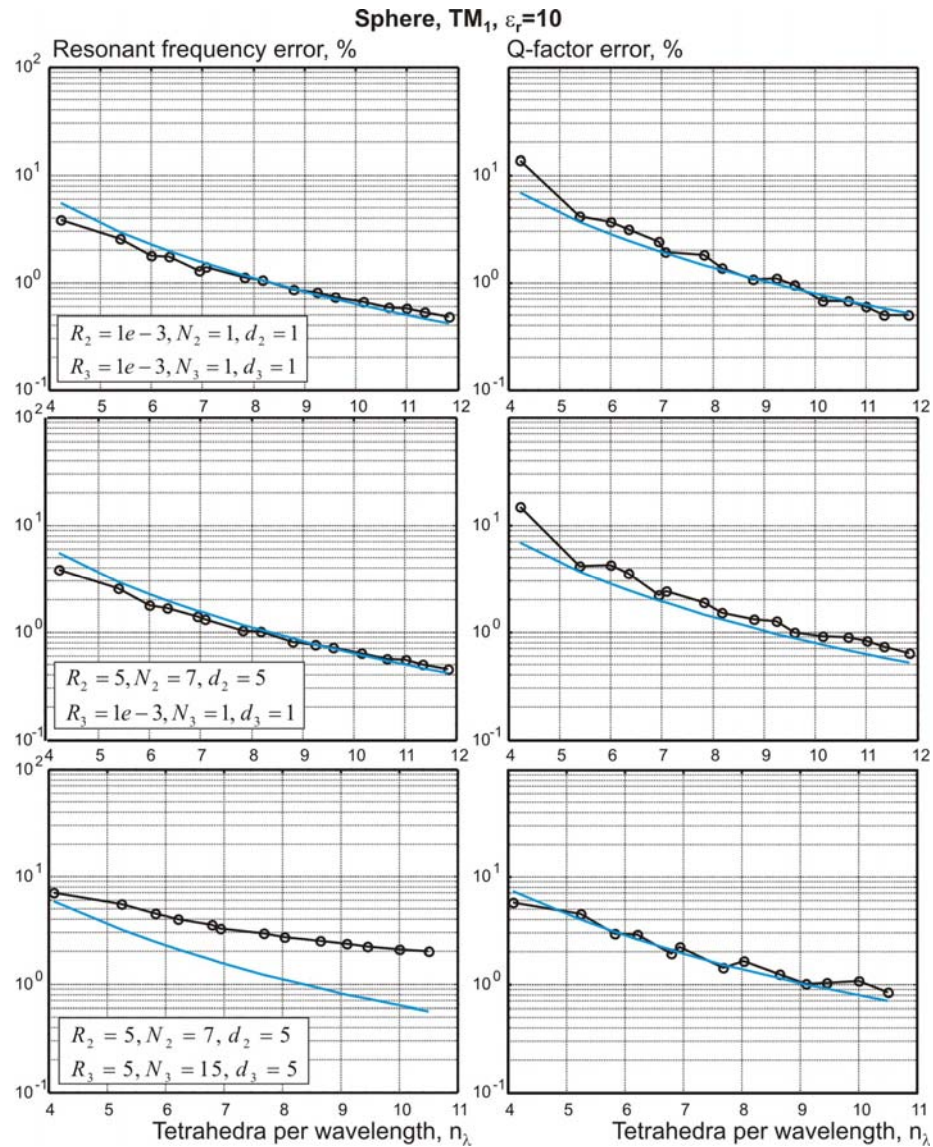
Figure 2.4-4. Convergence curves for the dielectric sphere - TM_1 mode. The corresponding analytical approximation is shown by solid curves without circles.

c. Sphere TE$_1$ $\varepsilon_r = 100$

The results are given in Fig. 2.4-5. The interpolation curves have the form

$$E_f = 50n_\lambda^{-2.5}, \quad E_Q = 250n_\lambda^{-2.5} \tag{2.4.10}$$

The results are very similar to those for the TE mode at $\varepsilon_r = 10$. However, the Q-factor is 19 times higher, which perhaps leads to the non-monotonic convergence in Fig. 2.4-5 – top. The low-order integration schemes (2.4.5) and (2.4.6) perform considerably better than the most precise integration scheme (2.4.7).
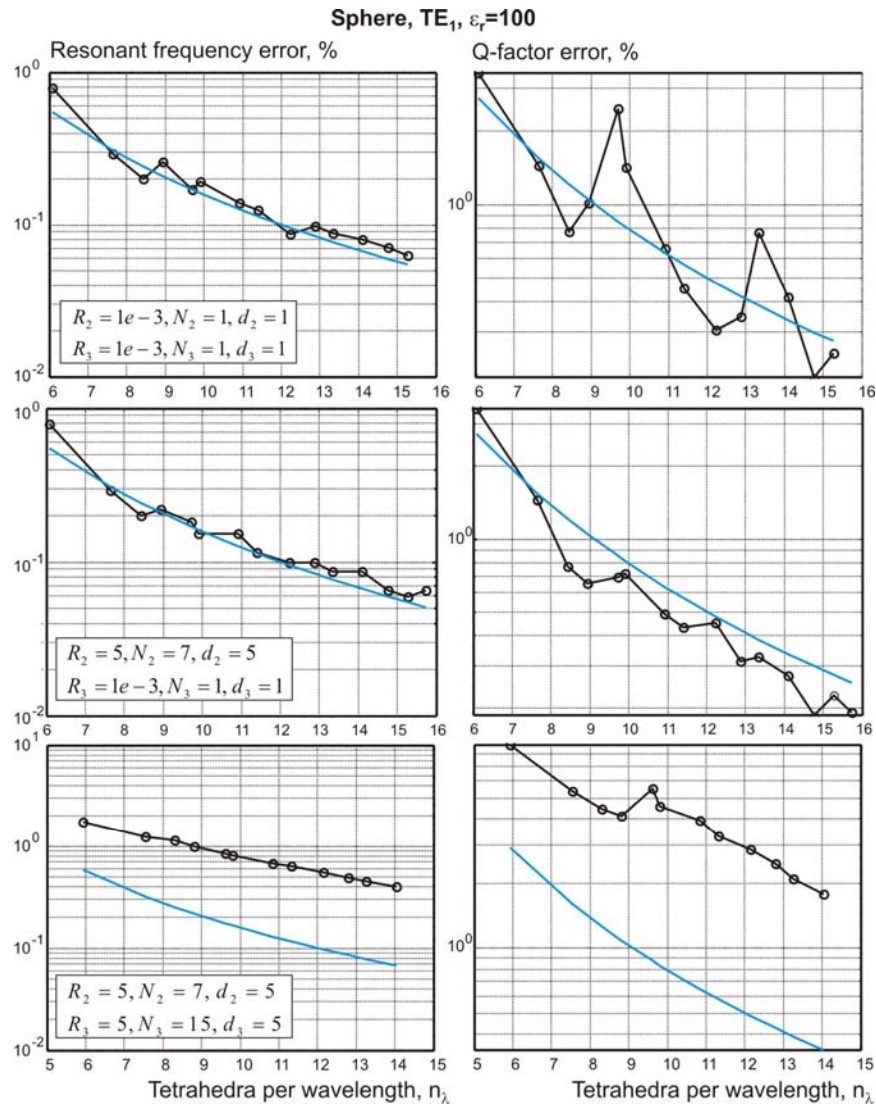
Figure 2.4-5. Convergence curves for the dielectric sphere - TE$_1$ mode for $\varepsilon_r = 100$. The corresponding analytical approximation is shown by solid curves without circles.

d. Disk TE$_{01\delta}$ $\varepsilon_r = 38$

The results are given in Fig. 2.4-6. Since improving the integration accuracy for the faces seems to have little influence in all the cases considered above, we restrict ourselves to two integration schemes. The former is given by Eq. (2.4.5); the latter has the form

$$R_2 = 1e-3, \ N_2 = 1, \ d_2 = 1$$
$$R_3 = 5, \ N_3 = 15, \ d_3 = 5 \tag{2.4.11}$$

and only takes into account the more accurate integration over tetrahedra. The effect of accurate integration in Fig. 2.4-6 is again negative – the convergence rate decreases when the integration accuracy increases. The interpolation curves have the form

$$E_f = 40n_\lambda^{-2.0}, \quad E_Q = 80n_\lambda^{-2.0} \tag{2.4.12}$$
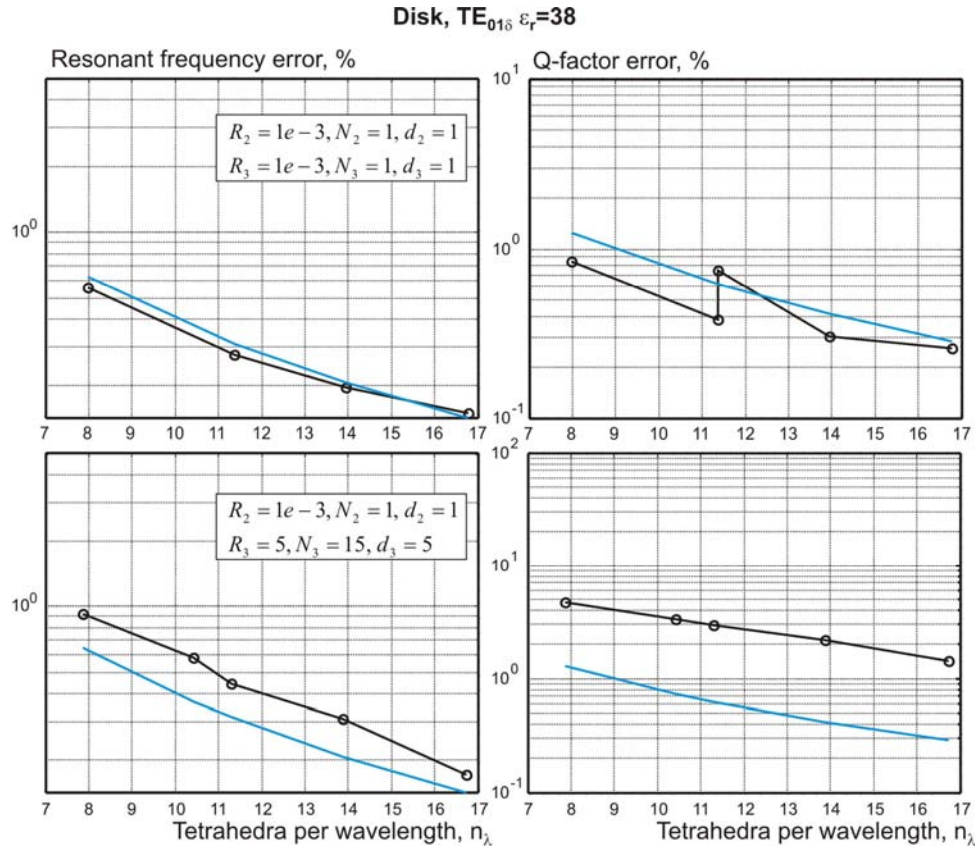
Figure 2.4-6 Convergence curves for the dielectric disk - TE$_{01\delta}$ mode for $\varepsilon_r = 38$. The corresponding analytical approximation is shown by solid curves without circles.

e. Disk $HEM_{12\delta}$ $\varepsilon_r = 38$

The results are given in Fig. 2.4-7. The results for the resonant frequency are in line with those for the TE mode. At the same time, we were unable to obtain a good agreement with the Ansoft HFSS solution with regard to the Q-factor. The present MoM solution gives Q=49.9, the Ansoft HFSS solution from Table 2.4.1 gives Q=53.7, the numerical simulation [32] gives Q=51.9, and the experiment [32] gives Q=64, which perhaps points to a certain problem with the Q-factor for this mode. The interpolation frequency curve has the form

$$E_f = 10n_\lambda^{-2.0} \tag{2.4.13}$$
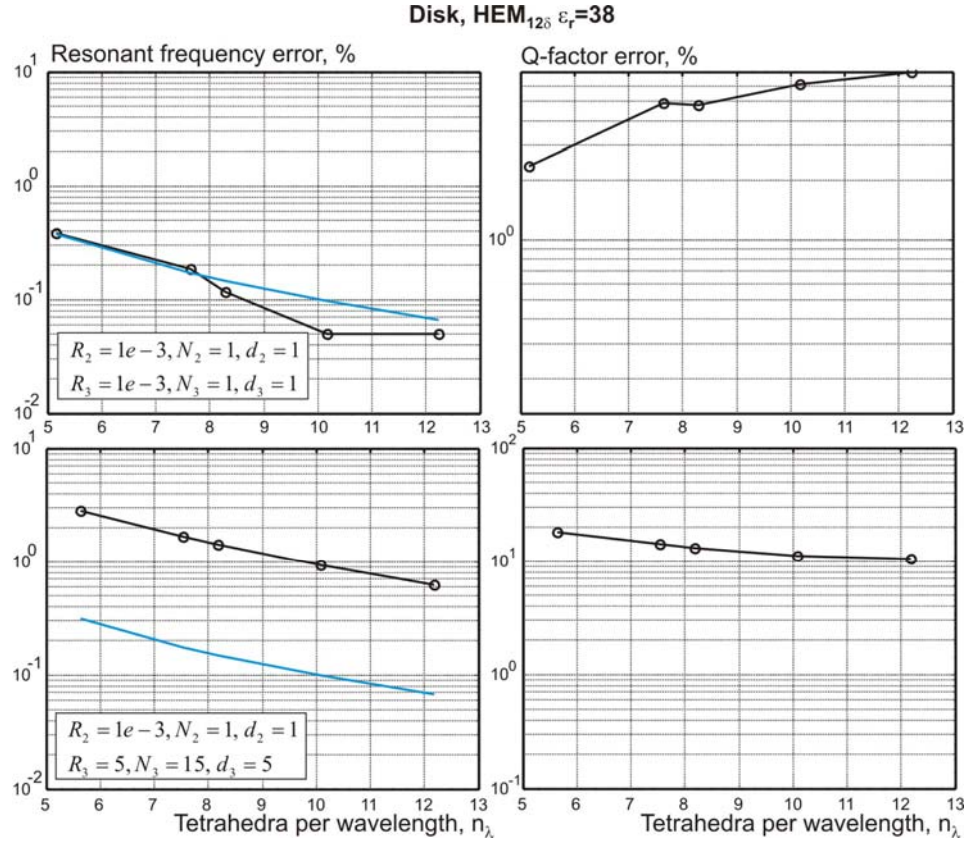
Figure 2.4-7. Convergence curves for the dielectric disk - $HEM_{12\delta}$ mode for $\varepsilon_r = 38$. The corresponding analytical approximation is shown by solid curves without circles.

f. Disk TM$_{01\delta}$ $\varepsilon_r = 38$

The results are given in Fig. 2.4-8. The interpolation curves have the form

$$E_f = 65 n_\lambda^{-2.0}, \quad E_Q = 50 n_\lambda^{-2.0} \tag{2.4.14}$$

The results are again similar to those for the TE mode.
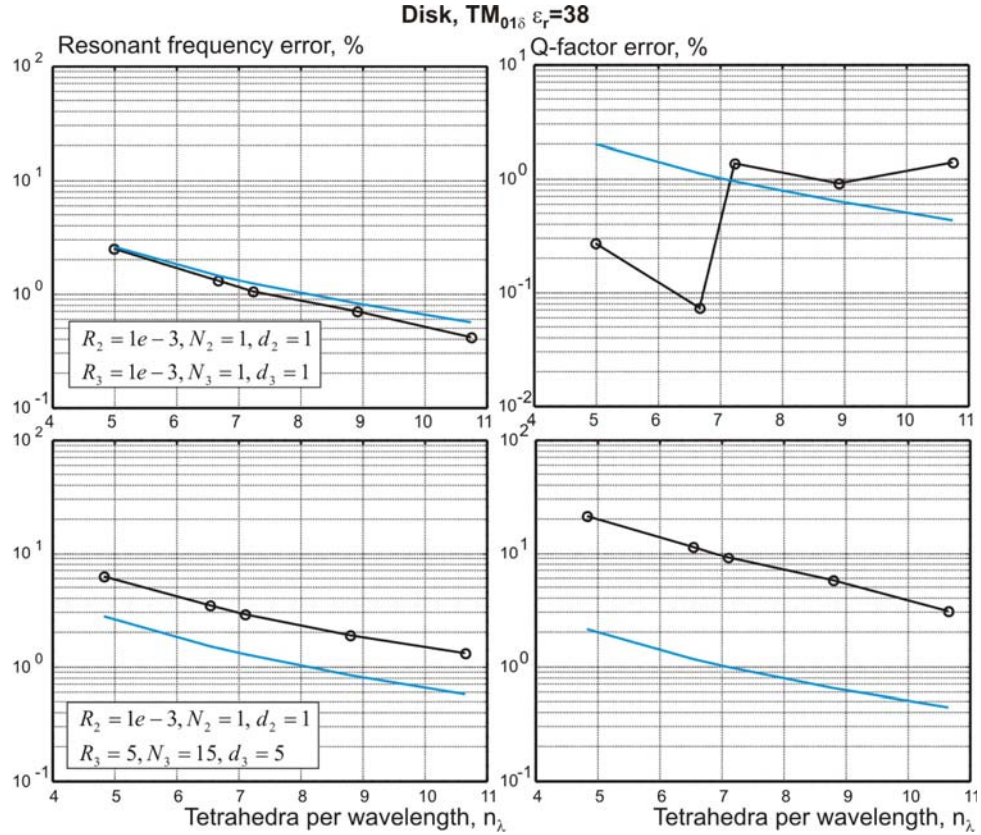
Figure 2.4-8. Convergence curves for the dielectric disk - TM$_{01\delta}$ mode for $\varepsilon_r = 38$. The corresponding analytical approximation is shown by solid curves without circles.

g. Common features

The most common feature of the six resonator cases considered above is that improving the integration accuracy has either insignificant or even negative effect on the convergence of the MoM solution. Improving the volumetric integration accuracy has a negative effect whereas improving the surface integration accuracy is mostly insignificant. Similar observations were made for other dielectric resonators including the

rectangular DR, the notch DR, and the inhomogeneous dielectric cylinder [70, 71]. The convergence in [70, 71] was tested with the low-quality meshes.

It should be noted that the negative effect of the higher integration accuracy is only observed for a relatively small number of basis functions per wavelength – cf. Table 2.4.1. Before we try to explain this effect it is interesting to test briefly the related performance of the standard surface RWG basis functions, for a pure metal structure.

2.4.4   Metal – driven solution

a. Integrals of the impedance matrix for RWG basis functions

The integrals of the impedance matrix with the RWG basis functions are well-known [53]

$$
\iint_{t_p t_q} (\vec{\rho}_i \cdot \vec{\rho}_j') g(|\vec{r} - \vec{r}'|) ds' ds = \iint_{t_p t_q} \frac{(\vec{\rho}_i \cdot \vec{\rho}_j')}{|\vec{r} - \vec{r}'|} ds' ds + \iint_{t_p t_q} \frac{(\exp(-jk|\vec{r} - \vec{r}'|) - 1)(\vec{\rho}_i \cdot \vec{\rho}_j')}{|\vec{r} - \vec{r}'|} ds' ds
$$

$$(2.4.15)$$

$$
\iint_{t_p t_q} g(|\vec{r} - \vec{r}'|) ds' ds = \iint_{t_p t_q} \frac{1}{|\vec{r} - \vec{r}'|} ds' ds + \iint_{t_p t_q} \frac{(\exp(-jk|\vec{r} - \vec{r}'|) - 1)}{|\vec{r} - \vec{r}'|} ds' ds \qquad (2.4.16)
$$

where $\vec{\rho}_i = \vec{r} - \vec{r}_i$ for any vertex i of triangular patch p and $\vec{\rho}_j' = \vec{r}' - \vec{r}_j$ for any vertex j of patch q. The analytical formulas for the inner potential integrals derived in [54] are used. In particular,

$$
\int_t \frac{\rho_j'}{|\vec{r} - \vec{r}'|} ds' = \int_t \frac{(\vec{r}' - \vec{r})_{\tan}}{|\vec{r} - \vec{r}'|} ds' + (\vec{r} - \vec{r}_j)_{\tan} \int_t \frac{1}{|\vec{r} - \vec{r}'|} ds' \qquad (2.4.17)
$$

where the two integrals on the right-hand side of Eq. (2.4.17) are directly given in [54].

b. Microstrip resonator driven by a lumped port

We study an open-circuited suspended microstrip resonator shown in Fig. 2.4-9a. The microstrip is driven from one end by a lumped port. The input impedance seen from this port is computed, as a function of frequency using different integration schemes in Eqs. (2.4.15) and (2.4.16). The solution is then compared to an Ansoft HFSS FEM simulation

obtained with about 40,000 tetrahedra. The realization of the lumped port is nearly identical in both cases.

In contrast to the dielectric case, no convergence rate is studied for a given integration scheme. Instead, we fix the metal mesh shown in Fig. 2.4-9b and gradually increase the accuracy of the numerical integration in Eqs. (2.4.15) and (2.4.16). Three integration schemes are used:

$$R_2 = 1e-3, \, N_2 = 1, \, d_2 = 1$$
$$R_2 = \sqrt{5}, \, N_2 = 7, \, d_2 = 5 \qquad\qquad (2.4.18)$$
$$R_2 = 5, \, N_2 = 25, \, d_2 = 10$$
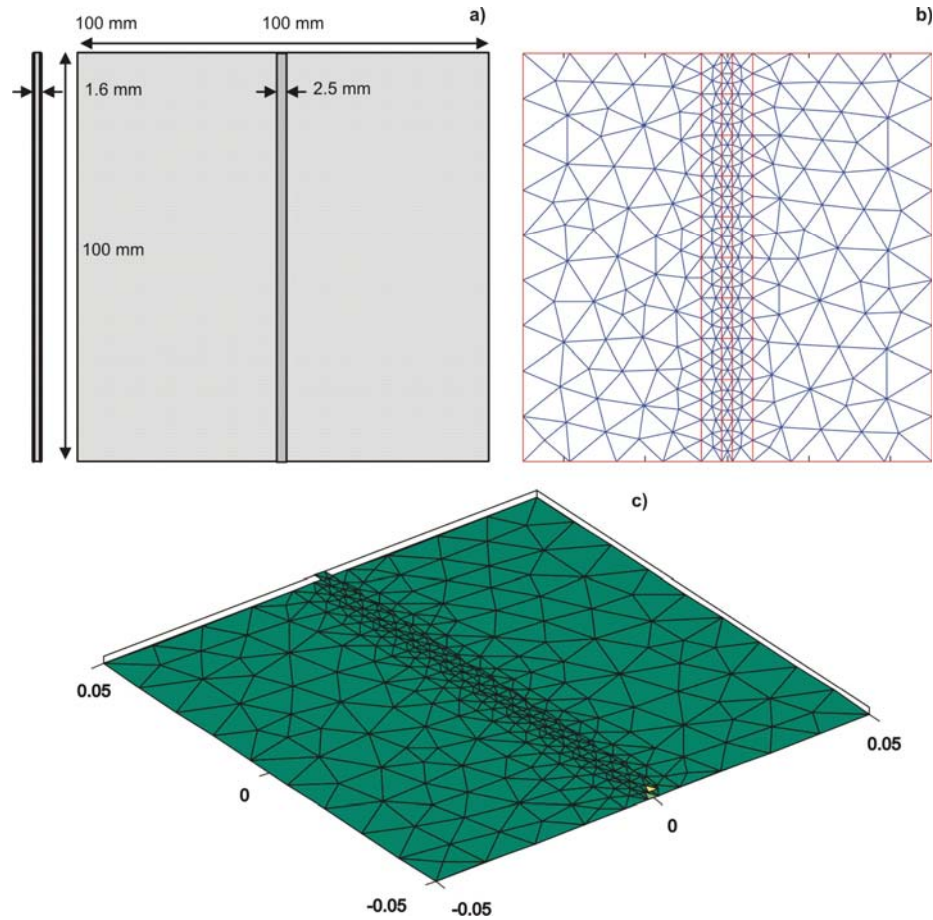
Figure 2.4-9. Suspended microstrip driven by a lumped port. a) – Geometry, b), c) –2D and 3D triangular surface meshes. The lumped port is located between two marked triangles in Fig. 2.4-9c.

Fig. 2.4-10 gives the input impedance of the lumped port as a function of frequency for these three cases.
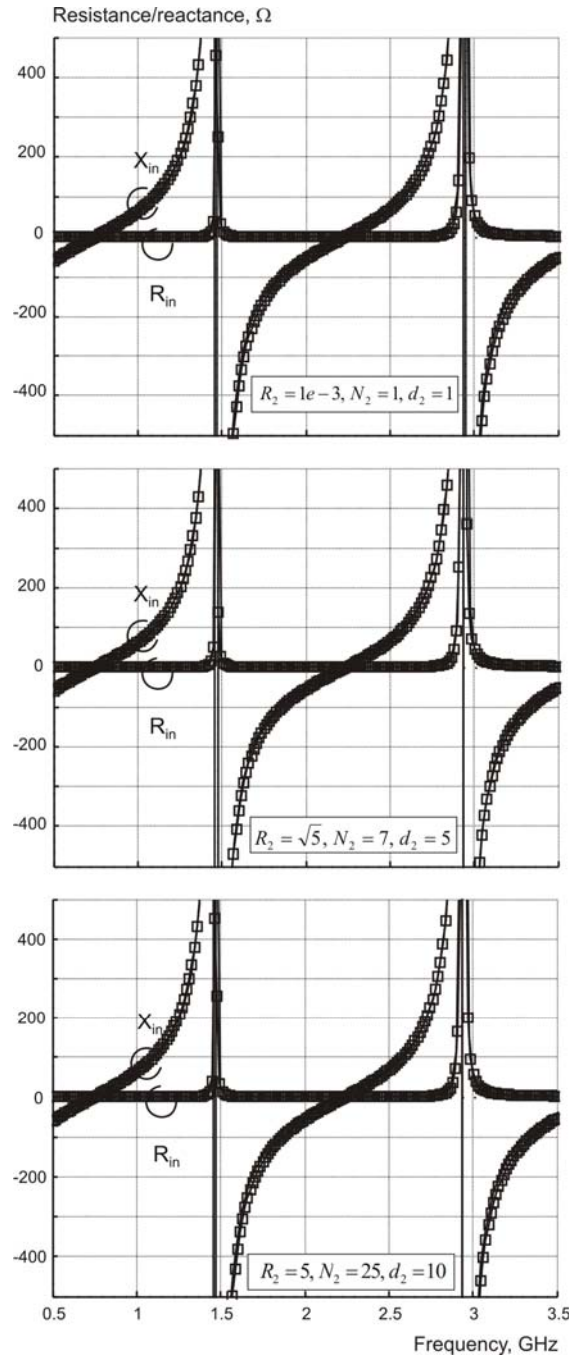
Figure 2.4-10. The input impedance of a suspended microstrip for the first resonances. The solid curve with squares gives the MoM solution; the solid curve without squares – Ansoft HFSS solution. The difference between two solutions is minimal.

The MoM solution for the resistance/reactance is marked by squares; the Ansoft solution is shown by the solid curves without marking. It is seen that different integration schemes lead to nearly identical results, which are in a good agreement with the FEM solution.

2.4.5 **Discussion**

In this section we intend to show that the faster convergence rate observed for the low-order integration schemes is a purely numerical phenomenon. This phenomenon is connected to an improper approximation of an integral containing the convolution product of a singular kernel and a discontinuous basis function set, with a higher-order integration rule. Consider for simplicity a real one-dimensional MoM solution $D(r)$ and a typical integral operator

$$F(r) = \int_a^b K(r - r')D(r')dr', \quad r \in [a, b] \tag{2.4.19}$$

with a (weakly singular) kernel K. When a piecewise-constant uniform basis function set of size M is applied, the solution $D(r)$ is a staircase approximation

$$D(r) \approx D_m = const, \quad r \in [a + \frac{m-1}{M}(b-a), \quad a + \frac{m}{M}(b-a)], \quad 1 \le m \le M \tag{2.4.20}$$

The integral (2.4.19) is thus transformed to an approximate expression

$$F'(r) \approx \sum_{m=1}^M D_m \int_{a+\frac{m-1}{M}(b-a)}^{a+\frac{m}{M}(b-a)} K(r-r')dr' \tag{2.4.21}$$

A numerical integration rule is then applied to every remaining integral on the right-hand of Eq. (2.4.21). A good test of this integration effort is: does the overall approximation error

$$E = \frac{\left\| F'(r) - F(r) \right\|_{L^2[a,b]}}{\left\| F(r) \right\|_{L^2[a,b]}} \tag{2.4.22}$$

of the original functional (significantly) decrease when a more precise integration is used in Eq. (2.4.21)? The answer to this question is clearly "no". For one basis function ($M = 1$) Eq. (2.4.21) is just an approximation for the original integral of the convolution of two functions. When one function (not constant) is taken out of the integration sign the full integral has a wrong value anyway – even if the remaining integral is calculated precisely.

Indeed, the operation

$$\int_{a+\frac{m-1}{M}(b-a)}^{a+\frac{m}{M}(b-a)} D(r')K(r-r')dr' \rightarrow D_m \int_{a+\frac{m-1}{M}(b-a)}^{a+\frac{m}{M}(b-a)} K(r-r')dr' \tag{2.4.23}$$

creates more and more accurate integral calculation when the number of basis functions increases. The reason is that the initial field $D(r)$ becomes more like a constant D_m on small intervals covered by the basis functions so that the approximation used in Eqs. (2.4.21) and (2.4.23) improves. Therefore, the more accurate integration schemes will be useful for a large number of basis functions as discussed in [72-75].

Keeping in mind the 3D applications with a relatively small number of the basis functions per wavelength the major question is now how many basis functions should we really employ in order to see the advantages of the higher-order numerical integration in Eq. (2.4.21)? As a test case, one may choose $D(r) = r$ on the interval $[0, \pi/2]$, which approximately corresponds to the quarter-wavelength approximation of one full wave period shown in Fig. 2.4-11.
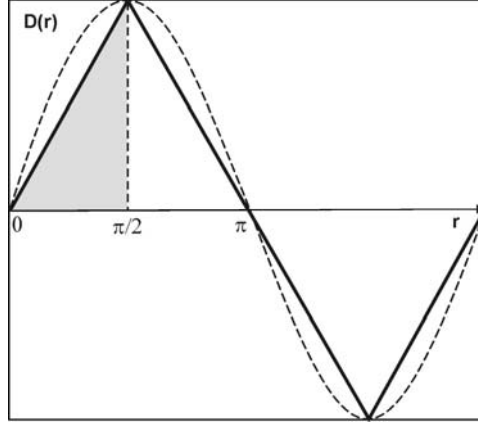
Figure 2.4-11 A test case with $D(r) = r$ on the interval $[0, \pi/2]$

Table 2.4.2 gives the error E from Eq. (2.4.22) assuming an arbitrary singular kernel of the form:

$$K(r - r') = \frac{1}{\left|r - r'\right|^{1/n}} \quad n > 1 \tag{2.4.24}$$

The observation points in Eq. (2.4.22) coincide with the integration points in order to assure the compatibility with the Galerkin method. The "self" integrals in Eq. (2.4.21) and in the original functional (2.4.19) are calculated analytically, for arbitrary n, a, b.

Table 2.4-2 Error percentage given by Eq. (2.4.22) for $a = 0, b = \pi/2$ and Euler integration rule with N equally spaced points. n is the power factor in Eq. (2.4.24).

M	E $N = 1, n = 2$	E $N = 20, n = 2$	E $N = 1, n = 3$	E $N = 20, n = 3$
2	**1.14**	**2.01**	**0.97**	**1.57**
3	1.26	1.25	0.97	0.92
4	1.26	0.86	0.92	0.60
5	1.22	0.63	0.86	0.43
10	1.02	0.23	0.64	0.14

One can see that the error for 20 integration points is considerably higher than for the central-point approximation when $M = 2$, i.e. for the eight basis function per wavelength! This is exactly in accordance with the 3D convergence observations made in section 2.4.2 for the dielectric resonator.
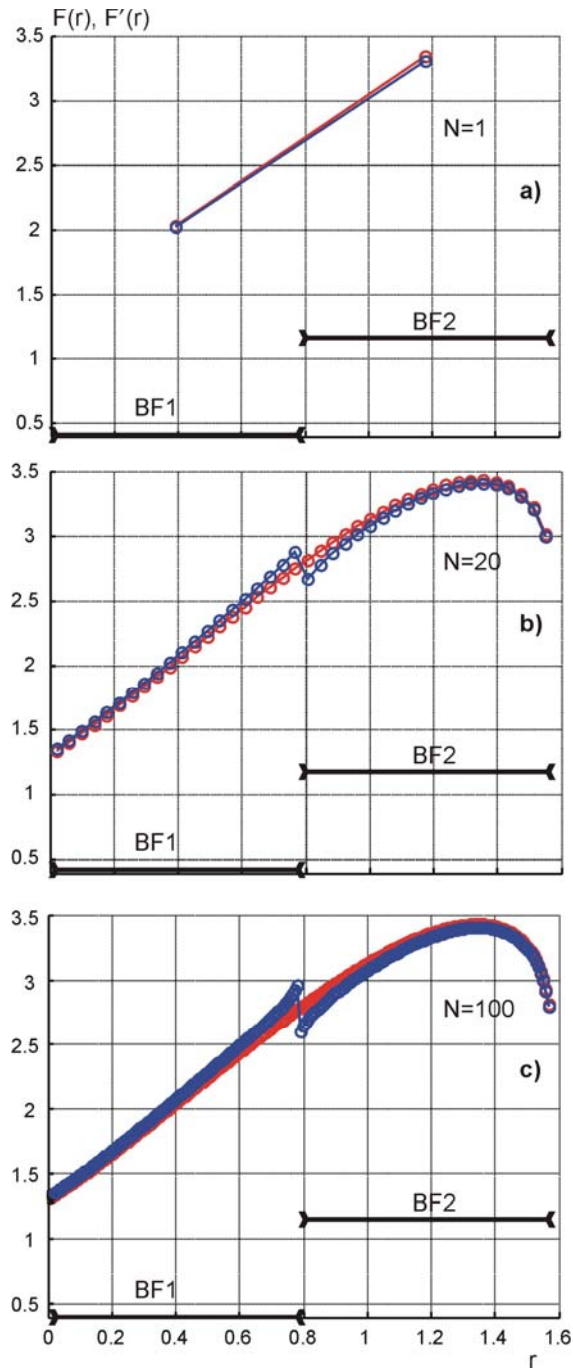
Figure 2.4-12 Error due to artificial discontinuity for variable-order integration schemes with two basis functions

The major source of this large error is an artificial discontinuity that appears in the final MoM functional (2.4.19) when the observation point crosses the boundary between the basis functions – see Fig. 2.4-12b, c. This discontinuity is caused by the corresponding

discontinuity of the basis function approximation itself. The discontinuity is clearly missing for the low-order integration – see Fig. 2.4-12a – simply because the low-order integration scheme just does not have enough resolution to cover this small discontinuity area! Hence the integral error in Table 2.4.2 becomes better for low-order integration.
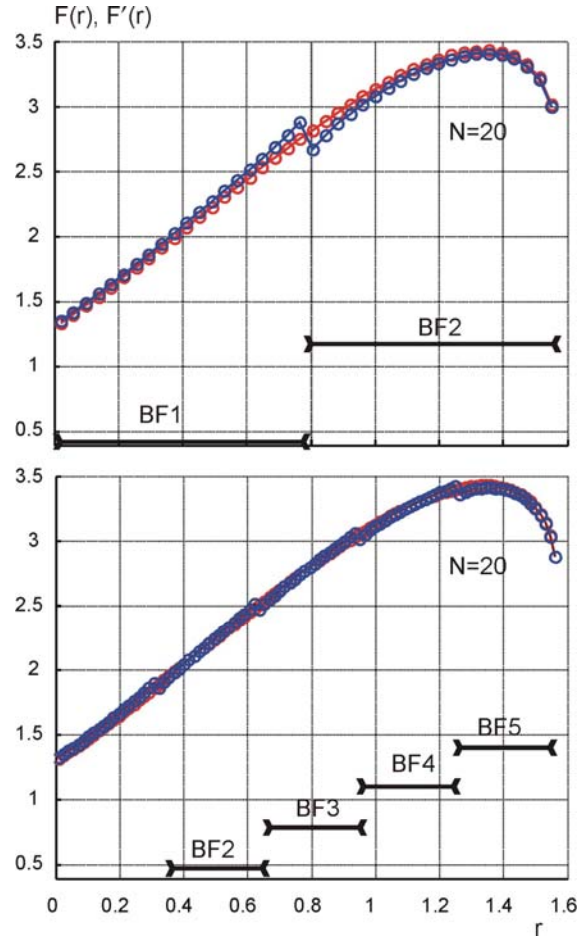
Figure 2.4-13 Error due to artificial discontinuity for 20 integration points and higher number of basis functions

When more basis function are employed the discontinuity jump decreases in the magnitude. This is seen in Fig. 2.4-13 for $M = 2$ and 5, respectively. Hence, the higher-order integration scheme in Table 2.4.2 is preferable for large numbers of basis functions and for less singular kernels. Note that the critical condition $M = 2$ corresponds to eight one-dimensional basis functions per wavelength. This is a reasonable assumption that

may perhaps be projected to a larger number of basis functions per wavelength in the 3D case.

The error in the approximation of the original functional shown in Fig. 2.4-12b,c propagates toward the elements of the impedance matrix. It might cancel out for the complete integral

$$\int_a^b F(r)dr \qquad\qquad (2.4.25)$$

but not for the particular row/column of the impedance matrix.

The results of this section suggest that the lowest-order integration scheme may be the best solution with regard to both MoM speed and accuracy, when the number of basis functions per wavelength is reasonably small (on the order of 10). However, the above results were obtained for high-quality meshes only, where the distance between two faces/tetrahedra is greater than or comparable to their size. An opposite situation is possible, when this distance is much smaller than the element size. An example is given by two closely spaced metal plates with large triangular faces (a mesh for a patch or slot antenna on a thin dielectric substrate). The potential integrals between two closely spaced faces should be calculated analytically. Thus, the radius of the neighboring sphere should be extended to at least one element size. This suggests a modification of the lowest-order integration scheme for arbitrary meshes that may perhaps have the form $R_2 \approx 2, N_2 = 3, d_2 = 2$ for the faces. For the tetrahedra, the central-point approximation $R_3 \approx 1e-3, N_3 = 1, d_3 = 1$ was found to yield reasonably good results for a patch/slot antenna on a thin substrate.

2.5 Effect of boundary conditions on the MoM VIE solution

2.5.1 <u>Challenges of Patch Antenna Modeling</u>

The convergence of the MoM VIE solution with low order basis functions for a patch antenna configuration with significant fringing fields is very slow. Typically, a significant positive offset in the resonant frequency is observed. This error is likely related to the nature of the SWG or other low-order dielectric basis functions, which are unable to exactly satisfy the boundary condition of the vanishing tangential E-field component on the metal-dielectric interface. This condition is approximately satisfied in an integral sense, within a dielectric volume close to the metal boundary, but not on the boundary itself. As a result, the patch antenna appears to be electrically smaller than expected. On the other hand, when the tangential E-field is small everywhere due to geometrical reasons, the VIE approach may produce accurate results. A simple example is a thin parallel-plate metal resonator where the dielectric substrate is fully covered by the metal plates. Within the resonator volume excited in the fundamental TM mode, the tangential E-field component becomes insignificant.

To improve the convergence rate of the VIE, enforcement of the boundary condition into the VIE model should be explicit. The proposed enforcement method is exact for piecewise-constant bases. For these basis functions, the tangential electric field for all tetrahedra in contact with metal faces must be zero, to ensure continuity. This tangential field will be eliminated from the VIE, using a projection operation on the original equation. However, the normal field for tetrahedra in contact with metal faces is retained as required by the boundary condition. Such an operation is a simple yet an effective method to improve the convergence rate. Various modifications on this approach are discussed in this section.

The section is organized as follows. Section 2.5.2 briefly outlines the VIE MoM model and the basis functions used in this study. Section 2.5.3 introduces the boundary

76

condition in the VIE along with the edge bases. Section 2.5.4 reports on test results for three patch antennas on thin substrates. Finally, Sections 2.5.5 and 2.5.6 present a discussion of results and conclusions, respectively.

2.5.2 <u>VIE model</u>

a. MoM VIE equations

Representation of metal is accomplished by replacing an infinitesimally thin metal sheet by equivalent surface current density $\vec{J}_M(\vec{r})$ and by the associated surface free charge density $\sigma_M(\vec{r})$. Using the volume equivalence principle [53], the piecewise inhomogeneous dielectric material is removed and replaced by equivalent volume polarization currents $\vec{J}(\vec{r})$ in V and the associated surface bound charge density $\sigma(\vec{r})$ on $S \in \partial V$. Herein the index M relates to metal. The EFIE is used in the present study, written in the mixed-potential form [48]. It includes two coupled equations – one for the dielectric volume V and another for a metal surface S_M, i.e.

$$\vec{E}^i = \vec{E} + \left[\quad j\omega\vec{A}(\vec{r}) + \nabla\Phi(\vec{r}) + j\omega\vec{A}_M(\vec{r}) + \nabla\Phi_M(\vec{r}) \right] \quad \vec{r} \in V \tag{2.5.1}$$

$$\vec{E}^i{}_{\tan} = \left[\quad j\omega\vec{A}_M(\vec{r}) + \nabla\Phi_M(\vec{r}) + j\omega\vec{A}(\vec{r}) + \nabla\Phi(\vec{r}) \right]_{\tan} \quad \vec{r} \in S_M \tag{2.5.2}$$

where $\vec{E}(\vec{r})$ is the total electric field; index i denotes the impressed field. The magnetic vector potential $\vec{A}(\vec{r})$ and the electric potential $\Phi(\vec{r})$ carry their typical meanings corresponding to metal and dielectric, respectively.

b. Basis functions

The metal surface is represented by an ensemble of RWG basis functions [53] on triangles. The dielectric volume is described in terms of an ensemble of piecewise-constant edge basis functions within tetrahedra [49-51]. Fig. 2.5-1a shows an edge basis function f attached to the metal surface S_M. This basis function supported by two adjacent

tetrahedra may be expressed as a combination of three SWG basis functions $g_{1,2,3}$ shown in Fig. 2.5-1b. Within tetrahedron ADEF, two linear SWG fields [43] associated with bases 1 and 2 are combined into a constant field parallel to edge AD by the proper choice of weight constants. Such a piecewise-constant combination of two SWG bases in one tetrahedron eliminates the major drawback of the SWG basis functions – the artificial volume charges [43] – from consideration but still retains the continuity of the normal E-across the faces.
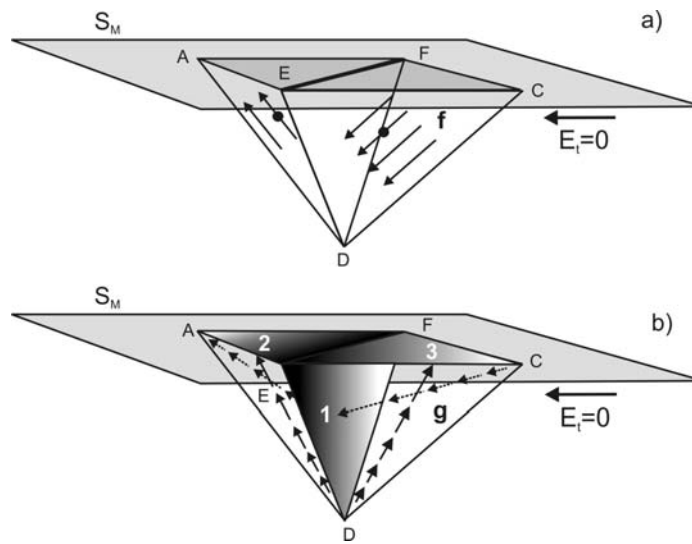
Figure 2.5-1 a) – Edge basis function f with two tetrahedra attached to the metal surface S_M ; b) – equivalent representation through three SWG basis functions 1 (pair of tetrahedra), 2 (single tetrahedron), and 3 (single tetrahedron). (Ref. [78] of Introduction © 2006 IEEE).

2.5.3 Condition for dielectric bases in contact with metal

a. Electric field close to the metal surface

Eq. (2.5.2) already enforces the boundary condition requiring that the tangential component of the total electric field on the metal surface is zero. On the other hand, both Eqs. (2.5.1) and (2.5.2) additionally employ a more general expansion of the same total electric field $\vec{E}(\vec{r})$ or electric flux $\vec{D}(\vec{r}) = \varepsilon \vec{E}(\vec{r})$ into N dielectric basis functions

$$\vec{D}(\vec{r}) = \sum_{n=1}^{N} D_n \vec{f}_n(\vec{r}) \tag{2.5.3}$$

everywhere in dielectric volume including the metal-dielectric boundary. Therefore, $\vec{D}(\vec{r})$ or $\vec{E}(\vec{r})$ should also have vanishing tangential component at the metal boundary. A very good test of the formulation is: do $\vec{D}_{\mathrm{tan}}(\vec{r})$ or $\vec{E}_{\mathrm{tan}}(\vec{r})$, obtained from the solution of Eqs. (2.5.1-3), really become zero when $\vec{r} \to S_M$? The answer to this question is generally "no". An integral error of the solution, measured as the average tangential-to-normal component ratio in all tetrahedra adjacent to a metal sheet, indeed, decreases when the mesh quality (especially in the transversal direction) improves. However, it still remains remarkably high – up 50%. It is believed that this error is the main reason for a poor convergence of the VIE approach in the general case and, specifically, for a printed patch antenna. Here, a significant $\vec{E}_{\mathrm{tan}}$ is observed in the fringing fields and the boundary condition is not well represented. At the same time, the VIE approach provides very accurate results for a thin parallel-plate metal-dielectric resonator (where $\vec{E}_{\mathrm{tan}}$ is almost negligible), even with only one layer of tetrahedra [49].

b. Formal boundary condition for volume bases in contact with the metal surface

The edge basis functions are piecewise-constant – cf. Fig. 2.5-1. The surface boundary condition $\vec{E}_{\mathrm{tan}}(\vec{r} \to S_M) = 0$ is therefore formally transformed to the condition $\vec{E}_{\mathrm{tan}} = 0$ throughout the whole tetrahedron volume that is attached to a given metal face. One thus has [78]

$$\vec{E} \equiv \begin{cases} (\vec{E} \cdot \vec{n})\vec{n} = \vec{E}_n & \text{in a tetrahedron attached to a metal face with normal } \vec{n} \\ \vec{E} & \text{otherwise} \end{cases} \tag{2.5.4}$$

Eq. (2.5.4) is the exact result for the piecewise-constant bases. One way to satisfy Eq. (2.5.4) automatically is to choose an appropriate basis function set in the expansion Eq. (2.5.3). However, for the case of edge bases, that leads to a nontrivial system of linear constraints on the basis functions that is difficult to handle and implement numerically.

Moreover, when Eq. (2.5.4) is enforced exactly in the entire volume of the attached tetrahedron, we effectively extend the metal boundary through this volume, which drastically reduces the accuracy for coarse meshes.

Thus, the boundary condition given in Eq. (2.5.4) cannot be explicitly enforced. A "softer" version of it, which allows a small tangential component to exist inside the tetrahedron in contact with the metal surface, is considered. The details are explained in the next section.

c. "Soft" conditioning of VIE close to the metal surface

A simpler but yet effective approach is to enforce the condition Eq. (2.5.4) in Eq. (2.5.1) directly. This means that the electric field $\vec{E}$ everywhere on the right-hand side of Eq. (2.5.1) is replaced by its normal component for all tetrahedra attached to metal faces. For these tetrahedra, one has

$$\vec{E} = \vec{E}_n \tag{2.5.5a}$$

Eq. (2.5.5a) completely eliminates the tangential electric field. Its numerical implementation is the result of substitution of the MoM expansion Eq. (2.5.3) into Eq. (2.5.5a) where $\vec{E}_n = \left(\vec{E} \cdot \vec{n} \right) \vec{n}$. Since the fields of separate bases are additive, the projection operation on the sum of the basis functions is equivalent to the same operation applied to every basis function. Therefore, it is formally equivalent to keeping only the normal component of the source dielectric basis functions in Eq. (2.5.3), for all contact tetrahedra. The first term on the right-hand side of Eq. (2.5.1) is found to be critical; other terms are almost unaffected. It should be emphasized that neither the source nor the testing dielectric bases are changed: the projection operation is applied to the $\vec{E}$-field in Eq. (2.5.1), on the contact tetrahedra only. However the boundary condition given in Eq. (2.5.4) is not explicitly enforced. Instead of that, a softer version of Eq. (2.5.5a) may be considered, in the form,

$$\vec{E} = \alpha \vec{E}_n + (1 - \alpha)\vec{E}_{\tan} \tag{2.5.5b}$$

or, more generally, in the form

$$\vec{E} = \alpha \vec{E}_n + \beta \vec{E}_{\tan} \tag{2.5.5c}$$

which still keeps a small tangential component in the contact tetrahedra ($\alpha \approx 1, |\beta| < \alpha$). The way it is implemented in the code is to calculate the tangential and normal component of the basis functions inside the tetrahedra in contact with the metal surface. The two components are then weighted using the parameters α and β ($\alpha \approx 1, |\beta| < \alpha$). Instead of neglecting the tangential component completely a small value (about 10%) is retained.

Eq. (2.5.5b, c) may be more appropriate for "longer" tetrahedra in the direction away from the metal faces, for tetrahedra in contact with two or more metal faces, as well as for coarse meshes. The equation (2.5.5b) is used in the MATLAB code (parameter α is given in the script f_basis.m in folder 2_basis). The parameter α was tested with values between 0.9 and 1. Good results were obtained for these cases.

A direct inspection of the field in the dielectric beneath a metal sheet indicates that a small but visible tangential component is still present in the tetrahedra adjacent to metal faces. Thus, Eq. (2.5.5b) is a reasonable approximation that provides more flexibility for the MoM solution related to more complicated edge geometries and to lower-quality meshes. Noticeably, the thinner the substrate is, the smaller is the effect of α-variation about 1 and the better is the solution accuracy.

2.5.4 Probe-fed patch antenna

a. Patch antenna configurations

In this section, the convergence is reported for three linearly-polarized rectangular patch antennas shown in Fig. 2.5-2.
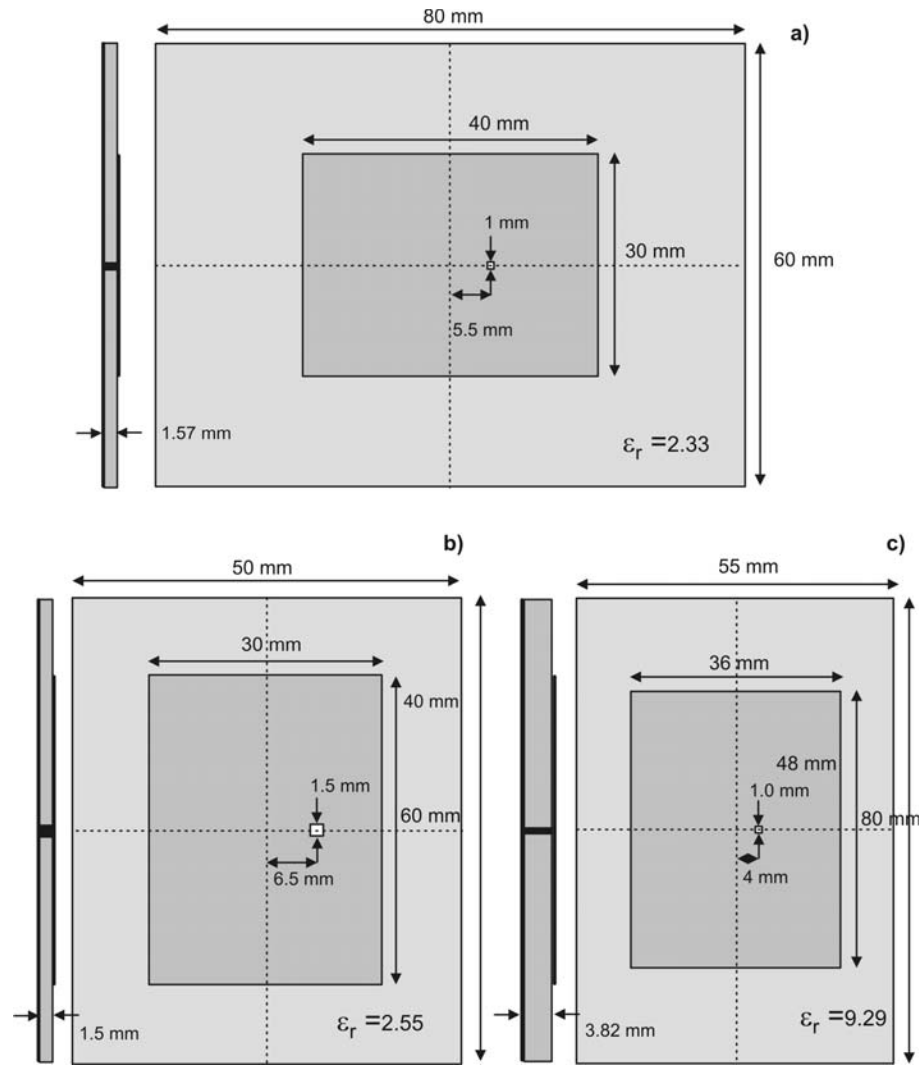
Figure 2.5-2 Three patch antenna configurations: a) – $\varepsilon_r = 2.33$ and TM mode along the longer patch dimension (lower Q); a) – $\varepsilon_r = 2.55$ and TM mode along the shorter patch dimension (higher Q); c) – thick narrowband antenna with $\varepsilon_r = 9.29$ and a higher Q-factor. (Ref. [78] © 2006 IEEE).

Other configurations including circularly-polarized and broadband patch antennas have been considered, and the similar results were obtained. They are discussed in the next chapter. The antenna parameters are listed in Table 2.5.1.

Table 2.5-1. Three patch antenna configurations. The fourth column indicates computed impedance bandwidth and the radiation Q-factor/resonant frequency of the equivalent metal-dielectric resonator (with the feed column removed).

Antenna #	Mode	Dielectric constant	Impedance bandwidth, % Q-factor/ f_{res}	Power gain, dBi
1	Fundamental TM along the longer patch dimension	$\varepsilon_r = 2.33$	1.0 63/2.38 GHz	7.1
2	Fundamental TM along the shorter patch dimension	$\varepsilon_r = 2.55$	2.0 35/2.98 GHz	7.1
3	Fundamental TM along the shorter patch dimension	$\varepsilon_r = 9.29$	0.6 102/1.29 GHz	4.3

Antennas #1 and #2 both have a low-epsilon thin dielectric substrate but considerably different bandwidth (Q-factor of the corresponding metal-dielectric resonator). Antenna #3 has a thick high-epsilon dielectric substrate, is relatively narrowband, and will be shown to have a larger back lobe. At the same time, this is perhaps the most complicated case from the numerical point of view – a thick high-epsilon dielectric with significant fringing fields close to patch edges.

b. Convergence for one-layer meshes (no boundary condition)

For all these cases, we keep only one layer of tetrahedra but refine the surface/volume mesh in the lateral direction. A typical planar mesh refinement procedure is outlined in Fig. 2.5-3 for antenna #2.
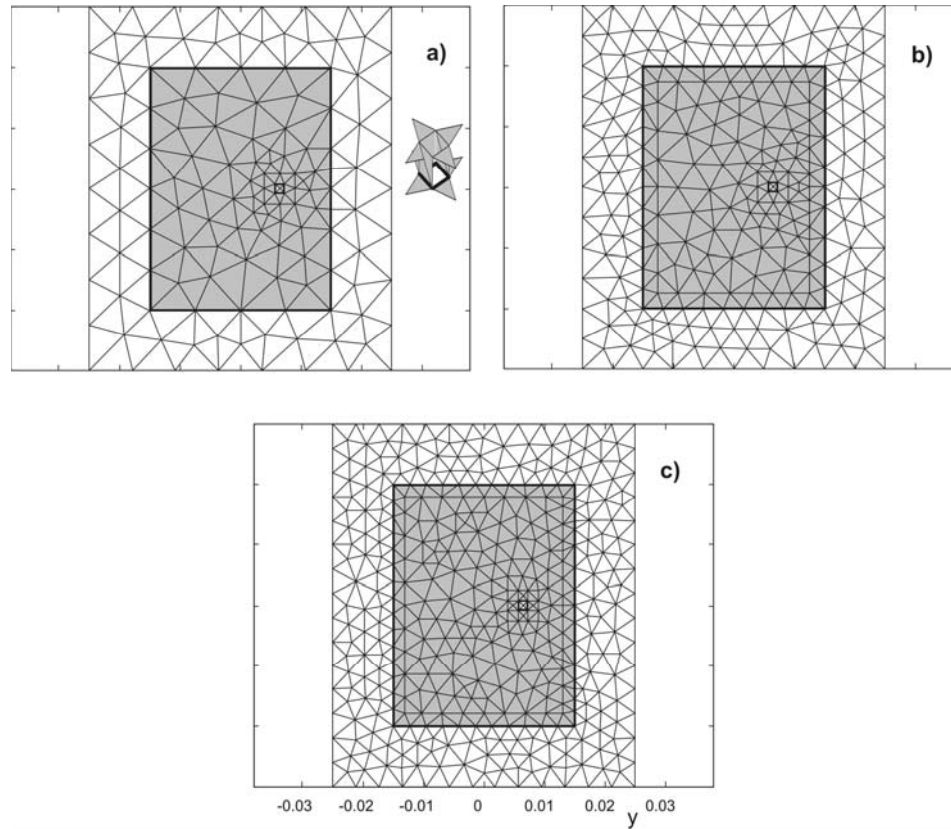
Figure 2.5-3 Mesh refinement procedure for antenna #2. Only the surface mesh is refined, keeping one layer of tetrahedra into the depth. The feed (a metal column with feeding edges on the bottom) is shown in Fig. 2.5.3a – right. (Ref. [78] © 2006 IEEE).

Fig. 2.5-3a also shows the feed structure with two metal triangles removed. A standard voltage gap feed and the extended feed model [79] are employed, with four (or eight) feeding edges around a metal column. The difference between these two approaches is not significant, for the present meshes. The solution is then compared to an equivalent Ansoft HFSS v 9.2 finite-element simulation, with an identical cross-section but a slightly shorter (by 20%) metal feeding column. This is necessary to introduce a lumped port connected to the ground plane, which takes 20% of the feed height. Fig. 2.5-4 shows the error in the resonant frequency compared to the corresponding Ansoft HFSS solution obtained on fine FEM meshes (60,000 to 150,000 tetrahedra) for the three patches.
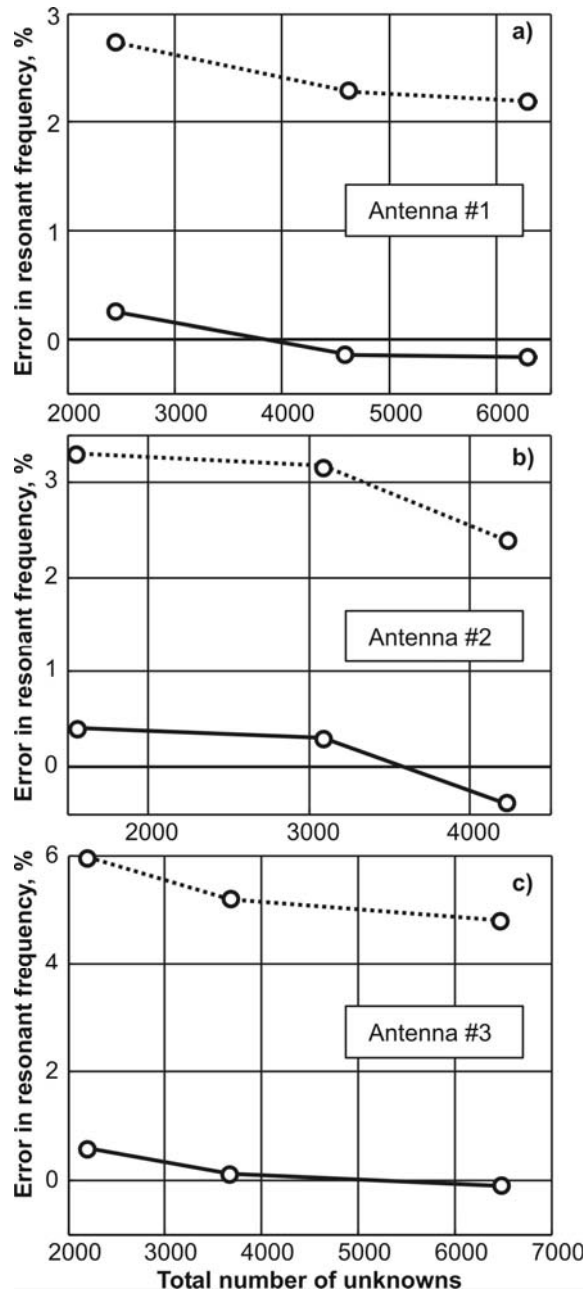
Figure 2.5-4. Converge curves for patch antennas #1-3 (a to c). Dotted line – original VIE; solid line – boundary condition on tetrahedra adjacent to metal faces is enforced. Circles denote error in the resonant frequency for the particular meshes. One layer of tetrahedra is refined in the lateral direction. (Ref. [78] © 2006 IEEE).

The error is denoted by a dotted line, as a function of the total number of unknowns (metal plus dielectric). One can see that a large systematic positive error of the MoM solution is observed, on the order of +2-6 %, even in the most favorable case of antenna

#1. This error cannot be significantly improved by finer meshing in the lateral direction, in either case.

Mesh refinement in the vertical direction does improve the fidelity of the simulation, but it requires two or more layers of tetrahedra. Such a procedure is hardly acceptable for a thin printed structure, since it leads to a large number of unknowns. More specifically, we were unable to obtain the VIE accuracy better than 1.2% with less than 7,000 unknowns for antenna #2 and, similarly, accuracy better than 2.6% with less than 7,000 unknowns for antenna #3 [80]. These numbers implied many different volume/surface mesh refinement schemes, with finer mesh refinement close to the patch borders and the antenna feed, as well as different feed models, etc.

Since the present VIE method operates on a complex dense symmetric matrix, it becomes very time-consuming at a large number of unknowns. Note that the equally poor convergence results have previously been observed for the VIE with the SWG basis functions [81, 82].

c. Convergence for one-layer meshes (boundary condition)

When the boundary condition on the contact dielectric tetrahedra is enforced in Eq. (2.5.1), the error curves shift toward zero as shown in Fig. 2.5-4 by solid lines labeled with circles. Very interestingly, these lines seem to follow the slope of the previous convergence result. At the same time, the boundary condition essentially eliminates the large positive offset in the resonant frequency, irrespectively of the antenna shape and the specific value of the dielectric constant under study.

Fig. 2.5-5 shows the input impedance behavior for three most coarse meshes corresponding to the left convergence points in Fig. 2.5-4, as a function of frequency close to the resonance. Figs. 2.5-5a to c correspond to antennas #1, 2, and 3. The HFSS solution is shown by solid curves whereas the MoM solution is indicated by squares. Both the resonant frequency and the shape of the resistance/reactance are reproduced accurately, for every patch antenna.
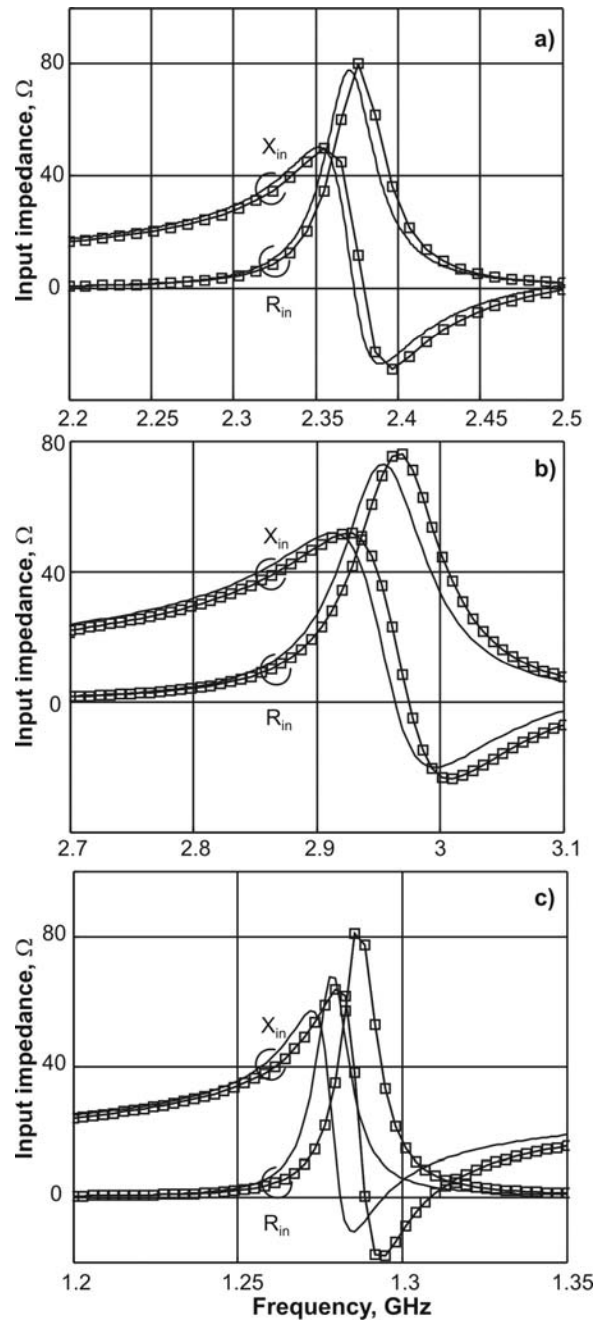
Figure 2.5-5 Input impedance curves corresponding to the most rough meshes for patch antennas #1-3 (a to c). The boundary condition on tetrahedra adjacent to metal faces is enforced. Squared curves – MoM solution for resistance/reactance; solid curves – Ansoft HFSS solution. (Ref. [78] © 2006 IEEE).

Next, Fig. 2.5-6 shows the antenna impedance behavior for three most fine meshes corresponding to the right convergence points in Fig. 2.5-4. The difference between these two sets of results is not significant, except for a slightly better agreement for antenna #3.
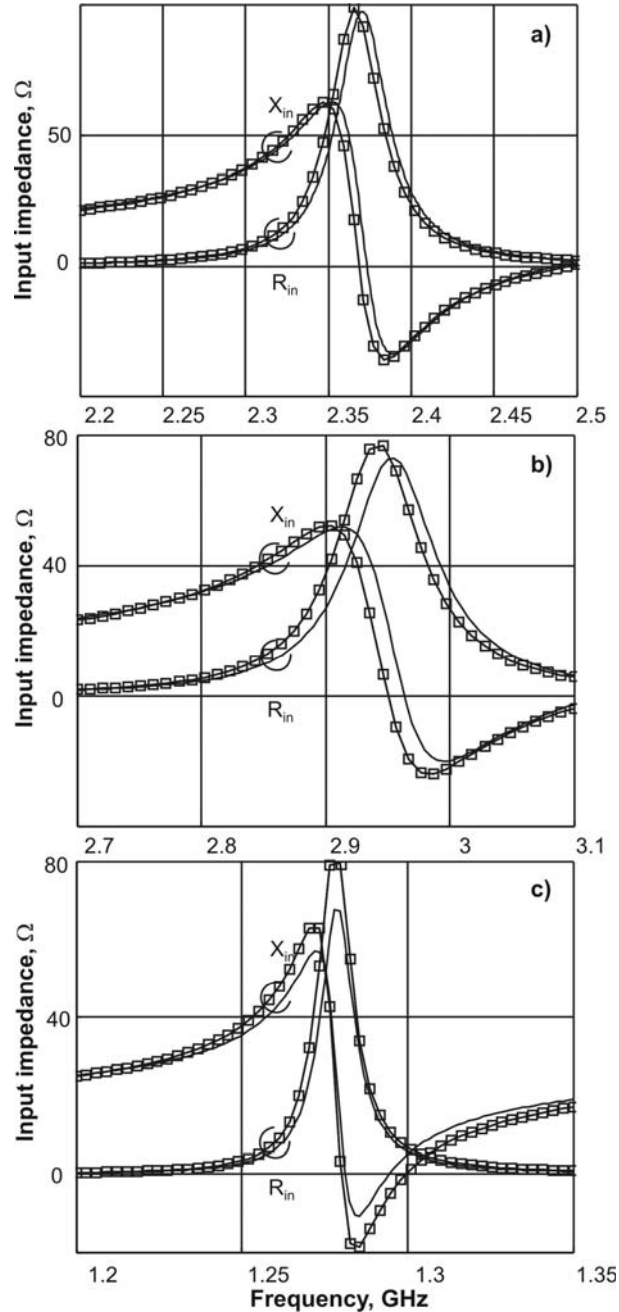
Figure 2.5-6 Impedance curves corresponding to the finest meshes for patch antennas #1-3 (a to c). The boundary condition on tetrahedra adjacent to metal faces is enforced. Squared curves – MoM solution for resistance/reactance; solid curves – the corresponding Ansoft HFSS solution. (Ref. [78] © 2006 IEEE).

d. Solution performance

For completeness, Table 2.5.2 below lists the solution performance for antenna #2. The execution times per frequency step include impedance matrix filling and the direct LU factorization of a complex symmetric impedance matrix (Intel Math Kernel Library), within the MATLAB shell. The corresponding C-routines are compiled using the standard MATLAB MEX environment. Typically, the LU factorization requires more than 90% of the total CPU time for mesh with 2000 unknowns or higher. About 2-5 sec per frequency step is necessary to achieve the accuracy of 1% or better in the resonant frequency. The number of unknowns for the VIE appears to be very close to the SIE approach, for the one-layer printed structure. The same tendency is expected to be true for a multi-layered inhomogeneous dielectric structure, where the VIE approach might perhaps require even a smaller number of unknowns than the SIE model.

Table 2.5-2 Number of unknowns VIE vs. SIE and the VIE execution times. The number of SIE unknowns is estimated by creating RWG basis functions for all outer dielectric faces and then adding to them the metal RWG bases. (Ref. [78] © 2006 IEEE).

Antenna #2	One-layer mesh with 726 tetrahedra	One-layer mesh with 1482 tetrahedra	One-layer mesh with 2298 tetrahedra
SIE unknowns (estimated)	1371	2685	4096
VIE unknowns and the ratio VIE/SIE	1545 (1.13)	3083 (1.15)	4742 (1.16)
VIE execution time on PIV 3.6 GHz (per frequency step, sec)	2.0	12.8	41.5

2.5.5 Discussion

Two potential points of concerns must to be discussed here. First, what is exactly the role of the parameter α in Eq.2.5.5b? Second, whilst the present approach seems to be

acceptable for printed antennas on thin dielectric substrates, will it be equally correct for an antenna utilizing the bulk dielectric material?

To answer the first question, we note that the exact condition $\alpha = 1$ was tested for all the antenna geometries presented above and was found to give somewhat less-accurate results, mostly for the patch antenna #3 on the high-epsilon thick dielectric substrate. Impedance bandwidth is rather affected. The radiation patterns remain the same. This observation might points us to the antenna feed, where the boundary condition has the most profound effect on the electric field in the tetrahedra adjacent to two and more metal faces. When the exact condition with $\alpha = 1$ is implemented for those tetrahedra, the total electric field may be exactly forced to zero – due to two simultaneously imposed boundary conditions, on two perpendicular planes.

One solution to this problem may be to keep $\alpha = 1$ but introduce a current-probe feed in dielectric, instead of the metal voltage-probe feed. However, this is likely not a general solution, which becomes questionable for a low-epsilon dielectric. Furthermore, the L-shaped or U-shaped metal edges may be present somewhere else. Another solution is to subdivide the tetrahedra with two (or more) neighbor metal faces into smaller tetrahedra, which have only one adjacent metal face. This solution requires additional mesh operations, increases the number of unknowns, and may lower mesh quality.

On the other hand, using Eq. 2.5.5b with an "average" value of α equal to 0.9 gives the accurate results for the considered antenna geometries. A direct inspection of the field in the dielectric beneath a metal sheet indicates that a small but visible tangential component, with the relative strength of 0 to 20%, is still presents in the tetrahedra adjacent to metal faces. Thus, Eq. (2.5.5b) is a reasonable approximation that provides more flexibility for the MoM solution related to the more complicated edge geometries and to the lower-quality meshes. Noticeably, the thinner is the substrate the smaller is the effect of α-variation about 1 and the better is the solution accuracy.

To answer the second question we choose, as an example, an antenna utilizing the bulk dielectric loading: a top-hat dielectrically-loaded cylindrically-symmetric monopole antenna – see Section 3.3. A good agreement with the FEM solution has been obtained in this case. Similar results have been obtained for a dielectric probe-fed HEM antenna [83]. These observations support a more general character of the present approach.

A more detailed validation is carried out for the present approach in the next sections by considering different planar antenna structures. Various antenna parameters like return loss, far fields, current and charge distributions are also compared with measured results or with other simulation methods.

3 Simulation results and validation

The theory described in chapter 2 was implemented using MATLAB and C/C++ codes, compiled under MATLAB environment as `mex` files. The use of mixed C/MATLAB codes helped in speeding up the algorithm and memory optimization. This chapter models some basic planar antenna structures using the MoM solver. It provides step by step procedure for creating the antenna structures and simulating them. The computed results are compared to existing mode matching solutions, to measured results or to the commercially available FEM software Ansoft HFSS.

The chapter is organized as follows. Section 3.1 models the half wavelength patch antenna. The design of a linearly polarized patch and a right hand circularly polarized patch antenna structure is presented in this section. Section 3.2 models the printed slot antennas where a microstrip fed slot antenna and a crossed cavity backed circularly polarized antenna are simulated. Finally section 3.3 models the quarter wavelength antennas. Simple monopole, a loaded monopole and planar inverted-F antenna are considered in this section.

3.1 Half wavelength patch antenna

The conventional patch antenna [16, 17, 84] is a half-wavelength cavity resonator where the (lowest) fundamental TM mode is mostly used. The patch length along the resonant dimension and the dielectric constant of the substrate determine the resonant frequency. The feed position determines which mode is excited (along a shorter or longer patch dimension) and is also responsible for the proper impedance matching. The feed thickness slightly tunes the resonant frequency (toward lower values when thickness increases). The antenna bandwidth is determined by the substrate thickness, dielectric constant, the patch shape, and the presence of substrate [16].

3.1.1 LP patch antenna

a. Geometry

This example describes a linearly-polarized patch antenna at 2.37 GHz on a Rogers RT/duroid® laminate [85] with $\varepsilon_r = 2.33$ and the thickness of 1.57 mm. The antenna geometry is shown in Fig.3.1-1. The loss tangent of the substrate is assumed to be zero. The antenna has the following features:

i.   The ground plane is finite but relatively large. Therefore, the antenna is expected to have a good front-to-back ratio.

ii. The corresponding metal-dielectric resonator (that includes the volume between the patch and the ground plane) is excited in the fundamental TM mode (TM_{10} in Fig. 3.1-1; see [16-17]), along the longer patch dimension. The dielectric constant of the substrate is rather small and the dielectric substrate is thin. Therefore, the antenna is expected to have a small bandwidth (due to a higher Q-factor of the corresponding TM resonator) and a relatively large size.

The feed will be offset by 5.5 mm from the patch center in order to achieve impedance matching. The feed is a rectangular metal column of 1 mm in width.
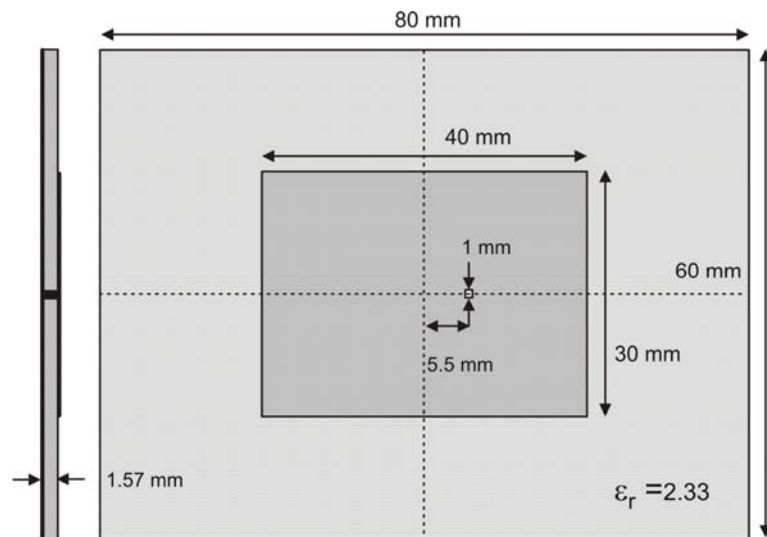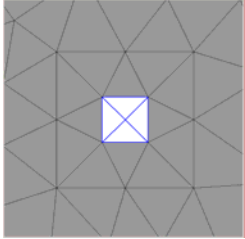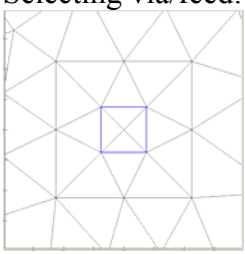
Figure 3.1-1 Rectangular-patch antenna at 2.37 GHz on a low-epsilon RT/duroid® laminate.

b. Code

Table 3.1-1 Operations to create and model a patch antenna with the probe feed.

Operation	Commands
Mesh generation 1_mesh Selecting tetrahedra to be removed Selecting via/feed:	1. Run `struct2d.m` and enter the dimensions of the structure; press the `Accept` mesh button to save the existing 2D mesh 2. Run `struct3d.m` and do the following: - Press OK on the first (layer) GUI - Remove tetrahedra within the feed column from the mesh using Zoom In option and individual selection (button select Individually). The removed tetrahedra will be beneath four removed faces (marked white) in the figure (Individually + DONE) - Select all metal faces of the ground plane (Select all + DONE) - When selecting `via` metal patches zoom in the feed area first. The feed edges are four edges of the inner rectangle. Select these four edges, one by one, by clicking on them (select individually). - Repeat same procedure for feed edge. - When selecting the top metal patch draw a rectangle enclosing only the patch faces and Close it. The selected patch becomes white. Press DONE. - Press OK on the Remove screen. Inspect the mesh and the feeding triangles visually. They should have a color different from that of other metal triangles. Also, plus and minus feeding triangles have distinct colors.
BF generation 2_basis	Run `wrapper.m` and inspect the resulting number of unknowns
MoM solution 3_mom	1. Open `impedance.m`. Input the frequency range and the number of discrete points. Run `impedance.m`. 2. Run `comp_z.m` to compare the impedance data with the corresponding Ansoft HFSS simulation (if present). 3. Run `radpattern.m` to obtain the patterns (cross-/co-pol) in the H-plane. 4. Run `comp_r.m` to compare the far-field data with the corresponding Ansoft HFSS simulation (if present). 5. Run `nearfield.m` to inspect the field/charge/current distribution within the patch antenna.

c. Mesh

Fig. 3.1-2 shows the patch antenna mesh obtained after the mesh generation operation. The final surface/volume mesh is inspected with the script `struct3d.m`. Special attention should be paid to feed assembly (removing tetrahedra from the feed and selecting the via patches for the feed column). The visual feed inspection is also done with `struct3d.m`.
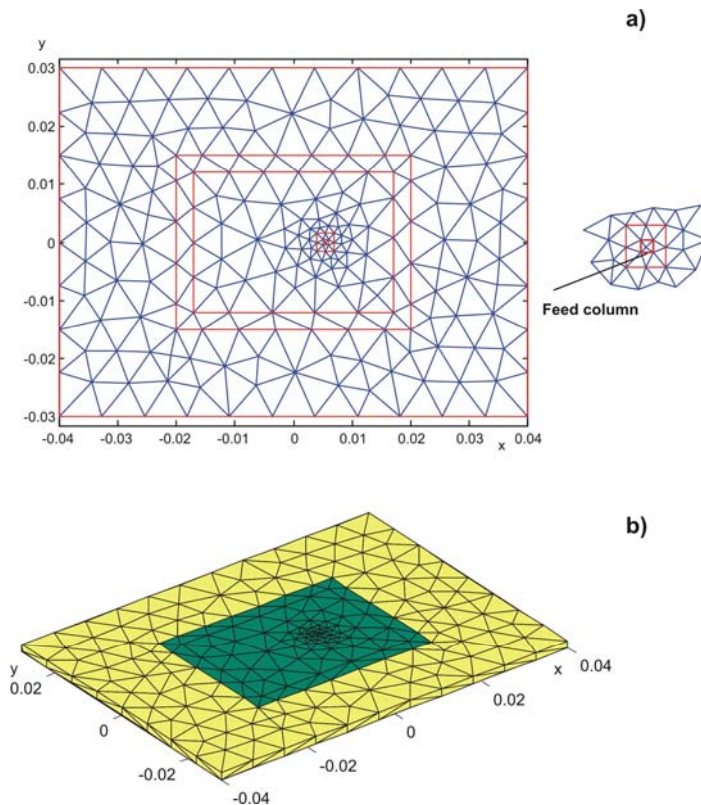
Figure 3.1-2 a) – Surface mesh created by struct2d.m; b) – volume/surface mesh for the patch antenna created by struct3d.m. The antenna feed is not seen.

d. Input impedance

The antenna input impedance $Z_A = R_{in} + jX_{in}$ is calculated in the script `impedance.m` at discrete frequency steps. It is a lengthy process. The number of steps and the frequency range are specified in that script. The simplest voltage gap feed model is given in the script; it can be replaced by an extended gap model [79] or the magnetic frill model [86].

The present antenna mesh has 2450 unknowns and needs about 5.2 sec per frequency step on a PIV 3.6 GHz. Fig. 3.1-3 shows the output of the script `comp_z.m`, which compared the present impedance data with the corresponding Ansoft HFSS simulation. The convergence for finer meshes for this particular patch antenna was studied in section 2.5.
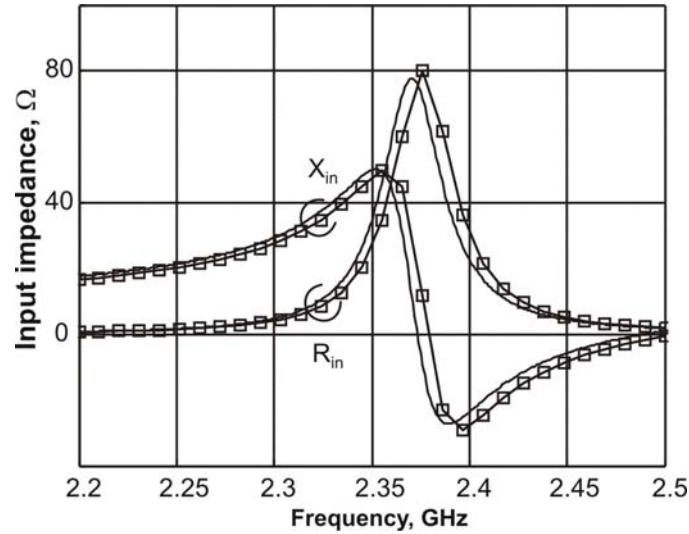
Figure 3.1-3 Input impedance curves for the patch antenna shown in Fig. 3.1-1. Squared curves – MoM solution for the resistance/reactance; solid curves – Ansoft HFSS solution.

The antenna resonance occurs when the reactance X_{in} becomes zero at a certain frequency. The resonant frequency is close to 2.37 GHz in Fig. 3.1-3. The script `impedance.m` simultaneously computes the power, $P_{feed} = P_{in}$, delivered to the antenna in the feed at every frequency, i.e.

$$P_{in} = \frac{1}{2}\text{Re}(IV^*) = \frac{1}{2}\text{Re}(I^*V) \qquad (3.1.1a)$$

where I is the total current in the feed and V is the applied feed voltage (1V).

The return loss (magnitude of the antenna reflection coefficient vs. 50 Ω) in dB

$$|\Gamma|_{dB} = -20\log_{10}\left(\left|\frac{Z_A - 50}{Z_A + 50}\right|\right); \quad Z = \frac{V}{I} \qquad (3.1.1b)$$

96

is calculated in the script `comp_s.m`. Note that the MATLAB figure shows the negative values for the return loss. The voltage standing wave ratio (VSWR) is defined by

$$\text{VSWR} = \frac{1+|\Gamma|}{1-|\Gamma|} \geq 1 \qquad\qquad (3.1.1c)$$

The impedance bandwidth (for a narrowband antenna, e.g. for the patch antenna) is estimated as the length of the frequency domain where the return loss falls below 10 dB vs. the antenna center frequency. The estimation for the present antenna gives the value of about 1.0%. The antenna center frequency is the frequency at which the return loss attains its maximum value. This value is also close to 2.37 GHz.

e. Radiation pattern – total directivity/gain [86]

The radiation characteristics are calculated in the script `radpattern.m`. The script accepts a frequency value, searches for the closest MoM solution saved in the file `out.mat` (output of `impedance.m`) and then calculates the electric and magnetic fields based on this solution – see Section 2.3. The fields are first calculated over a large sphere of radius R in order to find the total radiated power, P_{rad}

$$P_{rad} = \int_S \vec{W} \cdot \vec{n}\, ds, \quad \vec{W} = \frac{1}{2}\text{Re}\left[\vec{E} \times \vec{H}\,^*\right] \qquad\qquad (3.1.2)$$

Herein $\vec{W}$ is the time-averaged Poynting vector, $\vec{n}$ is the outer normal to the sphere surface. This value is compared to the already found antenna feed power, P_{in}. The ratio of these two powers characterizes the antenna radiation efficiency, e_{cd},

$$e_{cd} = \frac{P_{rad}}{P_{in}} \qquad\qquad (3.1.3)$$

The relative difference between these two powers characterizes the antenna losses. Since a lossless dielectric and a perfect metal conductor have been used, the relative difference

is expected to be small. The script `radpattern.m` gives a relative difference of 0.9% in the present case.

Next, the total or absolute logarithmic directivity, D, on the sphere surface is found in the form

$$D(\vec{r}) = 10\log_{10}\left(\frac{4\pi R^2 \vec{W}(\vec{r}) \cdot \vec{n}(\vec{r})}{P_{\text{rad}}}\right), \quad |\vec{r}| = R \tag{3.1.4}$$

For the antenna gain, G, the total radiated power, P_{rad} in Eq. (3.1.4) should be replaced by P_{in}. For the lossless antenna, $G = D$. The directivity plot over the sphere surface (script `radpattern.m`) for the present antenna is shown at the resonance in Fig. 3.1-4.
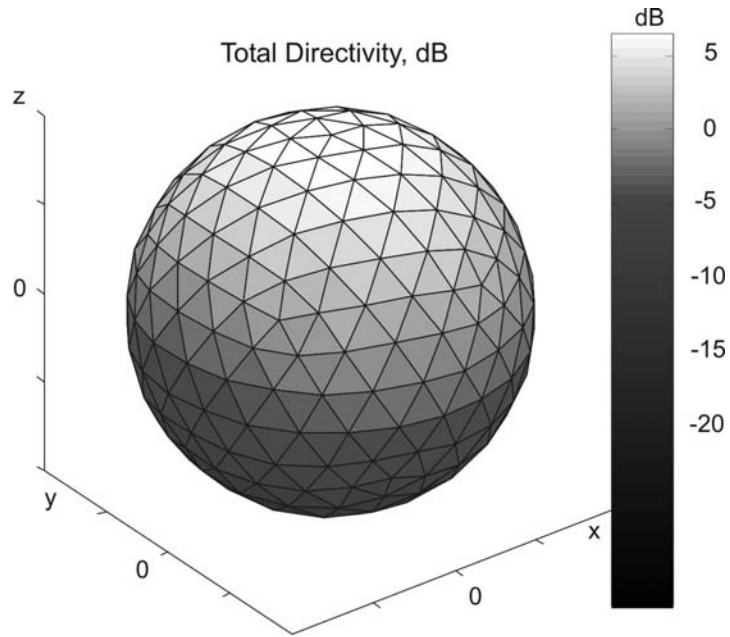
Figure 3.1-4 Total directivity for the patch antenna shown in Fig. 3.4-1 at the resonance. The maximum directivity (maximum gain in this lossless case) is approximately 7 dB.

f. Radiation pattern – co-polar and cross-polar components

For the elevation radiation patterns, one may use the elevation angle over the entire circle, $\theta \in 0, 2\pi$ as an independent variable in the script `radpattern.m`. Then, the xz- and yz-planes are described by

$\phi = 0$ for the xz‑plane and $\phi = \dfrac{\pi}{2}$ for the yz‑plane   (3.1.5)

in spherical coordinates

$$x = r\sin\theta\cos\phi, \quad y = r\sin\theta\sin\phi, \quad z = r\cos\theta \tag{3.1.6}$$

Instead of the Cartesian components of the electric field, one needs its spherical components found in the script `radpattern.m`

$$E_\theta = E_x \cos\theta\cos\phi + E_y \cos\theta\sin\phi - E_z \sin\theta \tag{3.1.7a}$$

$$E_\phi = -E_x \sin\phi + E_y \cos\phi \tag{3.1.7b}$$

Then, the co-polar directivity (directivity of the in-plane electric field component) or simply the co-polarization yields

$$D(\vec{r}) = 10\log_{10}\left(\frac{4\pi R^2 W}{P_{\mathrm{rad}}}\right), \quad W = \frac{1}{2\eta}\left|E_\theta\right|^2 \tag{3.1.8}$$

for any fixed large radius R. Similarly, the cross-polar directivity (directivity of the out-of-plane electric field component) or the cross-polarization gives

$$D(\vec{r}) = 10\log_{10}\left(\frac{4\pi R^2 W}{P_{\mathrm{rad}}}\right), \quad W = \frac{1}{2\eta}\left|E_\phi\right|^2 \tag{3.1.9}$$

Eqs. (3.1.8), (3.1.9) are only valid for the elevation radiation patterns.

The script `radpattern.m` outputs two radiation patterns for the present antenna, in the H-plane (the yz-plane in this case). In this plane, the cross-polar directivity dominates. The offset for the MATLAB polar plot is given as 60 dB. The script `comp_r.m` (which should be run after `radpattern.m`) compares these radiation patterns with the corresponding Ansoft HFSS radiation patterns. The output of this script is shown in Fig. 3.1-5 (the offset is removed). One can see a reasonably good agreement.
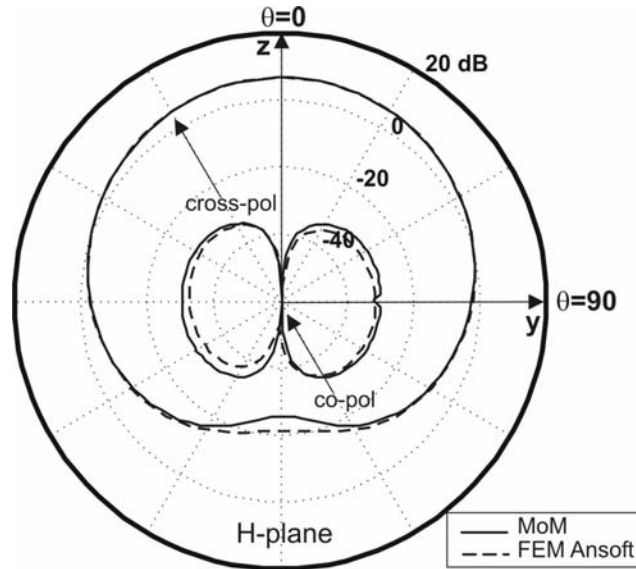
Figure 3.1-5. Directivity of the co-polar and cross-polar fields vs. elevation angle for the patch antenna at the resonant frequency (2.37 GHz), in the H-plane. The MoM solution is shown by a solid curve; the Ansoft solution is given by a dashed curve.

g. Near fields

It is also desired to inspect the near field distributions in the antenna volume or on the antenna surface. The script `nearfield.m` finds and displays such distributions at a given frequency. The script accepts a frequency value, searches for the closest MoM solution saved in the file `out.mat` and then calculates the electric and magnetic near fields based on this solution. The fields are calculated at the center of every dielectric tetrahedron. The bound surface charge density on the dielectric surface is found using the MoM solution. Next, the electric current density on the metal surface and the associated free charge distribution are found using the MoM solution for the metal patches. Figs. 3.1-6 and 3.1-7 show these distributions for the patch antenna. A typical TM-resonator behavior is observed for the dominant TM mode of the patch cavity, with the TM mode resonating in the xz-plane (the E-plane of the antenna).
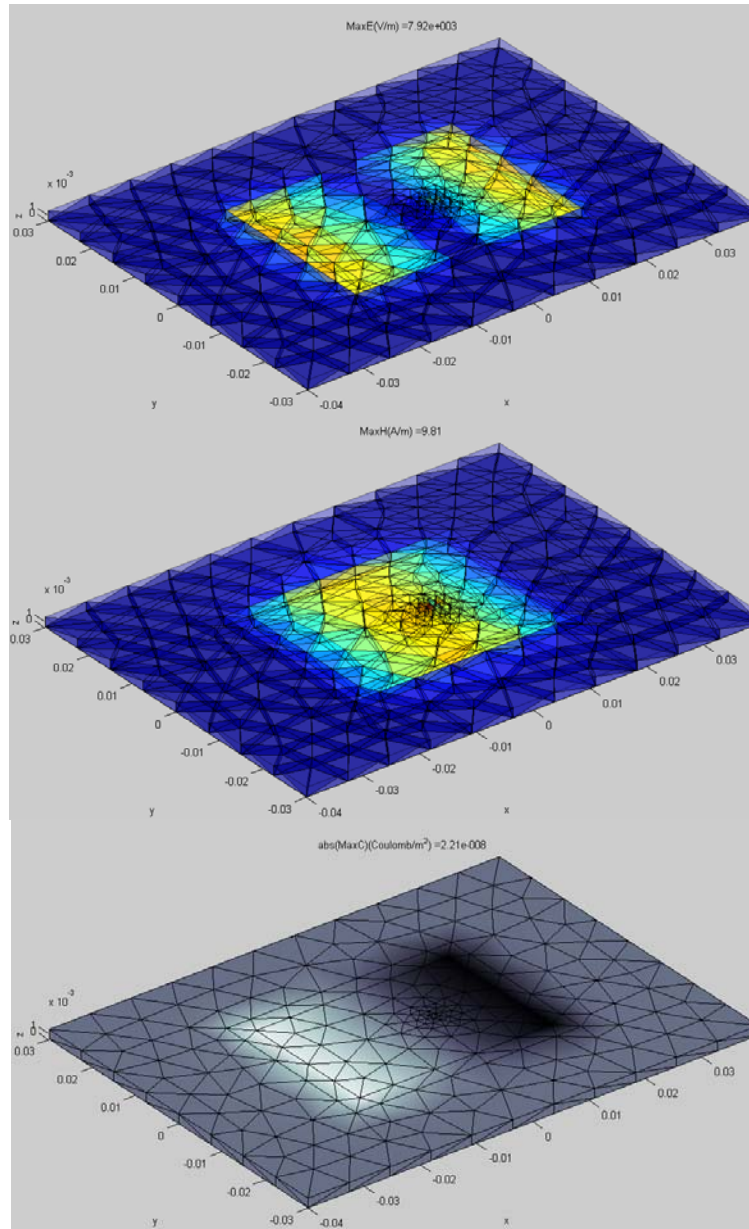
Figure 3.1-6 Fields within the patch antenna at the resonant frequency. Top – electric field (magnitude distribution) within the dielectric tetrahedra. Redder hues correspond to the larger field magnitudes. Center – magnetic field (magnitude distribution) within the dielectric tetrahedra. Redder hues correspond to the larger field magnitudes. Bottom - the surface bound charge density on the substrate surface – patch side. Light colors correspond to the positive charge, dark colors - to the negative charge.
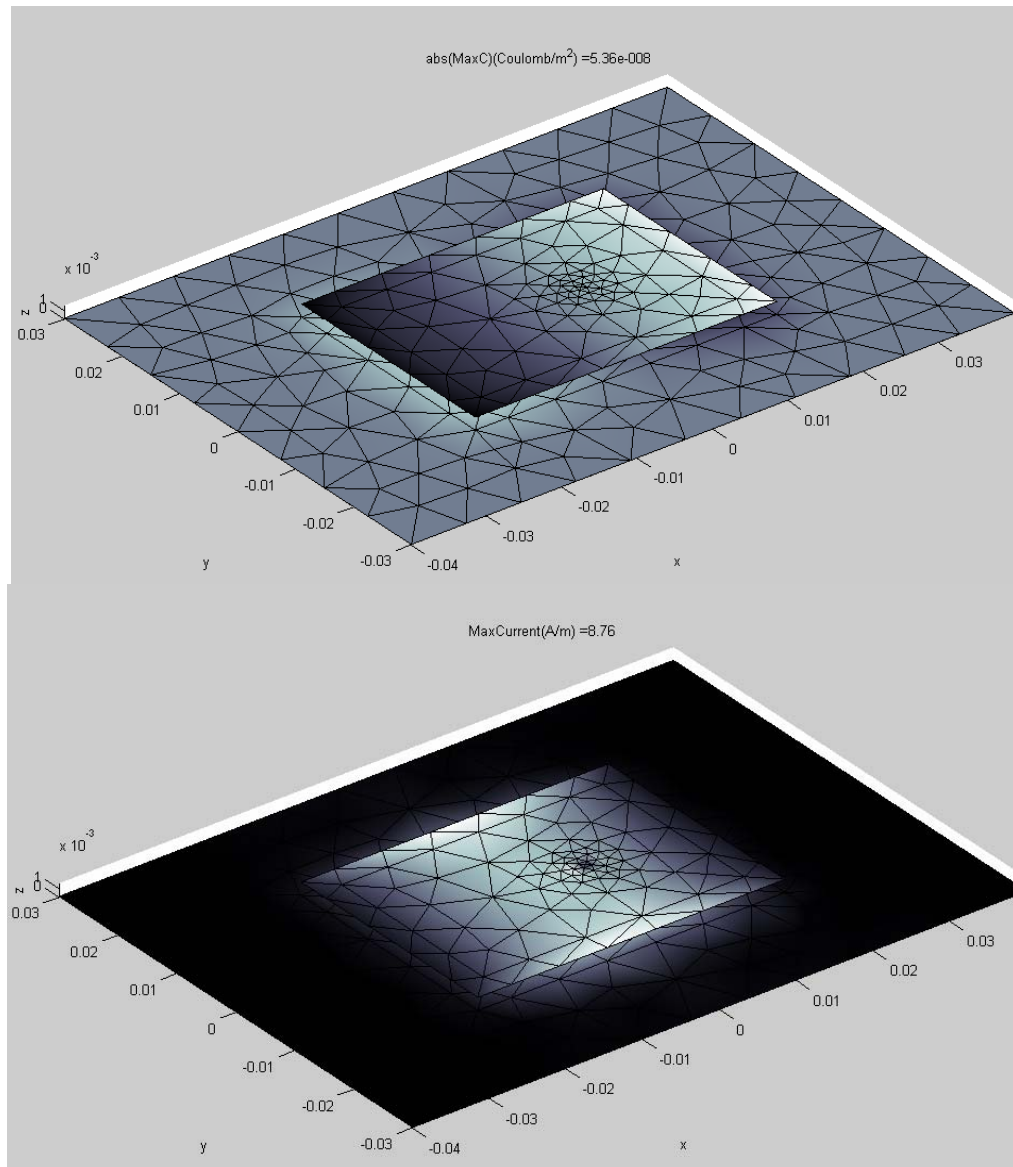
Figure 3.1-7. Top - free surface charge density on the metal surface. Light colors correspond to the positive charge, dark colors - to the negative charge. Bottom – the surface current distribution on the metal surface. Lighter colors correspond to large current magnitudes.

h. Other scripts

The script `eigenfreq.m` in the folder 3_mom is intended for the eigenfrequency search. It will not run for the present antenna configuration. To find the eigenfrequencies of the corresponding TM resonator one need to go back to the folder 1_mesh and create the same structure, but without the antenna feed (do not select the metal via patches for the feed and do not select the feed edges). Then, one creates the basis functions and runs

`eigenfreq.m` in order to find the resonant frequency and the Q-factor of the corresponding resonator. The resonator frequency found in this way (slightly less than 2.38 GHz) is close to the antenna center frequency. The Q-factor is about 63. The script output for this patch antenna is shown in Fig. 3.1-8.
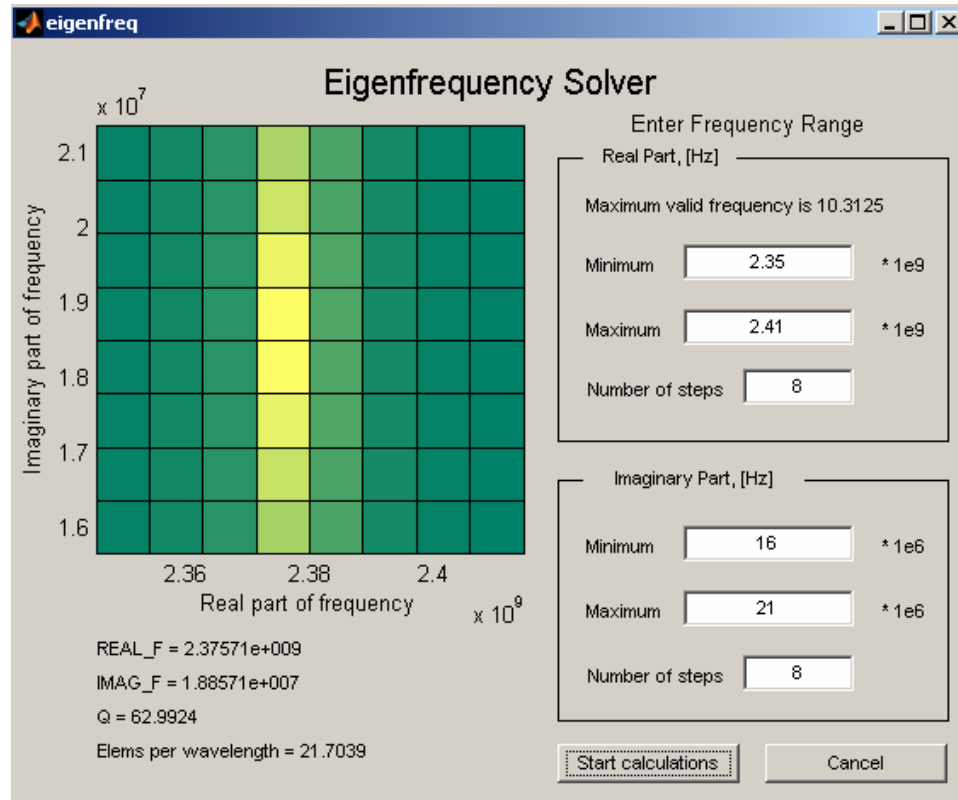
Figure 3.1-8 Resonant frequency and the Q-factor of the equivalent TM resonator. The feed column is removed from the antenna mesh, which includes only the ground plane, the patch, and the dielectric.

3.1.2   RHCP patch antenna for 2.4 GHz ISM band [87]

a. Geometry

This example describes a wideband circularly-polarized (CP) patch antenna for 2.40-2.48 GHz ISM band. The antenna utilizes a high-frequency Rogers 4003 substrate [85] with $\varepsilon_r = 3.38$ and the thickness of 5 mm. The antenna geometry is adopted from Ref. [87] (except for the feed position, which is slightly changed) and it is shown in Fig. 3.1-9. The antenna has the following features:

103

i.   The substrate is thick, which increases the bandwidth.

ii.   Two chamfer cuts are used to create the right-handed circular polarization (RHCP) by exciting simultaneously two nearly degenerate (90 deg out of phase) patch modes.

iii.   The variation between RHCP and LHCP is done either by rotating the feed or the chamfer edges of the patch by 90 degrees.

For the chamfer-cut patch, the impedance bandwidth and the polarization purity are primarily tuned by

i.   the cut width [88]

ii.   the feed position along one axis of the patch antenna.

When the cuts are large, there is a significant separation between two modes and low polarization purity for the higher resonance [88]. On the other hand, the small cuts lead to low polarization purity at the resonance. Therefore, a compromise is required between the impedance matching and the polarization purity.
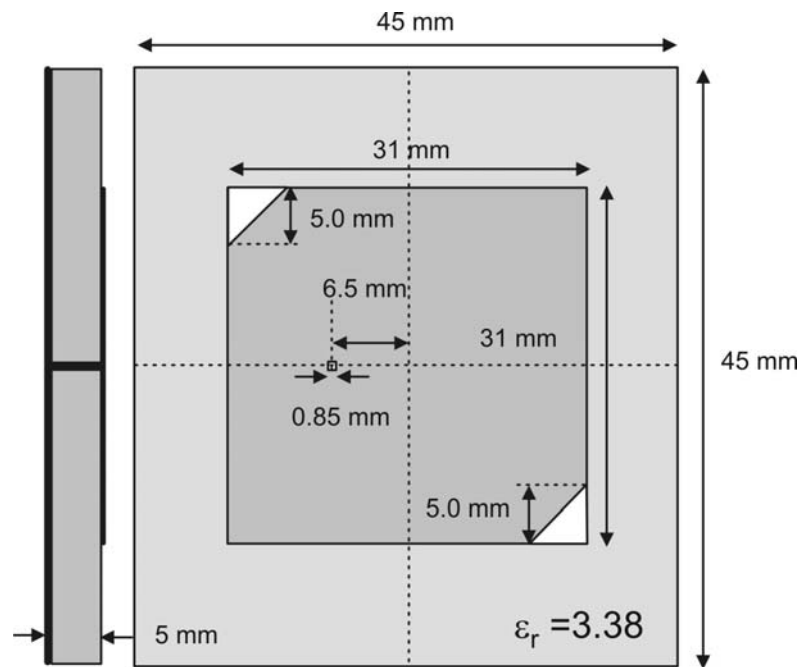
Figure 3.1-9 Rectangular RHCP patch antenna at 2.45 GHz on a Rogers RO4003 substrate [87].

We chose the feed offset by 6.5 mm from the patch center and chamfer cut width of 5 mm. These numbers were obtained by running a preliminary optimization search with the same code, which uses the coarse MoM meshes. They assure a wider antenna bandwidth but lead to a low polarization isolation for the upper end of the ISM band. Further antenna optimization may give better polarization isolation features.

b. Code

The antenna structure is created similar to the patch antenna structure in Section 3.1.1. A polygon tool is used in the script `struct3d.m` in order to create the chamfer-cut patch shape.

c. Mesh

Fig. 3.1-10 shows the patch antenna mesh obtained after the mesh generation operation.
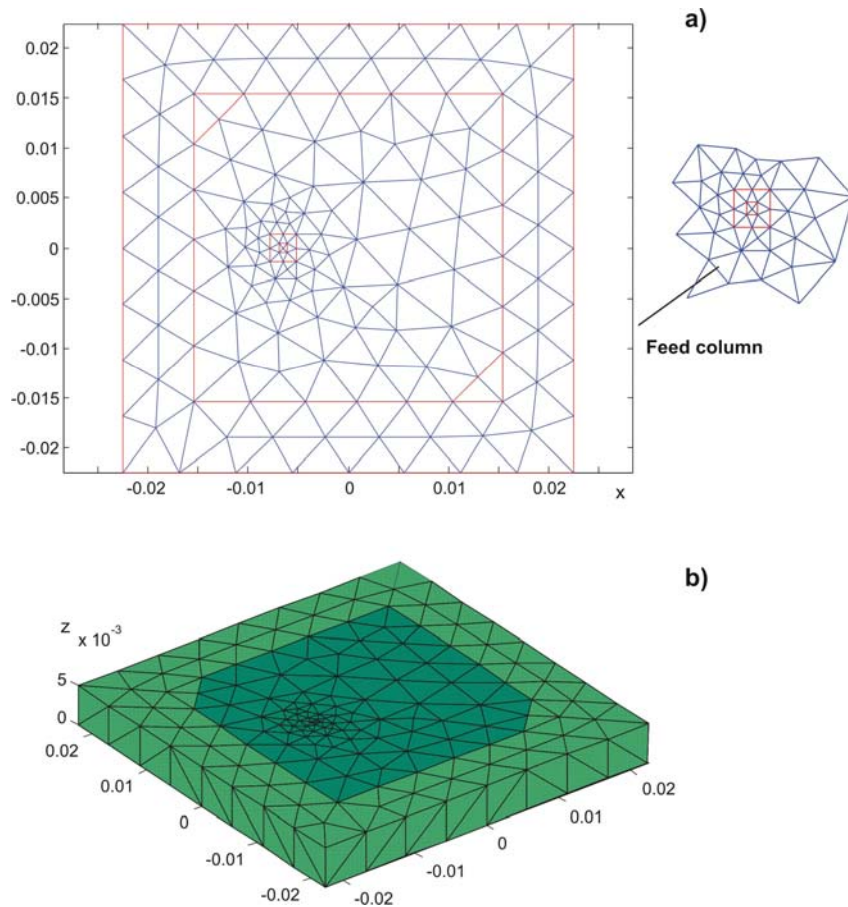
Figure 3.1-10 a) – Surface mesh created by struct2d.m; b) – volume/surface mesh created by struct3d.m. The feed column is not seen.

The final surface/volume mesh is inspected with the script `struct3d.m`. Special attention should be paid to feed assembly. The visual feed inspection is also done with the script `struct3d.m`.

d. Input impedance

The antenna input impedance is calculated in the script `impedance.m` at the discrete frequency steps. The present antenna mesh has 1780 unknowns and needs about 3 sec per frequency step on a PIV 3.6 GHz (double precision). The return loss is calculated in the script `comp_s.m`. The estimation for the present antenna gives a large value of about 8%. However, this value needs to be adjusted with regard to the desired RHCP and sufficient polarization isolation.
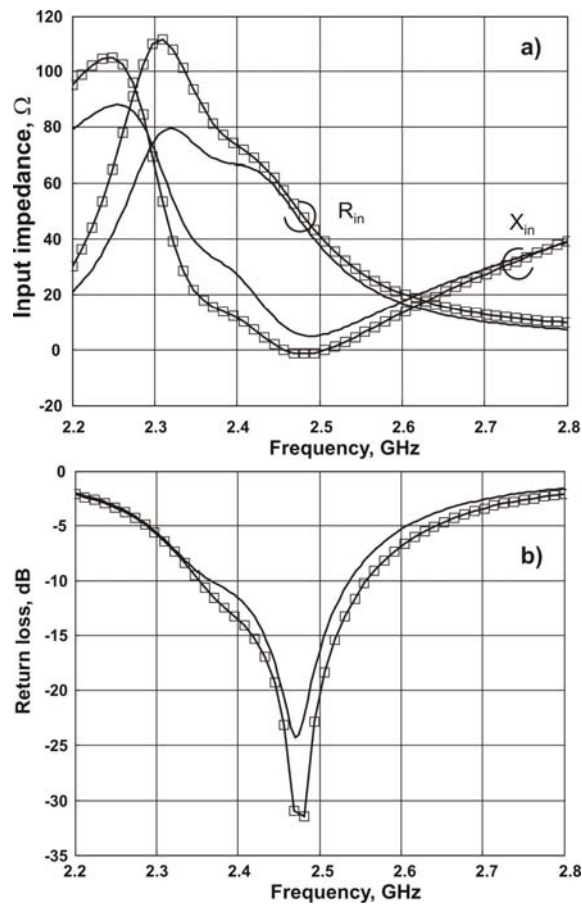
Figure 3.1-11 a) - Input impedance; and b) - return loss as a function of frequency for the RHCP patch antenna (from Ref. [87]). Solid curve – Ansoft HFSS solution; dashed curve – present solution with 1780 unknowns.

The antenna center frequency is close to 2.47 GHz. Fig. 3.1-11 shows the output of the scripts `comp_z.m` and `comp_s.m`, which compare the MoM impedance data and the return loss data with the corresponding Ansoft HFSS solution. The disagreement in the antenna impedance is marginal but will improve if finer meshes are used, with two or more dielectric layers of tetrahedra

e. Radiation pattern – total directivity/gain

The directivity plot over the sphere surface (script `radpattern.m`) for the present antenna at 2.40 GHz is shown at the resonance in Fig. 3.1-12. The script `radpattern.m` gives the relative difference of 0.29% between the radiated and the feed power in the present case.
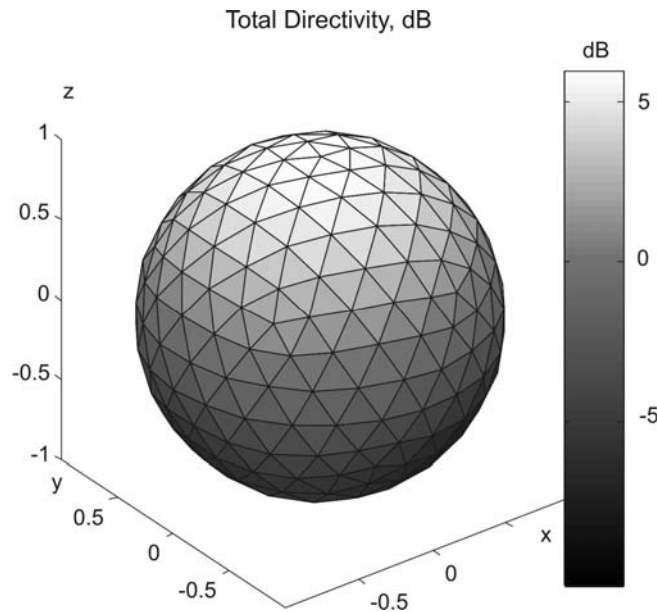
Figure 3.1-12. Total directivity for the patch antenna at 2.40 GHz.

f. Radiation pattern – RHCP and LHCP components

Once the spherical components E_θ, E_ϕ of the electric field in the script `radpattern.m` are known the right-handed circular polarization component (RHCP) and the left-handed circular polarization component (LHCP) of the electric field are given by

107

$$E_{\text{RHCP}} = \frac{1}{\sqrt{2}}\left(E_\theta + jE_\phi\right)$$

$$E_{\text{LHCP}} = \frac{1}{\sqrt{2}}\left(E_\theta - jE_\phi\right)$$

(3.1.10)

Then, the RHCP directivity yields

$$D_{\text{RHCP}}(\vec{r}) = 10\log_{10}\left(\frac{4\pi R^2 W}{P_{\text{rad}}}\right), \quad W = \frac{1}{2\eta}\left|E_{\text{RHCP}}\right|^2$$

(3.1.11)

for any fixed large radius R. Similarly, the LHCP directivity gives

$$D_{\text{LHCP}}(\vec{r}) = 10\log_{10}\left(\frac{4\pi R^2 W}{P_{\text{rad}}}\right), \quad W = \frac{1}{2\eta}\left|E_{\text{LHCP}}\right|^2$$

(3.1.12)
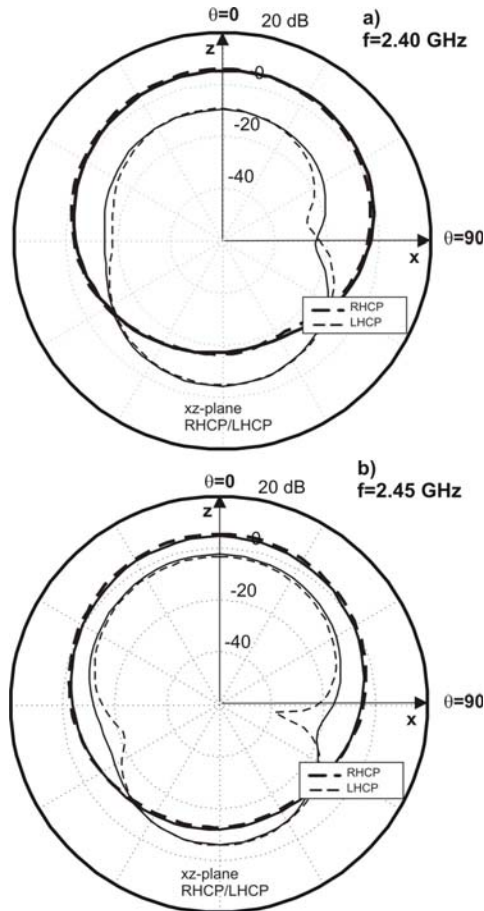
Figure 3.1-13. Absolute directivity of the RHCP/LHCP components vs. elevation angle for the CP patch antenna at 2.40 and 2.45 GHz (xz-plane). The corresponding HFSS solution at 2.40 GHz and 2.45 GHz is shown by two solid curves (RHCP and LHCP)

108

Both polarizations are found in the script `radpattern.m` and plotted in Fig. 3.1-13 at 2.40 and 2.45 GHz (the xz-plane). One can see that the cross-polarization isolation is slightly higher than 14 dB at 2.40 GHz and is about 9 dB at 2.45 GHz. However, it drops to approximately 5 dB at 2.50 GHz. Therefore, the present antenna has a smaller polarization bandwidth than the bandwidth predicted by the impedance matching. Assuming that the polarization isolation at zenith should be approximately 10 dB, one has the bandwidth of about 50 MHz, from 2.40 to approximately 2.45 GHz. Further antenna optimization may give better polarization isolation.

g. Near fields
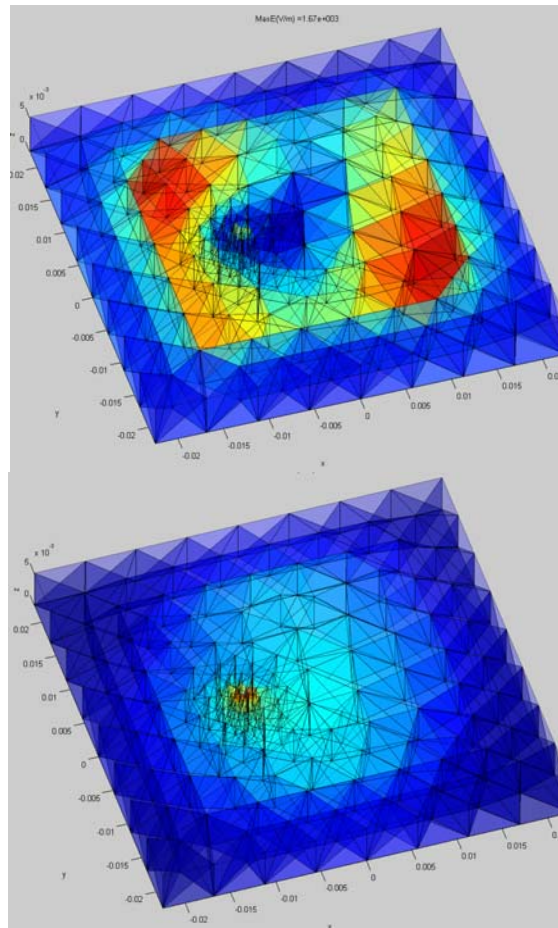
Figure 3.1-14. Fields within the patch antenna at the resonant frequency. Top – electric field (magnitude of the z-component) within the dielectric tetrahedra. Bottom – magnetic field (magnitude distribution) within the dielectric tetrahedra. Redder hues correspond to the larger field magnitudes.

The present example is characterized by the interaction of two orthogonal modes and the patch antenna cavity field becomes more complicated. Fig. 3.1-14 shows the electric field (magnitude of the vertical z-component) and the magnetic field (magnitude of the magnetic field vector) within the resonant cavity at 2.45 GHz.

h. Other scripts

To find the resonant frequency and the Q-factor, one needs to run the MATLAB GUI `eigenfreq.m` in folder 3_mom. It will not run for the present antenna configuration. To find the eigenfrequencies of the corresponding TM resonator one need to go back to the folder 1_mesh and create the same structure, but without the antenna feed (do not remove tetrahedra from the feed, do not select the metal via patches for the feed, and do not select any feed edges). Then, create the basis functions and run `eigenfreq.m` in order to find the resonant frequency and the Q-factor of the resonator. The script output for this patch antenna is shown in Fig. 3.1-15.
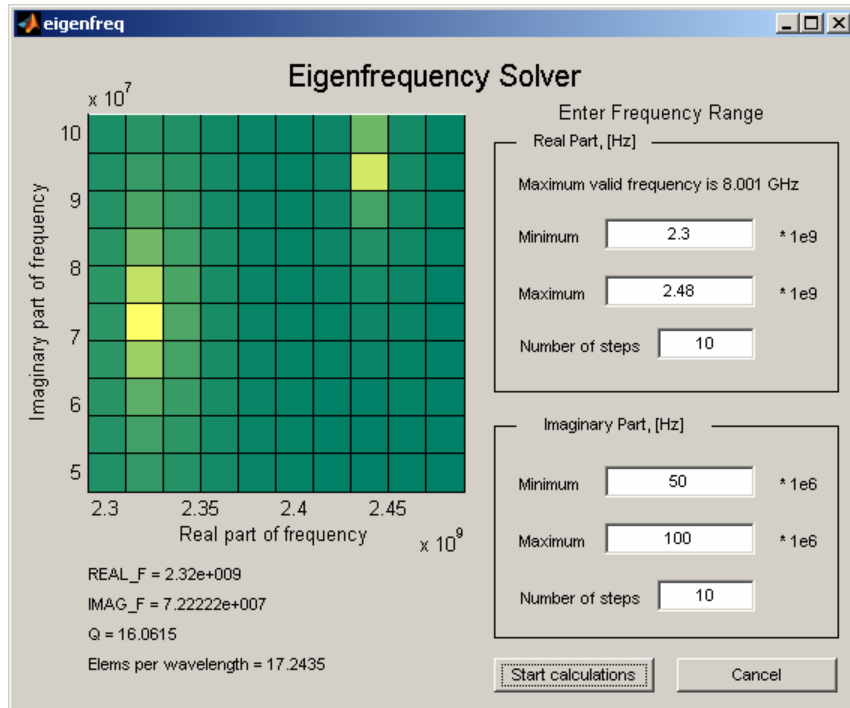
Figure 3.1-15 The GUI output for the direct eigenmode solution for the circularly-polarized patch antenna cavity (with the feed removed). The light dots in the plane of complex frequency indicate two close resonance(s).

One can see two close resonant modes, typical for the circular polarization, at approximately 2.32 and 2.44 GHz, respectively. The Q-factors are about 16 and 10, respectively. The eigenmode search can have a finer resolution. The eigenmode fields might be found using the script `mode.m` (works for the pure dielectric only).

3.2 Printed Slot Antenna

3.2.1 <u>Microstrip feed model</u>

Despite the significant amount of work on the modeling of the coaxial probe feed with the voltage gap sources, there is not much available from the literature with regard to exciting the microstrip line with a possible analog of the voltage gap. Putting the voltage gap directly on the microstrip line is mentioned in [89, 90]. In [90], the gap is placed somewhere in the middle of the microstrip. In the Ansoft HFSS note [91], the microstrip feed is modeled by a finite perfect H-boundary that has a predefined voltage and the related E-field along the impedance line - the lumped port from the ground plane to the microstrip. This is one of two available methods (together with the wave port) in Ansoft HFSS to feed the microstrip. We note that the microstrip length should approximate half wavelength for a lumped load in order to avoid impedance transformation [84]. For distributed loads, this value may vary.

In the code example of Section 3.2.2, a long narrow microstrip (somewhat shorter than the half wavelength [92]) will be connected to the ground at the end of the substrate by a metal via strip. The feeding edge is chosen as the bottom edge of this via strip.

A simple test with the present code shows that the exact position of the feeding edge on an unloaded thin microstrip does not really matter: the results for the one-port network's input impedance indicate differences of about 1% when the feed is placed either on the via, on various edges of the microstrip, or elsewhere.

One must emphasize that the direct-connection model becomes inaccurate for wide microstrips and shall not be used in these cases. A more accurate microstrip port model is currently programmed. The microstrip mesh is also important for accurate results close to the microstrip edges. This in contrast to the approaches based on the Green's function for an infinite dielectric substrate, where no special meshing for the microstrip is necessary.

3.2.2 <u>Microstrip-fed printed slot antenna</u>

a. Geometry

This example describes a linearly-polarized microstrip-fed wide-slot broadband antenna at 1.67 GHz on a FR4 substrate with $\varepsilon_r = 4.4$ and the thickness of 0.8 mm [92]. The antenna geometry is shown in Fig. 3.2.1.
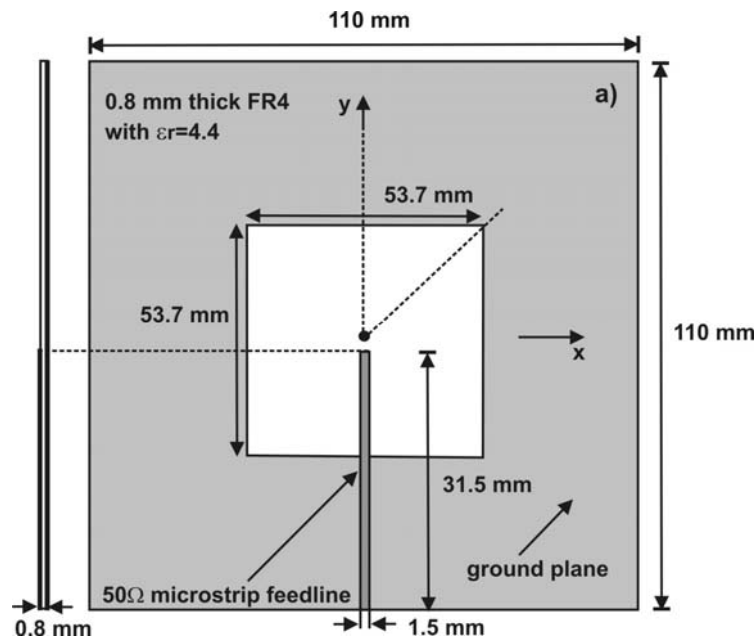
Figure 3.2-1.Microstrip-fed rectangular-slot antenna at 1.67 GHz on a FR4 substrate [92]. (Ref. [78] © 2006 IEEE)

The antenna has the following features:

i.   The wide slot is feed by a 50 Ω microstrip line of the width 1.5 mm (see [84] for the characteristic impedance of the microstrip line), which is printed on the
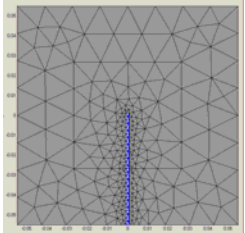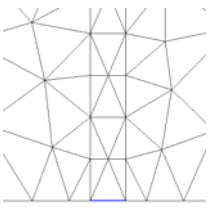
opposite side of the microwave substrate and placed symmetrically with respect to the centerline of the slot.

ii.   The printed slot antenna without a reflecting plane is a bi-directional radiator (the maximum gain occurs in the vertical direction). Current methods for reducing the back radiation of slot antennas use a metallic reflector or an enclosed cavity behind the slot [93, 94].

The microstrip end is offset from the slot center as shown in Fig. 3.2-1 in order to provide the impedance matching [92]. The microstrip feed is a voltage gap connector between the ground plane and the microstrip discussed above.

b. Code

Table 3.2-1 Operations to create and model a microstrip-fed slot antenna.

Operation	Commands
Mesh generation 1_mesh	1. Run `struct2d.m`, enter the existing patch dimensions and press the `Accept` mesh button to save the 2D antenna mesh
Select microstrip Select via\feed 	2. Run `struct3d.m` and - Press OK on the first (layer) GUI - Keep all tetrahedra in the mesh (Press DONE) - Select only the microstrip while selecting metal faces of the ground plane (bottom metal faces). Press DONE - When selecting via metal patches select only one edge – the bottom edge of the microstrip. Use the Zoom In option first. Then, draw a rectangle around this edge and Close it. The selected edge becomes blue. Press DONE. - Repeat the same operation for the feed edge. - When selecting top metal faces draw a multi-line polygon (or a number of polygons) that include all metal patches except the slot. Close every polygon. The selected metal patches become white. Use individual selection if for some reason the results are incorrect. Press DONE, then OK on the Remove screen.
BF generation 2_basis	Run `wrapper.m` and inspect the resulting number of unknowns.
MoM solution 3_mom	1. Open `impedance.m`. Enter the frequency range and the number of discrete points. Run `impedance.m`.

	2. Run `comp_s.m` to inspect the antenna return loss.
	3. Run `radpattern.m` to obtain the patterns (RHCP/LHCP) in the H-plane.
	4. Run `nearfield.m` to inspect the field/charge/current distribution in the slot antenna.

c. Mesh

Fig. 3.2-2 shows the slot antenna mesh obtained after the mesh generation operation with `struct3d.m`.
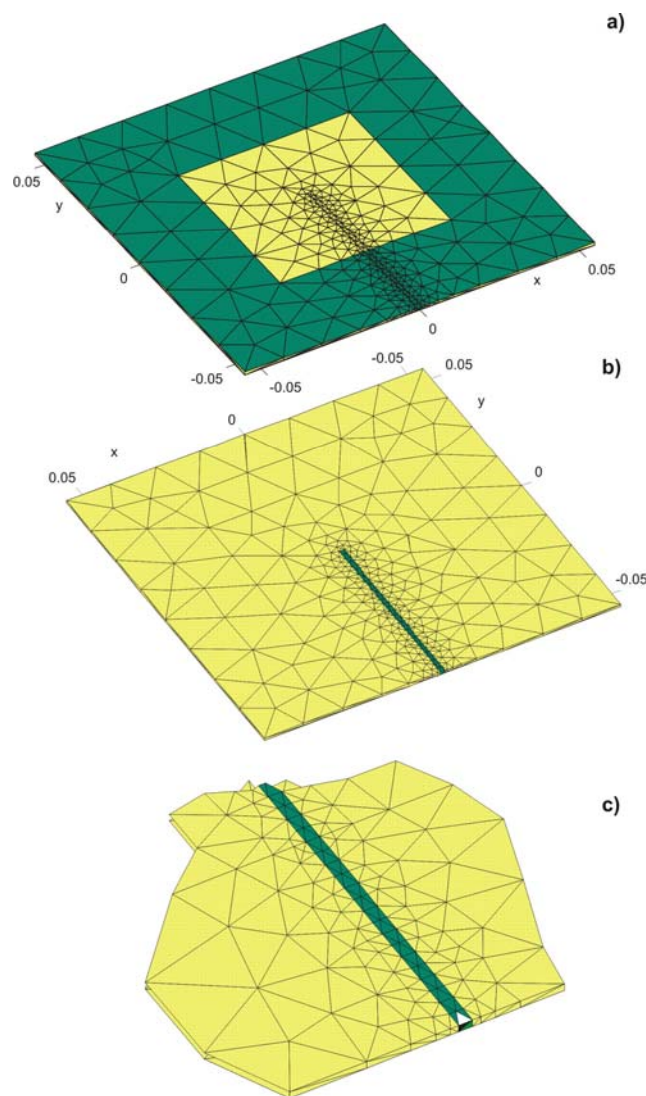
Figure 3.2-2. a) – Slot antenna – top view. The dielectric faces are shown by a light color; b) – bottom view of the slot antenna; c) – enlarged feed domain. The feed basis function is marked by white and black triangles.

The final surface/volume mesh is also inspected with the script `struct3d.m`. The microstrip-line feed is modeled by connecting the ground plane and the 50 Ω microstrip line at the end of the substrate by a vertical metal strip of the same thickness with a voltage gap. This model is only applicable to the long narrow strips.

d. Input impedance

The antenna input impedance is calculated in the script `impedance.m` at the discrete frequency steps. The present antenna mesh has 2836 unknowns, and the running time per frequency step is about 10 seconds. The resonant frequency is close to 1.67 GHz.

The return loss plot gives the bandwidth estimation for the present antenna at 21%, which is large compared to the previous patch antennas. Fig. 3.2-3 shows the output of the script `comp_s.m`, which calculates the antenna return loss (dotted curve) compared to the return loss measured in Ref. [92] – shown by a solid curve. The dashed curve is the return loss when the number of MoM unknowns increases to 3782. One can see a reasonably good agreement
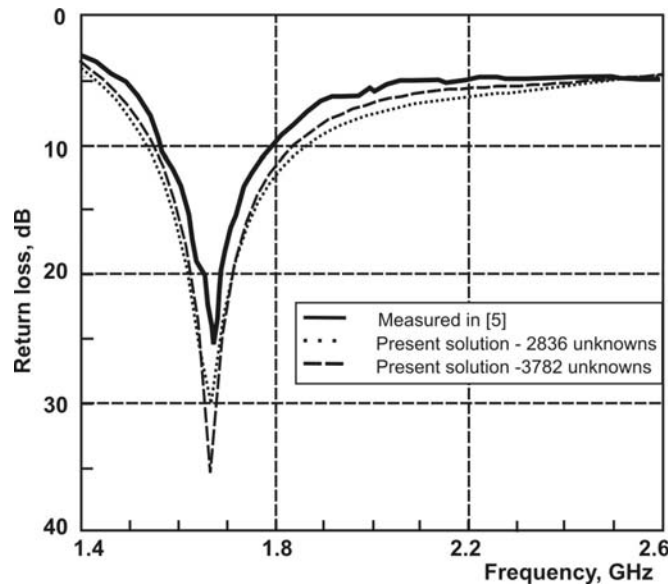
Figure 3.2-3. Return loss of the slot antenna as a function of frequency. Solid curve – measurements [92]; dotted curve – present solution with 2836 unknowns; dashed curve – present solution with 3782 unknowns. (Ref. [78] © 2006 IEEE)

115

e. Radiation pattern – total directivity/gain

The directivity plot over the sphere surface (script `radpattern.m`) for the present antenna is shown at the resonance (1.67 GHz) in Fig. 3.2-4. The script also gives a relative difference of 0.74% between the radiated and the feed power in the present case.
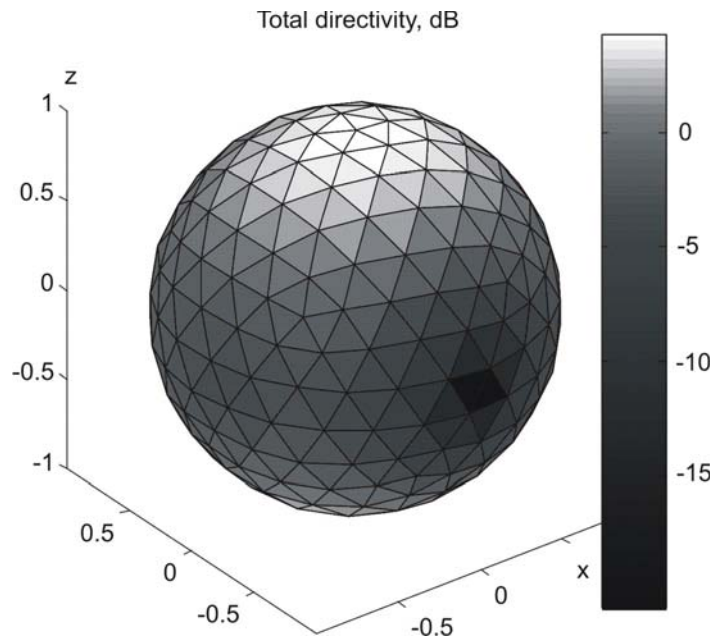
Figure 3.2-4. Total directivity for the slot antenna shown in Fig. 3.2-1 at the resonance. The maximum directivity is approximately 4.5 dB at zenith.

f. Radiation pattern – co-polar and cross-polar components

The co-polar and cross-polar directivity components are found similar to the approach described in Section 3.1.2. Here, we are interested in the H-plane radiation patterns (the xz-plane) for the present configuration.

The script `radpattern.m` outputs two radiation patterns for the present antenna, in the H-plane. In this plane, the cross-polarization directivity dominates. The offset for the MATLAB polar plot is given as 35 dB. Fig. 3.2-5a compares the radiation patterns in the H-plane with the measurement [92]. One can see a reasonably good agreement. The corresponding comparison for the E-plane is given in Fig. 3.2-5b.
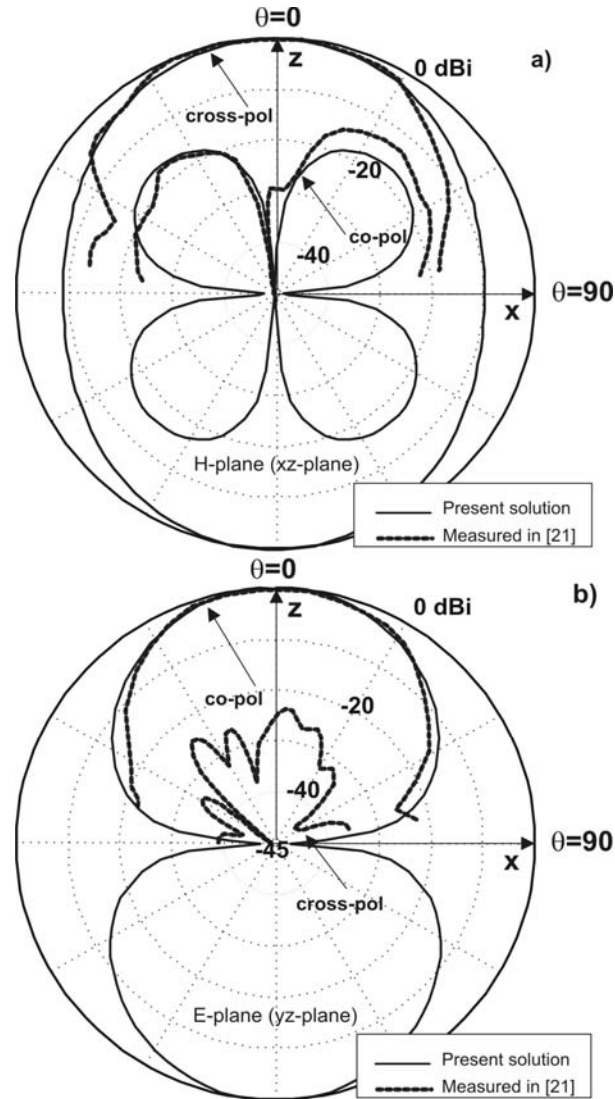
Figure 3.2-5 Normalized directivity of the co-polar and cross-polar fields vs. elevation angle for the slot antenna [92], at the resonant frequency, in the H- and E-planes, respectively. The coarsest MoM mesh with 2836 unknowns is used. The MoM solution is shown by a solid curve; the experimental data [92] is given by dashed curves. The MoM cross-polarization is below 45 dBi in the E-plane and is therefore not seen. (Ref. [78] © 2006 IEEE)

g. Near fields

Fig. 3.2-6 shows two such distributions for the present antenna; the Poynting vector density in the dielectric and the surface current density on the metal surface. It is seen in Fig. 3.2.6 how the energy is supplied to the cavity using the microstrip.
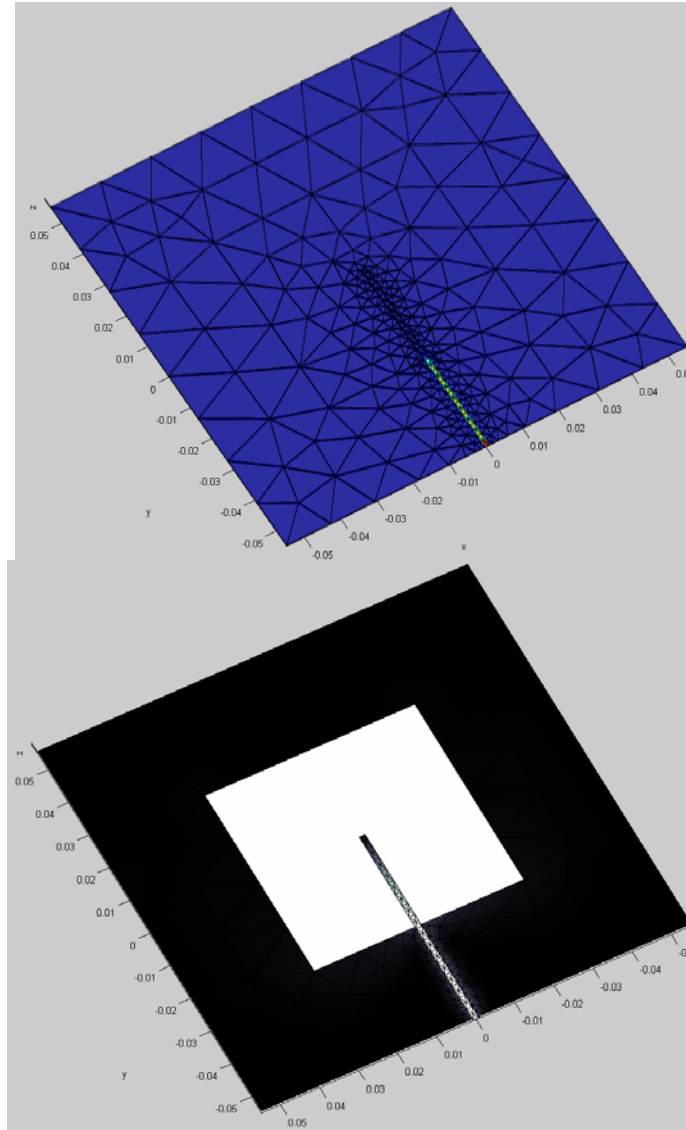
Figure 3.2-6 Fields within the slot antenna at the resonant frequency. Top – Poynting vector (magnitude distribution) within the dielectric tetrahedra. Redder hues (which have lighter colors) correspond to the larger power density magnitudes. Bottom – electric current (magnitude) distribution on the metal surface (bottom view).

h. Other scripts

The output of the script `eigenfreq.m` is shown in Fig. 3.2-7. To find the eigenfrequencies of the corresponding TM resonator one needs to go back to the folder 1_mesh and create the same structure, but without the antenna feed. Note that the cavity resonance strongly depends on the presence of the microstrip and disappears if the

microstrip is removed. The resonator frequency found in this way (about 1.57 GHz) is lower than the antenna center frequency. A finer mesh around the slot cavity may be necessary to reduce the difference. The Q-factor is about 5.6, which is a rather small value. Accordingly, the antenna impedance bandwidth is large – 21%. In the present case, the impedance bandwidth approximately agrees with the estimate
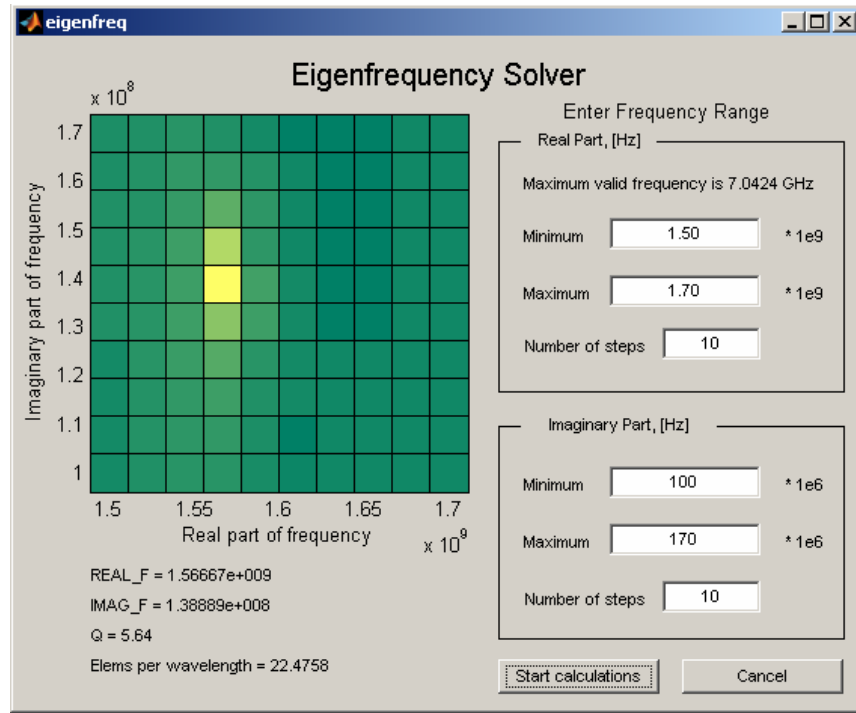
Figure 3.2-7 Resonant frequency and the Q-factor of the slot antenna cavity. The feed strip is removed from the antenna mesh, which includes only the microstrip, the slotted top metal plane, and the dielectric.

3.2.3 Crossed-slot cavity-backed circularly polarized antenna

a. Geometry

This example describes a circularly-polarized crossed-slot antenna at 2.34 GHz [94] on a high-frequency Rogers RT/duroid® 5880 laminate [85] with $\varepsilon_r = 2.20$ and a thickness of 3.0 mm. A crossed-slot multimode antenna at 2.34 GHz from Ref. [94] is intended for satellite digital audio radio service and needs to be circularly-polarized over most of the upper hemisphere, but vertically-polarized near the horizon. The antenna geometry with

two crossed slots of a slightly different length is shown in Fig. 3.2-8. Since the probe feed thickness is not reported, a metal column of cross-section 0.5×0.5 mm was chosen here.
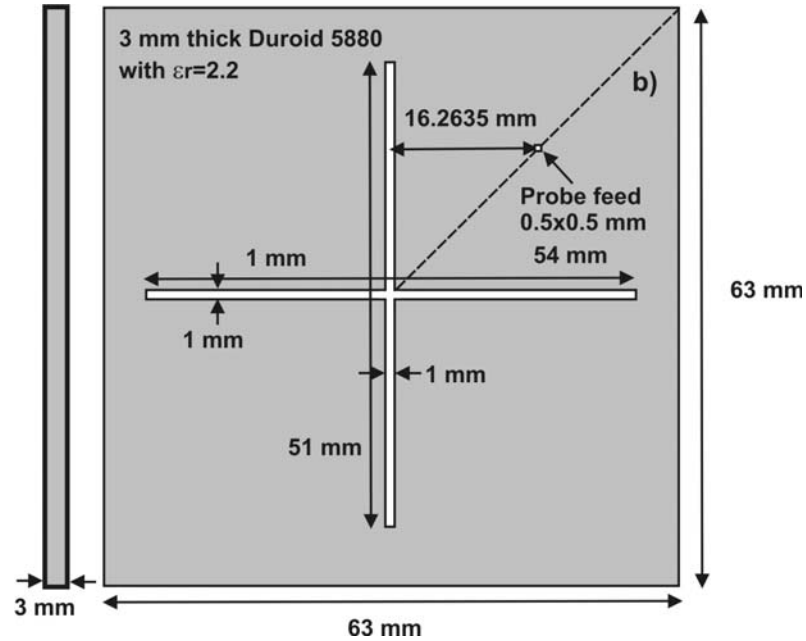
Figure 3.2-8. Crossed-slot probe-feed CP antenna from Ref. [94]. (Ref. [78] © 2006 IEEE)

The antenna has the following features:

i. The cavity provides the role of the reflector for the slot antenna. However, the front-to-back ratio still remains relatively poor unless a large metal ground plane is introduced [94].

ii. The dielectric cavity filling is intended to reduce the cavity size.

A number of different cavity TEM modes may be excited in this configuration [94].

b. Code

The antenna structure is created similar to the slot antenna structure in Section 3.2.1. To create the metal cavity, all border edges of the base planar mesh should be selected as via. The creation of the feed is similar to the patch antenna feed considered in Section 3.2.1. The dielectric tetrahedra must be removed from the feed.

120

c. Mesh

Fig. 3.2-9 shows the slot antenna mesh obtained after the mesh generation operation. The final surface/volume mesh is inspected with the script `struct3d.m`. Special attention should be paid to feed assembly (selecting the via patches for the feed column, and identifying the feeding edges).
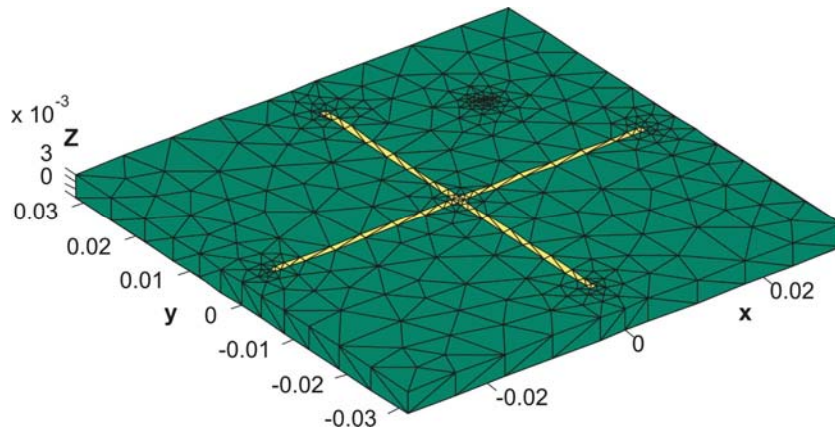
Figure 3.2-9. Volume/surface mesh for the slot antenna created by struct3d.m. The dielectric (inside the metal cavity) is shown by lighter color. The feed column inside the cavity is not seen.

d. Input impedance

The present antenna mesh has 4578 unknowns and needs about 37 seconds per frequency step on a PIV 3.6 GHz (double precision). The estimation of the return loss for the present antenna gives a bandwidth value of about 4.3%. The antenna center frequency is close to 2.34 GHz. Fig. 3.2-10 shows the output of the script `comp_s.m`, which compared the MoM return loss data with the corresponding experimental data [94].
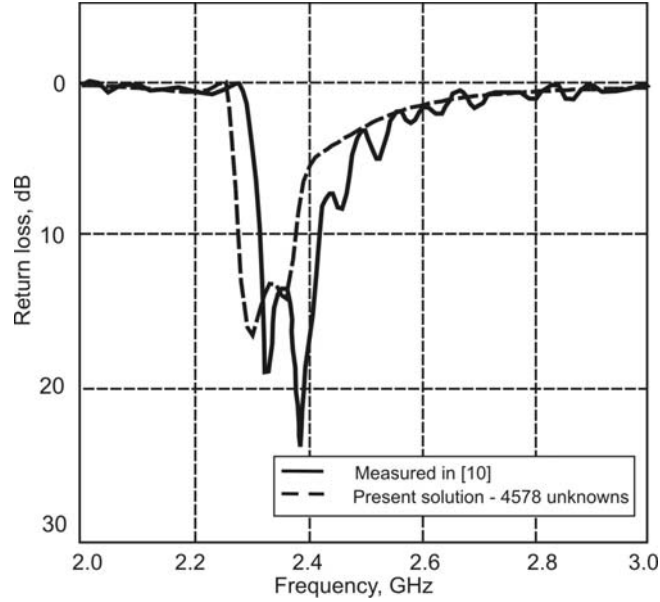
Figure 3.2-10. Return loss for the crossed-slot probe-fed CP antenna (from Ref. [94]).
Solid curve – measurements [94]; dashed curve – present solution with 4578 unknowns.
(Ref. [78] © 2006 IEEE)

e. Radiation pattern – total directivity/gain

The directivity plot over the sphere surface (script `radpattern.m`) for the present antenna is shown at the resonance in Fig. 3.2-11.The script also gives the relative difference of 0.81% between the radiated and the feed power in the present case.
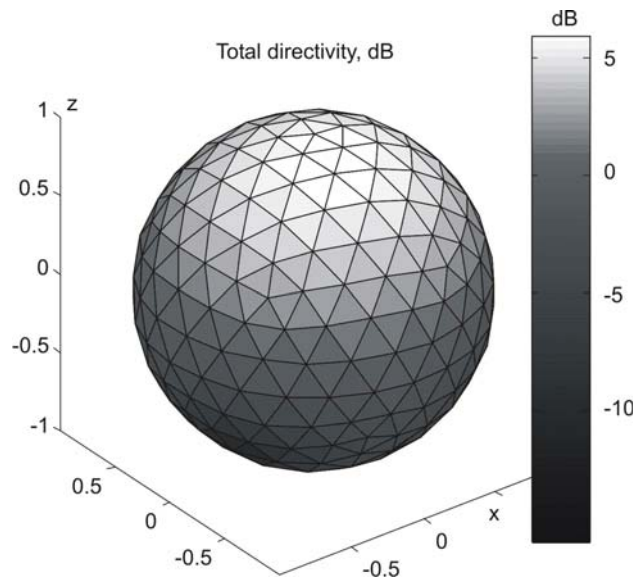
Figure 3.2-11. Total directivity of the slot antenna at 2.34 GHz.

f. Radiation pattern – RHCP and LHCP components

The radiation patterns are measured in [94] by mounting the antenna on a metallic pedestal and then placing it in the center of a 1m×1m ground plane. The measured results averaged over four elevation planes are shown in Fig. 3.2.12a, b, respectively. Since we are not able to reproduce these conditions exactly, only the free-space simulated radiation patterns are presented here (Fig. 3.2-12c, d).
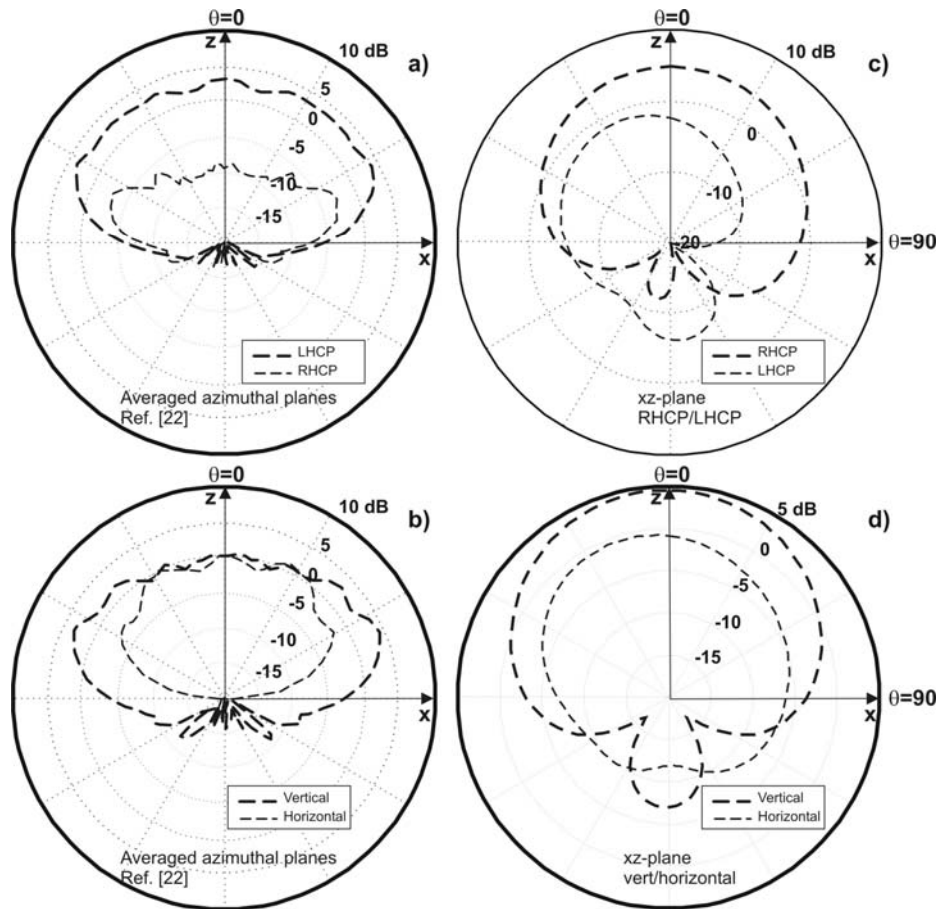
Figure 3.2-12 Absolute directivity of the LHCP/RHCP and co-/cross-polar fields vs. elevation angle for the slot antenna [94], at the resonant frequency of 2.34 GHz, in the xz-plane. a), b) – averaged over azimuthal angle experimental results [94] with a pedestal and a large ground plane; c), d) present solution for a free-space radiation – for circular (c) and linear (d) polarization, respectively. (Ref. [78] © 2006 IEEE)

Once the spherical components E_θ, E_ϕ of the electric field in the script `radpattern.m` are known the right-handed circular polarization component (RHCP) and the left-handed

circular polarization component (LHCP) of the electric field can be obtained using equation 3.1.10- 3.1.12. Both polarizations are plotted in Fig. 3.2-12c at 2.34 GHz. One can see that RHCP dominates by only 7 dB at zenith. However, the polarization isolation is not very significant and a considerable back lobe is observed. This means that noise from the backside of the antenna will be present in the spectrum of the received signal. While the cross-polarization isolation of about 10 dB toward zenith reported in [94] is to a certain extent confirmed in Fig. 3.2-12c, the vertical polarization is essentially missing for the antenna without the ground plane as shown in Fig. 3.2-12d. It follows from here that the present antenna setup may not be used without a sufficiently large ground plane.

g. Near fields

Fig. 3.2-13 shows the bound surface charge density at two frequencies: 2.30 GHz (lower band frequency) and 2.39 GHz (upper band frequency). The field inspection within the antenna indicates the typical TM "dipole" mode at 2.30 GHz (lower frequency band) in the slotted cavity volume, but a less common quadrupole mode is excited at 2.39 GHz (upper frequency band). Both these modes were observed in Ref. [94] using HFSS.
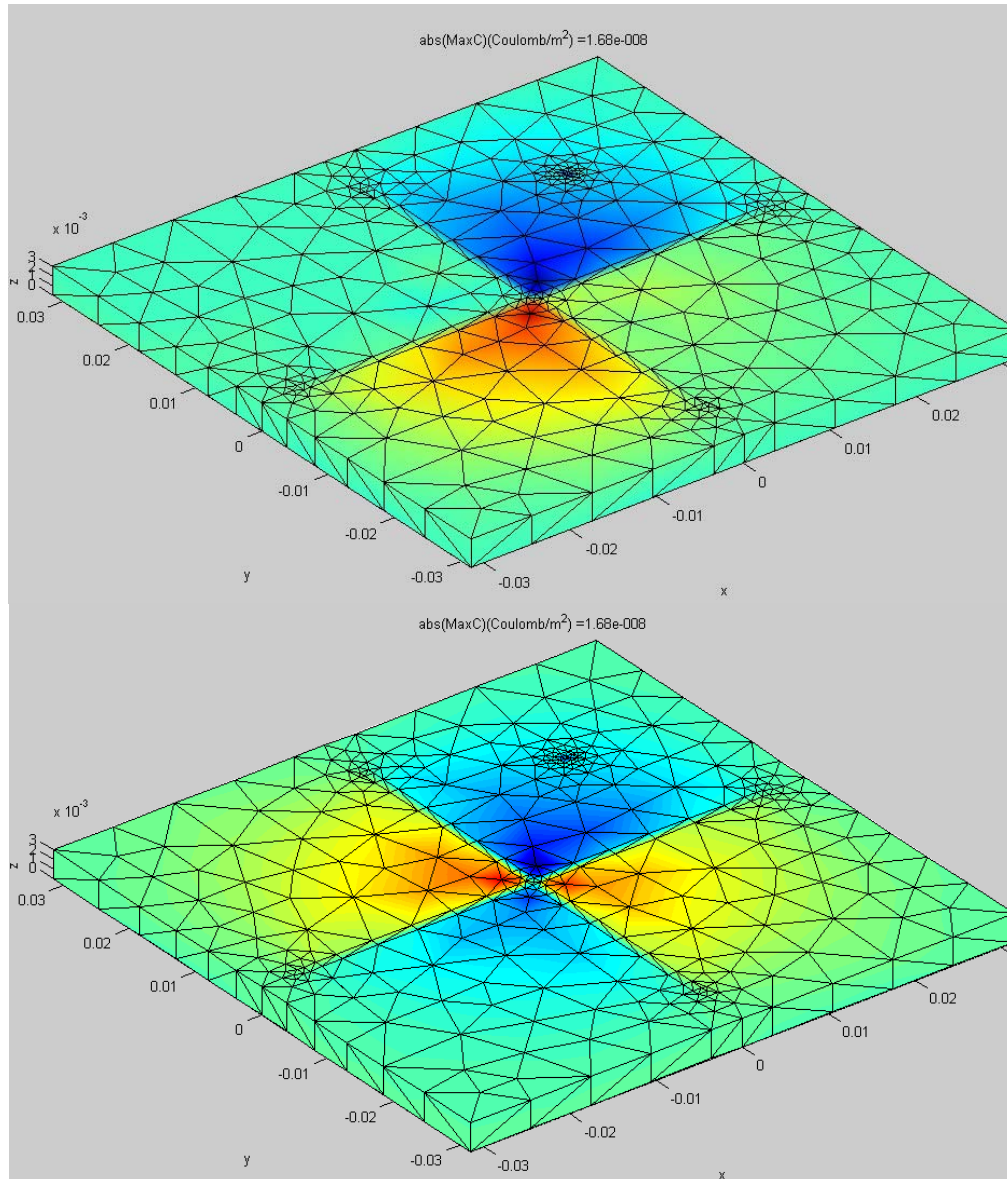
Figure 3.2-13. Fields within the slot antenna. Top – surface bound charge distribution at 2.30 GHz; bottom – the same distribution at 2.39 GHz. Redder hues correspond to positive charge, bluer hues to negative charge.

3.3 Quarter-Wavelength Antenna

3.3.1 <u>Metal monopole at 400 MHz</u>

The monopole antenna (cf. [86]) is the simplest quarter-wavelength single-band omnidirectional antenna with a relatively large bandwidth – up to 10% or so. The

monopole is fed by a coaxial cable and does not require a balun transformer. However, the monopole performance is affected by the size of the ground plane, which ideally should be large. The dependence of the input impedance on monopole thickness is less significant. The scholarly papers on the monopole on a finite ground plane include Refs. [95, 96].

A thin monopole antenna is a numerically challenging example for a surface patch code since a fine surface mesh of the entire monopole length is necessary in order to obtain accurate results. This is in contrast to the patch antenna where finer meshing of the feeding column has little influence on the antenna behavior.

a. Geometry

This example describes a monopole antenna of height 180 mm on a small ground plane – a square metal plate with a size of 400 mm. The antenna geometry is shown in Fig. 3.3-1.
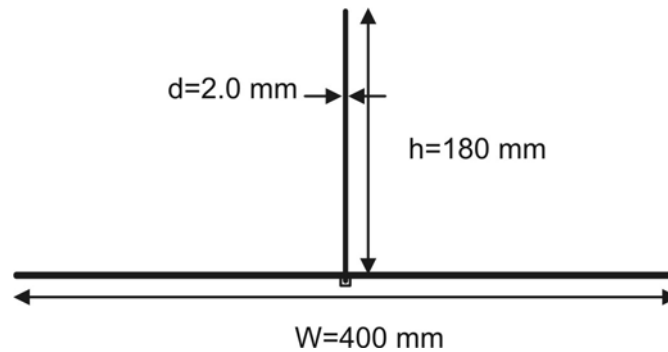
Figure 3.3-1 Monopole antenna.

The antenna has the following features:

i.   The monopole has an omnidirectional radiation pattern, vertical polarization, and a relatively large bandwidth. However, it cannot be matched to 50 Ω automatically, in contrast to the dipole, since the monopole impedance is twice as small as that of the dipole.

ii.   The monopole is a thin cylindrical column with a diameter of d=2.0 mm. One may replace it with a rectangular column of equivalent width w. This yields ([86], p. 514)
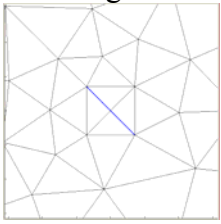
$$w = \frac{d}{1.18} < d \qquad\qquad (3.3.1)$$
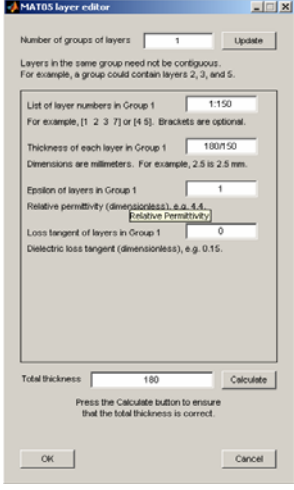
From Eq. (3.3.1) one can find that $w \approx 1.7\ \text{mm}$ for the present antenna. Approximation (3.3.1) works better for lower frequencies.

iii.   Another possible approximation of the monopole in the surface code is a metal strip whose width is four times the cylinder radius – see [86], p. 514. We will use this approximation since it requires a smaller number of unknowns. In either case, a fine surface mesh along the monopole is necessary. This is a disadvantage of the surface patch code compared to the wire code.

iv.   The ground plane is modeled as a metal sheet of infinitesimal thickness.

v.   The feed is modeled as a voltage delta-gap for every mesh edge between the monopole and the ground plane. The number of such edges can be arbitrary, depending on the cross-section shape of the monopole column.

vi.   The metal is an ideal conductor; metal losses are ignored.

b. Code

Table 3.3-1 Summary of operations to create and model a monopole antenna.

Operation	Commands
Mesh generation 1_mesh Selecting via/feed Layer editor	1. Run `struct2d.m` and press the View mesh button to see the planar mesh. Zoom in the feed area of the planar mesh to inspect the mesh structure close to the feed. Press the Accept mesh button to save the 2D mesh. 2. Run `struct3d.m` and fill the layer editor as shown. The large number of layers is chosen to make a fine mesh along the monopole length. Then: - Press OK on the first (layer) GUI - Remove all tetrahedra from the mesh (Select all + DONE) - Select all metal faces of the ground plane (Select all +

	DONE) - When selecting via metal patches zoom in the feed area first. The feed edges are the two bottom edges of the metal strip. Select these two edges, one by one, by drawing a small polygon around each edge and using the Close Polygon button. Press DONE. - Repeat the procedure above for selecting the feed edges - When selecting top metal patches press DONE. Press OK on the Remove screen. - Inspect the mesh and the feeding triangles visually. They should have a color different from that of the other metal triangles. Also, plus and minus feeding triangles have distinct colors.
BF generation 2_basis	Run `wrapper.m` and inspect the resulting number of unknowns (metal edges).
MoM solution 3_mom	1. Open `impedance.m`. Select the frequency range and the number of discrete points. Run `impedance.m`. 2. Run `comp_s.m` to inspect the return loss and impedance bandwidth. 3. Run `radpattern.m` to obtain the patterns (cross-/co-pol) in the E-plane (elevation plane). 4. Run `nearfield.m` to inspect the charge/current distribution of the antenna.

c. Mesh

Fig. 3.3-2 shows the monopole antenna mesh obtained after the mesh generation operation. There is a difference in the feed assembly between the MoM voltage gap and the corresponding HFSS project shown in Fig. 3.3-2c. The lumped port in Ansoft HFSS is defined on a finite-width circular ring face between the monopole and the rest of the ground plane. When the outer radius of this face tends to its inner radius, both definitions of the lumped port should coincide with each other.
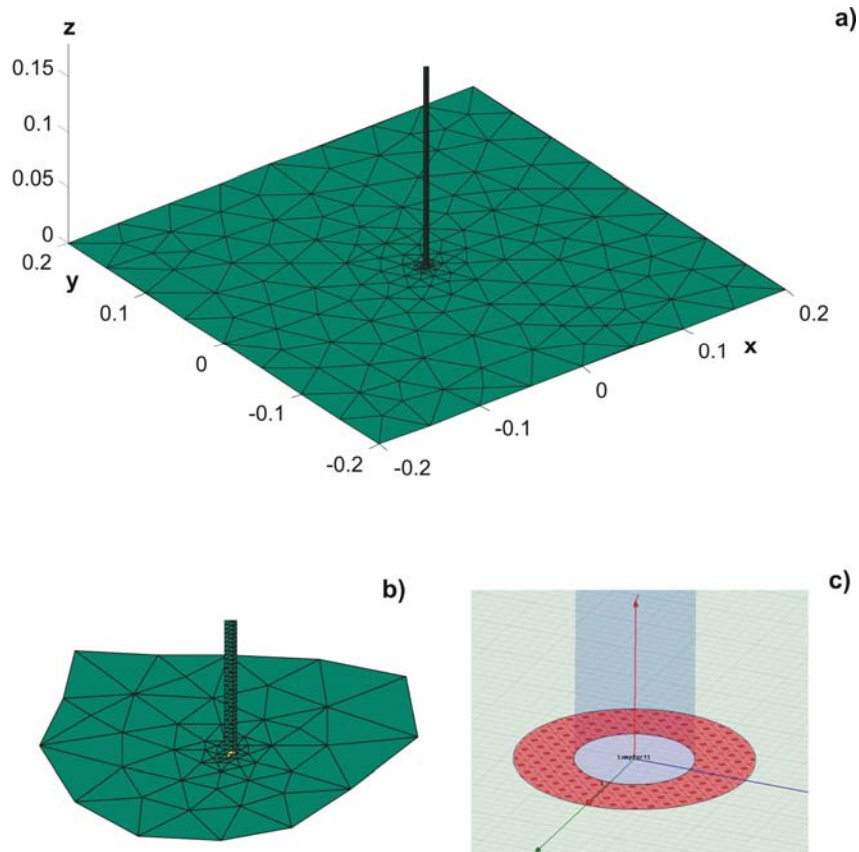
Figure 3.3-2. a) – Metal mesh created by struct3d.m; b) – voltage gap feed implemented in MATLAB for bottom feeding edges; c) – HFSS lumped port with the port face (a ring) between the ground plane (a hole was cut in the ground plane) and the monopole. The voltage is given along a feed line in this face.

d. Input impedance

The present antenna mesh has 1229 metal unknowns and needs about 1 second per frequency step on a PIV 3.6 GHz. The resonant frequency by inspection is close to 400 MHz. Fig. 3.3-3 shows the output of the scripts `comp_z.m` and `comp_s.m` for the impedance and return loss. These scripts compare the MoM solution with the Ansoft HFSS solution. Whilst there is a good agreement at low frequencies, the impedance curves show a significant error for the higher frequencies, when the monopole length is the half wavelength in free space. Generally, the surface patch code is not very appropriate for the modeling of thin-wire antennas.

129
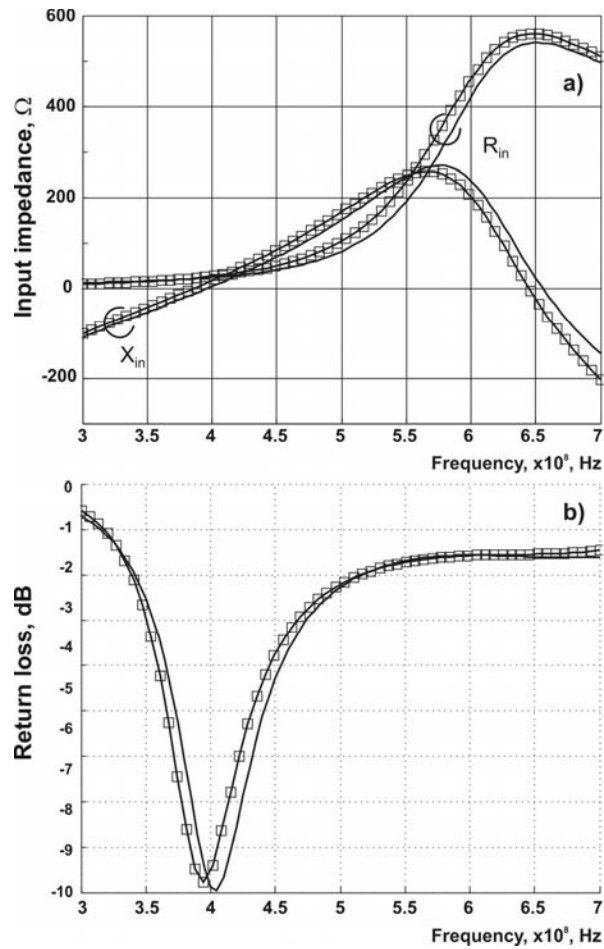
Figure 3.3-3. Return loss for the monopole antenna shown in Fig. 3.3-1. Squared curves – MoM solution. Solid curves – Ansoft HFSS solutions.

e. Radiation pattern – total directivity/gain

The directivity plot over the sphere surface (script `radpattern.m`) for the present antenna is shown at the resonance in Fig. 3.3-4. One can see that the monopole pattern becomes directional due to the ground plane; however, this effect is small.
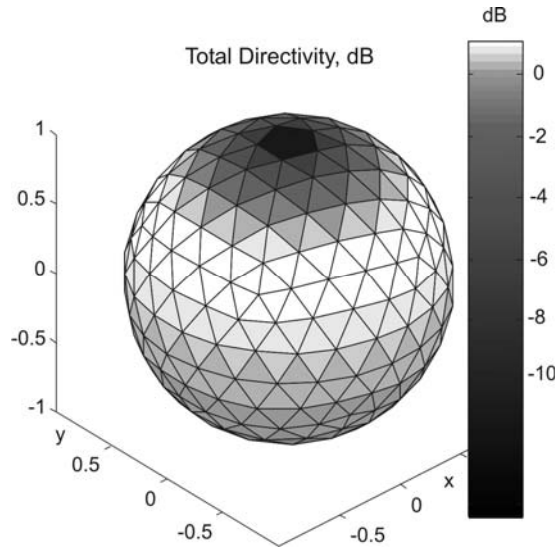
Figure 3.3-4. Total directivity for the monopole antenna in Fig. 3.3-1 at the resonance. The maximum directivity (maximum gain in this lossless case) is approximately 1.15 dB.

f. Radiation pattern – co-polar and cross-polar components

The script `radpattern.m` outputs two radiation patterns for the present antenna, in the E-plane (the yz-plane in our case). In this plane, the co-polar directivity clearly dominates. The output of this script is shown in Fig. 3.3-5.
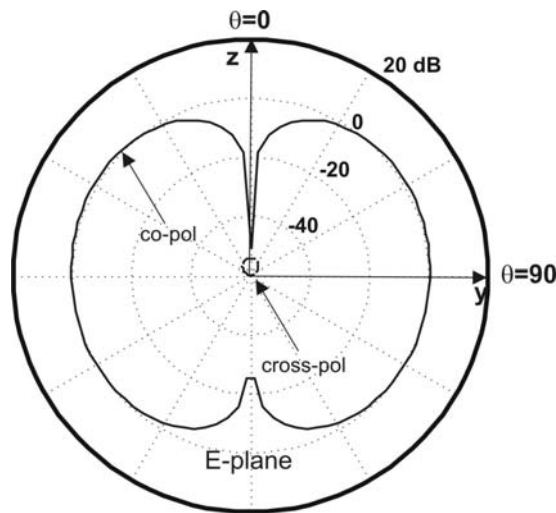
Figure 3.3-5 Directivity of the co-polar and cross-polar fields vs. elevation angle for the monopole antenna at the resonant frequency, in the E-plane.

Fig. 3.3.6 shows the typical current distribution for the monopole antenna
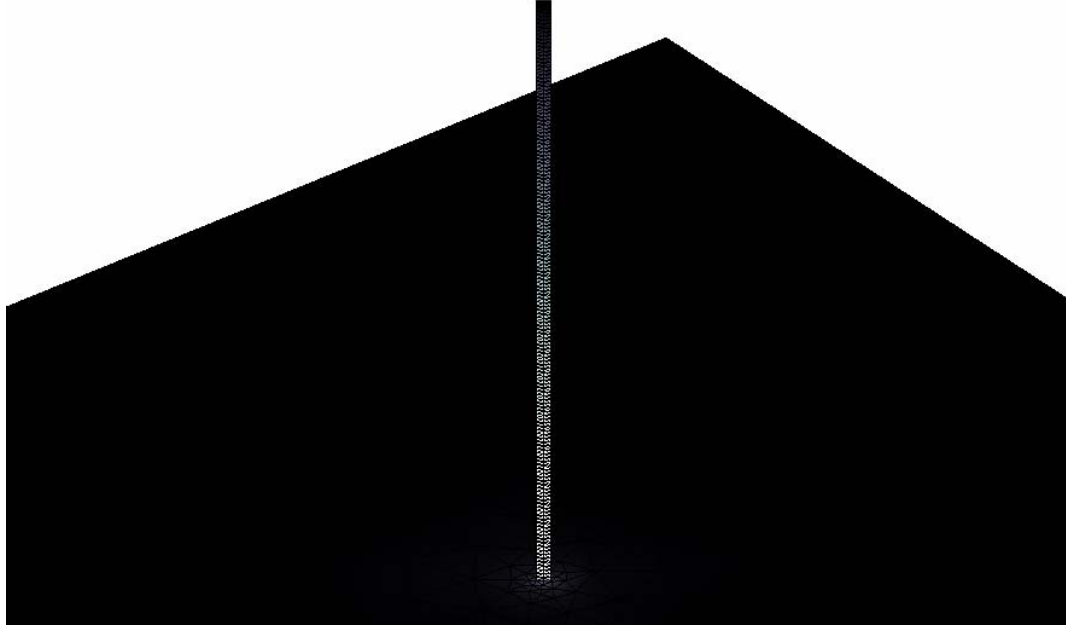
Figure 3.3-6. Typical current distribution along the lower half of the monopole antenna at the resonant frequency. Lighter colors correspond to larger current magnitudes.

3.3.2 Loaded monopole

Loading of electrically small monopole antennas to improve their impedance characteristics (provide impedance matching at a smaller size, that is, height) has been employed for many decades. Such techniques may include end-disks or top hats [97], dielectric coatings [98], or both techniques combined [99, 100]. The antenna size can be reduced significantly, but at the expense of decreasing the impedance bandwidth. In this section we consider a top hat dielectric-loaded monopole.

a. Geometry

This example is adopted from Ref. [100] and describes a top-hat dielectric-loaded monopole with $\varepsilon_r = 10.0$. The antenna geometry is shown in Fig. 3.3-7. Here, $\varepsilon_r = 10.0$ for dielectric #1. Dielectric #2 is air.
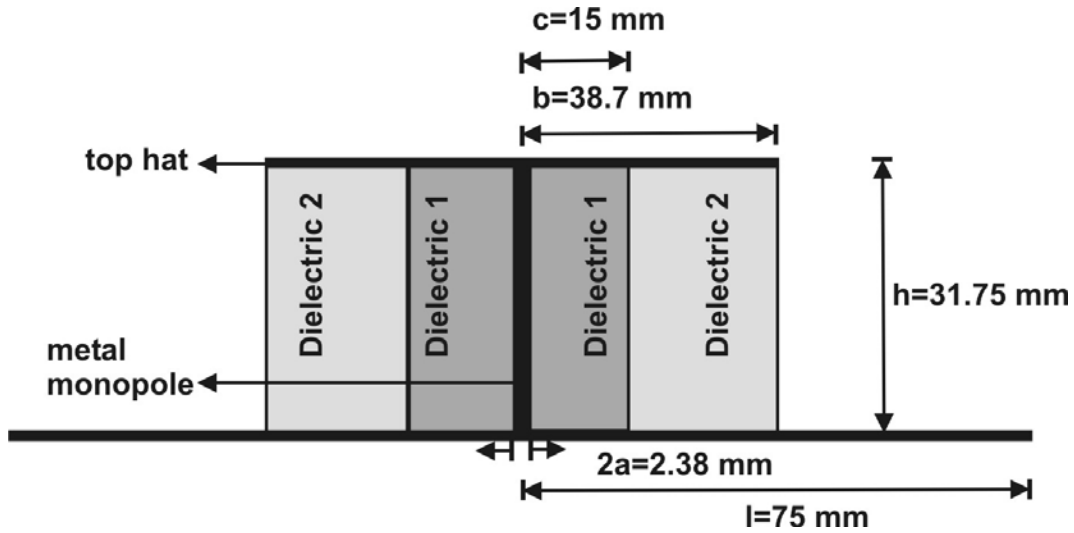
Figure 3.3-7 Top hat dielectric-loaded monopole [100]. (Ref. [78] © 2006 IEEE)

The antenna has the following features:

i. Both the top hat and the dielectric reduce the physical size of the monopole antenna (decrease its resonant frequency) but at the expense of reducing the bandwidth. The dielectric loading plays a major role in reducing the bandwidth.

ii. Although the dielectric loading is relatively thick, no dielectric resonant (DR) modes are excited yet.

b. Code

The creation of this structure is essentially identical to the monopole antenna considered in Section 3.3.1, including the antenna feed. The dielectric tetrahedra must be removed from the feed column and the entire antenna volume except for the coating cylinder.

Fig. 3.3-8 shows the dielectric mesh obtained after running the script struct3d.m. The circular feed column is replaced by a rectangular column according to Eq. 3.3.1.
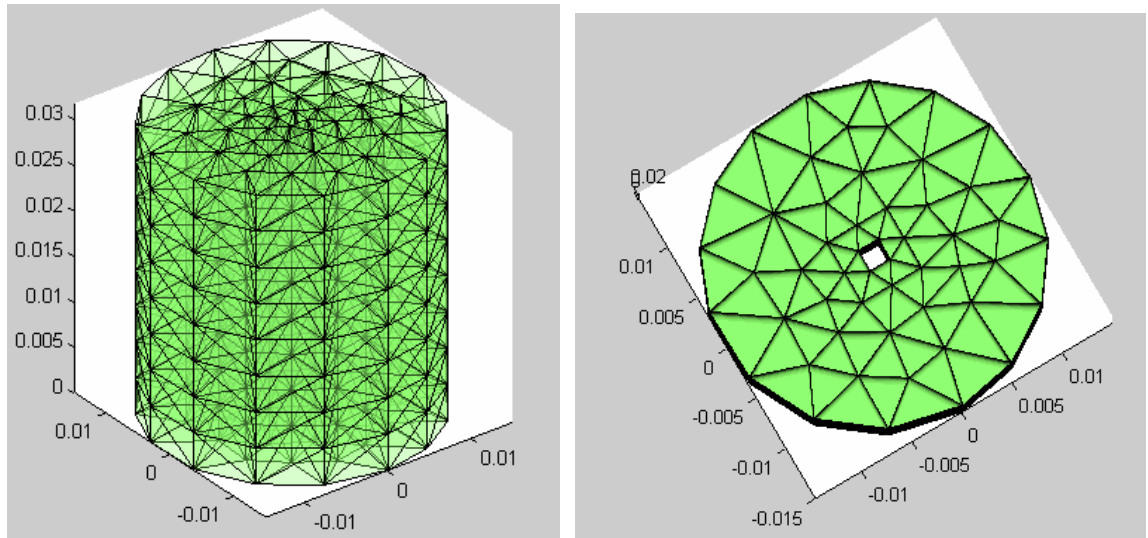
Figure 3.3-8. Tetrahedral mesh obtained after running the script struct3d.m.

c. Mesh

Fig. 3.3-9 shows the complete antenna mesh obtained after the mesh generation operation. Running the script `feed.m` should give eight feeding edges – two for each side of the metal column.
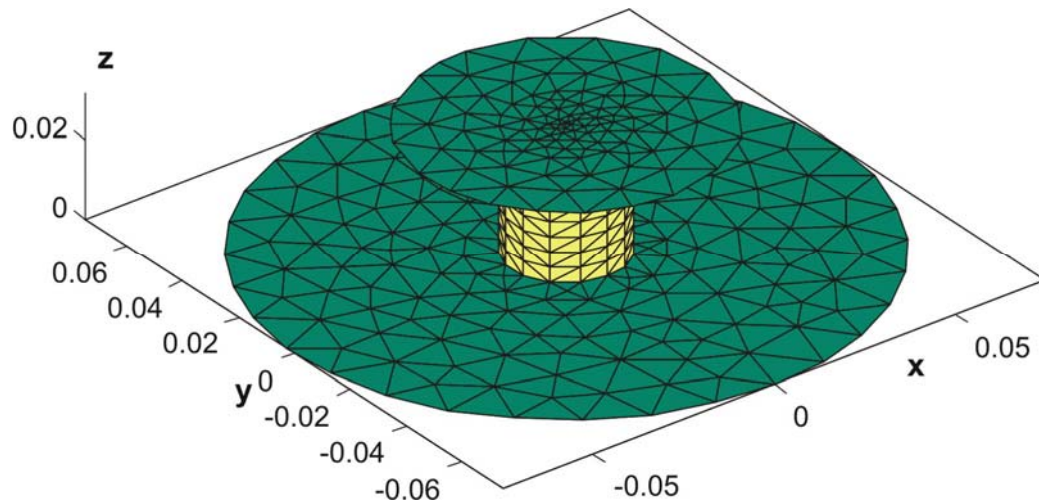
Figure 3.3-9. a) – Metal-dielectric mesh for the loaded monopole created by struct3d.m. The lighter color corresponds to dielectric faces.

d. Input impedance

The present antenna has a mesh with 3296 unknowns (986 metal unknowns and 2310 dielectric unknowns) and needs about 15.3 seconds per frequency step on a PIV 3.6 GHz. The total time for 50 frequency steps is thus 15 minutes. Fig. 3.3-10 shows the output of the script `impedance.m` compared to the equivalent Ansoft HFSS solution (a circular column feed with r=1.19 mm is used) obtained using a mesh with 39,000 tetrahedra, a PML enclosure, and an interpolating frequency sweep. This result is obtained by running the script `comp_z.m`. The Ansoft solution shown in Fig. 3.3-10 requires about 40 minutes of CPU time on the same machine.

Figure 3.3-10. Input impedance curves for the loaded monopole antenna shown in Fig. 4.8. Squared curves – MoM solution for the resistance/reactance; solid curves – Ansoft HFSS solution. (Ref. [78] © 2006 IEEE)

The resonant frequency is close to 760 MHz in Fig. 3.3-10. Note that both the MoM solution and the Ansoft HFSS solution could be run at a smaller number of unknowns. For the MoM solution, for example, one can reduce the number of layers in the dielectric column. However, a larger error in the resonant frequency will be observed in both cases. The resonant frequency reported in [100] is somewhat larger, about 800 MHz; however,

the impedance shape remains the same. The shift in the resonant frequency may be explained by the finite, relatively small ground plane used here (the solution in [100] assumes an infinite ground plane).This antenna is not matched to 50 Ω, so its impedance bandwidth is not considered here.

e. Radiation pattern – total directivity/gain

The radiation patterns of the loaded monopole are very similar to those of the unloaded monopole and are not shown here. The script `radpattern.m` gives a relative difference of 0.7% between the radiated and the feed power at 0.76 GHz.

f. Near fields

In the case of the loaded monopole, the DR modes are not developed and the inspection of the dielectric fields does not add much significance to the analysis (the fields are mostly concentrated around the feed). It is interesting to inspect the current distribution on the metal surface – see Fig. 3.3-11. In particular, one can observe a large current on the top of the monopole, thus giving rise to a significant magnetic field in that region. This large current indicates that the top hat significantly contributes to the effective length of the antenna.

Figure 3.3-11 Surface current distribution on the metal surface. Lighter colors correspond to larger current magnitudes.

3.3.3   <u>Baseline planar-inverted F-antenna (PIFA)</u>

The PIFA, originally introduced in [10, 101], is one of the most popular antenna designs for wireless communications. PIFA's inherent bandwidth is higher than the bandwidth of the conventional patch antenna (since a thick air substrate is used). Furthermore, it can be considerably enhanced.

a. Geometry

This example is adopted from Refs. [17, 101] and describes the original PIFA at 1.5 GHz. The antenna geometry is shown in Fig. 3.3-12. Here, $\varepsilon_r = 1$ (no dielectric substrate is used). The feed does not have to be on the edge and can be moved vertically toward the patch centerline [102] keeping the distance from the shorting ground plane the same.
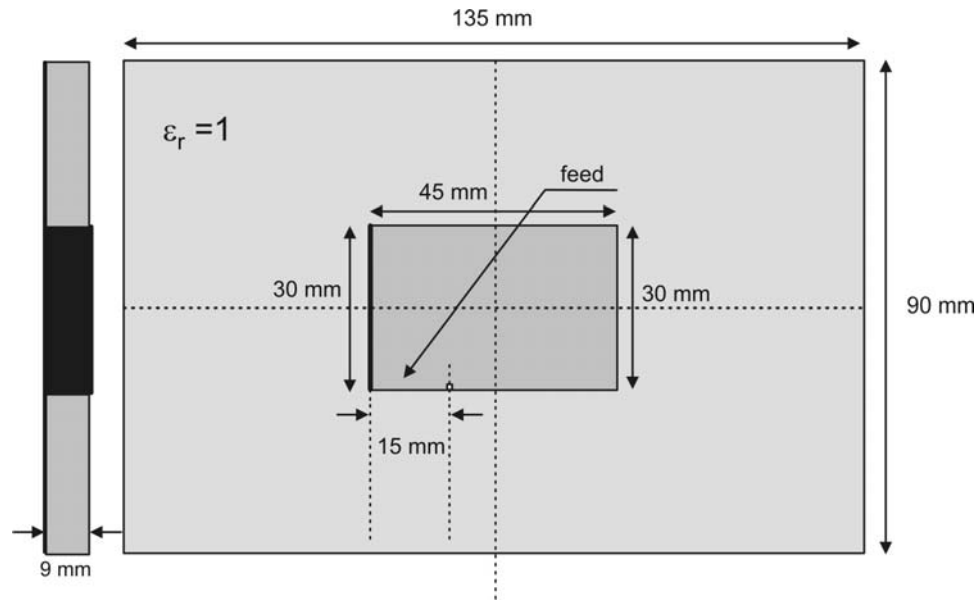
Figure 3.3-12. PIFA geometry (top and side view).

The antenna has the following features:

i.   The ground plane is finite. This is in contrast to Refs. [17, 101].

ii.   Since no exact feed diameter was reported, the rectangular feed column is chosen to be 0.5 mm in width. The width variation in the range 0.5-1.5 mm does not significantly alter the results.

b. Code

The creation of this structure is essentially a combination of the patch and the monopole antenna considered in section 3.1.1 and 3.3.1 respectively. The dielectric tetrahedra must be removed from the entire volume. The shorting ground plane should be identified at the via stage in the script `struct3d.m`. The top patch should be selected using the polygon tool. It is recommended to zoom in on the mesh and make sure that all the triangles are selected properly for the top patch.

c. Mesh

Fig. 3.3-13 shows the metal mesh obtained after running the script `struct3d.m`.
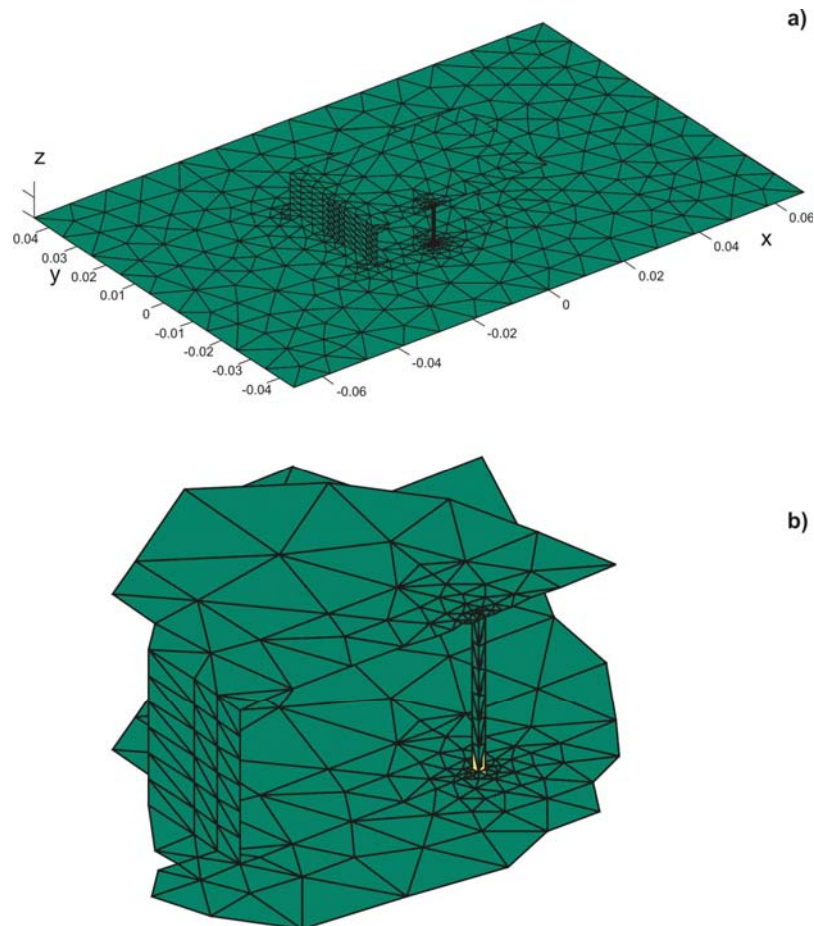
Figure 3.3-13 Complete metal mesh obtained after running the script struct3d.m. The feed triangles/edges are seen (enlarged in Fig. 3.3-13b).

d. Input impedance

The present antenna mesh has 1519 unknowns and needs about 1 second per frequency step on a PIV 3.6 GHz. The total time for 60 frequency steps is thus about 1 minute. Fig. 3.3-14a shows the output of the script `impedance.m` compared to the equivalent Ansoft HFSS solution (a rectangular column feed is used) obtained using a mesh with about 20,000 tetrahedra, a radiating enclosure, and an interpolating frequency sweep. This result is obtained by running the script `comp_z.m`. The HFSS solution shown in Fig. 3.3-14 takes about 20 minutes on the same machine. The resonant frequency is close to 1.35 GHz in Fig. 3.3-14.
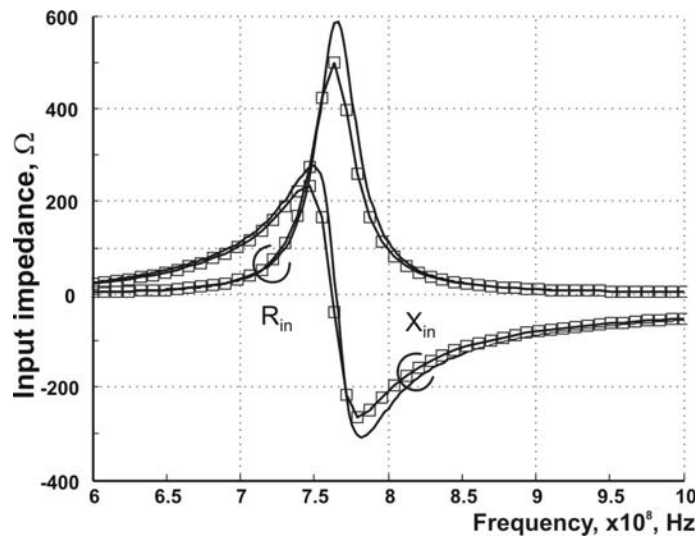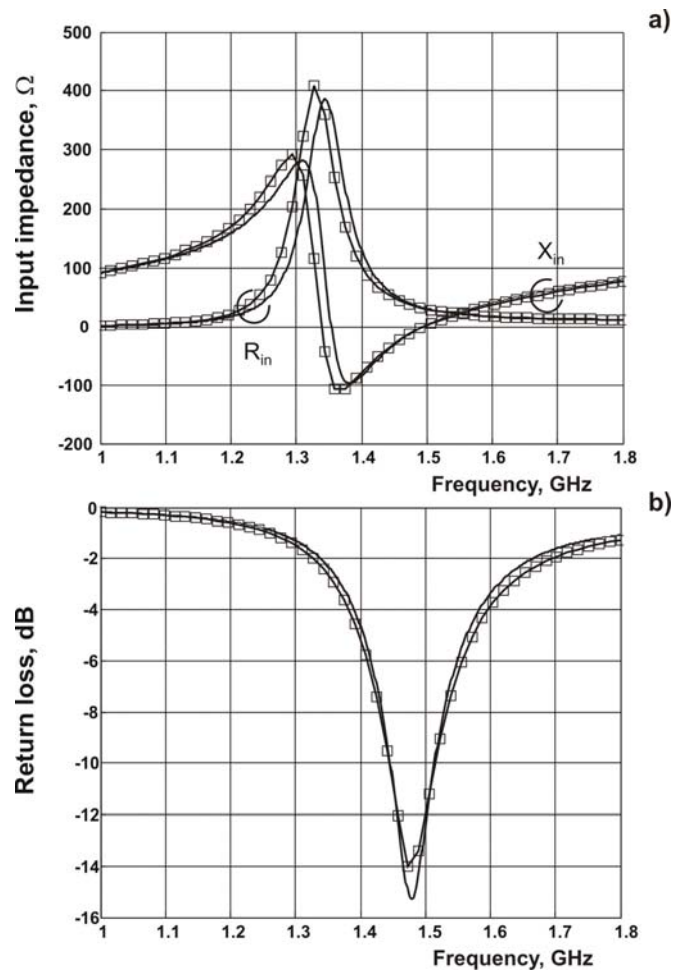

Figure 3.3-14. a) - Input impedance curves; b) – return loss curves for the PIFA antenna shown in Fig. 3.3-12. Squared curves – MoM solution for the resistance/reactance; solid curves – Ansoft HFSS solution.

The return loss is plotted in Fig.3.3-14b. This antenna is now matched to 50 Ω at 1.5 GHz, which is a rather significant difference from the physical resonance. Also note that Fig. 3.3-14b is in very close agreement with the corresponding FDTD simulation results for the PIFA given in Ref. [17], pp. 202-203.

Both the MoM solution and the Ansoft HFSS solution could be run at a smaller number of unknowns. For the MoM solution, for example, one can reduce the mesh quality. For the Ansoft solution, one can use 3 to 5 passes. However, a larger error in the return loss behavior – impedance bandwidth – will be observed in both cases.

e. Radiation pattern – total directivity/gain

The directivity plot over the sphere surface (script `radpattern.m`) for the present antenna is shown at 1.5 GHz (center of the impedance bandwidth) in Fig. 3.3-15. One can see that the symmetric radiation pattern is slightly distorted. The script also gives a relative difference of 0.56% between the radiated and the feed power in the present case.
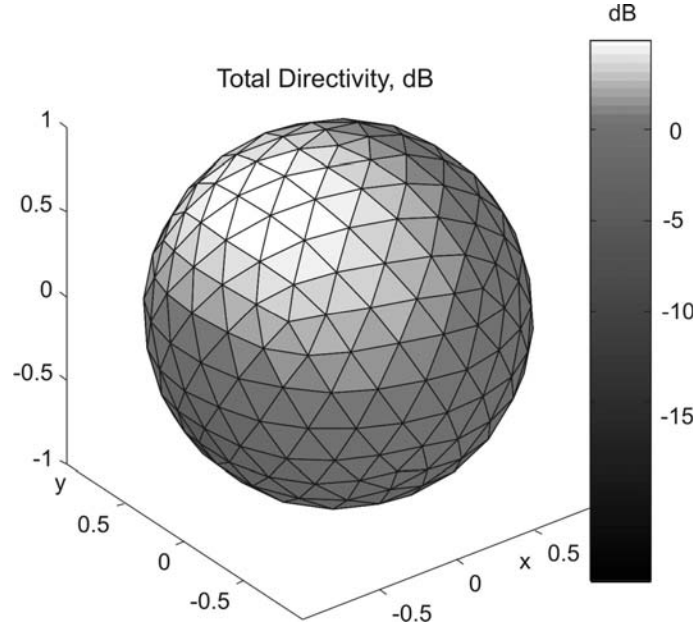
Figure 3.3-15. Total directivity for the PIFA antenna at 1.5 GHz. The maximum directivity (maximum gain in this lossless case) is approximately 5 dB.

f. Radiation pattern – co-polar and cross-polar components

The co-polar and cross-polar directivity components are found in a manner similar to the approach described in Section 3.1.2. However, we are interested in the E-plane radiation patterns (the xz-plane) for the present configuration. The script `radpattern.m` outputs two radiation patterns (co-pol and cross-pol components) for the present antenna, in the E-plane (the xz-plane in our case). In this plane, the co-polar directivity dominates. The script `comp_r.m` (which should be run after `radpattern.m`) compares these radiation patterns with the corresponding Ansoft HFSS radiation patterns. The output of this script is shown in Fig. 3.3-16. One can see a reasonably good agreement. The front-to-back ratio for the present patch antenna is small, and the antenna is rather "omnidirectional" in every plane.
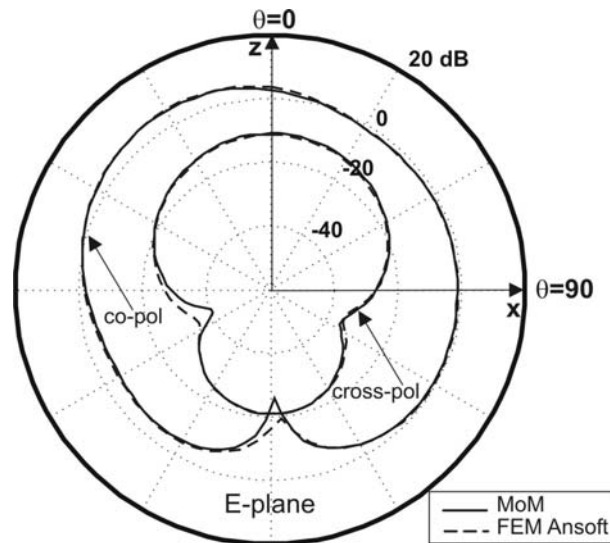
Figure 3.3-16 Directivity of the co-polar and cross-polar fields vs. elevation angle for the PIFA at 1.5 GHz in the E-plane.

g. Near fields

It is desired to inspect the near field distributions in the antenna volume or on the antenna surface. The script `nearfield.m` finds and displays such distributions at a given frequency. In the case of the PIFA the TM mode is not as prominent as for the half-wave

patch. It is interesting to inspect the current distribution on the metal surface – Fig. 3.3.17. In particular, a large current returns from the top patch through the shorting ground plane. A large current is also observed on the side of the shorting plane that is opposite to the feed.
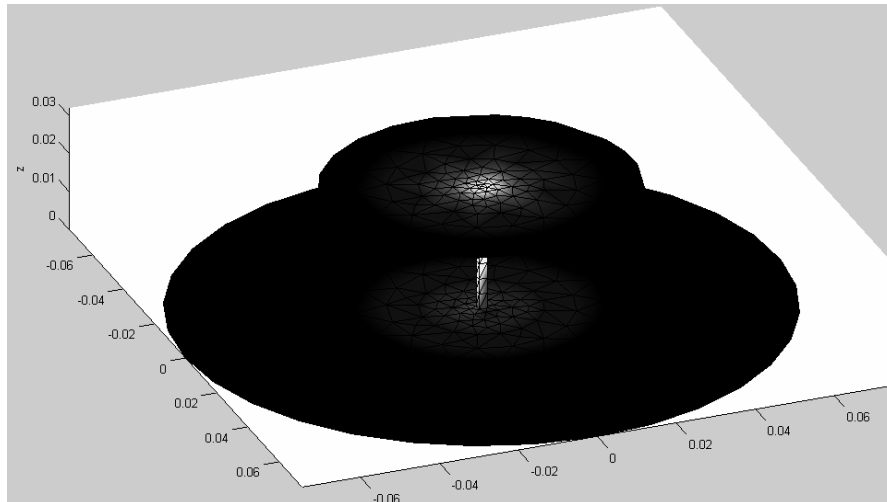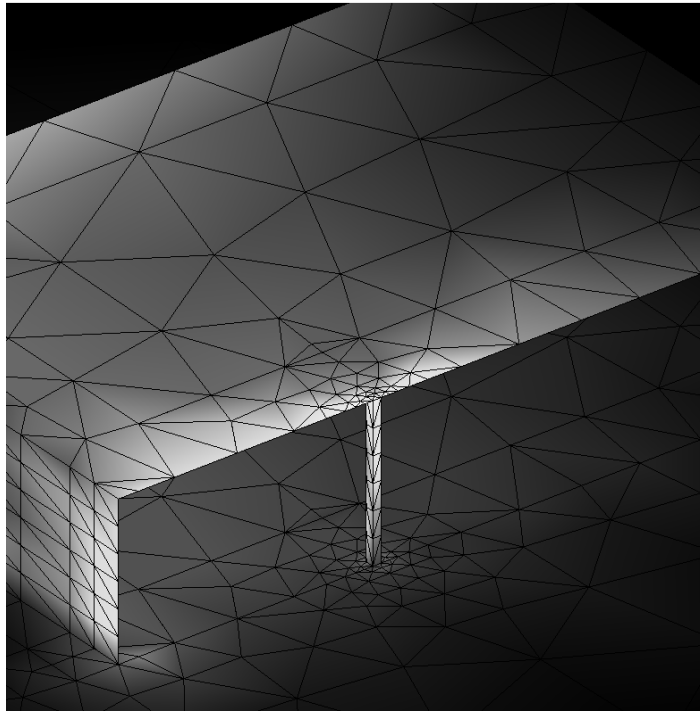

Figure 3.3-17 Surface current distribution on the metal surface at 1.35 GHz. Lighter colors correspond to larger current magnitudes.

4 Linearly polarized PIFA design in UHF band

This chapter describes a compact transmitting antenna designed for the Precision Personnel Locator (PPL) system at Worcester Polytechnic Institute for indoor positioning. The system required a linearly-polarized low-cost UHF antenna with the center frequency at 440 MHz and with the bandwidth of about 14%. The antenna had to be relatively small in size, with no additional matching network (low loss), almost omnidirectional radiation pattern, and be conformal (wearable).

The chapter is organized as follows. Section 4.1 gives a literature review for the antenna configurations which can satisfy the design objectives. Section 4.2 describes the antenna design challenges and the final reduced-size PIFA design. Section 4.3 describes the antenna fabrication procedure. Section 4.4 gives the simulation and measurement results. The effect of antenna close to the human body is discussed in section 4.5 while section 4.6 describes the calculation of the antenna-to-antenna transfer function.

4.1 Introduction

The design specifications limited the anticipated antenna type to patches (conformal TM resonators) and loops. Whilst the UHF loop antennas [103] are small and have an acceptable performance close to the human body [104], they are narrowband and generally lossy due to the necessity of an impedance matching network. A UHF array of cavity-backed annular microstrip half-wave patches with dual polarization has been considered in Ref. [105]. The single antenna element has a large bandwidth (46%); its center frequency is 350 MHz. The single element size is 43.2cm×43.2 cm, which scales to 34.4×34.4 cm at 440 MHz. This dimension is still too big for our purposes. Similarly, the cavity-backed CP antenna developed in Ref. [106] has the size of 15×15×6 cm at the center frequency of about 500 MHz and is not very appropriate due to the large vertical dimension. The DR-based UHF antenna developed in Ref. [107] has an exceptional

performance but requires a complicated layered magnetodielectric substrate material and a large metal ground plane. A printed fractal UHF antenna discussed in [108] has a small size; its bandwidth, however, remains unknown.

The quarter wave patch antenna or PIFA appeared to be a natural candidate for our task since it has the approximate size of $0.25\,\lambda_0$ (cf. [109, 110]). PIFA is a quarter-wavelength open-short microstrip resonator with a dominant quasi-TEM mode. The probe feed is located close enough to the shorting stub to achieve proper impedance matching. Instead of the probe feed, a slot feed or another kind of capacitive/inductive coupling can be used. Typical impedance bandwidth of a conventional PIFA is about 4% for a small ground plane and reaches 8% when the length of the ground plane is on the order of a wavelength [111]. The larger ground plane is rather a positive factor for the present work since the allocated space can be used for housing the anticipated transmitter hardware. Furthermore, the size of the PIFA can be further reduced by using various techniques discussed below without reducing the operating bandwidth. This is a very inviting property for developing a compact portable UHF antenna system.

The PIFA antenna proposed [112, 113] and evaluated in this section satisfies the design requirements, performs satisfactorily over a considerably wider than expected frequency range (~18% 10 dB return loss impedance bandwidth), and seems to be appropriate for the use in a short-range UHF indoor geolocation link.

4.2 Antenna Design

The miniaturization of the PIFA can be achieved using several approaches established previously for L- and S-bands:

  i.   employing a dielectric material of higher permittivity [114];

 ii.   capacitive loading of the patch structure [115];

iii.   capacitive (proximity coupled) feed [115];

 iv.   using slots on the patch to increase the electrical length of the antenna [110];

v.   tapering the patch [116].

The high dielectric constant of the substrate is not very appropriate for our purpose. Therefore, the method based on capacitive loading [115] and tapering the patch [116], and the method that involves slots for longer current path [110] along the patch edges have been chosen for bandwidth improvement.
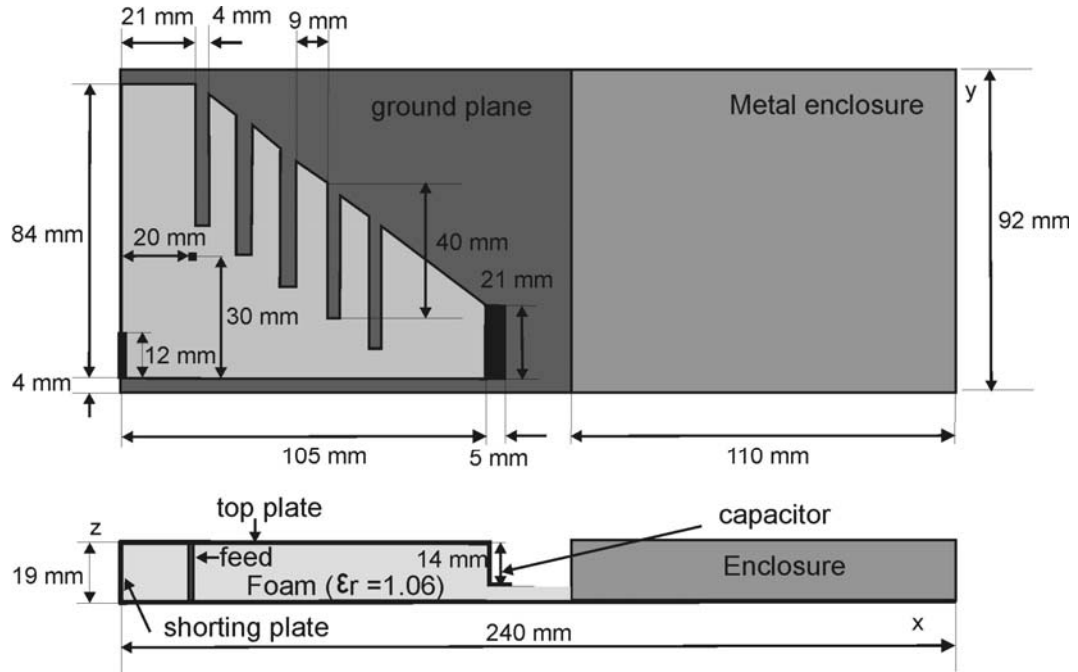
Figure 4.2-1Optimized PIFA dimensions for 440 MHz. (Ref [112] © 2006 IEEE/APS).

The proposed tapered-type PIFA shown in Fig 4.2-1 was designed and simulated at 440 MHz using the appropriately scaled antenna prototype from Ref. [116] as a starting point. It consists of a linearly tapered top plate (radiating patch), ground plane, feeding wire (probe feed), and a shorting plate. The height of the top plate above the ground plane is fixed ($\approx 0.04\lambda_0$).Further, the capacitive loading and the slots were added as suggested in [115] and [110], respectively. The capacitive load was formed by folding the open end of the PIFA toward the ground plane and adding a plate (parallel to the ground plane) to produce a parallel-plate capacitor. The length of the slots, the number of slots, the vertical

length of the capacitor plate, the location of the shorting plate and the feeding point have been carefully optimized in order to achieve the best performance.

The antenna design and optimization were done using Ansoft HFSS v10 and the MoM solver. The HFSS solution had tetrahedral meshes that typically include 20,000-30,000 tetrahedra per structure. The parametric sweeps were organized separately over eight independent antenna geometry parameters. The results for every sweep were then analyzed and the best parameter fit was identified. Then, the parameter value was updated. This procedure was repeated a few times to assure the multivariable search.
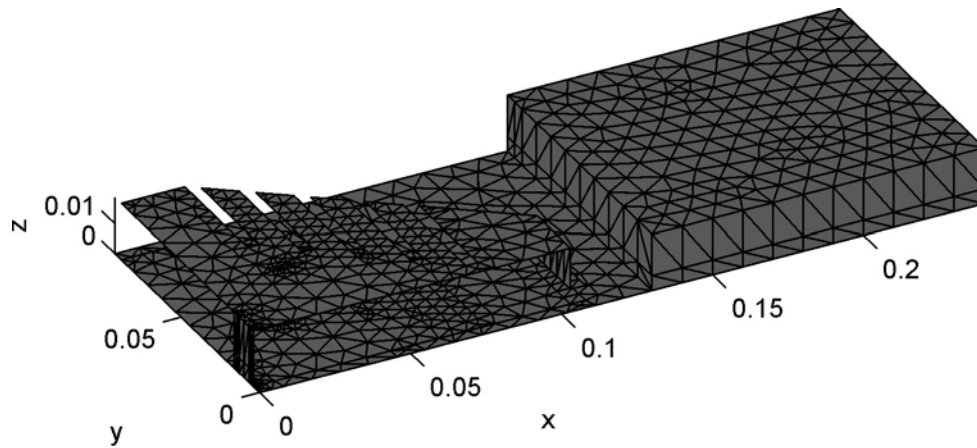
Figure 4.2-2 PIFA mesh using the MoM solver

Fig.4.2-2 shows the mesh developed using the MoM solver. The structure includes 3466 RWG basis functions and requires a solution time of about 11 seconds per frequency step on a PIV 3.6 GHz processor with 3GB of RAM.

4.3 Antenna fabrication

In order to investigate the effect of manufacturing uncertainty two identical antenna prototypes were built and tested. Fig. 4.3-1 shows a foam-based prototype optimized at 440 MHz. The patch, ground plane, and the shorting plate are made of copper foil and are supported by high-density polystyrene foam (3 pcf) from Dow Chemical Company. The

dielectric constant of the foam was measured using the suspended ring resonator method and was approximately equal to 1.06. The foam loss tangent was not measured (expected to be about 0.002 for the present foam type). The foam is cut using the HCM-2S hotwire foam cutter of Manix. A phantom for the anticipated metal enclosure is seen on the left. The size of the phantom can be varied from 85 to 110 mm. One division on the grid corresponds to 5 mm. The antenna was fed through a 50 Ω SMA connector attached to the ground plane (not seen in Fig. 4.3-1) by a nut/washer. A thin long screw was soldered to the SMA connector prior to assembly.
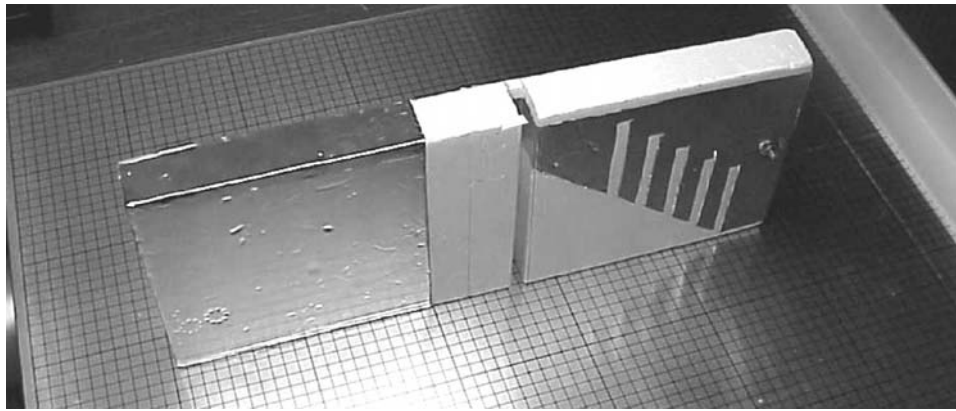
Figure 4.3-1 Antenna prototype (Ref [112] © 2006 IEEE/APS)

The antenna feed was then attached in a solderless way, using screw fastening with the second nut/washer seen in Fig. 4.3-1 and two small aluminum fastening plates attached directly to the foam from both top and bottom. This method demonstrated a good electrical contact and mechanical stability.

4.4 Simulation and Measured Results

Fig. 4.4-1a gives simulated and measured (HP 85047A Network Analyzer) return loss for the two PIFA prototypes. The antenna bandwidth is almost identical in both cases - about 80 MHz (414 MHz – 494 MHz). However, both antennas are slightly shifted in center frequency vs. simulations toward the left. We believe that this shift is due to dielectric

147

constant of the foam that has been set to one for the numerical optimization. The maximum simulated return loss is -20 dB at 442 MHz and the impedance at this resonant frequency is 43.37 –j6.34. Fig. 4.4-1b shows two simulated radiation patterns (total directivity in free space) for the PIFA in two elevation planes. The antenna radiation is thus almost omnidirectional with the maximum directivity of about 2.9 dB at zenith; the polarization isolation in the upper half-space is above 10 dB.
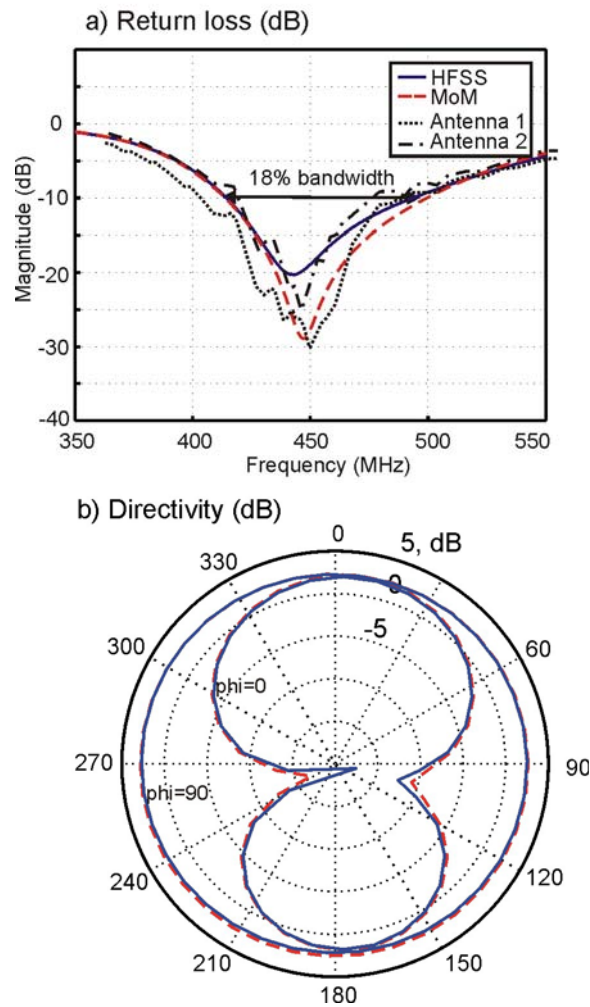
Figure 4.4-1 Optimized PIFA performance at 440 MHz –a) Return loss; simulated using HFSS (solid line), MoM solver (dashed line) and measured (dotted and dash-dotted lines); and –b) two simulated elevation radiation patterns; HFSS (solid line), MoM solver (dashed line) (Ref [112] © 2006 IEEE/APS)

A second resonance inherently exists for the present PIFA at around 1 GHz (approximately twice the fundamental resonant frequency). This resonance is associated with the vertical patch length. Fig. 4.4-2b shows the return loss for the dual-band antenna operating at 915 MHz. The tuning at 915 MHz is achieved by introducing additional (horizontal) slots shown in Fig. 4.4-2a. Whilst the second resonance can be always tuned properly toward 915 MHz (Fig. 4.4-2b), its depth and bandwidth need to be optimized further.
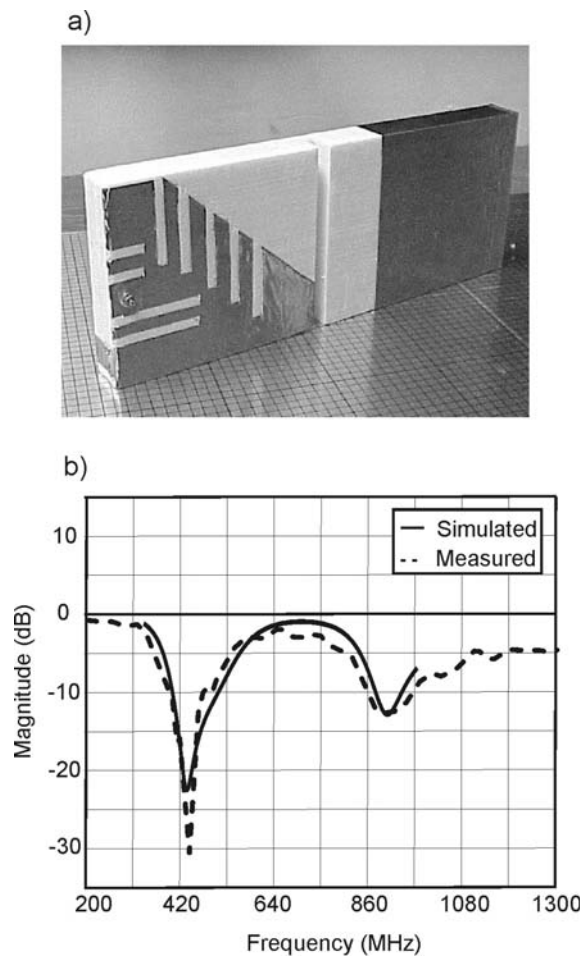
Figure 4.4-2 a) Dual band PIFA prototype operating at 440MHz and 915MHz; –b) Simulated (solid line) and measured (dashed line) return loss for the dual band operation. (Ref [112] © 2006 IEEE/APS)

4.5 Simulations close to the human body

To use the antenna as a wearable element its performance close to the human body needs to be determined. Depending on the operating frequency, the proximity to the human body can lead to high losses caused by bulk power absorption, radiation pattern fragmentation, and antenna detuning [104]. Biological tissue is, for most practical purposes, non-magnetic with permeability μ (H/m) close to that of free space. The electromagnetic characteristics of tissues are described by the relative permittivity ε_r and effective conductivity σ (S/m) at the frequency of interest. Hence, the human body interacts with an electromagnetic wave as an inhomogeneous, lossy dielectric structure. Over the UHF frequency range 300-1000 MHz, biological tissues have a typical effective conductivity of $\sigma = 1.5$S/m and a relative permittivity of $\varepsilon_r = 75$ [104].

Initial simulations of PIFA performance close to the body have been carried out using Ansoft HFSS v10. The body was approximately modeled as a large dielectric structure with material properties as described above. Fig 4.5-1a shows the simulated return loss plot for the PIFA in proximity to the human body. As expected the present antenna gets slightly detuned and now gives the maximum return loss of -13 dB.

The radiation pattern (Fig. 4.5-1b) would be ideal for placing the antenna on the sleeve. This circumstance has a further advantage of reducing the radiation to the head [117]. The ground plane also reduces the back radiation to other parts of the human body.
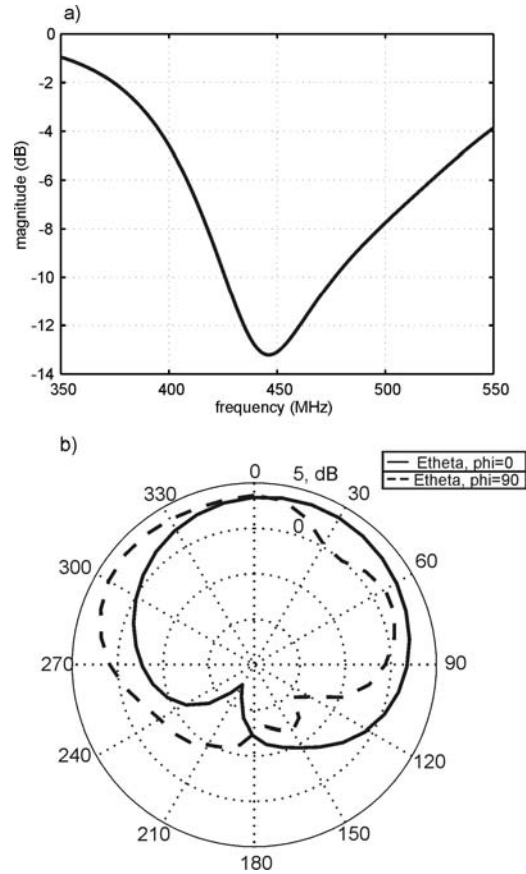
Figure 4.5-1 Performance of the PIFA close to the human body (wearable application) – a) Simulated return loss; and –b) two simulated elevation radiation patterns.

4.6 Antenna-to-antenna transfer function

One of the antenna requirements for the geolocation link is to have controllable phase characteristic over the band. This can be studied by obtaining the antenna system transfer function. Though it is more common to consider a transfer function for a single antenna rather than for a complete two-antenna system [118-121], however, for the present task we are directly interested in the antenna-to-antenna system transfer function. For the two-antenna system, this transfer function is essentially a tool to estimate to what extent the wideband spectrum of the transmitted signal is modified or distorted by both the transmitting and the receiving antenna, and by their relative orientation.

The antenna transfer function is defined from the known S-parameters, which may either be calculated or measured with a vector network analyzer [122-123]. Below, we present a calculation that is based on the direct modeling and evaluation of the S-matrix for two antennas separated by 4.5λ.

Consider a link shown in Fig. 4.6-1a. The transmitting antenna is connected to an ideal voltage source $V_{in} = 1V$. The receiving antenna is terminated in a matched load (50 Ω).
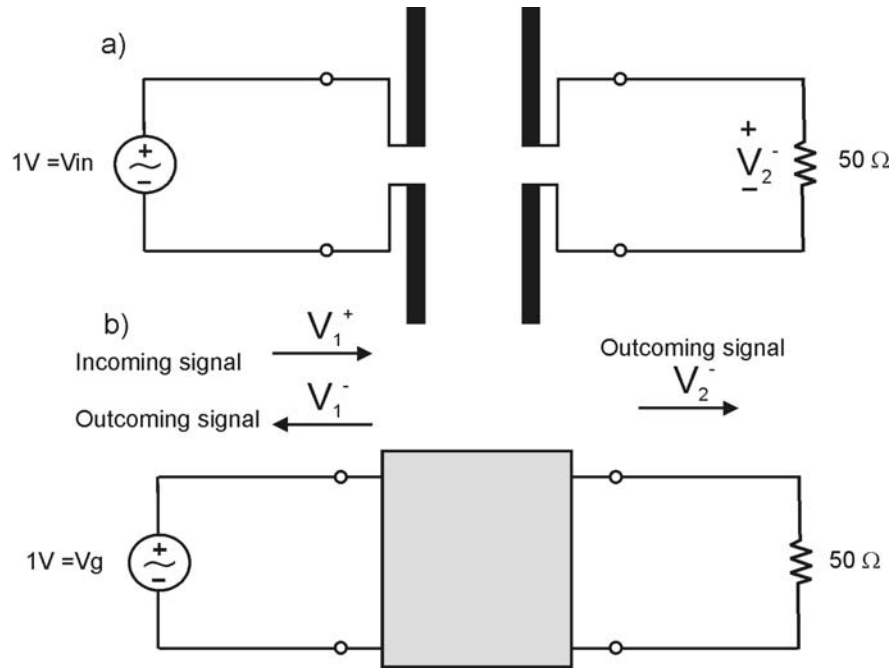
Figure 4.6-1 a) Circuit schematic for a two antenna system, −b) an equivalent two-port network representation

The antenna-to antenna transfer function is then given by the ratio of two voltages, i.e.

$$T(\omega) = \frac{V_2^-(\omega)}{V_g(\omega)}$$

(4.6.1)

The transfer function can be expressed in terms of the S-parameters of the equivalent two-port network. This network is shown in Fig. 4.6-1b. From the network model the S-parameters are given as

$$S_{11} = \frac{V_1^-}{V_1^+}, \quad S_{21} = \frac{V_2^-}{V_1^+}$$
(4.6.2)

For the transmitting antenna, one has

$$V_1^+ + V_1^- = 1 = V_g$$
(4.6.3)

Using Eq. (4.6.2) and (4.6.3) gives

$$V_1^+ = \frac{V_g}{1 + S_{11}} \text{ and } V_2^- = S_{21}V_1^+$$
(4.6.4)

Therefore, Eq. (4.6.1) leads to

$$T(\omega) = \frac{V_2^-(\omega)}{V_g(\omega)} = \frac{S_{21}(\omega)}{1 + S_{11}(\omega)}$$
(4.6.5)

Eq. (4.6.5) is used to numerically evaluate the transfer function for two antennas, using Ansoft HFSS simulator v.10.1 and the two-port antenna model. Alternatively, it has been used to measure the transfer function experimentally, using the Agilent 8722ET network analyzer. Fig. 4.6-2a shows the magnitude and phase plot of the numerically evaluated transfer function when the antennas are separated by a distance of 4.5λ and are facing each other (no tilt). The values on the plots are calculated using an interpolating sweep over the frequency range of interest (400-500 MHz).

For comparison purposes, Fig. 4.6-2b shows the ideal linear phase behavior with increasing frequency - $\theta = \theta_0 - 2\pi(f - f_0)/c_0 x$ - a dashed line. Here, x is the antenna-to-antenna separation distance, θ is the phase. The phase plot indicates a significant deviation from the predicted ideal line but still an almost linear behavior of the phase over the band of interest.
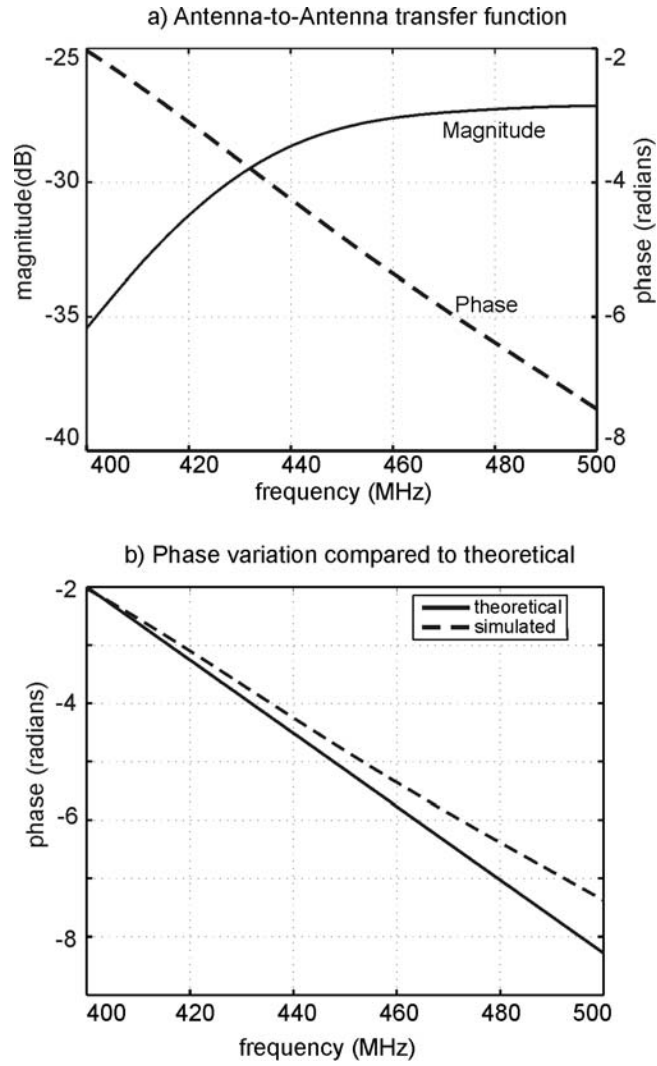
Figure 4.6-2 , –a) The simulated magnitude and phase plot of the antenna-to-antenna transfer function; b) comparison of the simulated phase plot with the ideal (linear) phase model.

4.7 Summary

A reduced-size PIFA with a bandwidth of about 18% in the main band and a patch length of about 0.165λ has been presented. The impedance bandwidth of the proposed PIFA is much larger as compared to traditional PIFA elements in the UHF band [124]. The PIFA manufactured on a foam substrate have shown the performance that agrees well with the simulations.

5 Circularly polarized antenna design in UHF band

This chapter describes a circularly polarized receiving antenna designed for the Precision Personnel Locator (PPL) system at Worcester Polytechnic Institute for indoor positioning. This chapter is organized as follows. Section 5.1 gives the definition of circular polarization, its advantages in communication systems and explains the antenna orientations to transmit and receive circular polarized signals. Section 5.2 gives the design details of the turnstile bowtie antenna. The fabricated antenna along with the simulated and measured results is also presented.

5.1 Circular polarization

A time-harmonic wave is circularly polarized at a point in space if the electric (or magnetic) field vector at that point traces a circle as a function of time. The necessary and sufficient conditions to accomplish this are if the field vector processes all of the following:

  i.   the field must have two orthogonal linear components, and

  ii.   the two components must have the same magnitude, and

  iii.   the two components must have a time-phase difference of odd multiples of 90°

The sense of rotation is always determined by rotating the phase-leading component towards the phase lagging component and observing the field rotation as the wave is viewed traveling away from the observer. So a circularly polarized wave radiates energy in the horizontal plane, vertical planes and every plane in between. If the rotation is clockwise the wave is right-hand circularly polarized (RHCP); if the rotation is counterclockwise the wave is left-hand circularly polarized (LHCP).

5.1.1 <u>Advantages of circular polarization</u>

Although most wireless systems use linear polarization the use of circular polarization will eventually become advantageous for all mobile systems. The advantages of using circular polarization are listed below [125].

i. Reflectivity:-Radio signals are reflected or absorbed depending on the material they come in contact with. Because linearly polarized antennas transmit and receive signals in only one plane, if the reflecting surface does not reflect the signal precisely in the same plane, that signal strength will be lost. Since circular polarized antennas send and receive in all planes, the signal strength is not lost, but is transferred to a different plane and is still utilized.

ii. Absorption:-As stated above, radio signal can be absorbed depending on the material they come in contact with. Different materials absorb the signal from different planes. As a result, circular polarized antennas provide a higher probability of a successful link because it is transmitting on all planes.

iii. Phasing Issues/ Multipath:-Reflected linear signals return to the propagating antenna in the opposite phase, thereby weakening the propagating signal. Conversely, circularly-polarized systems also incur reflected signals, but the reflected signal is returned in the opposite orientation, largely avoiding conflict with the propagating signal. The result is that circularly-polarized signals are much better at penetrating and bending around obstructions.

iv. Signal to noise ratio: Due to absence of common circularly polarized noise sources as opposed to linearly polarized noise sources, the circular polarized system has a better signal to noise ratio.

v. Inclement Weather:-Rain and snow cause a microcosm of conditions explained above (i.e. reflectivity, absorption, phasing, multi-path and line of sight). Circular

polarization is more resistant to signal degradation due to inclement weather conditions for all the reason stated above.

vi.   Line-of-Sight:-When a line-of-sight path is impaired by light obstructions (i.e. foliage or small buildings), circular polarization is much more effective than linear polarization for establishing and maintaining communication links.

5.1.2 <u>Antenna orientation for circular polarization [126]</u>

The key element for understanding the CP transmit/receive antenna orientation is an analog phase shifter. The phase shifter (a transmission line of length $\lambda/4$ in the simplest case) always adds a phase shift of $-\pi/2$ to the incoming signal, no matter what direction does the signal go, in transmit or in the receive mode.

Consider the operation of a RHCP antenna schematically shown in Fig. 5.1-1. In the transmit mode, the input current is equally split between two orthogonal dipoles (or other antennas). The y-oriented dipole has a $-\pi/2$ phase shift. The radiated electric field for either dipole is proportional to the current. This yields

$$\vec{E} = \left(E_x, E_y\right) = G\left(\cos\omega t, \sin\omega t\right) \tag{5.1.1}$$

where G is a constant. Eq. (5.1.1) predicts a clockwise rotation of the electric field in the xy-plane when looking into positive z-direction – the propagation direction. This is an RHCP signal.
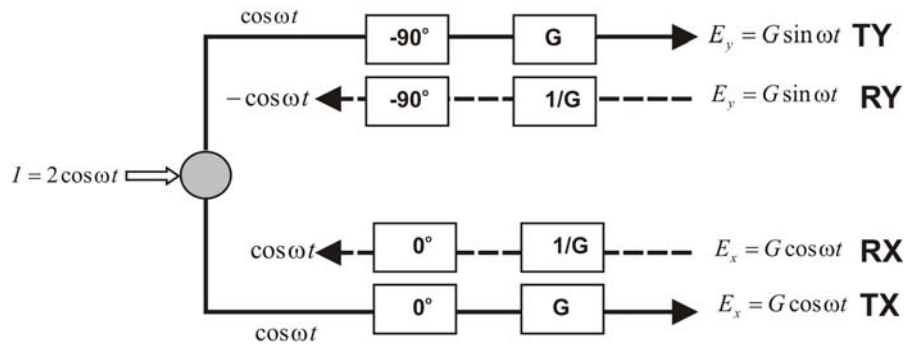
Figure 5.1-1 Operation of RHCP antenna [126]

However, if we will consider the receiving mode and feed exactly the same signal (5.1.1) back to the same RHCP antenna, we will finally obtain zero received current, due to the accumulating phase shift. Such an operation is shown in Fig. 5.1-1 by dashed lines. This result does not change when a constant phase shift is added to both E-field components, due to a finite propagation distance. In other words, two identically oriented RHCP antennas shown in Fig. 5.1-2I will not provide with any power transmission, if one of them is working as a transmitter and another as a receiver.
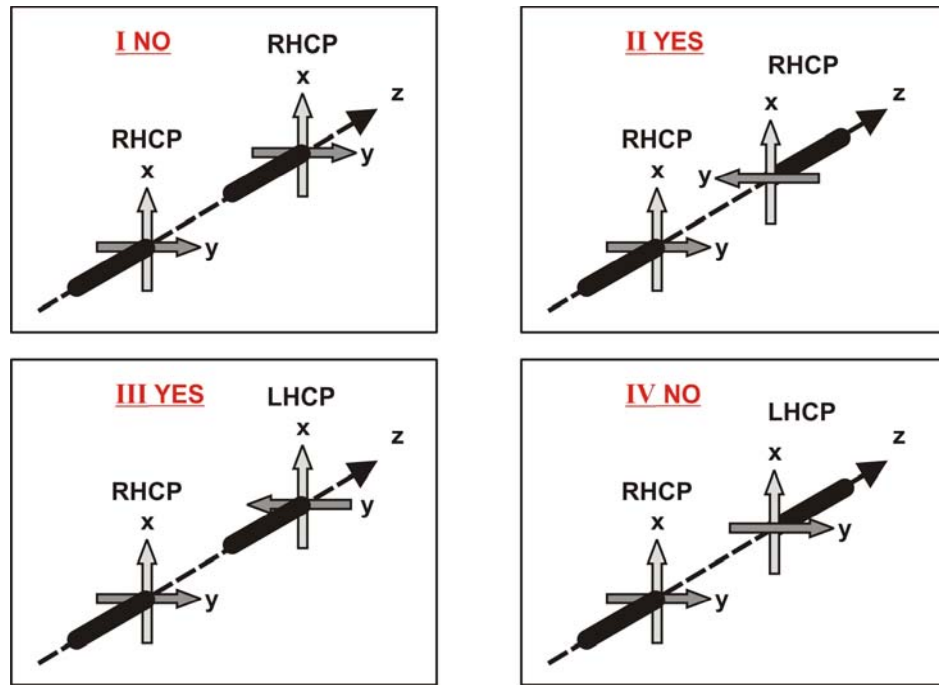
Figure 5.1-2 RHCP/LHCP antenna orientations [126]

On the other hand, two RHCP antennas facing each other as shown in Fig. 5.1-2II, will have zero polarization loss factor (full transmitted power) due to the fact that the direction of the y-oriented dipole is opposite and one more minus sign is added. It means that $E_y = -G\sin\omega t$ in Fig. 5.1-1 in the receiving mode. Two other cases shown in Fig. 5.1-2, which include LHCP antennas, are treated in the same way.

5.2 Turnstile antenna design

This section reports on a design of a low-cost circularly polarized turnstile bowtie antenna in the low UHF band (550MHz-700MHz) that has a wide impedance and polarization bandwidth (in excess of 20% at zenith assuming 3 dB axial ratio) [127]. In addition, the antenna has a near omnidirectional RHCP radiation pattern in the upper hemisphere and a good front to back gain ratio.

5.2.1 <u>Introduction</u>

The crossed-dipole antenna or the turnstile antenna invented in 1936 by Brown [127] is a valuable tool to create a circularly-polarized pattern (RHCP or LHCP). Since the invention many efforts have been made to design an efficient built-in phase shifting network [128-134], achieve a wider impedance bandwidth [135], nearly hemispherical coverage with droopy dipoles [134-139], and a good axial-ratio bandwidth [131,134,140]. The turnstile antenna usually operates at the fundamental (series) resonance of the dipole-like antenna. Some variations are known, such as a "rhombic" turnstile considered in [123] that in fact operate at the second (parallel) resonance. These variations may have larger impedance/polarization bandwidth but typically have a non-omnidirectional radiation pattern in the upper hemisphere. Therefore, they are not considered.

In order to achieve circular polarization, the turnstile antenna has either an external quadrature hybrid as a 90° power divider/combiner [131,141] or an internal built-in phase shifting network that, in its simplest case, is a narrowband $\lambda/4$ transmission line connecting two dipoles in parallel [131]. The internal network may be also based on the impedance difference of two crossed antennas [129-131] or on adding a transmission line (folding) to one of the antennas [132]. The impedance diversity method is less bulky, does not require lumped components, can simply be achieved in practice, and is therefore the subject of the present study.

5.2.2 <u>Antenna design</u>
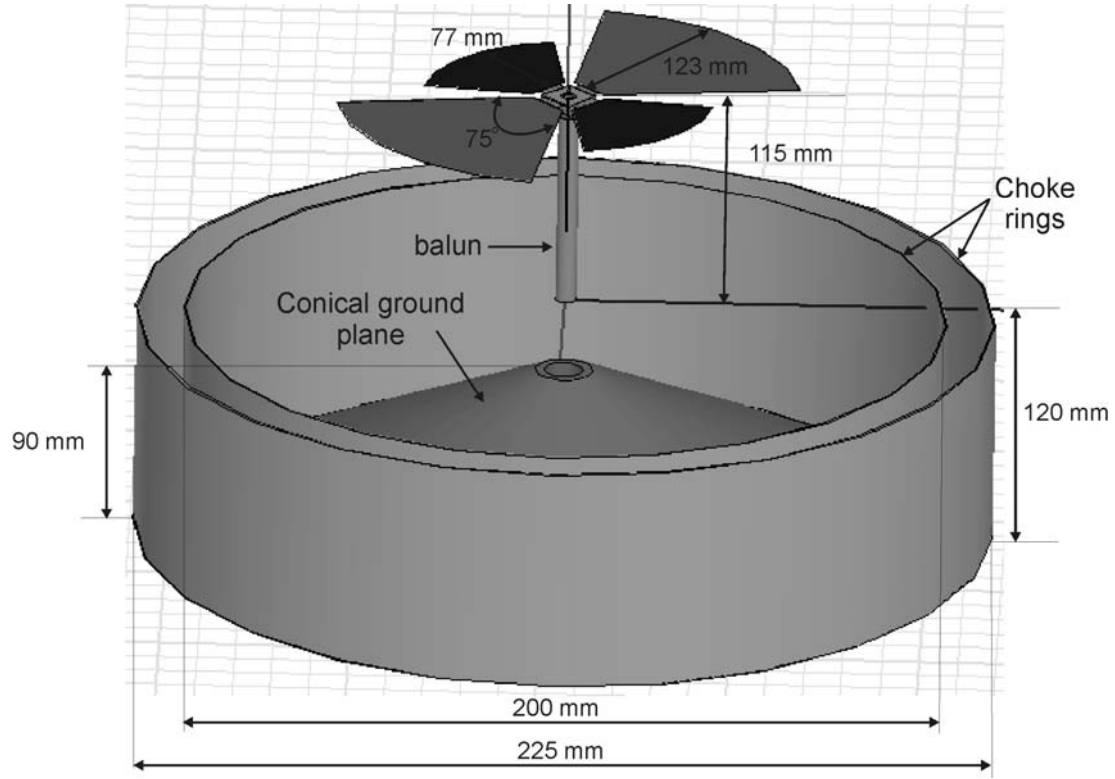
Figure 5.2-1 Antenna structure – centered at 625 MHz (Ref [127] © 2007 IEEE/APS)

The antenna designed in the present case uses a split-coaxial balun; does not employ an external hybrid; is all-metal made and is well suited for outdoor long-term wideband applications. The necessary 90° phase shift is obtained by using two bowties that have complex conjugate impedances over the wide bandwidth. The method of complex conjugate impedances was described in Refs. [129-131]. Its idea is simple - to have two non-equal antennas A and B with complex conjugate impedances of the type $Z_{A,B} = R \mp jR$. For two crossed perpendicular antennas fed in parallel, the radiated electric field ratio at zenith is given in (5.2.1).

$$\frac{E_A}{E_B} = \frac{I_A}{I_B} = \frac{Z_B}{Z_A} = j \qquad\qquad (5.2.1)$$

Fig. 5.2-1 shows the proposed antenna structure. The conical ground plane and special bowtie shaping helps in achieving good CP radiation patterns over the entire frequency range of interest (550- 700 MHz) and up to ±60° elevation angles from zenith. The two bowties have each a flare angle of 75° and have rounded edges. This combination has found to provide a better polarization bandwidth compared to the wire dipole, straight bowtie, or the transmission line-based partially folded dipole. The two rings surrounding the cone are the choke rings. These rings are $\lambda/4$ deep at the center frequency (625 MHz). The choke ring configuration is fairly successful in reducing the amount of radiation along the horizon and the backscattered radiation [131,132,143]. The detailed choke ring theory is explained in the next section. The impedance matching is achieved using a single split-coax balun as shown in Fig 5.2-2a.
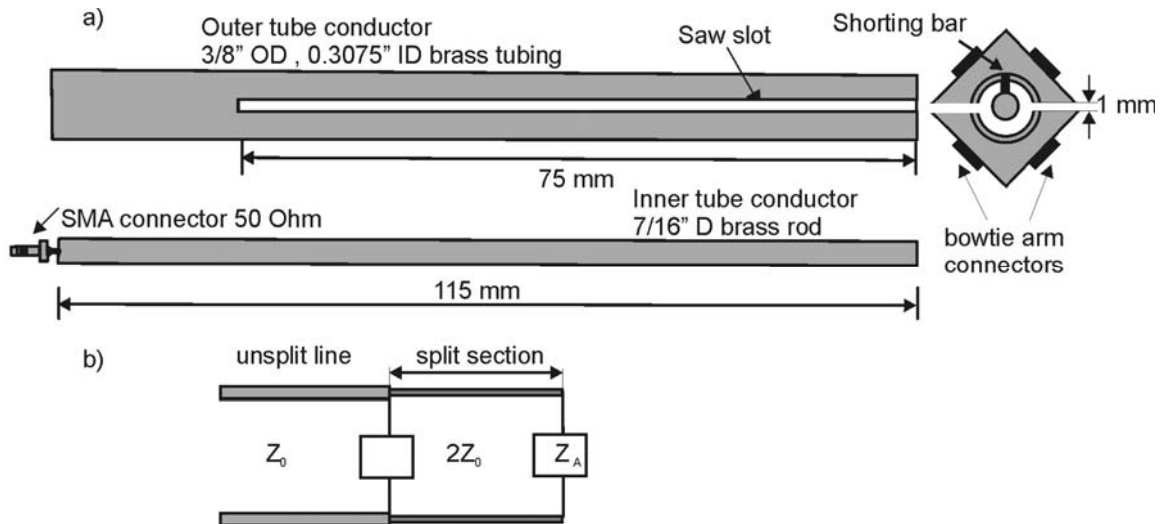
Figure 5.2-2 a) Balun assembly; b) Impedance transformation

The figure also shows the details for connecting the bowtie elements to the balun. The split balun or slotted feed is a compact balun arrangement and is suitable for frequencies above 300 MHz [144]. The system provides an impedance transformation. If the un-split line has a characteristic impedance of Z_0 then the other end of the split section has an

impedance of $2Z_0$ as shown in Fig 5.2-2b. Characteristic impedance is determined by the size and spacing of the conductors and the type of dielectric used between them. For ordinary coaxial cable, the characteristic impedance depends on the dimensions of the inner and outer conductors, and on the characteristics of the dielectric material between the inner and outer conductors. The following formula can be used for calculating the characteristic impedance of the coaxial cable [145]

$$Z_0 = \frac{138}{\sqrt{\varepsilon_r}} \log_{10}\left(\frac{D}{d}\right) \qquad (5.2.2)$$

where D is the inner diameter of the cable shield, d is the diameter of the center conductor and ε_r is the dielectric constant of the medium between the two conductors. For the present balun setup the value of $Z_0 = 29.18\Omega$. The length of the cable does not affect the characteristic impedance.

5.2.3 <u>Choke ring theory [146]</u>

A choke ring ground plane typically consists of several concentric thin walls, or rings, around the center where the antenna element is located. The area between the rings creates "grooves". The principle of the operation of choke ring ground planes is as follows. The signal that is received by the antenna is composed of two components; "direct" signal and "reflected" signal. The grooves have no effect on the direct signal other than decreasing the antenna gain at low elevation angles. For high elevation angles the ground plane works almost like a flat ground plane. The grooves have an affect on reflected signal from underneath.

The electromagnetic field of the reflected signal in the vicinity of the choke ring ground plane can be viewed as sum of two field waves. One is a field wave that surrounds the ground plane along an imaginary conductive surface S (see Fig 5.2.3) which is attached to the top edges of grooves and continues to the back side of the ground plane. This

reflected wave is the same as the reflected wave in a flat ground plane. We call this the "primary" wave. The second reflected wave is created by the electromagnetic field of the grooves. We call this wave the "secondary" wave. Field inside grooves can be viewed as sum of two waves. One wave that propagates vertically towards the bottom surfaces of the grooves and can be treated as a wave entering the grooves from outside. This wave is excited by the "primary" wave. The other wave that propagates vertically upwards along the grooves walls and can be treated as a wave reflected from the grooves bottoms surfaces to the outside. This wave excites the "secondary" wave.

Primary and secondary reflected signals propagate to the antenna element and contribute to the total signal that also includes direct signal from the satellite to the antenna element. The objective of the choke ring ground plane is for the primary and secondary reflected signals to substantially cancel each other and the direct signal to the antenna to remain as the dominant signal.
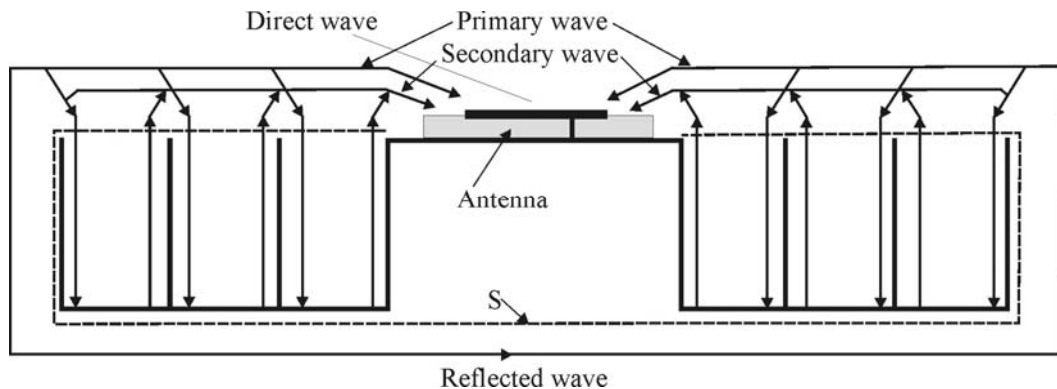
Figure 5.2-3 Field waves in choke ring [146]

The phase relationship between the primary and the secondary reflected signals at the antenna output depends on the difference in path lengths that each signal travels. This path difference is twice the depth of the grooves. The amplitude ratio of the two signals depends on the characteristics of the antenna element, its location on the ground plane, the width and the number of the grooves. If the amplitude of the primary and the

secondary waves are equal and the phase difference between them is 180 degrees, then the two components of the reflected signal cancel each other at the antenna output and multipath is suppressed. So, a given choke ring has optimum effect only on the particular frequency that has resonance behavior.

For a given choke ring ground plane the complete suppression of multipath only occurs for certain elevation angles and for others the multipath is partially suppressed. The maximum suppression usually occurs for the angles close to zenith and minimal suppression at angles close to horizon.

5.2.4 <u>Simulation and Measured Results</u>

The antenna design and optimization have been performed using analytical models and Ansoft HFSS v10.1. Two scaled antenna prototypes have been fabricated – see Fig. 5.2-4a. The bowtie wings and the cone are made of aluminum; the balun uses brass rods/tubing. The antenna does not have any dielectric parts except for a supporting Teflon rod seen in Fig. 5.2.-4a. Fig. 5.2-4b gives measured (HP 85047A Network Analyzer) and simulated return loss for optimized antenna with the matched balun. The return loss is less than -10 dB over the entire frequency band of 550 MHz to 700 MHz.
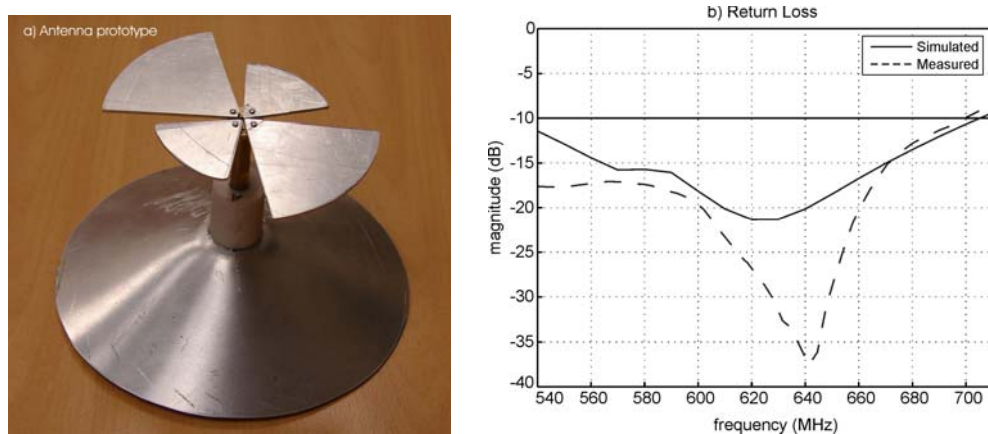
Figure 5.2-4. a) Antenna prototype; b) Simulated and measured return loss (Ref [127] © 2007 IEEE/APS)

Fig. 5.2-5 shows the variation in the polarization isolation (dB) in the xz plane for different values of theta. As can be observed from the figure, the isolation curves are fairly flat and fall down to about 10dB at ±60° from zenith in the xz plane and about 9dB in the yz plane. The polarization isolation at zenith is greater than 12 dB for the entire frequency range (24% bandwidth) and greater than 15 dB over the bandwidth of 21%.

Figure 5.2-5 Polarization isolation variation for different vales of theta and different frequency values over the entire bandwidth in the a) xz plane and b) yz plane (Ref [127] © 2007 IEEE/APS)

Fig. 5.2-6 shows the antenna gain patterns at the start, end, and center frequencies of the band. The solid line represents the RHCP gain while the dashed line indicates the LHCP gain patterns. The patterns indicate a moderate front-to-back gain ratio of about 15 dB for all the frequencies within the band. This ratio can further be improved. The RHCP gain drops down by about 6 dB for angles greater than 60 degrees from zenith.
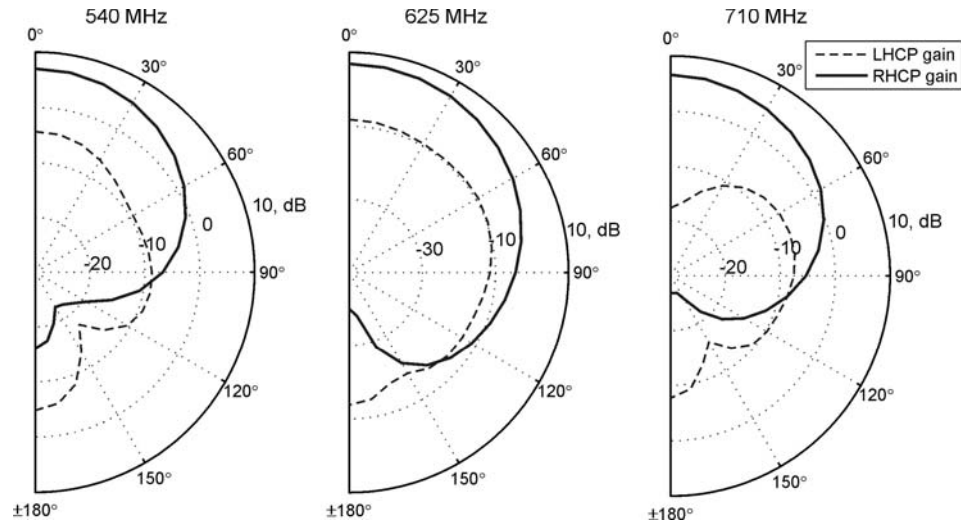
Figure 5.2-6 LHCP and RHCP gain patterns at the start, center and end frequencies; solid line corresponds to the RHCP gain while the dashed line corresponds to the LHCP gain. (Ref [127] © 2007 IEEE/APS)

5.2.5 <u>Summary</u>

A circularly polarized turnstile bowtie with 24% CP and impedance bandwidth is presented. The antenna has a moderate front-to-back gain ratio of about 15 dB for all the frequencies within the band. The manufactured antenna has shown the performance that agrees well with the simulations.

166

6 Conclusion

In this dissertation, the MoM VIE based modeling method was developed and validated for a patch or slot antenna on a thin finite dielectric substrate. Two new key features of the method are the use of proper low-order dielectric basis functions and the proper VIE conditioning, close to the metal surface, where the surface boundary condition of the zero tangential –component must be extended into adjacent tetrahedra. These operations allow one to achieve good accuracy with one layer of tetrahedra for a thin dielectric substrate and greatly reduce computational cost. Considering that we need eight or more tetrahedra per wavelength in the lateral direction in order to obtain accurate results and that the tetrahedron quality still needs to be kept adequate while "stretching" the one-layer mesh in the transversal direction, the maximum electrical thickness accessible with one layer of tetrahedra may be estimated as $\lambda_{diel}/8$. The same method has recently been applied to open and terminated microstrip transmission lines. For some high Q microstrip resonators, it demonstrated a good accuracy at the resonances.

The present VIE-based modeling approach is applicable not only to antennas with a thin dielectric substrate but also to bulk dielectric loading. However, in such a case, it essentially loses its advantages to the SIE approach, which enables faster treatment of a bulk homogeneous dielectric. Enforcing the boundary condition in the VIE should be considered as a way to improve its convergence for coarse meshes. Another significant mechanism that affects the convergence accuracy for coarse and moderate meshes is the way of calculating potential integrals for neighboring metal/dielectric bases.

The second part of this dissertation is devoted to practical antenna designs. The dissertation describes the design of a reduced-size PIFA with a bandwidth of about 18% in the main band and a patch length of about 0.165λ. The impedance bandwidth of the proposed PIFA is much larger as compared to traditional PIFA elements in the UHF band [124]. With the addition of the capacitive load, slots and tapered patch the size of the

antenna is significantly reduced for a given resonant frequency without affecting the antenna bandwidth. The PIFA manufactured on a foam substrate have shown the performance that agrees well with the simulations. The major disadvantage of the foam material – potential fragility and uncertainty of shape – is of little importance for the present broadband UHF PIFA. The observed degree of repeatability of the antenna characteristics is fully sufficient for our purposes.

Finally, the design of a circularly polarized turnstile bowtie antenna at low UHF frequencies (550-700 MHz) is also discussed. The antenna uses a split-coaxial balun; does not employ an external hybrid; is all-metal made and is well suited for outdoor long-term wideband applications. The necessary 90° phase shift is obtained by using two bowties that have complex conjugate impedances over the wide bandwidth. The polarization isolation at zenith is greater than 12 dB for the entire frequency range (24% bandwidth) and greater than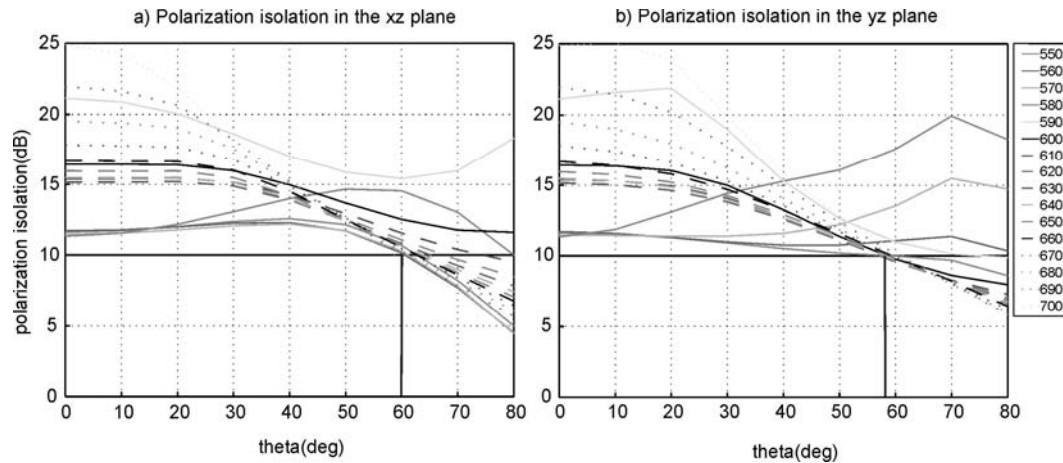 15 dB over the bandwidth of 21%. The antenna also has a 24% impedance bandwidth. The antenna has a moderate front-to-back gain ratio of about 15 dB for all the frequencies within the band.

7 References

[1] Kin-Lu. Wong, *Planar Antennas for Wireless Communications*, John Wiley & Sons, New York, 2003.

[2] S. M. Rao and N. Balakrishnan, "Computational Electromagnetics-A review," Current Science, vol.77, no.10, Nov 1999.

[3] S. M. Rao, *Time Domain Electromagnetics*, Academic Press, New York, June 1999.

[4] J.L. Volakis and L.C Kempel, "Electromagnetics: computational methods and considerations", IEEE Computational Science and Engineering, vol. 2, pp. 42-57, 1995.

[5] R. F. Harrington, *Field Computation by Moment Methods*, Macmillan, New York, 1968

[6] T. Cwik, J. Partee, and J. Patterson, "Method of Moment solution to scattering problems in the parallel processing environment", IEEE Trans. on Magnetics, vol. 27, no. 5, pp. 3837- 3840, Sept. 1991.

[7] D.B. Davidson, "Large Parallel Processing Revisited- A second tutorial", IEEE Antennas and Propagation Magazine, vol. 34, pp. 9-21, Oct 1992.

[8] Kin-Lu Wong, *Compact and Broadband Microstrip Antennas*, Wiley, New York, 2002.

[9] G. Kumar and K.P. Ray., *Broadband Microstrip Antennas*, Artech House, Norwood, MA, 2003.

[10] T. Taga amd K. Tsunekawa, "Performance analysis of a built-in PIFA for 800 MHz hand portable radio units", IEEE J. Select. Areas Communication, vol.5, pp. 921-929, June 1987.

[11] Z.D Liu, P.S. Hall and D. Wake, "Dual frequency PIFA," IEEE Trans. Antennas and Propagation, vol. AP-45, pp. 1451-1458, Oct 1997.

[12] S. Tarvas and A. Isohatala, "An internal dual-band mobile phone antenna," IEEE Antenna Propagation Soc. Int. Symposium Digest, pp. 266-269, 2000

[13] T.W. Chiou and K.L Wong, "Broadband dual-polarized single microstrip patch antenna with high isolation and low cross polarization," IEEE Trans. Antennas and Propagation, vol. AP-50, pp. 399-401, March 2002

[14] K.L Wong, H.C Tung and T.W. Chiou, "Broadband dual-polarized aperture coupled patch antennas with modified H-shaped coupling slots," IEEE Trans. Antennas and Propagation, vol. AP-50, pp. 181-191, Feb 2002

[15] I. Nystrom and D. Karlsson, "Reduction of back radiation and cross-coupling in dual polarized aperture coupled patch antennas," IEEE Antenna Propagation Soc. Int. Symposium Digest, pp. 2222-2225, 1997.

[16] K. Carver, and J. Mink, "Microstrip antenna technology," IEEE Trans. Antennas and Propagation, vol. AP-29, no. 1, pp. 2-24, Jan 1981.

[17] R. Bancroft, *Microstrip and Printed Antenna Design*, Noble Publishing, 2004, Atlanta, GA.

[18] R.J Mailloux, "Microstrip array technology," IEEE Trans. Antennas and Propagation, vol. AP-29, no. 1, pp. 25-37, Jan 1981.

[19] J.R. James et al, "Some recent development in microstrip antenna technology," IEEE Trans. Antennas and Propagation, vol. AP-29, no. 1, pp. 124-128, Jan 1981.

[20] J.R. James and P.S Hall, *Handbook of microstrip antennas*, vol. 1, London: Peter Peregrinus, 1989.

[21] H.F Lee and W. Chen, *Advances in microstrip and printed antennas*, Wiley, New York, 1997.

[22] R.A. Sainati, *CAD of microstrip antennas for wireless applications*, Artech House, Norwood, MA, 1996

[23] Y.L. Kuo and K.L Wong, "Planar inverted-L patch antenna for 2.4/5.2 GHz dual band operation", Microwave Opt. Tech. Letters, vol.31, pp. 394-396, Dec 2001

[24] H.W. Son, J. Yeo, G.Y. Choi, and C.S. Pyo, "A Low-Cost, Wideband Antenna for Passive RFID Tags Mountable on Metallic Surfaces," in Proc. IEEE Antennas and Propagation Society Int. Symp., pp. 1019–1022, July 2006.

[25] M. Hirvonen, P. Pursula, K. Jaakkola, and K. Laukkanen, "Planar inverted-F antenna for radio frequency identification", Electron. Lett., vol. 40, no. 14, pp. 848–850, July 2004.

[26] L. Ukkonen, L. Sydänheimo, and M. Kivikoski, "Patch antenna with EBG ground plane and two-layer substrate for passive RFID of metallic objects", IEEE Antennas and Propagation Society Int. Symp., vol. 1, pp.93-96, July 2004.

[27] Sung-Joo Kim, Byongkil Yu, Ho-Jun Lee, Myun-Joo Park, Frances J. Harackiewicz, and Byungje Lee, "RFID Tag Antenna Moutable on Metallic Plates," Microwave Conference Proceedings, 2005. APMC 2005. Asia-Pacific Conference Proceedings, vol. 4, 4-7 Dec. 2005.

[28] Byunggil Yu, Sung-Joo Kim, Byungwoon Jung, Frances J. Harackiewicz, Myun-Joo Park, and Byungje Lee, "Balanced RFID Tag Antenna Mountable on Metallic Plates," in Proc. IEEE Antennas and Propagation Society Int. Symp., pp. 3237–3240, July 2006.

[29] W. Choi, H. W. Son, Ji-H. Bae, G. Y. Choi, C. S. Pyo, and J.-S. Chae, "An RFID tag using a planar inverted-F antenna capable of being stuck to metallic objects," ETRI Journal, vol. 28, no. 2, pp.216-218, April 2006.

[30] R.Garg, P. Bhartia, I. Bahl, I. Ittipiboon, *Microstrip Antenna Design Handbook,* Artech House, Norwood, MA, November 2000.

[31] P. Salonen, L Sydanheimo, M. Keskilammi, M Kivikoski, "A small planar inverted-F antenna for wearable applications", International. Conf. on Wearable Computers, pp. 95-100, Oct. 1999.

[32] A. W. Glisson, D. Kajefez, and J. James, "Evaluation of modes in dielectric resonators using a surface integral equation formulation," IEEE Trans. Microwave Theory Tech., vol. MTT-31, pp. 1023–1029, Dec.1983.

[33] S. M. Rao, T. K. Sarkar, P.Midya, and A. R. Djordevic, "Electromagnetic radiation and scattering from finite conducting and dielectric structures: Surface/surface formulation," IEEE Trans. Antennas Propag., vol. 39, pp. 1034–1037, Jul. 1991.

[34] L. Yaxun, S. Safavi-Naeini, S. K. Chaudhuri, and R. Sabry, "On the determination of resonant modes of dielectric objects using surface integral equations," IEEE Trans. Antennas Propag., vol. 52, pp. 1062–1069, Apr.2004.

[35] J. Chen, A. A. Kishk, and A. W. Glisson, "Application of a new MPIE formulation to the analysis of a dielectric resonator embedded in a multilayered medium

coupled to a microstrip circuit," IEEE Trans. Microwave Theory Tech., vol. 49, pp. 263–279, Feb. 2001.

[36] B. M. Kolundˇzija, J. S. Ognjanovic´, and T. K. Sarkar, *WIPL-D: Electromagnetic Modeling of Composite Metallic and Dielectric Structures*. Norwood, MA: Artech House, 2000.

[37] M. R. Abdul-Gaffoor, H. K. Smith, A. A. Kishk, and A. W. Glisson, "Simple and efficient full-wave modeling of electromagnetic coupling in realistic RF multilayer PCB layouts," IEEE Trans. Microwave Theory Tech., vol. 50, pp. 1445–1457, Jun. 2002.

[38] S.N. Makarov, "MoM antenna simulations, with Matlab: RWG basis functions", IEEE Antennas and Propagation Magazine, vol. 43, no. 5, pp.100 − 107, Oct. 2001.

[39] S. Makarov, S. Kulkarni, A. Berezin, I. Waldron, "Microwave radiation force on a parallel-plate resonator", Microw. Symp. Dig. IEEE MMT-S Int., vol. 3, pp. 2043 − 2046, June 2004.

[40] S. Makarov, A. Apte, A. Berezin, "Geometry optimization of a finite array of microstrip patches using Matlab", IEEE Antennas Propag. Int. Symp., vol. 1, pp. 710 − 713, June 2002.

[41] A. Fernandez-Garcia, S. Makarov, K. Pahlavan, "Matlab-based simulation of a slot antenna for pulse radiation", IEEE Conf. on UW System and Tech., pp. 341 − 344, May 2002.

[42] A. Apte, S. Makarov, "Execution times for the solution of MoM equations in Matlab", IEEE Antennas Propag. Int. Symp., vol. 1, pp. 692 − 695, June 2002.

[43] D. H. Schaubert, D. R. Wilton, and A. W. Glisson, "A tetrahedral modeling method for electromagnetic scattering by arbitrarily shaped inhomogeneous dielectric bodies," IEEE Trans. Antennas Propag., vol. AP-32, pp. 77–85, Jan. 1984.

[44] L. Yaxun, S. Safavi-Naeini, S. K. Chaudhuri, and R. Sabry, "Simulation of resonant modes of a rectangular DR in MIC environment using MPIE-MoM with combined entire-domain and sub-domain basis functions," in Microw. Symp. Dig. IEEE MMT-S Int., vol. 3, pp. 1901–1904, Jun. 2002.

[45] L. Yaxun, S. Safavi-Naeini, and S. K. Chaudhuri, "Comparison of SIE-MoM and VIE-MoM for determination of complex resonant frequency of dielectric resonators," in IEEE Antennas Propag. Int. Symp., vol. 1, pp. 641–644, Jun. 2003.

[46] C.-C. Lu, "A fast algorithm based on volume integral equation for analysis of arbitrarily shaped dielectric radomes," IEEE Trans. Antennas Propag., vol. 51, pp. 606–612, Mar. 2003.

[47] X.-C. Nie, L.-W. Li, N. Yang, T. S. Yeo, and Y.-B. Gan, "Precorrected- FFT solution of the volume integral equation for 3-D inhomogeneous dielectric objects," IEEE Trans. Antennas Propagation, vol. 53, pp. 313–320, Jan. 2005.

[48] T. K. Sarkar, S. M. Rao, and A. R. Djordjevic, "Electromagnetic scattering and radiation from finite microstrip structures," IEEE Trans. Microwave Theory Tech., vol. 38, pp. 1568–1575, Nov. 1990.

[49] S. Kulkarni, S. Uy, R. Lemdiasov, R. Ludwig, and S. Makarov, "MoM VIE solution for an isolated metal-dielectric resonator with the zeroth order edge-based basis functions," IEEE Trans. Antennas Propagation, vol. 53, pp. 1566–1571, Apr. 2005.

[50] S. A. de Carvalho and L. de Souza Mendes, "Scattering of EM waves by inhomogeneous dielectrics with the use of the method of moments and the 3-D solenoidal basis functions," Microw. Opt. Technol. Lett., vol. 23, no. 1, pp. 42–46, Oct. 1999.

[51] S. Kulkarni, R. Lemdiasov, R. Ludwig, and S. Makarov, "Comparison of two sets of low-order basis functions for tetrahedral VIE modeling," IEEE Trans. Antennas Propag., vol. 52, pp. 2789–2795, Oct. 2004.

[52] A. F. Peterson, S. L. Ray, and R. Mittra, *Computational Methods for Electromagnetics*, IEEE Press, Piscataway, New Jersey, 1998.

[53] S. M. Rao, D. R. Wilton, and A. W. Glisson, "Electromagnetic scattering by surfaces of arbitrary shape," IEEE Trans. Antennas and Propagation, vol. AP-30, no. 3, pp. 409-418, May 1982.

[54] D. R. Wilton, S. M. Rao, A. W. Glisson, D. H. Schaubert, O. M. Al-Bundak, and C. M. Butler, "Potential integrals for uniform and linear source distribution on polygonal and polyhedral domains," IEEE Trans. Antennas and Propagation, vol. AP-32, no. 3, pp. 276-281, March 1984.

[55] T. F. Eibert and V. Hansen, "On the calculation of potential integrals for linear source distributions on triangular domains," IEEE Trans. Antennas and Propagation, vol. AP-43, no. 12, pp. 1499-1502, Dec. 1995.

[56] R. Cools, "An Encyclopedia of Cubature Formulas," J. Complexity, vol. 19, 445-453, 2003.

[57] Z. Wang, J. Volakis, K. Saitou, and K. Kurabayashi, "Comparison of semi-analytical formulations and Gaussian-quadrature rules for quasi-static double-

surface potential integrals," IEEE Antennas and Propagation Magazine, vol. 45, no. 6, pp. 96-102, 2003.

[58] N. A. Ozdemir and J. F. Lee, "Single level dual rank SVD algorithm for volume integral equations of electromagnetic scattering," in Antennas and Propagation Society, 2003 IEEE International Symposium, vol. 2, pp. 302 - 305, June 2003.

[59] M. L. Barton and Z. J. Cendes, "New vector finite elements for three dimensional magnetic field computation", J. Appl. Phys., vol. 61, No 8, pp. 3919-3921, 1987.

[60] A. Bossavit, "Whitney forms: a class of finite elements for three dimensional computations in electromagnetism", IEE Proceedings, vol. 135, Pt. A, No 8, pp. 493-499, Nov. 1988.

[61] Jin Fa Lee and R. Mittra, "A note on the application of edge elements for modeling three-dimensional inhomogeneously-filled cavities," IEEE Trans. Microwave Theory and Techniques, vol. MTT-40, pp. 1767-1773, Sept. 1992.

[62] J. B. Manges and Z. J. Cendes, "A generalized tree-cotree gauge for magnetic field computation," IEEE Trans. on Magnetics, vol. 31, pp. 1342-1347, May 1995.

[63] I. Tičar, O. Bíró, and K. Preis, "Vector potential expanded by edge basis functions associated with loops on finite-element facets," IEEE Trans. on Magnetics, vol. 38, pp. 437-440, March 2002.

[64] C. D. Meyer, *Matrix Analysis and Applied Linear Algebra*, SIAM, Philadelphia, PA, 2000.

[65] B. J. Rubin, "Divergence-free basis for representing polarization current in finite-size dielectric regions," IEEE Trans. Antennas and Propagation, vol. 41, no. 3, pp. 269-277, March 1993.

[66] Y. Saad, *Iterative Methods for Sparse Linear Systems*, Yousef Saad, p. 245, 2000.

[67] D. Kajfez and A. A. Kishk, "Dielectric resonator antenna – possible candidate for adaptive antenna arrays," Tutorial on Dielectric Resonator Antenna; online http://www.ee.olemiss.edu/darko/dra-pcfaaa.pdf

[68] Intel Math Kernel Library Reference Manual. 2004.

[69] D. H. Staelin, A. W. Morgenthaler, and Jin A. Kong, Electromagnetic Waves, Prentice Hall, Upper Saddle River, NJ, 1990.

[70] S. Kulkarni and S. Makarov, "Accuracy of MoM VIE eigenmode solution obtained with edge basis functions," 2005 IEEE Antennas and Propagation Int. Sym., Washington, DC, July 3-8, 2005.

[71] S. Kulkarni and S. Makarov, "The effect of numerical integration on MoM VIE solution for some isolated dielectric resonators," 2005 ACES/IEEE Int. Conf. Wireless Communications Applied Electromagnetics, Honolulu, 3-7 April 2005

[72] K. F. Warnick and W. Cho Chew, "Accuracy of the method of moments for scattering by a cylinder," IEEE Trans. Microwave Theory Techniques, vol. MTT-48, no 6, pp. 1652-1660, Oct. 2000.

[73] K. F. Warnick and W. Cho Chew, "Error analysis of the moment method," IEEE Antennas and Propagation Magazine, vol. AP-46, no. 6, pp. 38-53, Dec. 2004.

[74] C. P. Davis and K. F. Warnick, "High-order convergence with a low-order discretization on the 2-D MFIE," IEEE Antennas and Wireless Propagation Letters, vol. 3, pp. 355-358, 2004.

[75] C. P. Davis and K. F. Warnick, "Error analysis of 2D MoM for MFIE/EFIE/CFIE based on the circular cylinder," IEEE Antennas and Propagation Magazine, vol. AP-53, no. 1, pp. 312-331, Jan. 2005.

[76] Per-Olof Persson and G. Strang, "A simple mesh generator in MATLAB," SIAM Review, vol. 46, no. 2, pp. 329-345, 2004. Available onl.: http://www-math.mit.edu/~persson/mesh/

[77] P. Affolter and B. Eliasson, "Electromagnetic resonances and Q-factor of lossy dielectric spheres", IEEE Trans. Microwave Theory and Techniques, vol. MTT-21, no. 9, pp. 573-578, Sep. 1973.

[78] S. Makarov, S. Kulkarni, A. Marut, L. Kempel, "Method of Moment solution for a printed patch/slot antenna on a thin finite dielectric substrate using the volume integral equations" IEEE Trans. Antennas and Propagation, vol.54, no.4, pp. 1174-84, April 2006

[79] P. Junker, A. A. Kishk, and A. W. Glisson, "A novel delta gap source model for center fed cylindrical dipoles," IEEE Trans. Antennas and Propagation, vol. AP-43, no. 5, pp. 537-540, May 1995.

[80] S. D. Kulkarni, "MoM modeling of metal-dielectric structures using volume integral equations," MS Thesis, Worcester Polytechnic Institute, Worcester, MA, 2004, 155 p.

[81] A. D. Apte, "Simulation of patch antennas on arbitrary dielectric substrates," MS Thesis, Worcester Polytechnic Institute, Worcester, MA, 2003, 118 p.

[82] S. Kulkarni, A. Apte, S. Makarov, "Performance Evaluation of Patch Antenna Solver – RWG Elements" 19th Annual Review of Progress in Applied Computational Electromagnetics, pp.484-489, March 2002.

[83] R. Chair, A. A. Kishk, and K. F. Lee, "Wideband Simple Cylindrical Resonator Antennas," IEEE Microwave and Wireless Components Letters, vol. 14, no. 4, April 2005, pp. 241-243.

[84] D. M. Pozar, *Microwave Engineering*, Wiley, New York, 2005, third edition.

[85] A summary of Rogers laminates can be found at http://www.secomtel.com /UpFilesPDF/PDF/ROGERS/rt312.pdf

[86] C. A. Balanis, *Antenna Theory- Analysis and Design*, Wiley, New York, 2005, third edition.

[87] L. Unterberger and M. Comments, An introduction to HFSS Optimetrics™, 2002 Ansoft HFSS/Ensemble Users' Workshop.

[88] E. Semouchkina, G. Semouchkin, M. Lanagan.; L. Ivanchenko, S. ; Koroljev, and N. Popenko, "A new approach for enhancement circular polarization output in square shaped microstrip patch antennas, " In: IEEE 2004 Antennas and Propagation Society Int. Symposium, vol. 1, pp. 491-494, 20-25 June 2004.

[89] L. Matekovits, G. Vecchi, P. Pirinoli, and M. Orefice, "Network parameters of printed antennas from the MoM solution," In: International Sym. Antennas and Propagation, 1998. IEEE, vol. 4, pp. 1838 – 1841, 21-26 June 1998.

[90] B. G. Salman and A. McCowen, "The CFIE technique applied to finite-size planar and non-planar microstrip antenna," Third International Conference on

Computation in Electromagnetics, 1996. Conf. Publ. No. 420, 10-12, pp. 338 - 341, April 1996.

[91] Application note "Gap Model", Ansoft Corp., 2001. Available online: ftp://ftp.ansoft.com/techsup/download/web/ftproot_inet/products/hfss/faqs/portmicrostrip.htm.

[92] J.-Y. Sze and K.-L. Wong, "Bandwidth enhancement of a microstrip-line-fed printed wide-slot antenna," IEEE Trans. Antennas and Propagation, vol. AP-49, no. 7, pp. 1020-1024, July 2001.

[93] R. Qinjiang and T. A. Denidn, "A single-substrate microstrip-fed slot antenna array with reduced back radiation," Antennas and Wireless Propagation Letters, vol. 3, no. 1, pp. 265-268, 2004.

[94] D. Sievenpiper, H.-P. Hsu, and R. M. Riley, "Low-profile cavity backed crossed-slot antenna with a single probe feed designed for 2.34-GHz Satellite Radio applications," IEEE Trans. Antennas and Propagation, vol. AP-52, no. 3, pp. 873-879, March 2004.

[95] K. Awadalla and T. Maclean, "Input impedance of a monopole antenna at the center of a finite ground plane," IEEE Trans. Antennas and Propagation, vol. AP-26, no. 2, pp. 244-248, March 1978

[96] K. Awadalla and T. Maclean, "Monopole antenna at the center of circular ground plane," IEEE Trans. Antennas and Propagation, vol. AP-27, no. 2, pp. 151-153, March 1979.

[97] A. F. Gangi, S. Sensiper, and G. R. Dunn, "The characteristics of electrically short umbrella top loaded antennas," IEEE Trans. Antennas and Propagation, vol. AP-13, p. 864, 1965.

[98] C. Y. Ying, "Theoretical study of finite dielectric-coated cylindrical antennas," J. Math. Physics, vol. 10, pp. 480-483, 1969.

[99] M. A. Morgan and F. K. Schwering, "Eigenmode analysis of dielectric loaded top-hat monopole antennas," IEEE Trans. Antennas and Propagation, vol. AP-42, no. 1, pp. 54-61, Jan. 1994.

[100] L. A. Francavilla, J. S. McLean, H. D. Foltz, and G. F. Crook, "Mode-matching analysis of top-hat monopole antennas loaded with radially layered dielectric," IEEE Trans. Antennas and Propagation, vol. AP-47, no. 1, pp. 179-185, Jan. 1999.

[101] T. Taga, K. Tsunekawa, and A. Sasaki, "Antennas for detachable mobile radio units," Review of the ECL, NTT, Japan, vol. 35, no. 1, pp. 59-65, Jan. 1987.

[102] R. Feik, H. Carrasco, M. Olmos, and H. D. Hristov, "PIFA input bandwidth enhancement by changing feed plate silhouette," Electronics Letters, vol. 40, no. 15, July 2004, pp. 921-922.

[103] P. J. Massey, "New formulae for practical pager design," IEE Eleventh Intl. Conference on Antennas and Propagation, vol. 1, pp. 265-268, April 2001.

[104] W. G. Scanlon and N. E. Evans, "Numerical analysis of bodyworn UHF antenna systems," Eng. J of Electronics & Comm., vol. 13, no. 2, pp. 53-64, April 2001.

[105] R. E. Thomas and J. Huang, "Ultra-wideband UHF microstrip array for GeoSAR application," IEEE Antennas and Propagation Society International Symposium, vol. 4, pp. 2096-2099, June 1998.

[106] D. Psychoudakis and J. L. Volakis, "Miniature wideband UHF circularly polarized antenna using textured dielectric loading," IEEE Antennas and Propagation Society International Symposium, vol. 3A, pp. 573-576, July 2005.

[107] A. Buerkle and K. Sarabandi, "A wide-band, circularly polarized, magnetodielectric resonator antenna," IEEE Trans. Antennas and Propagation, vol. AP-53, no. 11 pp. 3436-3442, Nov. 2005.

[108] C. Xuan, L. Yaxin, and S. Safavi-Naeini, "Printed plane-filling fractal antennas for UHF band," IEEE Antennas and Propagation Society International Symposium, vol. 4, pp. 3425-3428, June 2004.

[109] F. Wang, Z. Du, Q. Wang, and K. Gong, "Enhanced-bandwidth PIFA with T-shaped ground plane", Electronic Lett, vol. 40, no. 23, pp. 1504-1505, Nov. 2004.

[110] B. Kim, J. Hoon, and H. Choi, "Small wideband PIFA for mobile phones at 1800 MHz," Vehicular Technology Conference, vol. 1, pp. 27-29, May 2004.

[111] M. C. Huynh and W. Stutzman, "Ground plane effects on planar inverted-F antenna (PIFA) performance," IEE Proc.-Microw. Antennas Propag., vol. 150, no. 4, pp. 209-213, Aug. 2003.

[112] S. Kulkarni, S. Makarov, "A dual-band linearly polarized PIFA" IEEE AP-S International Symposium, 3-8 July 2006.

[113] S. Kulkarni, R. Boisse, S. Makarov, "A linearly polarized compact UHF PIFA with foam support" 2006 ACES International Conference, 3-7 April 2006.

[114] T. K. Lo and Y. Hwang, "Bandwidth enhancement of PIFA loaded with very high permittivity material using FDTD," IEEE Antennas and Propagation Society International Symposium, vol. 2, pp. 798-801, June 1998.

[115] C. R. Rowell and R. D. Murch, "A capacitively loaded PIFA for compact mobile telephone handsets," IEEE Trans. Antennas and Propagation, vol. AP-45, no. 5, pp. 837-842, May 1997.

[116] B. Kim, J. Park, and H. Choi, "Tapered type PIFA design for mobile phones at 1800 MHz," Vehicular Technology Conference, vol. 2, pp. 1012-1014, April 2005.

[117] P. Solonen, L. Sydanheimo, M. Keskilammi, and M. Kivikoski, "A small planar inverted-F antenna for wearable applications", Wearable Computers International Symposium, pp. 95-100, Oct. 1999.

[118] D. Lamensdorf and L. Susman," Baseband-pulse-antenna technique", Antennas and Propagation Magazine, vol. 36, no. 1, pp. 20 – 30.,Feb. 1994.

[119] Ma Tzyh-Ghuang and Jeng Shyh-Kang, "Planar miniature tapered-slot-fed annular slot antenna for ultrawide-band radios," IEEE Trans. Antennas and Propagation, vol.-53, no. 3, pp. 1194-1202, March 2005.

[120] B. Scheers, M. Acheroy, and A. Vander Vorst, "Time-domain simulation and characterization of TEM horns using a normalized impulse response," IEE Proc.-Microw. Antennas Propagation, vol.-147, no. 6, pp. 463-468, December 2000.

[121] S. Zwierzchowski and P. Jazayeri, "A system and network analysis approach to antenna design for UWB communications," Antennas and Propagation Society International Symposium, vol. -1, pp. 826-829, June 2003.

[122] Mohammadian, A.H.; Rajkotia, A.; Soliman, S.S, "Characterization of UWB Transmit-Receive Antenna System", IEEE Conf. on Ultra Wideband Systems and Technologies, pp.157 – 161, Nov. 2003.

[123] Xianming Qing; Zhi Ning Chen; Chia, M.Y.W., "Network approach to UWB antenna transfer functions characterization", 2005 European Microwave Conference, vol. 3, Oct. 2005.

[124] S. Makarov, S. Kulkarni, and R. Ludwig, "Some considerations for compact resonant UHF PIFAs," 2006 IEEE Antenna Applications Symposium, pp. 56-67, Sep. 2006.

[125] Application note, "Circular polarity technology", Luxul Technology, available online http://www.luxul.net/luxulTech.pdf

[126] S. Makarov, "Antenna orientation for circular polarization," unpublished, Nov. 2006.

[127] S. Kulkarni and S. Makarov," A Circularly Polarized UHF Antenna at 550-700 MHz" accepted -IEEE Antennas and Propagation Society Int. Symp., June 2007.

[128] G. H. Brown, "The turnstile antenna," Electronics, April 1936, pp. 14-17.

[129] G. H. Brown, "A pre-tuned turnstile antenna," Electronics, vol. 18, June 1945, pp. 102-107.

[130] J. D. Kraus, *Antennas*, McGraw Hill, New York, 1950, pp. 424-428.

[131] T. A. Milligan, *Modern Antenna Design*, Wiley-IEEE Press, New York, 2005, second ed., pp. 231-237.

[132] Maamria and T. Nakamura, "Simple antenna for circular polarization," IEE Proceedings on Microwaves, Antennas and Propagation, vol. 139, no. 2, April 1992, pp. 157-158.

[133] R. K. Zimmerman, "Crossed dipoles fed with a turnstile network," IEEE Trans. Microwave Theory Techniques, vol. 46, no. 12, Dec. 1998, pp. 2151-2156.

[134] M. S. Gatti and D. J. Nybakken, "A circularly polarized crossed drooping dipole antenna," IEEE AP-S International Symposium, May 1990, vol. 1, pp. 254-257.

[135] Hu Cheng-Nan, Chuang Ching-Song, Chou Der-Chorng, Liu Koong-Jeng, and Hung Chia-I, "Design of the cross-dipole antenna with near-hemispherical coverage in finite-element phased array by using genetic algorithms," IEEE International Conference on Phased Array Systems and Technology, pp. 303 – 306, May 2000,

[136] A. Kerkhoff, and S. Ellingson, "A wideband planar dipole antenna for use in the long wavelength demonstrator array (LWDA)," IEEE AP-S International Symposium, vol. 1B, pp. 553-556, July 2005.

[137] S. Ellingson and A. Kerkhoff, "Comparison of two candidate elements for a 30-90 MHz radio telescope array," IEEE AP-S International Symposium, vol. 1A, pp. 590-593, July 2005.

[138] J. A. MacDonald, D. M. McPherson, and M. J. Devine, "Axial ratio optimization of an array of crossed-dipoles using phasing posts," IEEE AP-S International Symposium, vol. 2, pp. 1252-1255, June 1994.

[139] V. V. Ovsyanikov, A. L. Olshevsky, A. V. Reuta, K. V. Rodin, E. D. Romanenko, and E. R. Beznosova, "Dual-frequency turnstile antenna with impedance elements," 12th International Conference Microwave and Telecommunication Technology, pp. 339 – 340, Sep. 2002.

[140] D. E. Ping, J. T. Shaffer, L. U. Brown, and R. B. Dybdal, "A broadband rolled edged cavity antenna," IEEE AP-S International Symposium, vol. 1, pp. 787-790, June 2004.

[141] H. Morishira, H. Hamada, K. Nishida, and T. Nagao, "A Wideband Circularly Polarized Dipole Antenna," IEEE AP-S International Symposium, vol. 4, pp. 2348-2350., June 1998

[142] R. C. Johnson, Ed., Antenna Engineering Handbook, McGraw Hill, New York, third ed., pp. 43-23 - 43-27, 1993.

[143] L. Basilio, J. Williams, D. Jackson, and M. Khayat, "Comparative study of new GPS reduced-surface-wave Antenna," IEEE Antennas and Wireless prop. Letters, vol. 4, pp. 233-236, 2005.

[144] R.A. Burberry, *VHF and UHF antennas*, Peter Peregrinus Ltd., London, pp. 242-245, 1992.

[145] H.W. Sams, *Reference data for radio engineers*, Howard .W. Sams & Co, pp 24-21, 1975.

[146] Application note, "GPS Tutorial", Javad Navigation system, pp. 39-40, available online http://www.javad.com/index.html?/jns/gpstutorial/index.html

.

Appendix A Code details

Code execution flowchart

The figure below shows the code execution flowchart for the MoM solver.
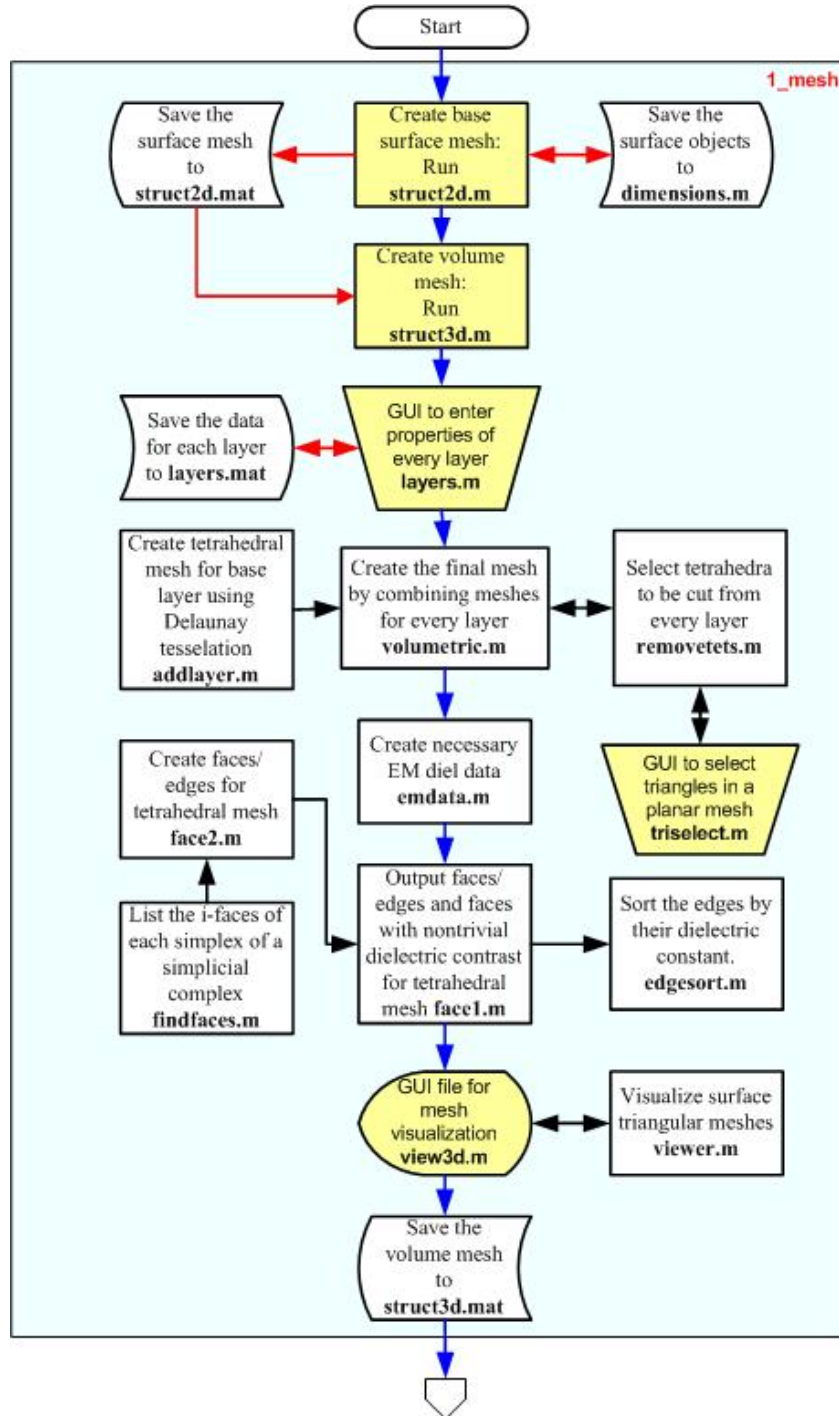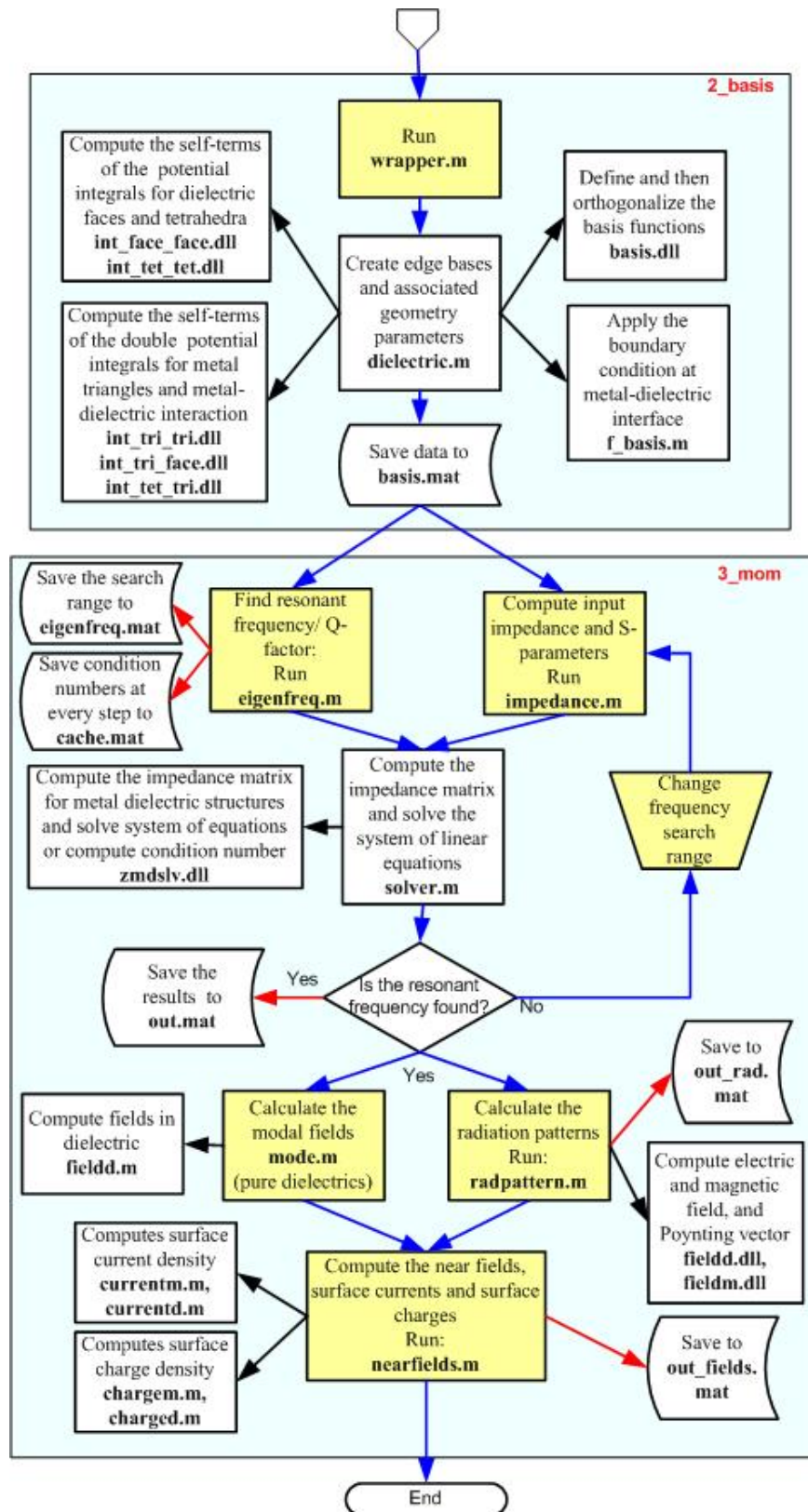
Figure. A.1 Code execution flowchart

Summary of the potential integrals for the impedance matrix

The potential integrals for the metal MoM impedance matrices are pre-calculated and saved in structure `geom` (metal) and in the structure `GEOM` (dielectric and metal-dielectric) in the sparse matrix format.

Table A.1 Summary of the potential integrals for the impedance matrix

Integral	Code in 2_basis\codes	Reference	Remarks
METAL			
$\iint\limits_{t_p t_q} \dfrac{1}{\|\vec{r}-\vec{r}'\|} ds'ds$	int_tri_tri.cpp int_tri_tri.m	Eqs. (2.1.22) and (2.1.23)	Structure geom; fields: ttSS-array of potential integrals (divided by the product of face areas) ttIS - indices of observation faces ttJS - indices of integration faces
$\iint\limits_{t_p t_q} \dfrac{\vec{\rho}_i \cdot \vec{\rho}'_j}{\|\vec{r}-\vec{r}'\|} ds'ds$	int_tri_tri.cpp int_tri_tri.m	Eqs. (2.1.21), (1.1.24), (2.1.25)	Structure geom; fields: ttRS - array of potential integrals (divided by the product of face areas) with 3x3 matrix elements (rho_i x rho_j) assembled as a 1D array ttIS - indices of observation faces ttJS - indices of integration faces
DIELECTRIC			
$\iint\limits_{V_p V_q} \dfrac{1}{\|\vec{r}-\vec{r}'\|} d\vec{r}d\vec{r}'$	int_tet_tet.cpp int_tet_tet.m	Eqs. (2.2.24) and (2.2.28)	Structure GEOM; fields: TTSS - array of potential integrals (divided by tetrahedra volumes) TTIS - indices of observation tetrahedra TTJS - indices of integration tetrahedra
$\int\limits_{\Omega_p} \int\limits_{\Omega_q} \dfrac{1}{\|\vec{r}-\vec{r}'\|} d\Omega'd\Omega$	int_face_face.cpp int_face_face.m	Eqs. (2.2.25), (2.2.22) and (2.2.23)	Structure GEOM; fields: FFSS - array of potential integrals (divided by face areas) FFIS - indices of observation faces FFJS - indices of integration faces This integral is identical to the first metal potential integral
METAL-DIELECTRIC			

Integral	Code	Reference	Remarks

$\displaystyle\iint_{t_p\,V_{p'}}\frac{\vec{\rho}_i}{\left\lvert\vec{r}-\vec{r}'\right\rvert}\,d\vec{r}'ds$	`int_tet_tri.cpp`
	`int_tet_tri.m`
		Eq. (2.3.23)	`Structure GEOM; fields:`
			`TtSS - array of potential`
			`integrals (divided by`
			`tetrahedron volume/face`
			`area) with 3x1 vector`
			`elements (rho_i) assembled as`
			`a 1D array`
			`TtIS - indices of observation`
			`faces (metal)`
			`TtJS - indices of integration`
			`tetrahedra (dielectric)`

$\displaystyle\iint_{t_q\,\Omega_{q'}}\frac{1}{\left\lvert\vec{r}-\vec{r}'\right\rvert}$	`int_tri_face.cpp`
	`int_tri_face.m`
		Eq. (2.3.24)	`Structure GEOM; fields:`
			`tFSS - array of potential`
			`integrals (divided by the`
			`product of face areas)`
			`tFIS - indices of observation`
			`faces (metal)`
			`tFJS - indices of observation`
			`faces (dielectric)`
			`This integral is identical to`
			`the first metal potential`
			`integral`

Then, the potential integrals are used in the impedance matrix script `zmdslv.cpp` (folder `3_mom\codes`).

<div align="center">

Summary of the field integrals (far- and near-field)

</div>

The potential field integrals are not pre-calculated. They are computed in the scripts `fieldm.cpp` and `fieldd.cpp` (folder `3_mom\codes`) along with the non-singular frequency-dependent part.

<div align="center">

Table A.2 Summary of the field integrals

</div>

Integral	Code in `3_mom\codes`	Reference	Remarks
METAL			
$\displaystyle\int_{S}\nabla\frac{\exp(-ik\left\lvert\vec{r}-\vec{r}'\right\rvert)}{\left\lvert\vec{r}-\vec{r}'\right\rvert}\,ds'$	`fieldm.cpp` `fieldm.m`	Eq. (2.1.26) and Eqs. (2.1.29), (2.1.30)	`void ScatTri in` `fieldm.cpp`
$\displaystyle\int_{S}\frac{\exp(-ik\left\lvert\vec{r}-\vec{r}'\right\rvert)}{\left\lvert\vec{r}-\vec{r}'\right\rvert}\,ds'$	`fieldm.cpp` `fieldm.m`	Eq. (2.1.26)	`void pot_t in` `fieldm.cpp`
DIELECTRIC			
$\displaystyle\int_{V}\nabla\frac{\exp(-ik\left\lvert\vec{r}-\vec{r}'\right\rvert)}{\left\lvert\vec{r}-\vec{r}'\right\rvert}\,d\vec{r}'$	`fieldd.cpp` `fieldd.m`	Eq. (2.2.19), (2.2.20) and (2.2.30)	`void ScatTet in` `fieldd.cpp`

$\int\limits_{V} \dfrac{\exp(-ik\|\vec{r}-\vec{r}'\|)}{\|\vec{r}-\vec{r}'\|} d\vec{r}'$	`fieldd.cpp` `fieldd.m`	Eq. (2.2.19)	`void int_tetc in` `fieldd.cpp`

The subroutines for the field integrals related to the triangular metal faces are also used for the dielectric field integrals (in `fieldd.cpp`).

Within a neighboring sphere of radius R, the N and d for the Gaussian formula on facets are hard coded for the field integrals as $N = 7, d = 5$. Similarly, the N and d for the Gaussian formula on tetrahedra (also applied to the non-singular integral parts) are hard coded for the field integrals as $N = 5, d = 3$. Outside the neighbor sphere, the central-point approximation is used. Note that the integrals for the impedance matrix allows for higher integration accuracy.

Summary of the matrix solver - LAPACK routines (Intel Math Kernel Library)

The summary of LAPACK routines used in the code is given in Table A.3. The C++ scripts containing the LAPACK routines are compiled using the command (Intel Math Kernel Library needs to be installed) `mex filename.cpp *.lib`.

Table A.3 Summary of LAPACK routines

C++ script	LAPACK routine
`basis.cpp` in folder `2_basis`	`dgetrf` Computes the LU factorization of a general real matrix

`zmdslv.cpp` in folder `3_mom`	`zlansy`
	Returns the value of 1-norm of a complex symmetric matrix
	`zsytrf`
	Computes the Bunch-Kaufman factorization of a complex symmetric matrix
	`zsycon`
	Estimates the reciprocal of the condition number of a complex symmetric matrix
	`zsysv`
	Computes the solution to the system of linear equations with a complex symmetric impedance matrix. Diagonal pivoting

The routines `zlansy`, `zsytrf` , `zsycon` are used for the eigenmode solution only.